Bulletin 37
Part 2
(of 7 Parts)

THE SHOCK AND VIBRATION BULLETIN

JANUARY 1968

A Publication of
THE SHOCK AND VIBRATION
INFORMATION CENTER
Naval Research Laboratory, Washington, D.C.

Office of
The Director of Defense
Research and Engineering

SYMPOSIUM MANAGEMENT

THE SHOCK AND VIBRATION INFORMATION CENTER

William W. Mutch, Director
Henry C. Pusey, Coordinator
Rudolph H. Volin, Coordinator
Katherine G. Jahnel, Administrative Secretary

37th Program Committee

David Askin, U.S. Army Frankford Arsenal
Jerry Sullivan, Naval Ship Systems Command Hdq.
Robert F. Wilkus, Systems Engineering Group, W-PAFB
Dennis J. Martin, NASA Langley Research Center

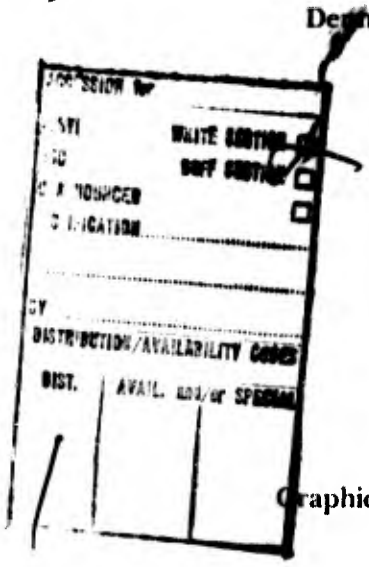

Navy Liaison

Naval Training Device Center

William Powell
Allan Collier

Bulletin Production

Graphic Arts Branch, Technical Information Division,
Naval Research Laboratory

Bulletin 37
Part 2
(of 7 Parts)

THE SHOCK AND VIBRATION BULLETIN

JANUARY 1968

A Publication of
THE SHOCK AND VIBRATION
INFORMATION CENTER
Naval Research Laboratory, Washington, D.C.

The 37th Symposium on Shock and Vibration was held in Orlando, Florida, on 24-26 October 1967. The U.S. Navy was host.

Office of
The Director of Defense
Research and Engineering

FOREWORD

It is the aim of the staff of the Shock and Vibration Information Center to publish the Shock and Vibration Bulletin as promptly as possible after each Symposium. It shall contain all of the papers programmed for that Symposium, together with the discussions of those papers, and additional papers which were contributed but could not be accommodated on the program. All of these are to be edited and put up in good style and form as befits research and development reports of the high quality and reference value which has become a tradition in these volumes.

In recent years distribution of the Bulletin has begun about four months after the Symposium. Some of the causes for this delay are set forth here to explain to impatient readers why publication takes so long, and in the hope that potential authors may cooperate to reduce the time interval in the future.

As this is written, six weeks after the last day of the Symposium, and eight and a half weeks after the "deadline," five of the 100 manuscripts are still outstanding. Although authors are provided with specific guidelines for the style and form in which manuscripts should be prepared, too often these are ignored with the result that time and costly editing are required.

In the 37th Bulletin a number of interesting discussions were missed because of difficulties with one tape recorder. Restrictions on the use of half tones account for the absence in Bulletin No. 37 of authors' pictures at the beginning of each paper. Unfamiliar new regulations limiting the distribution of some unclassified material have caused delays in the release of some manuscripts. Finally, printing regulations aimed at achieving economy impose limitations which sometimes require slower, less costly procedures.

Ways are being explored which may result in overcoming some of the delays which presently affect publication of the Bulletin. Be assured that the staff of the Shock and Vibration Information Center is aware of the problems and is as anxious as you are to improve the quality and speed the publication of the Bulletins.

BLANK PAGE

CONTENTS

PART 2

Instrumentation and Analysis

PORTABLE LASER INSTRUMENT FOR VIBRATION ANALYSIS AND TRANSDUCER CALIBRATION 1
G. A. Massey and R. R. Carter, Sylvania Electronic Systems, Mountain View, California

HIGH-FREQUENCY MICROPHONE CALIBRATION USING A SUPERSONIC FREE-FLIGHT RANGE 7
C. D. Hayes, Jet Propulsion Laboratory, Pasadena, California, and R. C. Binder, University of Southern California, Los Angeles, California

METHOD OF MEASURING VIBRATORY DISPLACEMENTS IN TERMS OF A LIGHT WAVELENGTH 13
J. L. Goldberg, National Standards Laboratory, Sydney, Australia

CALIBRATION OF ACCELEROMETERS BY IMPULSE EXCITATION AND FOURIER INTEGRAL TRANSFORM TECHNIQUES 17
J. D. Favour, The Boeing Company, Seattle, Washington

BIDIRECTIONAL SHOCK AND HIGH-IMPACT EFFECTS ON SHOCK TRANSDUCERS 29
V. F. DeVost and P. S. Hughes, Naval Ordnance Laboratory, Silver Spring, Maryland

INFLUENCE OF FIXTURE STRESS CONCENTRATIONS ON RING ACCELEROMETERS . . 43
J. A. Nagy and C. E. Henley, Jr., NASA Goddard Space Flight Center, Greenbelt, Maryland

SONAR TRANSDUCER VIBRATION REQUIREMENTS AND MEASUREMENT TECHNIQUES. 51
G. M. Mayer and E. G. Marsh, Navy Underwater Sound Laboratory, New London, Connecticut

AUTOMATED VIBRATION ANALYSIS 57
R. J. Pabich and W. H. Sellers, Raytheon Company, Bedford, Massachusetts

A COMPACT, LOW-COST SHOCK-SPECTRUM ANALYZER 65
W. W. Mebane, Naval Ordnance Laboratory, Silver Spring, Maryland

DYNAMIC PHASE PLOTTING 77
T. E. Smart, Sandia Corporation, Albuquerque, New Mexico

RANDOM-VIBRATION-INDUCED ERRORS IN A MISSILE CAUSED BY NONLINEAR INERTIAL ACCELEROMETERS 87
N. A. Leifer, Bell Telephone Laboratories, Inc., Whippany, New Jersey

VIBRATION DISTRIBUTIONS IN MULTIPANEL STRUCTURES: COMPARISON OF MEASUREMENTS WITH STATISTICAL ENERGY PREDICTIONS 99
E. E. Ungar and N. Koronaios, Bolt Beranek and Newman Inc., Cambridge, Massachusetts

CONSTANT BANDWIDTH FM DATA SYSTEM DESIGNED FOR SATURN S-IVB/V VIBRATION TESTS 109
D. F. Redford, Thiokol Chemical Corporation, Brigham City, Utah

DYNAMICS PORTION OF GEMINI AGENA TARGET VEHICLE ENGINE MODIFICATION AND TEST PROGRAM (PROJECT SURE FIRE) 117
N. Angelopulos, Lockheed Missiles & Space Company, Sunnyvale, California

DYNAMIC ANALYSIS OF COMPLEX STRUCTURES 173
M. D. Benton, G. K. Hobbs, Hughes Aircraft Company, El Segundo, California, and J. R. Dickerson, University of Texas, Austin, Texas

PAPERS APPEARING IN PART 1
Part 1 - Classified
(Titles Unclassified)

RECENT WORK ON SHOCK AT N.C.R.E.
A. M. MacIntosh, Naval Construction Research Establishment, Dunfermline, Fife, Scotland

STATE OF SHOCK IN THE NAVY, 1967
H. L. Rich, Naval Ship Research and Development Center, Washington, D.C.

NAVY DYNAMIC DESIGN ANALYSIS METHOD - PANEL SESSION

SHOCK HARDENING RIVERINE WARFARE CRAFT FOR VIETNAM
O. H. Porter and F. Weinberger, Naval Ship Research and Development Center, Washington, D.C.

SHOCK TESTING OF SONAR TRANSDUCERS -- A STATUS REPORT
G. M. Mayer and C. D. Johnson, Navy Underwater Sound Laboratory, New London, Connecticut

AN EXPLOSION SHOCK-TESTING METHOD FOR SHIPBOARD EQUIPMENT
R. R. Higginbotham, Naval Ship Research and Development Center, Portsmouth, Virginia

RIGID BODY RESPONSE OF NAVAL SURFACE VESSELS TO AIR BLAST
J. T. Irick, AVCO Corporation, Lowell, Massachusetts, S. Silverman and W. E. Baker, Southwest Research Institute, San Antonio, Texas

REACTION OF MILD STEEL TARGETS TO EXPLODING MUNITIONS
J. W. Apgar, Ballistic Research Laboratories, Aberdeen Proving Ground, Maryland

RESPONSE OF A MISSILE STRUCTURE UNDER HIGH VELOCITY IMPACT
C. Riparbelli, General Dynamics/Pomona, Pomona, California

AIM4D/F4 CAPTIVE-FLIGHT VIBRATION LOADS AND ENVIRONMENTAL MEASUREMENTS PROGRAM
C. D. Knauer, Jr. and P. E. McHorney, Hughes Aircraft Company, El Segundo, California

PAPERS APPEARING IN PART 3

Vibration Testing

WHOM DO WE THINK WE ARE FOOLING?
J. P. Salter, Royal Armaments Research and Development Establishment, Fort Halstead, Sevenoaks, Kent, England

INTERNAL VIBRATION OF ELECTRONIC EQUIPMENT RESULTING FROM ACOUSTIC AND SHAKER INDUCED EXCITATION
A. D. Houston, Lockheed Missiles & Space Company, Sunnyvale, California

RANDOM-VIBRATION RESPONSE DATA FOR ORBITING GEOPHYSICAL OBSERVATORY: FLIGHT, ACOUSTIC, AND VIBRATION TEST
W. G. Elsen, NASA Goddard Space Flight Center, Greenbelt, Maryland

RANDOM-VIBRATION TEST LEVEL CONTROL USING INPUT AND TEST ITEM RESPONSE SPECTRA
A. J. Curtis and J. G. Herrera, Hughes Aircraft Company, Culver City, California

RANDOM-FORCE VIBRATION TESTING
J. V. Otts and N. F. Hunter, Jr., Sandia Corporation, Albuquerque, New Mexico

CONTROL POINT AVERAGING FOR LARGE SPECIMEN VIBRATION TESTS
H. R. Berkman, Litton Systems, Inc., Van Nuys, California

VIBRATION METHODS FOR MULTIPLE RANDOM EXCITATION
W. E. Noonan, McDonnell Company, St. Louis, Missouri

DYNAMIC TESTING OF FULL-SCALE SATURN LAUNCH VEHICLES
B. R. Jacobs, Northrop Nortronics, Huntsville, Alabama

BUFFET RESPONSE MEASUREMENTS OF A SEVEN PERCENT AEROELASTICALLY SCALED MODEL OF VARIOUS TITAN III CONFIGURATIONS
J. T. Uchiyama and F. W. Peters, Martin-Marietta Corporation, Denver, Colorado

HIGH-FORCE VIBRATION TESTING OF THE SATURN S-IVB/V STAGE
L. G. Smith, McDonnell Douglas Corporation, Huntington Beach, California

SIMPLIFIED METHOD OF CONDUCTING A DUAL RANDOM-VIBRATION INTEGRATED SYSTEM TEST
J. G. Colt, Radio Corporation of America, Burlington, Massachusetts

CONTROL STABILIZATION FOR MULTIPLE SHAKER TESTS
N. F. Hunter, Jr., Sandia Corporation, Albuquerque, New Mexico, and J. G. Helmuth, Chadwick-Helmuth Company, Inc., Monrovia, California

THE SHIM SPRING ISOLATOR
L. Wallerstein, Jr., Lord Manufacturing Company, Erie, Pennsylvania

Test Facilities

ADVANCED COMBINED ENVIRONMENTAL TEST FACILITY
E. J. Kirchman and C. J. Arcilesi, NASA Goddard Space Flight Center, Greenbelt, Maryland

DEVELOPMENT OF SIMULATED AIRCRAFT DELIVERY USING A ROCKET SLED
W. R. Kampfe and K. M. Timmerman, Sandia Corporation, Albuquerque, New Mexico

AERODYNAMIC NOISE INVESTIGATION IN A SHORT-DURATION SHOCK TUNNEL
D. H. Ross, Aerospace Corporation, El Segundo, California

IMPACT TESTING WITH A FOUR-INCH AIR GUN AND LEAD TARGETS
H. J. Davis, Harry Diamond Laboratories, Washington, D. C.

PAPERS APPEARING IN PART 4

Shock Analysis and Simulation

MEASUREMENT AND ANALYSIS OF SPACECRAFT SEPARATION TRANSIENT RESPONSE FOR MARINER-TYPE SPACECRAFT
P. Barnett, Jet Propulsion Laboratory, Pasadena, California

MECHANICAL SHOCK OF HONEYCOMB STRUCTURE FROM PYROTECHNIC SEPARATION
J. R. Olsen, J. R. West, Jr., H. Himelblau, North American Rockwell Corporation, Los Angeles, California, C. D. Knauer, Jr., and P. E. McHorney, Jr., Hughes Aircraft Company, El Segundo, California

A SIMPLE STRENGTH CONCEPT FOR DEFINING PRACTICAL HIGH-FREQUENCY LIMITS OF SHOCK SPECTRUM ANALYSIS
M. Gertel and R. Holland, Allied Research Associates, Concord, Massachusetts

TRANSIENT VIBRATION SIMULATION
T. E. Fitzgerald and L. C. Kula, The Boeing Company, New Orleans, Louisiana

PREDICTING MECHANICAL SHOCK TRANSMISSION
J. E. Manning and K. Lee, Bolt Beranek and Newman Inc., Cambridge, Massachusetts

SHOCK DAMAGE MECHANISM OF A SIMPLE STRUCTURE
L. T. Butt, Naval Ship Research and Development Center, Portsmouth, Virginia

GENERAL MOTORS ENERGY-ABSORBING STEERING COLUMN AS A COMPONENT OF SHIP-BOARD PERSONNEL PROTECTION
J. T. Hawkins and A. E. Hirsch, Naval Ship Research and Development Center, Washington, D. C.

HEAVY WEIGHT SHOCK TEST FIXTURES: DESIGN AND RESULTS
C. G. Schrader, San Francisco Bay Naval Shipyard, San Francisco, California

DERIVATION AND IMPLICATIONS OF THE NAVY SHOCK ANALYSIS METHOD
F. J. Heymann, Westinghouse Electric Corporation, Lester, Pennsylvania

DYNAMIC ANALYSIS OF A TYPICAL ELECTRONIC EQUIPMENT CABINET SUBJECTED TO NUCLEAR-WEAPON-INDUCED SHOCK
J. H. Putukian, Kaman Avidyne, Burlington, Massachusetts

DEVELOPMENT OF A ZERO-G COAST PHASE AIR GUN
S. Rodkin, General Electric Company, Philadelphia, Pennsylvania

DEVELOPMENT OF A MISSILE LAUNCH SHOCK TEST FACILITY FOR SHILLELAGH
R. W. Stevens, Martin-Marietta Corporation, Orlando, Florida

USE OF EXPLODING WIRE APPARATUS FOR LABORATORY SIMULATION OF SHOCK WAVES
F. B. Safford, Mechanics Research Inc., El Segundo, California, and R. C. Binder, University of Southern California, Los Angeles, California

NIKE-X SHOCK TUBE FACILITY
R. G. Donaghy and J. J. Healy, Office of the Chief of Engineers, Department of the Army, Washington, D.C.

DESIGN AND PERFORMANCE OF DUAL MODE SHOCK MACHINE
W. D. Everett, Naval Missile Center, Point Mugu, California

Air Blast and Ground Shock

INFLUENCE OF SHIP MOBILITY ON INTERNAL FORCES PRODUCED BY BLAST
A. Chajes, F. J. Dzialo, and M. P. White, Department of Civil Engineering, University of Massachusetts, Amherst, Massachusetts

DYNAMIC BEHAVIOR OF SHIPBOARD ANTENNA MASTS SUBJECTED TO BLAST-GENERATED OVERPRESSURES
F. A. Britt and R. H. Anderson, Mechanics Research, Inc., El Segundo, California

*HARDENED ANTENNA TECHNOLOGY
D. A. Benson, A. F. Gurdo, R. W. Mair and D. J. Waters, Rome Air Development Center, Griffiss AFB, New York

ABSOLUTE UPPER AND LOWER BOUNDS FOR THE CRITICAL BLAST LOADING ENVIRONMENT OF TARGET ELEMENTS AND SYSTEMS
E. Sevin and W. D. Pilkey, IIT Research Institute, Chicago, Illinois

ELASTIC-PLASTIC COLLAPSE OF STRUCTURES SUBJECTED TO A BLAST PULSE
W. B. Murfin, Sandia Corporation, Albuquerque, New Mexico

INTERNAL LOADING OF STRUCTURES BY BLAST WAVES
J. F. Melichar, Ballistic Research Laboratories, Aberdeen Proving Ground, Maryland

EFFECTS OF SLIDING ON BLAST LOADS REQUIRED TO OVERTURN STRUCTURES
C. E. Gebhart, IIT Research Institute, Chicago, Illinois

USE OF DETONABLE GAS EXPLOSIONS FOR BLAST AND SHOCK STUDIES
M. R. Johnson and M. J. Balcerzak, General American Research Division, Niles, Illinois

INCORPORATION OF SHOCK PROTECTION IN EXISTING ABOVEGROUND CYLINDRICAL STRUCTURES SUBJECTED TO NUCLEAR BLAST
E. Cohen, S. Weissman and L. Sanchez, Ammann and Whitney, New York, New York

PAPERS APPEARING IN PART 5

Large Vibro-Acoustic Test Facilities

VIBROACOUSTIC ENVIRONMENTAL SIMULATION FOR AEROSPACE VEHICLES
K. McK. Eldred, Wyle Laboratories, El Segundo, California

*RTD SONIC FATIGUE FACILITY, DESIGN AND PERFORMANCE CHARACTERISTICS
A. W. Kolb and H. A. Magrath, Air Force Flight Dynamics Laboratory, Wright-Patterson AFB, Ohio

*This paper appears in Shock and Vibration Bulletin 37, Supplement.

OPERATIONAL CHARACTERISTICS OF A 100,0[illegible] CUBIC FOOT ACOUSTIC REVERBERATION CHAMBER
F. M. Murray, Wyle Laboratories, Huntsville, Alabama

CONCEPT, DESIGN, AND PERFORMANCE OF THE SPACECRAFT ACOUSTIC LABORATORY
R. J. Wren, W. D. Dorland, J. D. Johnston, Jr., NASA Manned Spacecraft Center, Houston, Texas, and K. McK. Eldred, Wyle Laboratories, El Segundo, California

THEORETICAL STUDY OF ACOUSTIC SIMULATION OF IN-FLIGHT ENVIRONMENTS
R. W. White, Wyle Laboratories, Huntsville, Alabama

DATA HANDLING METHODS FOR LARGE VEHICLE TESTING
D. J. Bozich, Wyle Laboratories, Huntsville, Alabama

DEVELOPMENT AND VERIFICATION OF THE VIBRATION TEST REQUIREMENTS FOR THE APOLLO COMMAND AND SERVICE MODULES
D. E. Newbrough, General Electric Company, Houston, Texas, R. A. Colonna, NASA Manned Spacecraft Center, Houston, Texas, and J. R. West, North American Rockwell Corporation, Downey, California

DEVELOPMENT AND VERIFICATION OF THE APOLLO LUNAR MODULE VIBRATION TEST REQUIREMENTS
D. E. Newbrough, General Electric Company, Houston, Texas, M. Bernstein and E. F. Baird, Grumman Aircraft Engineering Company, Bethpage, New York

SATURN S-II, S-IVB, AND INSTRUMENT UNIT SUBASSEMBLY AND ASSEMBLY VIBRATION AND ACOUSTIC EVALUATION PROGRAMS, PARTS 1 AND 2
R. W. Schock, J. M. Everitt, NASA Marshall Space Flight Center, Huntsville, Alabama, and J. R. Seat, Brown Engineering Company, Huntsville, Alabama

DEVELOPMENT OF ACOUSTIC TEST CONDITIONS FOR APOLLO LUNAR MODULE FLIGHT CERTIFICATION
W. D. Dorland, R. J. Wren, NASA Manned Spacecraft Center, Houston, Texas, and K. McK. Eldred, Wyle Laboratories, El Segundo, California

*FACILITY SONIC FATIGUE PROOF TESTING
O. F. Maurer, Air Force Flight Dynamics Laboratory, Wright-Patterson AFB, Ohio

VIBROACOUSTIC TEST METHODS FOR VIBRATION QUALIFICATION OF APOLLO FLIGHT HARDWARE
R. W. Peverley, General Electric Company, Houston, Texas

ACOUSTICAL QUALIFICATION OF S-IC FIN STRUCTURES
C. J. Beck, Jr., The Boeing Company, Huntsville, Alabama, and D. R. Kennedy, Brown Engineering Company, Huntsville, Alabama

*SIMULATION OF ACOUSTIC FATIGUE FAILURE IN THE WIDEBAND NOISE TEST FACILITY OF THE AIR FORCE FLIGHT DYNAMICS LABORATORY
R. C. W. van der Heyde, Air Force Flight Dynamics Laboratory, Wright-Patterson AFB, Ohio

REAL-TIME COMBINED ACOUSTIC-VACUUM TESTING OF SPACECRAFT
L. J. Demas, NASA Goddard Space Flight Center, Greenbelt, Maryland

PAPERS APPEARING IN PART 6

Helicopter Environments

HELICOPTER VIBRATIONS
C. D. Roach, U. S. Army Aviation Materiel Laboratories, Fort Eustis, Virginia

HELICOPTER VIBRATION -- A MAJOR SOURCE, ITS PREDICTION AND AN APPROACH TO ITS CONTROL
R. P. White, Jr., and F. A. DuWaldt, Cornell Aeronautical Laboratory, Inc., Buffalo, New York

*IN-FLIGHT VIBRATION AND ACOUSTIC STUDY ON THE UH-1F HELICOPTER
C. E. Thomas and J. T. Ach, Air Force Flight Dynamics Laboratory, Wright-Patterson AFB, Ohio

*This paper appears in Shock and Vibration Bulletin 37, Supplement.

HELICOPTER FUSELAGE VIBRATION PREDICTION BY STIFFNESS MOBILITY METHODS
J. J. Sciarra, The Boeing Company, Morton, Pennsylvania

ISOLATION OF HELICOPTER ROTOR-INDUCED VIBRATIONS USING ACTIVE ELEMENTS
P. C. Calcaterra and D. W. Schubert, Barry Research & Development, Watertown, Massachusetts

HYBRID VIBRATION-ISOLATION SYSTEM FOR HELICOPTERS
D. A. Bies and T. M. Yang, Bolt Beranek and Newman Inc., Los Angeles, California

RECENT ADVANCES IN THE STUDY OF SYNCHRONOUS VIBRATION ABSORBERS
A. V. Srinivasan, Kaman Corporation, Bloomfield, Connecticut

OPTIMIZING THE DYNAMIC ABSORBER TO INCREASE SYSTEM DAMPING
G. K. Jones, NASA Goddard Space Flight Center, Greenbelt, Maryland

APPLICATION OF THE DYNAMIC ANTIRESONANT VIBRATION ISOLATOR TO HELICOPTER VIBRATION CONTROL
R. Jones and W. G. Flannelly, Kaman Corporation, Bloomfield, Connecticut

PAPERS APPEARING IN PART 7

Environmental Data

SURVEY OF THE CARGO-HANDLING SHOCK AND VIBRATION ENVIRONMENT
F. E. Ostrem, General American Research Division, Niles, Illinois

A NEW LOOK AT TRANSPORTATION VIBRATION STATISTICS
J. W. Schlue and W. D. Phelps, Jet Propulsion Laboratory, Pasadena, California

RECENT SHOCK AND VIBRATION MEASUREMENTS ON THE M-151 (JEEP) VEHICLE
R. D. Brunnemer and G. M. Pomonik, Hughes Aircraft Company, Canoga Park, California

LATERAL IMPACT SHOCK DURING SHIP LOADING OF THE A3 POLARIS MISSILE
E. G. Fischer, C. R. Brown, and A. J. Molnar, Westinghouse Electric Corporation, Pittsburgh, Pennsylvania

*RF-4C VIBRATION AND ACOUSTIC ENVIRONMENT STUDY
J. F. Dreher, Air Force Flight Dynamics Laboratory, and W. D. Hinegardner, Systems Engineering Group, Wright-Patterson AFB, Ohio

EMPIRICAL CORRELATION OF FLIGHT VEHICLE VIBRATION RESPONSE
W. H. Roberts, Martin-Marietta Corporation, Orlando, Florida

VIBRATION DATA SUMMARY OF MINUTEMAN WING VI FLIGHT TEST MISSILES
R. R. Burnett and R. E. Morse, TRW Systems, Redondo Beach, California

SPACECRAFT VIBRATION: COMPARISON OF FLIGHT DATA AND GROUND TEST DATA
G. Kachadourian, General Electric Company, Philadelphia, Pennsylvania

MEASUREMENT AND ANALYSIS OF GUN FIRING AND VIBRATION ENVIRONMENTS OF THE RIVER PATROL BOAT
R. S. Reed, Naval Ordnance Laboratory, Silver Spring, Maryland

*RESPONSE OF THE AIM-9D (SIDEWINDER) MISSILE TO CAPTIVE-FLIGHT VIBRATION
W. W. Parmenter, Naval Weapons Center, China Lake, California

SCALE-MODEL WIND-TUNNEL ACOUSTIC DATA
J. R. Baratono and F. A. Smith, Martin-Marietta Corporation, Denver, Colorado

*This paper appears in Shock and Vibration Bulletin 37, Supplement.

INSTRUMENTATION AND ANALYSIS

PORTABLE LASER INSTRUMENT FOR VIBRATION ANALYSIS AND TRANSDUCER CALIBRATION*

G. A. Massey and R. R. Carter
Sylvania Electronic Systems
Mountain View, California

The design and performance of a 6328A laser heterodyne system providing sensitive broadband measurement of vibrations of mechanical structures and electromechanical transducers are described. Using this device, it is not necessary to attach any mass to the vibrating object. A single-frequency laser is used as the source, and a liquid acoustic-diffraction cell is used to shift the frequency of the reference or "local oscillator" beam in an interferometer. A second unshifted beam is reflected from the vibrating surface. When the reflected and shifted beams are combined on a photodetector, a beat frequency at 25 MHz is produced. Periodic motion of the reflecting surface then produces modulation sidebands about the 25-MHz difference or intermediate frequency. Equal phase shifts on the reflected light and on the intermediate frequency are produced by the motion. Thus the amplitude and frequency of the vibration can be recovered by demodulation of the phase-modulated 25-MHz signal, or by direct measurement using an ordinary radio-frequency spectrum analyzer. The 25-MHz frequency offset removes the directional ambiguity of the Doppler shift usually found in interferometer devices of this type. The single-frequency laser allows the working distance to be adjusted over a 5-in. range, with a nominal working distance of 4 ft between the surface and the instrument. An optical system with a 3-in. aperture makes measurement possible not only on polished surfaces but also on many diffuse reflecting surfaces, such as white paint. Thus it is possible to measure vibrations in many cases without special surface preparation or the addition of mirrors or corner reflectors to the vibrating structure. Measurements of vibration amplitudes from 0.25 in. to less than 0.04 in. and frequencies from 10 Hz to 700 kHz have been made with the prototype instrument in the laboratory; these measurements verify the enormous dynamic range possible with devices of this type. Theoretical and practical performance limits are discussed.

INTRODUCTION

This paper describes the design and performance of a portable laser heterodyne instrument for measurement of vibrations of mechanical structures. The development of reliable single-frequency lasers and optical frequency translators had made possible a new type of interferometer which is useful in a wide variety of measuring applications. Basically, the present instrument resembles a Michelson interferometer with the two beams of unequal path length, in which the frequency of one beam is shifted by 25 MHz from the frequency of the other. Frequency translation is accomplished by Bragg diffraction from traveling 25-MHz sound waves in water. The unshifted beam is focused on the vibrating surface, and the Doppler shift on the reflected light is heterodyne detected, with the frequency-shifted beam used as the phase reference.

Since other devices for vibration analysis and transducer calibration are already in use and have been extensively developed, it is reasonable to ask whether a laser measuring system offers any advantages over the older methods. There are, in fact, a number of important advantages, including the following:

1. Measurements can often be made without attaching any mass to the structure. This technique works with diffuse reflectors as well as specular surfaces, provided enough of the incident power is reflected.

2. The distance between the structure and the test instrument can be varied over a wide range by suitable design of the optical system.

*This work was sponsored by the National Aeronautics and Space Administration, Ames Research Center, Moffett Field, California, under Contracts NAS2-3137, NAS2-3643, and NAS2-4176.

3. The area over which the surface is measured can be very small, since the laser beam is focused on the surface.

4. The measurement frequency response is determined electronically and is not limited by resonances such as those present in mechanical strain gages or accelerometers.

5. The sensitivity to small motion is very good; usually it is much better than minimum requirements of practical applications.

BASIC OPTICAL CONFIGURATION

The optical system of the instrument is illustrated schematically in Fig. 1. Linearly polarized light from the laser is passed through the Bragg diffraction cell, in which a 25-MHz traveling sound wave in water acts as a moving grating to diffract approximately half of the incident light into the first order. This diffracted beam is frequency-shifted by 25 MHz and leaves the Bragg cell at an angle approximately 0.6 deg away from the zero order or undiffracted beam. A knife-edge prism deflects the shifted beam onto a beamsplitter mirror, where it becomes the reference beam or local oscillator signal for heterodyne detection. The zero-order beam passes the knife-edge prism and is folded by a mirror and calcite prism through a quarter-wave plate and into a relay telescope system which focuses the energy on the vibrating surface. The exit aperture of this telescope is 3 in., and the working distance between the exit aperture and the focus is 4 ft.

By designing the optical system with a large f/number (f/16 in this case), it is possible to make the large lenses single elements of high index glass, with a slight aspherical correction to hold the wavefront error to less than 1/8 wavelength for a single transmission through the entire system. The heterodyne system is very sensitive to reflections from surfaces oriented normal to the incident light. The reflections produce beat signals in the receiver that interfere with the detection of weak signals from diffusely reflecting vibrating surfaces. Therefore, the small lens in the relay telescope is an off-axis doublet; this is required to eliminate the troublesome specular reflections along the system axis which would otherwise be present with an on-axis element, even with the best antireflection coatings.

Reflected energy from the moving surface returns along the same path through the relay telescope and quarter-wave plate. However, the double passage through the quarter-wave plate rotates the polarization by 90 deg so that the returning light is refracted along a separate path by the birefringent calcite prism. The quarter-wave plate and calcite prism thus act as an optical directional coupler; this is essential because it permits the use of a single, self-aligning relay optical system for transmitting and receiving.

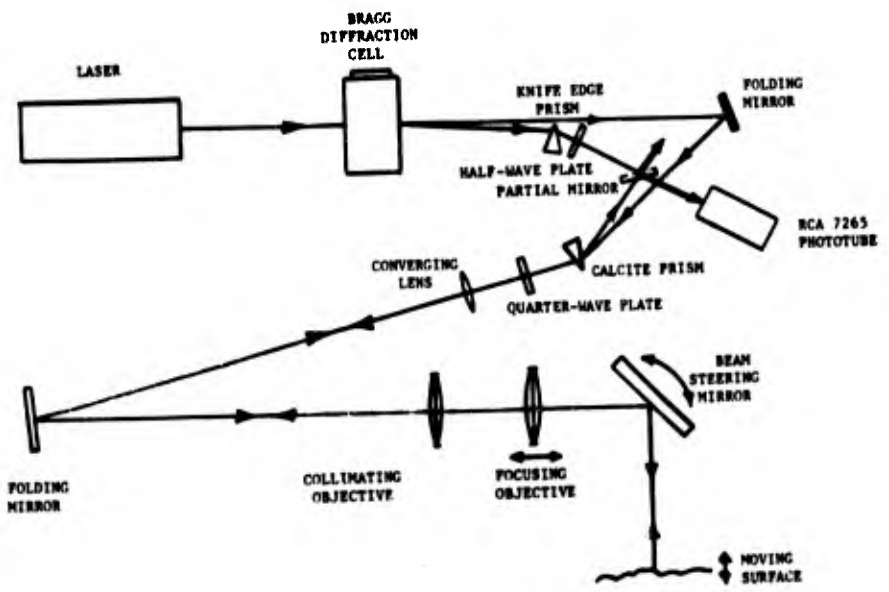

Fig. 1. Schematic diagram of vibration analyzer optical system

The long-focal-length optical system is folded so that the overall instrument dimensions are approximately 2 by 3 by 4 ft, including the electronic components. Figure 2 shows the folded optical configuration.

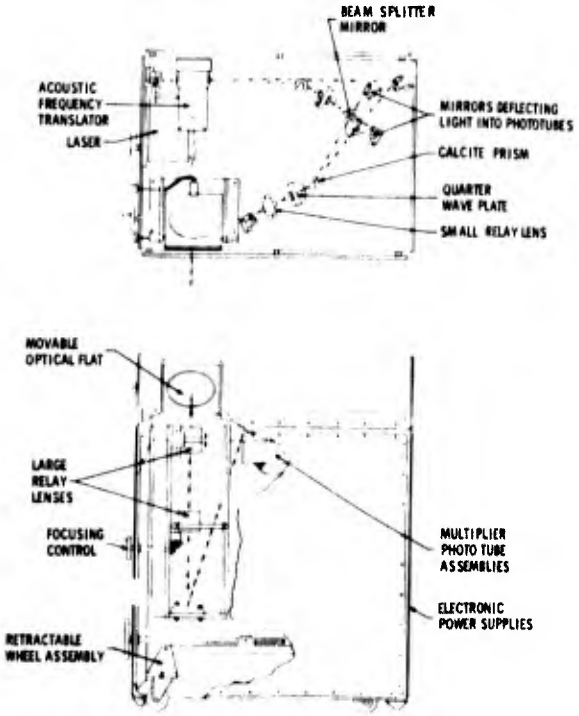

Fig. 2. Actual configuration of optical system in the instrument

Components are located such that the returning energy interferes with the reference wave on the beamsplitter mirror. The two resulting beams, which are modulated near 25 MHz with modulation envelopes 180 deg out of phase, leave the beamsplitter and are incident on a pair of RCA 7326 phototubes. Since the photoemission process is square law, the current outputs contain dc components because of the average incident light levels, and also rf components near 25 MHz because of the interference or beat between the frequency-shifted reference beam and the reflected light. The two outputs are combined electronically before passing to the demodulating receiver. If the reflecting surface is in motion, a Doppler shift is produced on the returning optical signal and therefore on the beat-frequency rf signal from the phototubes. The phase shift of the beat frequency is linearly related to the excursion of the moving surface; a motion of only 1/2 optical wavelength produces a complete cycle of phase shift at the beat frequency. The time rate of phase shift, which is the Doppler frequency shift, corresponds to surface velocity. Obviously, then, it is possible to measure the surface motion components along the optical axis by demodulation of the phototube outputs in a circuit such as an FM discriminator, or by direct display using a spectrum analyzer.

A single-frequency laser, Spectra-Physics Model 119, was used in the present instrument. Several advantages accrue if a single-frequency laser is used instead of a multimode laser. Among them are an insensitivity to unequal paths in the interferometer; the working distance can be varied over a range of several inches with no reduction in heterodyne signal. Also, the spurious low-frequency amplitude and phase modulations usually present in multifrequency lasers because of the free-running modes are absent.

The acoustic diffraction cell for translating the optical frequency uses 25-MHz sound waves in water as an effective traveling-wave diffraction grating. The acoustic source is an x-cut quartz crystal, 2 in. in diameter, with a fundamental resonance at 5 MHz. The crystal is excited using an impedance matching transformer resonant at the frequency of the fifth overtone of the crystal. Approximately one watt of power at 25 MHz is required to cause half of the incident light to be diffracted into the first order. To achieve a pure translated optical frequency, the light must interact with a traveling sound wave. In the present device the effects of standing waves are avoided by reflecting the sound beam at an angle after the first interaction so that the reflected sound does not cross the light beam at the Bragg angle.

The gain of the 7326 multiplier phototubes is sufficient to insure that the output noise levels are determined by amplified shot noise in the photocathode currents and not by thermal noise at the output terminals. Since the modulations at the heterodyne beat frequency are of opposite polarity in the two phototubes (as a result of conservation of optical energy at the beamsplitter mirror), the tube rf outputs must be subtracted electronically to obtain ideal balanced-mixer operation of the heterodyne receiver. It is this combined differential signal that is applied to the demodulation circuitry.

SIGNAL DEMODULATION AND DISPLAY

Some typical results using the prototype instrument with a spectrum analyzer as the

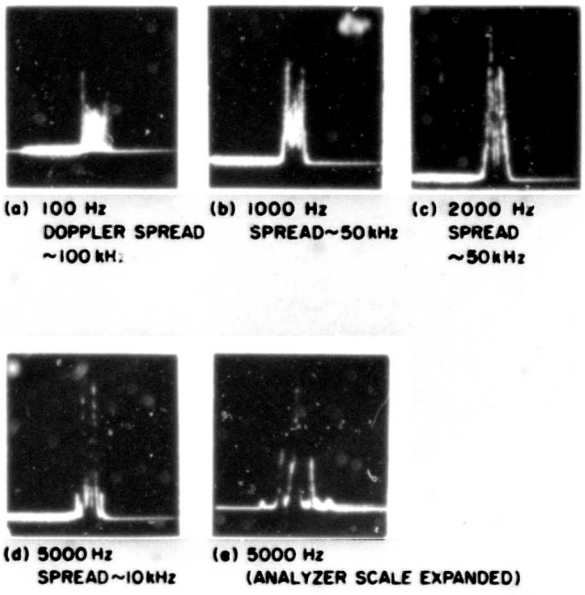

Fig. 3. Spectra obtained from surface with aluminum paint at various vibration frequencies

demodulation device are shown in Fig. 3. An unpolished metal surface covered with aluminum paint was the target; vibration was produced by attaching the sample to a loudspeaker voice coil. The peak amplitudes for these spectra were between 2000 μin. and about 3.6 μin., with the greater excursions at the lower frequencies. Similar results have been obtained with surfaces of white paper, flat white paint, and Scotchlite tape. Amplitudes of vibration from 0.5 in. to 0.04 μin. have been measured in this way with an aluminized mirror surface. The spectrum analyzer display is useful when the vibration is essentially sinusoidal, because interpretation of the spectrum is most easily carried out.

There are additional advantages of the spectrum analyzer display technique, because the controls on such an instrument provide a variable-parameter receiver. It is possible to adjust the instantaneous bandwidth to very small values, when the signal strength or vibration amplitude is weak, and yet the vibration frequency or the peak Doppler shift may be several megahertz. However, it is not convenient to measure vibration phase in this way; in such cases it is usually necessary to demodulate the FM signal.

We have conducted experiments with two types of demodulator circuits. The first was a conventional limiter-discriminator, with the discriminator characteristic chosen to accommodate the largest expected Doppler shift, approximately 2 MHz. This approach is satisfactory when the signal strength is large, but the need for limiting at stages in the circuit where the bandwidth is very wide (before detection) implies poor performance when there is a relatively low signal-to-noise ratio. This problem occurs when the vibrating surface is diffusely reflecting, because the random interference patterns resulting from the surface roughness often produce a signal of less than the expected value. In such cases the limiter-discriminator is less than optimum by the ratio of the limiter bandwidth to the desired instantaneous bandwidth.

An optimum receiver configuration, using a voltage-controlled oscillator (VCO) which is phase locked to the beat frequency signal, is illustrated schematically in Fig. 4. In this device the heterodyne signal and the output of the VCO are mixed to provide a low-frequency error signal. The error signal, which passes through a low-pass filter adjusted to give the desired instantaneous bandwidth, is applied to the frequency-tuning terminals of the VCO as negative feedback to force the oscillator output to track the incoming heterodyne signal in rf phase quadrature. The demodulated output is simply the error voltage itself. This provides a direct indication of the surface velocity, since the frequency shift of the heterodyne signal, and hence the shift of the VCO tracking frequency, is proportional to surface velocity. To obtain the surface displacement it is necessary to pass the output through a filter which integrates over the audio spectral range to be expected from the vibrating surface.

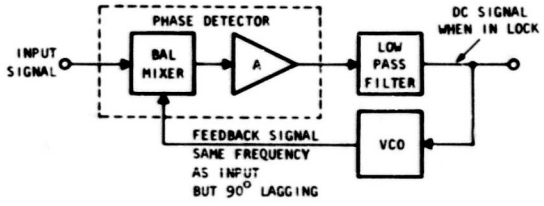

Fig. 4. Frequency-tracking receiver block diagram

To bring the error signal frequency within the passband of the low-pass filter in the feedback loop at the start of a measurement, the VCO is tuned manually until the tracking receiver locks onto the heterodyne signal from the vibrating object. At that point the vibration signal suddenly appears at the receiver output;

the receiver will then maintain its tracking as long as the signal remains above the receiver noise in amplitude and the vibration frequencies of the larger surface motions remain within the bandwidth of the control loop filter. No limiter stages are required; therefore, the advantages of detecting the audio-frequency vibration with a circuit having only audio bandwidth can be realized, even when the peak heterodyne Doppler shifts have frequency deviations far beyond audio.

Some results obtained with various reflecting surfaces using the tracking receiver described above are indicated in Fig. 5. The peak vibration amplitude in these tests was 0.020 in. at a 100-Hz rate. The fact of particular interest here is that the reflected signal, even from flat white paint, was sufficient to actuate the receiver control loop and force the VCO to track the Doppler shift. Obviously, with this circuit one can measure the phase as well as the amplitude of the vibration, and it is possible to monitor complex, nonsinusoidal motions as well as single-frequency excitations.

The instrument has been used to measure mode patterns across extended flexible surfaces, such as sheet metal panels, as well as single-point deflections on rigid objects. The mode patterns are obtained by manually scanning the probe beam across the moving surface, recording the amplitude at suitable intervals. Patterns on ceramic piezoelectric transducers, vibrating at frequencies up to 700 kHz, have also been measured using this technique with the spectrum analyzer display. Of course, the procedure might be automated in a variety of ways to provide an amplitude vs distance display directly.

THEORETICAL SENSITIVITY

In an ideal heterodyne receiver, the photocurrent in the detector is given by:

$$i(t) = I_{LO} + I_S + 2\sqrt{I_{LO} I_S} \cos(\omega t + \phi_S - \phi_{LO}),$$

where I_{LO} and I_S are the direct currents which would be produced by the local oscillator and signal beams separately, ω is the angular frequency difference between the local oscillator and signal, and ϕ_S and ϕ_{LO} are the phases of the signal and local oscillator waves, respectively. If the signal wave reflects from a surface which vibrates sinusoidally at a frequency ω_v and an amplitude x_0, we can choose a time reference such that

$$\phi_S = \frac{4\pi x_0}{\lambda} \sin \omega_v t ,$$

where λ is the optical wavelength. For simplicity we set $\phi_{LO} = 0$. Then the ac component of the photocurrent may be written as the Bessel series:

$$i_{ac} = 2\sqrt{I_{LO} I_S}\left[J_0\left(\frac{4\pi x_0}{\lambda}\right)\cos \omega t + \sum_{n=1}^{\infty} J_n\left(\frac{4\pi x_0}{\lambda}\right)\cos(\omega + n\omega_v)t - \sum_{n=1}^{\infty} J_n\left(\frac{4\pi x_0}{\lambda}\right)\cos(\omega - n\omega_v)t\right]$$

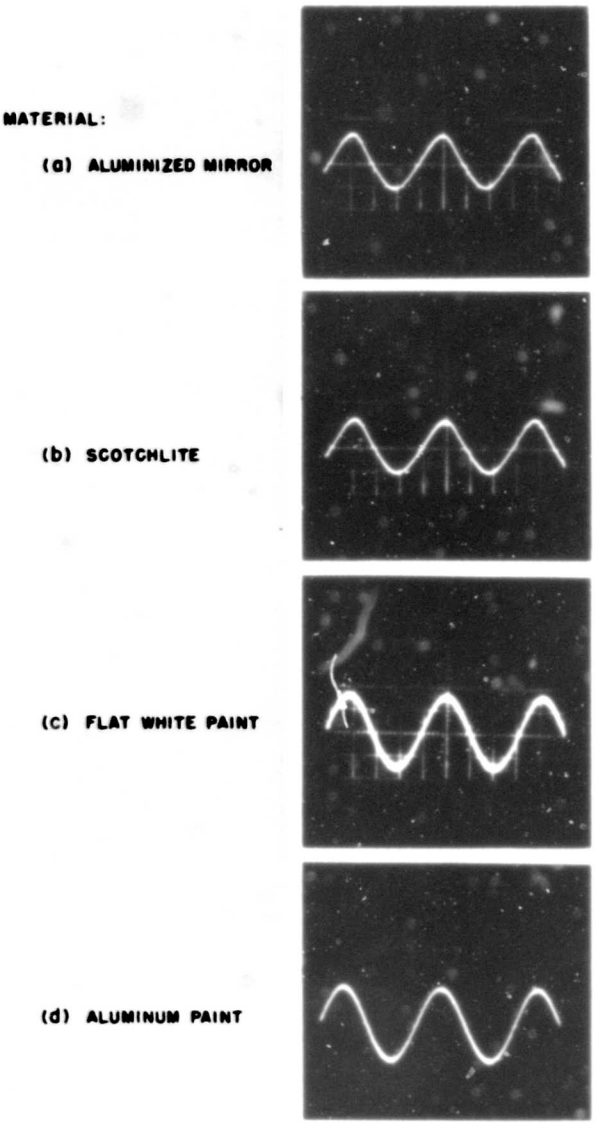

Fig. 5. Tracking receiver output with various surface materials (vibration double amplitude ≈ 1 mm, frequency ≈ 100 Hz; output voltage is proportional to surface velocity)

For very small vibration amplitudes, we need to consider only the three frequencies of lowest order, and the above expression is approximated by:

$$i_{ac} \approx 2\sqrt{I_{LO} I_S}\left[\cos \omega t + \frac{2\pi x_0}{\lambda}\cos(\omega + \omega_v)t\right]$$

The mean square photocurrent in one sideband is therefore

$$\overline{i_{ac}^2} = 2 I_{LO} I_S \left(\frac{2\pi x_0}{\lambda}\right)^2$$

Now the mean square shot-noise current component in a current of value I is $\overline{i_n^2} = 2eIB$, where B is the bandwidth and e is the electronic charge. For a typical heterodyne system, I_{LO} is much larger than I_S; therefore $I \approx I_{LO}$ and $\overline{i_n^2} \approx 2eI_{LO}B$. Then the system signal-to-noise ratio is

$$(S/N) = \left(\frac{2\pi x_0}{\lambda}\right)^2 \frac{I_S}{eB}$$

This corresponds to a minimum detectable displacement

$$(x_0)_{min} = \frac{\lambda}{2\pi}\left(\frac{eB}{I_S}\right)^{1/2}$$

If we rewrite I_S in terms of the optical power P_S, the detector quantum efficiency η, and photon energy $h\nu$, we have

$$(x_0)_{min} = \frac{\lambda}{2\pi}\left(\frac{h\nu B}{\eta P_S}\right)^{1/2}$$

As a typical example, suppose $P_S = 10^{-6}$ w, B = 2000 Hz, $\eta = 10^{-2}$, and λ = 6328A. The corresponding $(x_0)_{min}$ is roughly 0.25A, or 10^{-3} μin., an amplitude considerably below the sensitivity level required for most vibration analysis applications.

For large vibration amplitudes the upper limit is set by the bandwidth of the intermediate frequency (i-f) stages in the receiver electronics and by the depth of focus of the optical system. The latter is generally a more stringent limit for low audio vibration frequencies and relatively large collecting apertures. For example, the peak Doppler shift of the beat frequency away from the nominal i-f is given by:

$$\Delta\omega = \pm \frac{4\pi x_0 \omega_v}{\lambda}$$

or

$$\Delta f = \pm \frac{4\pi x_0 f_v}{\lambda}$$

Thus if the vibration frequency f_v = 10 Hz and x_0 = 1 cm (again with λ = 6328A), the peak-to-peak spectral bandwidth occupied by the modulated signal is approximately $B = 2\Delta f \approx 4$ MHz for this example. However, the range of target positions for which the reflected signal returns with the proper wavefront curvature for uniform interference with the reference beam may be much less than the 1-cm amplitude above. For example, the present instrument uses a 3-in. aperture located roughly 48 in. from the surface. With this geometry, measurements show that the heterodyne signal is within 3 db of maximum over a range of only 0.050 in. in surface location, centered about the optimum focal distance. Of course, this limitation is significant only at very low vibration frequencies, where such large excursions are possible without excessive accelerating forces. Reducing the aperture of the instrument increases the useful focal depth but also reduces the signal level if the surface is diffusely reflecting.

CONCLUSIONS

It has been demonstrated that vibrations with a very wide range of amplitudes and frequencies can be detected using optical heterodyne techniques. Use of an optical directional coupler allows efficient transmission and reception of the light through the same optical system, thus eliminating the need for ultraprecise mechanical alignment of the optical components. The frequency offset in this instrument is particularly convenient when vibration amplitudes less than one optical wavelength are to be measured, because the system output is always a simple phase-modulated signal requiring relatively straightforward detection electronics. Successful detection of motions on rough as well as optically smooth surfaces is possible, even with a laser power output of only 100 μw and working distances of several feet. The utility of this device in measuring vibrational modes on extended structures has also been demonstrated.

* * *

HIGH-FREQUENCY MICROPHONE CALIBRATION USING A SUPERSONIC FREE-FLIGHT RANGE*

Charles D. Hayes
Jet Propulsion Laboratory
Pasadena, California

and

Raymond C. Binder
University of Southern California
Los Angeles, California

A method using a supersonic free-flight range was developed for the calibration of microphones over a wide frequency range. The apparatus includes a gun and a test section for measuring projectile speed and taking shadowgraph pictures. Material on the properties of shock pulses developed by supersonic projectiles is presented. The N-type shock wave developed by the supersonic projectile provides the input shock pulse acting on the microphone face. Using a digital computer program, a Fourier transform of the microphone output (from an oscilloscope trace) is combined in a particular manner to calibrate the microphone over a range of frequencies. The results of this technique show real promise for frequencies up to 100,000 Hz.

INTRODUCTION

There is a need to develop techniques for the calibration of pressure transducers or microphones over a wide frequency range. This need arises from the very important present-day studies of various acoustic-noise phenomena, such as the spectral properties of boundary-layer turbulence and aircraft-produced sonic booms.

There are several possible methods of performing a wideband calibration of pressure transducers. This study focuses attention on a particular method that uses a supersonic ballistic or free-flight range. The method developed here has the advantages of simplicity of calibration system setup, flexibility in varying the range parameters which determine the input pressure amplitude and frequency components, and repeatability. The data obtained with this technique are organized by the Fourier transform method.

SUPERSONIC FREE-FLIGHT RANGE

Figure 1 is a schematic of the apparatus used. The enclosed range includes a rifle (Swift 0.220) and a test section. At the test section the projectile speed can be measured (with the photoelectric cells and the timer) and shadowgraph pictures can be taken.

Two microphones were used to obtain photographic records of the response pressure-time shock pulse. Each microphone was calibrated while the other served as the triggering transducer for the oscilloscope. Each microphone was calibrated with and without its protecting grid, for a total of four calibrations. These calibrations were then compared with the corresponding calibrations of the microphones which were obtained by other techniques.

INPUT SHOCK PULSE

The supersonic projectile develops an N-wave type of shock pulse, with the pressure-time curve resembling the letter N; this is illustrated in Fig. 2a. Much of the reference literature deals with the aerodynamics of this shock wave. As illustrated in Fig. 2a, the classical N-wave consists of a very sharp rise. As illustrated in Fig. 2b, there is a question as to the possibility of a significant rise time. The work of DuMond, Cohen, Panofsky, and Deeds (2)

*Material herein was adapted from the first author's Master's thesis (1).

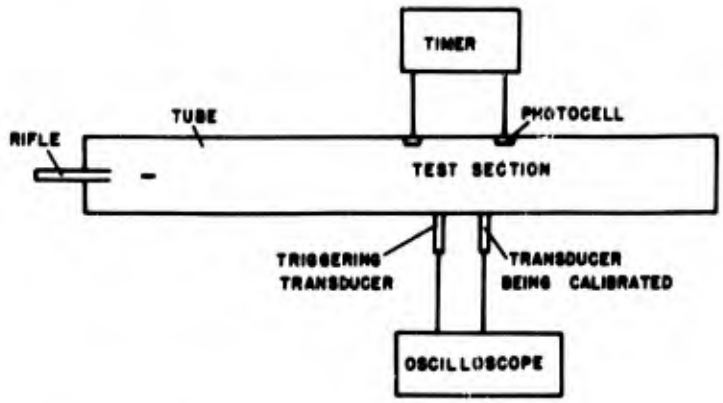

Fig. 1. Diagram of University of Southern California free-flight range

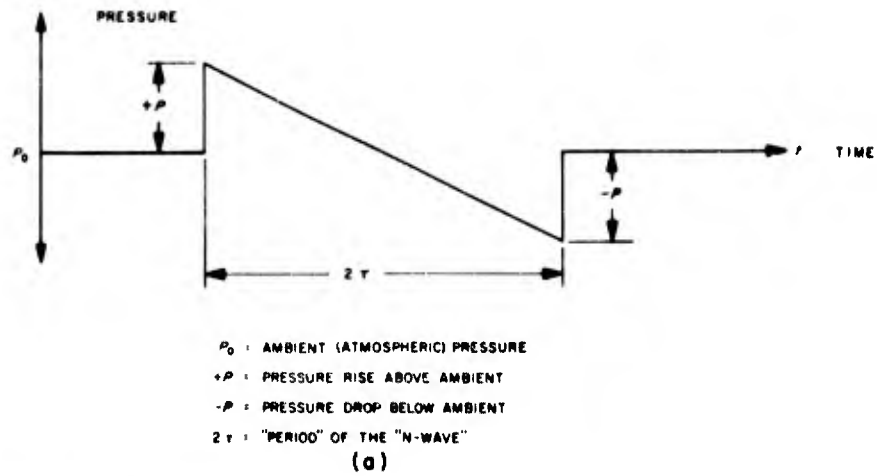

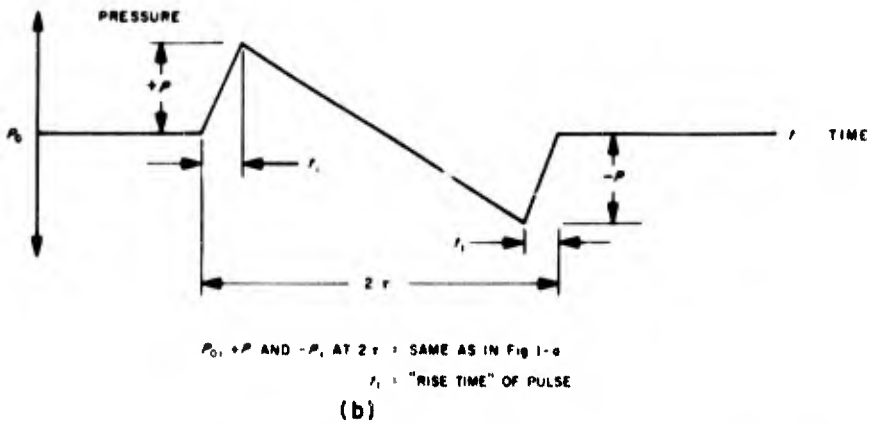

Fig. 2. (a) Classical N-wave pulse; (b) pulse with finite rise time

has indicated the results shown in Fig. 3, which shows different pressure-time signatures as a function of miss distance, or the perpendicular distance between projectile and microphone face. For a suitable miss distance, the projectile shock pulse can be regarded as a classical N-wave.

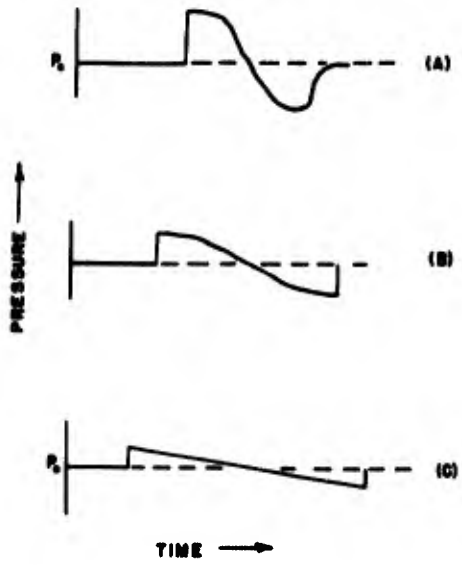

Fig. 3. Pressure-time signatures; (a) short miss distance; (b) medium miss distance; (c) large miss distance

For the work in this investigation, for Swift 0.220 projectiles, shadowgraph pictures at the miss distance used (5.39 in.) showed that the N-wave condition was realized. Thus the present analysis is based on a classical N-wave shock input to the microphone face.

MICROPHONE TRANSFER FUNCTION

Let ω represent angular frequency (as radians per second). As shown in Fig. 4, the desired microphone transfer function $H_1(\omega)$ is part of the total circuit transfer function $H(\omega)$. Since the total function $H(\omega)$ is the series combination of $H_1(\omega)$ and $H_2(\omega)$, then $H_1(\omega)$ becomes

$$H_1(\omega) \quad \frac{H(\omega)}{H_2(\omega)} \tag{1}$$

The magnitude of $H_1(\omega)$ is

$$|H_1(\omega)| \quad \left| \frac{H(\omega)}{H_2(\omega)} \right| \tag{2}$$

The function $H_2(\omega)$ is determined by a calibration of the electrical system from the microphone cathode follower through the oscilloscope. The function $H(\omega)$ will be found from measurements with the range. Then the microphone calibration is determined by Eq. (2).

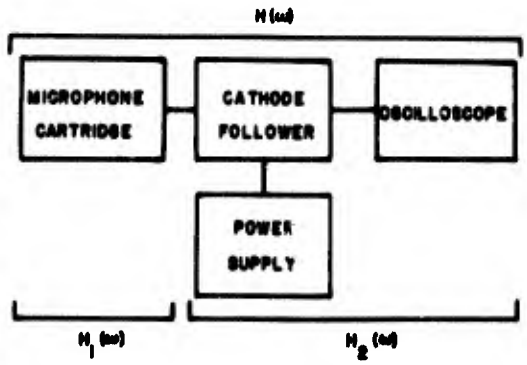

Fig. 4. Block diagram of electrical system: $H_1(\omega)$ is transfer function of microphone cartridge, $H_2(\omega)$ is transfer function of remaining circuit, $H(\omega)$ is transfer function of entire electrical circuit

Let t = time, $i \quad \sqrt{-1}$, $F_o(t)$ = output function of time, and $F_i(t)$ = input function of time. The frequency response of the transducer is given by

$$H(\omega) \quad \frac{\int_0^\infty F_o(t)\, e^{-i\omega t}\, dt}{\int_0^\infty F_i(t)\, e^{-i\omega t}\, dt} . \tag{3}$$

where the numerator is the Fourier transform of the output, the denominator is the Fourier transform of the input, and it is assumed that the pulse starts at $t \quad 0$.

$H(\omega)$ can be written as

$$H(\omega) \quad F(\omega)\, G(\omega) \tag{4}$$

where

$$F(\omega) \quad \int_0^\infty F_o(t)\, e^{-i\omega t}\, dt .$$

and

$$G(\omega) = \int_0^{\infty} F_i(t)\, e^{-i\omega t}\, dt .$$

This response function is computed by dividing the Fourier transform of the output pulse time history by the Fourier transform of the input time history. Measurements show that the output pulse is a distorted N-wave pulse. Figure 5 shows an example. The input time history, being taken as a pure classical N-wave pulse, can be Fourier transformed in closed form, with the results

$$G(\omega) = \frac{p}{\omega^2 \tau}\left[(1 - \omega\tau \sin 2\omega\tau - \cos 2\omega\tau) + i(\sin 2\omega\tau - \omega\tau - \omega\tau \cos 2\omega\tau)\right]. \quad (5)$$

where p is maximum overpressure attained by the N-wave, τ is one half of the total N-wave period (time lag between maximum overpressure and the maximum negative pressure), and $\omega = 2\pi f$ where f is frequency in hertz.

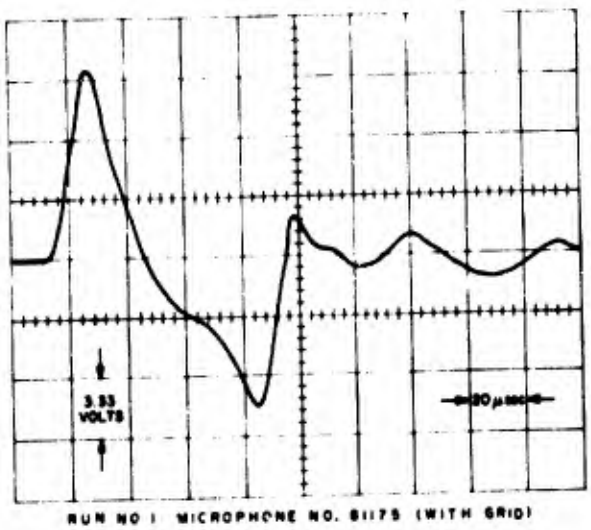

Fig. 5. Example of output pressure-time pulse

Figure 6 is a plot of $|G(\omega)|\ p$ vs frequency. Equation (5) can be written in the form

$$G(\omega) = G_R(\omega) + iG_I(\omega) . \quad (6)$$

where $G_R(\omega)$ is the real part and $G_I(\omega)$ is the imaginary part of $G(\omega)$. The modulus of the Fourier transform is

$$|G(\omega)| = \left\{\left[G_R(\omega)\right]^2 + \left[G_I(\omega)\right]^2\right\}^{1/2} \quad (7)$$

and the phase angle $\psi(\omega)$ is given by

$$\psi(\omega) = \tan^{-1}\left[\frac{G_I(\omega)}{G_R(\omega)}\right] \quad (8)$$

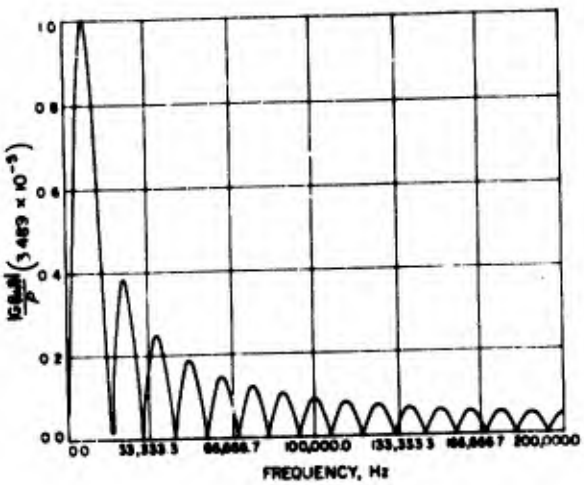

Fig. 6. Spectrum analysis for N-wave

The Fourier transform of the output time history does not lend itself to a simple closed-form solution since it is difficult to describe the time history in equation form. The technique of numerical determination of the Fourier transform of the output time history is thus applied. The method described by Huss and Donegan (3) was used. In this case the time function is fitted with a staircase function using equal time intervals (Δt) in such a way that the area under the staircase function equals the area under the corresponding time history. In this study the amplitudes of the various steps of the staircase function were tabulated and used with a digital computer to obtain the real and imaginary parts of the Fourier transform of the time function. In this study 201 intervals of Δt were used to assure maximum accuracy with a reasonable number of intervals.

The values of $G_R(\omega)$ and $G_I(\omega)$, with the corresponding values of the magnitude of $G(\omega)$,

were obtained by a digital computer program which evaluated Eqs. (5), (7), and (8) over a frequency range of 250 Hz to 2×10^5 Hz at frequency increments Δf of 250 Hz. The period of the pulse 2τ was measured as 8×10^{-5} sec, which indicated significant frequency components up to at least 2×10^5 Hz. The effective usable range of the particular condenser microphones tested is between 20 and 1×10^5 Hz; analysis to 2×10^5 Hz assures accurate data over the complete frequency range of these microphones.

RESULTS

Four calibration runs were made of two condenser microphones to demonstrate the method. Figures 7, 8, 9, and 10 show the final results. In each plot the response, in decibels, is given as a function of frequency. In each plot the solid curve is the factory calibration, whereas the dashed curve is the calibration using the range. There is good correlation at the lower frequencies (less than 1×10^5 Hz) with fair correlation above this frequency.

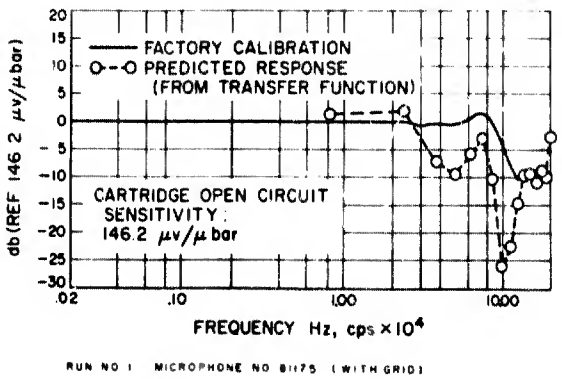

Fig. 7. Microphone calibration

This method of calibration, using a supersonic free-flight range, has real promise especially when more elaborate techniques and equipment are not available. This method will yield a wideband pressure calibration that is suited both to transducers which have low sensitivities and a high mechanical diaphragm impedance, as well as to transducers of much

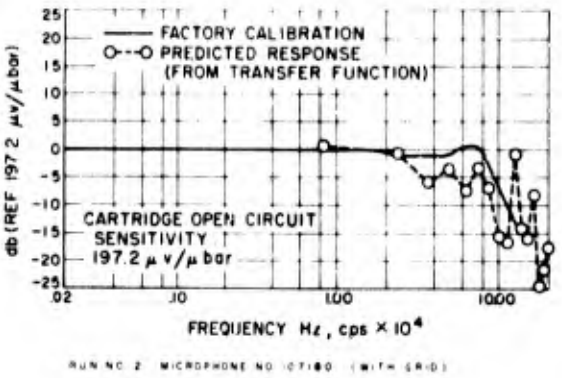

Fig. 8. Microphone calibration

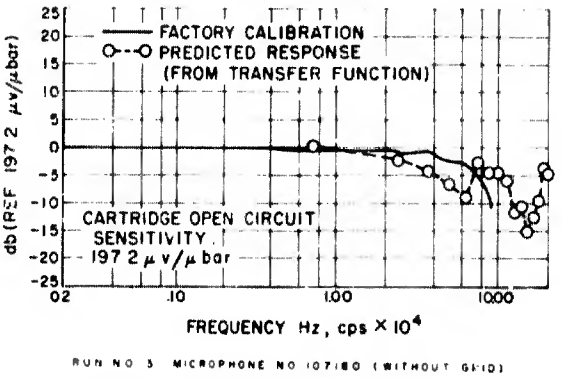

Fig. 9. Microphone calibration.

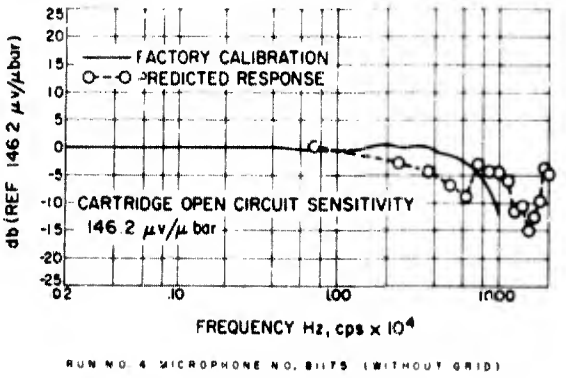

Fig. 10. Microphone calibration

higher sensitivities and lower mechanical diaphragm impedance, such as the 0.25-in.-diam condenser microphones calibrated in this study.

REFERENCES

1. C. D. Hayes, "High Frequency Microphone Calibration Using Ballistic Shock Pulses," unpublished Master's thesis, University of Southern California, Aug. 1967

2. J. W. M. DuMond, E. R. Cohen, W. K. H. Panofsky, and E. Deeds, "A Determination of the Wave Forms and Laws of Propagation and Dissipation of Ballistic Shock Waves," J. Acous. Soc. Amer., 18(1): (1946)

3. C. R. Huss and J. J. Donegan, "Tables for the Numerical Determination of the Fourier Transform of a Function of Time and the Inverse Fourier Transform of a Function of Frequency, With Some Applications to Operational Calculus Methods," NACA Tech. Note 4073, Oct. 1957

* * *

METHOD OF MEASURING VIBRATORY DISPLACEMENTS IN TERMS OF A LIGHT WAVELENGTH

J. L. Goldberg
National Standards Laboratory
Sydney, Australia

A method of determining the peak-to-peak displacement of a sinusoidal vibration in terms of the wavelength of light is described. The interferometer used is of the Fizeau multiple-beam type in which the silvered adjacent surfaces of the optical flats act as the two electrodes of a capacitor, in addition to performing their function in the interferometer. The two electrodes are surrounded by a third or guard electrode so that the capacitance change between the silvered films which occurs when one of the optical flats is moved can be measured by comparison with a standard three-terminal capacitor in a transformer bridge.

The sinusoidal motion is imparted to one surface of the interferometer and the capacitance change recorded on a direct-writing oscillograph. This capacitance change is then calibrated by slowly moving the surface of the interferometer in a rectilinear manner and recording by a photoelectric detector the passage of interference fringes past a slit aperture in the optical field. The chart is thus calibrated in terms of interference fringes and the peak-to-peak displacement of the motion is readily determined.

An example of an oscillatory motion measured by this method is presented.

INTRODUCTION

In a correctly adjusted Fizeau multiple-beam interferometer (1), the interference fringes are of excellent contrast and consist of either dark straight bands on a light background (the reflected system) or light bands on a dark background (the transmitted system). To extract a useful electrical signal from either system of fringes, a slit aperture is used between the photodetector and the fringe image with the long dimension of the slit parallel to the fringes. It has been found (2) that with a geometric mean reflectance of 0.8 in the silvered surfaces, the slit width relative to a fringe spacing (R) must be about 0.1 to obtain maximum signal-to-noise ratio in the photoelectric current. If the interference pattern is vibrated sinusoidally, the bandwidth needed in the output of the photoelectric detector to obtain all the fringe pulses with equal amplitude depends on the velocity of the interference pattern as well as on the sharpness of the fringes.

If the peak amplitude of vibration is n_0 fringe spacings with a vibration frequency of f Hz, then it has been shown (2) that a bandwidth B equal to $14\pi n_0 f$ is needed in the photodetector output. If this bandwidth requirement is not met, the fringe pulses will be of unequal amplitude and will be smallest at the maximum velocity of the interference pattern. This phenomenon is illustrated in Fig. 1 for one peak-to-peak excursion of the interferometer surface. In the upper oscillogram the detector bandwidth is adequate. In the lower one it is inadequate, and the deterioration of the fringe signal near the maximum velocity of the surface is evident. If this second pattern of pulses were presented to a trigger circuit preceding an electronic counter, there would be a possibility of miscount.

The basic difficulty in the fringe counting method described above is that the bandwidth requirement for the fringe signal conflicts with the necessity of keeping the bandwidth as narrow as possible to mitigate the effects of the "white" noise of the photomultiplier. This difficulty could be overcome if the counting could be carried out very slowly. A way of doing this is presented in the next section.

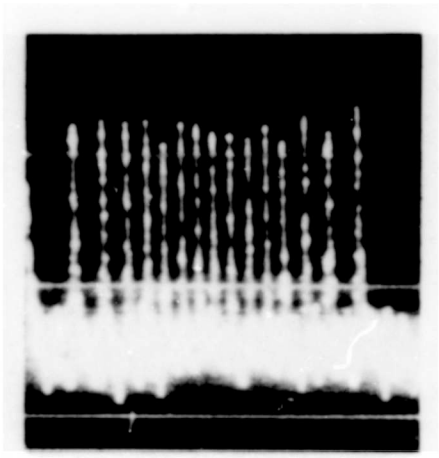

Fig. 1. Oscillograms showing effect of detector bandwidth on fringe signal-to-noise ratio

NEW METHOD FOR DETERMINING VIBRATION AMPLITUDES

The multiple-beam interferometer is constructed in such a way that the silvered adjacent surfaces of the optical flats act as the two electrodes of a parallel-plate capacitor as well as performing their function in the interferometer.

In Fig. 2, the optical flats with the two active electrodes (designated 1 and 2) are shown surrounded by a guard electrode (designated 3). Electrode 1 is deposited as a fully silvered film of a 92 percent reflectivity and electrode 2 of 70 percent reflectivity. Connections are made to the films using indium solder. Collimated mercury light of 0.5461-μm wavelength is projected by way of a beam divider onto the optical flats, and the multiple-beam interference is imaged on a slit aperture through a lens system. This slit aperture, for the reason mentioned above, is set to about 0.1 of a fringe spacing with its long dimension parallel to the fringes. Any departure from parallelism will reduce the available modulation. A photomultiplier with a trialkali cathode detects the passage of interference fringes; the photocurrent is fed to one galvanometer of a direct-writing oscillograph. The detector bandwidth is deliberately limited by the galvanometer response time in order to improve the fringe signal-to-noise ratio, since the fringes are not recorded simultaneously with the sinusoidal movement but are recorded separately while the plate is moved slowly at a uniform rate. In this way, by reducing the detector bandwidth, there is a considerable improvement in fringe signal-to-noise ratio. This has necessitated an increase in observation time for the fringe signal, but this is not considered to be a serious limitation.

The capacitance change between electrodes 1 and 2 is measured by comparison with another fixed three-terminal capacitor in a transformer bridge (3) using an adjustable ratio. The demodulated output of the bridge is directly proportional to the displacement of electrode 1, provided the displacement is small compared with the total electrode separation. The bridge output is recorded on a second galvanometer of the oscillograph. Electrode 1 can be moved by an electromagnetic vibration generator with either a sinusoidal current or a slow sweep current, whereas electrode 2 is nominally fixed.

The bridge detector amplifier, the phase sensitive demodulator, and the second galvanometer have a bandwidth extending from 0 to 600 Hz. The galvanometer frequency response sets the limiting frequency of the apparatus.

The silvered films are circular and are approximately 0.875 in. in radius. With an air gap of 0.034 in., the static value of the capacitor is approximately 17 pf; this is compared with a standard 10-pf air capacitor in the bridge.

The sinusoidal motion to be measured is first applied to electrode 1 and the sinusoidal capacitance change is recorded on the oscillograph. It is then arranged that the zero of sinusoidal displacement corresponds to capacitive balance of the bridge. The chart recording is then calibrated by applying the slow sweep current to the vibration generator and simultaneously recording the interference fringe pulses from the photomultiplier. A change of capacitance of 5 mpf is found to correspond to a displacement of one fringe or 0.273 μm in the interferometer.

A typical recording made by this procedure is shown in Fig. 3. A vibration of 40-Hz frequency is shown together with the chart calibration. In this case the peak-to-peak displacement is 1.92 μm with a precision of at least a half-fringe or 0.13 μm. To have attempted this measurement by direct electronic counting of the fringes during the peak-to-peak excursion of the interferometer surface, a detector bandwidth if approximately 6000 Hz would have been necessary.

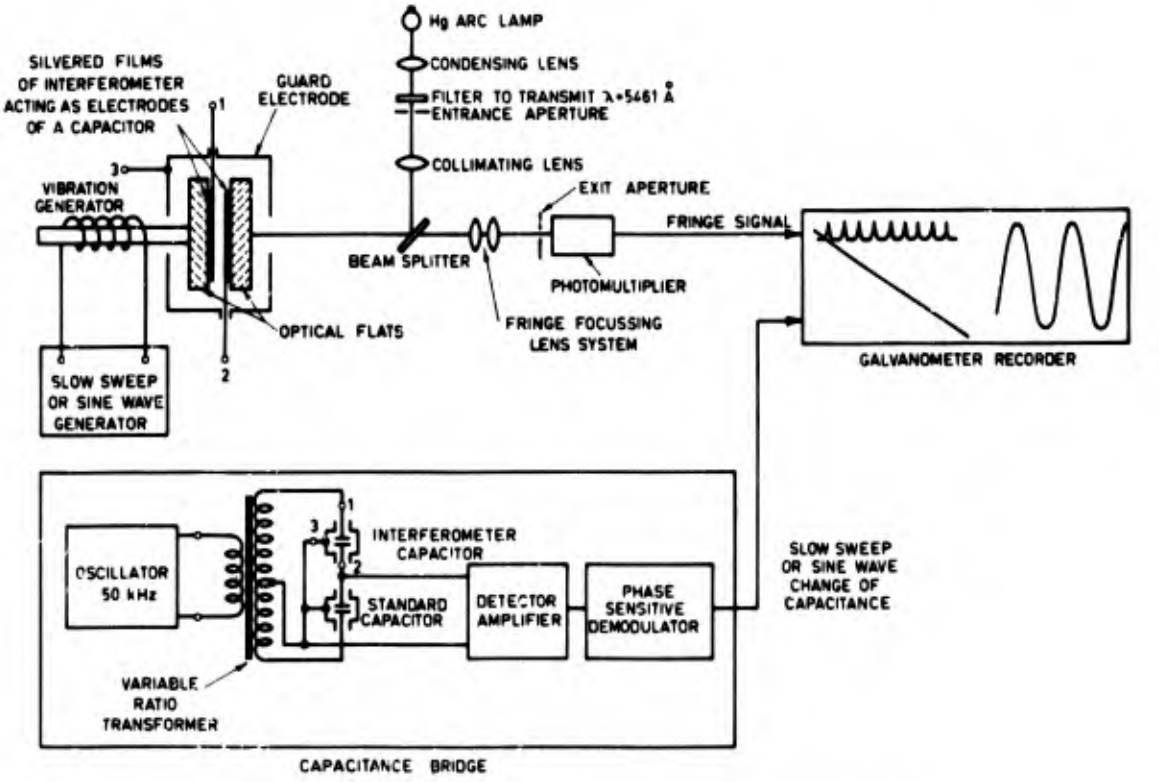

Fig. 2. Diagram illustrating way in which an interferometer is used in new method of vibratory displacement measurement

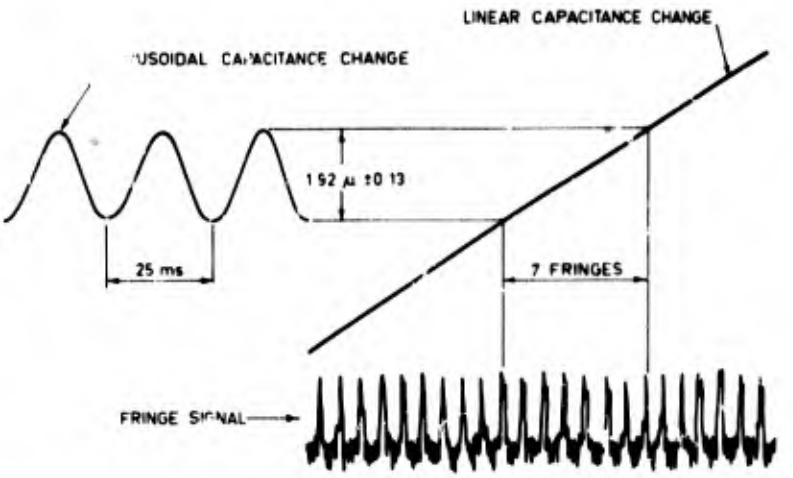

Fig. 3. Record taken with apparatus illustrated in Fig. 2

CONCLUSION

A new method of measuring vibratory displacements in terms of a light wavelength has been demonstrated. By making use of the silvered surfaces of the interferometer as the electrodes of a three-terminal capacitor, the counting of the fringes can be carried out very slowly with greatly reduced bandwidth in the detector. The technique avoids the uncertainty associated with the counting of interference fringes while the surface is vibrating.

ACKNOWLEDGMENTS

The author thanks F. P. Sharples for preparing the silvered surfaces of the interferometer and making the soldered connections to them. B. H. Meldrum capably assisted the author in the experimental work.

REFERENCES

1. S. Tolansky, "Low-Order Multiple-Beam Interferometry," Proc. Phys. Soc. 58(Part 6): 654 (1946)

2. J. L. Goldberg, "The Frequency Spectrum of the Photoelectric Signal from an Oscillating Interference Fringe Pattern," Aust. J. Appl. Sci. 14:231 (1963)

3. A. M. Thompson, "The Precise Measurement of Small Capacitances," IRE Trans. I-7 (Nos. 3 & 4):245 (1958)

* * *

CALIBRATION OF ACCELEROMETERS BY IMPULSE EXCITATION AND FOURIER INTEGRAL TRANSFORM TECHNIQUES

John D. Favour
The Boeing Company
Seattle, Washington

A new technique for the dynamic calibration of accelerometers has been developed. It is based upon digital computer calculation and ratioing of the Fourier integral transforms of the test accelerometer output signal and of a standard accelerometer output signal when excited by an acceleration impulse. The basic technique is completely outlined. The system was tested and shown to be faster, cheaper, more accurate, and more versatile than the conventional sinusoidal excitation technique. The design, fabrication, and initial testing of an impulse exciter are discussed.

INTRODUCTION

Most dynamic accelerometer calibrations are currently performed on electromagnetic exciters, at a series of discrete sinusoidal frequencies. The test accelerometer is calibrated by comparing its output signal, via its signal conditioning equipment, with the output of a standard accelerometer system whose calibration is accurately known and traceable to the National Bureau of Standards. Both accelerometers are mounted, usually back to back, so that they experience identical acceleration (see Fig. 1). There are several other methods [1-4] and devices with which to calibrate accelerometers; however, this paper is concerned with the production calibration of accelerometers where the comparison technique on an electromagnetic exciter has provided the best combination of accuracy, speed, and cost savings. For this reason, the above technique has been used and accepted for many years. The increasing complexity of spacecraft testing has required the calibration of from 40 to 60 channels of accelerometers per given test setup. Because of this, and in spite of the usefulness of the techniques for production, it becomes evident that it is slow, limited, inaccurate, and expensive.

The accuracy of the technique (which does not include the error or uncertainities of the standard accelerometer) is considered to be about ±2 percent but by no means better than ±1 percent. The technique is highly limited in the information which is achieved during a typical calibration. First, the electromagnetic exciter is bandwidth limited. It has no static response and poor response below 20 Hz. Second, the highest acceleration level that can be produced, without serious wave shape distortion, on our present system is 50 g rms and then only at certain frequencies. In view of this, the present system is unacceptable for calibration of accelerometers that will be used in tests where the acceleration level will exceed 50 g rms sine or 70.7 g peak. The normal calibration data is limited to 5 to 10 discrete data points in the frequency spectrum. The operation of the present system is time consuming; adjusting the acceleration amplitude and frequency, observing the meter readings, and recording the data and plotting must be accomplished to obtain each individual data point. On an average, it requires about 45 min to calibrate each accelerometer. One final disadvantage of the above system is the high cost of maintenance of the system. The overall cost of an accelerometer calibration by the present technique is $10 or more. In our laboratories, we are performing between 1000 and 1500 calibration per year.

Previous experience [5-7] in the definition of system dynamics by Fourier transform analysis of impulse data indicated that calibration of accelerometers by the same Fourier transform techniques could improve on all the above disadvantages.

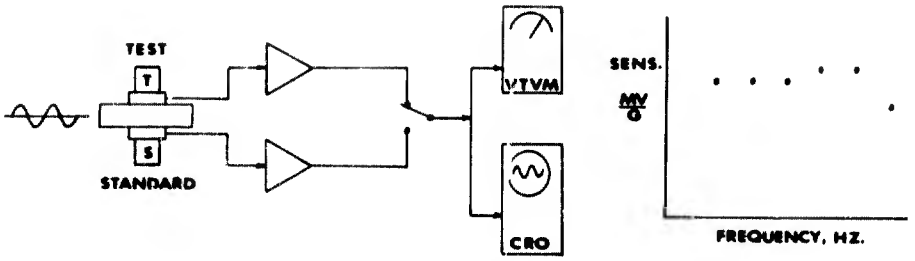

1 SLOW, ¾ HOUR/CALIB.

2 LIMITATIONS
- A BANDWIDTH, NOT BELOW 20 HZ.
- B ACCELERATION LEVEL, 50 G'S RMS
- C NUMBER OF DATA POINTS, 2 TO 10

3 LIMITED ACCURACY, ≃ 2%

4 EXPENSIVE, ≃ $10/CALIB.

Fig. 1. Present technique

FUNDAMENTAL THEORY

Review of Fourier Integral Transform [8]

Any periodic function of time $f(t)$ can be equated to a summation of sinusoidal harmonics as follows:

$$f(t) = \frac{1}{T} \sum_{n=-\infty}^{\infty} C_n e^{j\omega_n t} \qquad (1)$$

where

$$C_n = \int_0^T f(t)\, e^{-j\omega_n t}\, dt , \qquad (2)$$

and $\omega_n = 2\pi n/T$; $n = 0, 1, 2, 3, \ldots$.

The above is known as a Fourier series. (This is the complex exponential form of the Fourier series. Fourier series can be expressed in different forms.) As a matter of review, consider the periodic square wave illustrated in Fig. 2(a). The pulse duration is τ, and the period is T. The Fourier series of this periodic function is illustrated in Fig. 2(b). Note that the spacing between successive harmonics is

$$\Delta\omega = \omega_{n+1} - \omega_n = \frac{2\pi}{T} . \qquad (3)$$

By substituting Eq. (3) into Eq. (1), Eq. (1) may then be rewritten as follows:

$$f(t) = \frac{1}{2\pi} \sum_{n=-\infty}^{+\infty} C_n e^{j\omega_n t} \Delta\omega . \qquad (4)$$

At this point, to develop the Fourier integral transform, one must leave the realm of time function periodicity and consider the limiting case where $T \to \infty$. Then, from Eq. (3), $\Delta\omega \to 0$ and the discrete sinusoidal harmonics merge to form a continuous spectrum (see Fig. 3). Also, $\omega_n \to \omega$ and C_n becomes a continuous function $F(j\omega)$:

$$F(j\omega) = \lim_{T \to \infty} C_n \qquad (5)$$

From this is developed the Fourier integral transform for nonperiodic time functions:

$$f(t) = \frac{1}{2\pi} \int_{-\infty}^{+\infty} F(j\omega)\, e^{j\omega t}\, d\omega \qquad (6)$$

and

$$F(j\omega) = \int_{-\infty}^{+\infty} f(t)\, e^{-j\omega t}\, dt \qquad (7)$$

Equation (7) provides the basis upon which this technique is developed, for it provides a means of transforming any nonperiodic, transient, or impulsive type of time function $f(t)$ into a distinct function of frequency $F(j\omega)$. This function of frequency $F(j\omega)$ is an exact determination of the frequency content of the time function $f(t)$; it contains both amplitude and

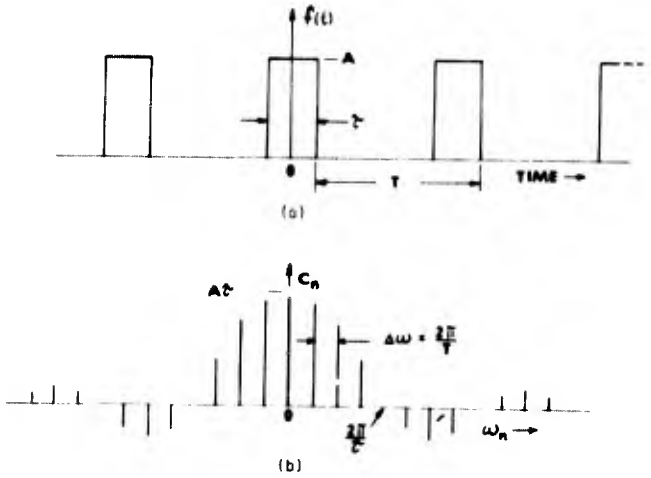

Fig. 2. (a) periodic time function;
(b) Fourier series

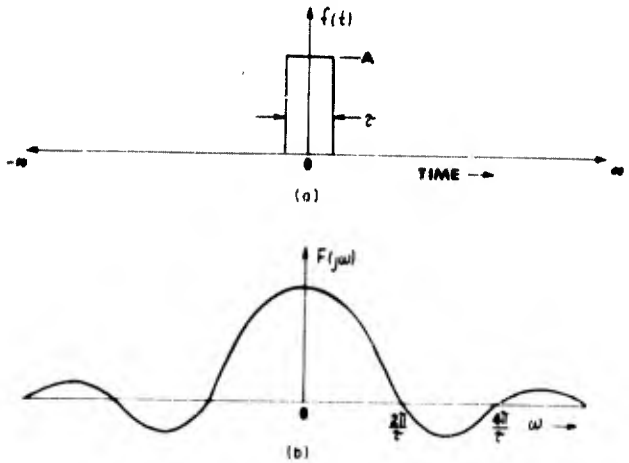

Fig. 3. (a) Nonperiodic time function;
(b) Fourier integral transform

phase information. It should be noted that Eq. (7) involves an integration from $-\infty$ to $+\infty$ in time. This, of course, is unrealistic in the real world of engineering; however, Eq. (7) can be modified to

$$F(j\omega) = \int_0^T f(t)\, e^{-j\omega t}\, dt\,, \qquad (8)$$

under the condition that $f(t) = 0$ for $t < 0$ and for $t > T$.

Application of the Fourier Integral Transform

The application of Eq. (8) makes it possible to calibrate accelerometers with a transient or impulse type of acceleration excitation (see Fig. 4). A test accelerometer, to be calibrated, and a standard accelerometer, whose calibration is known and traceable to the National Bureau of Standards, must be properly mounted to an excitable base so that they identically experience the acceleration of the base. The base must then be subjected to some transient acceleration, and the output signals (from the associated individual signal conditioning units) -- $e_T(t)$ from the test accelerometer and $e_S(t)$ from the standard accelerometer -- recorded for analysis by a digital computer. The output signals are converted from analog voltages to 10-bit plus-sign binary samples and recorded on magnetic tape in a multiplex arrangement by a Data Technology Systems portable data system (DTS). The DTS has an upper sampling rate of 20,800 samples per second. Each of the two

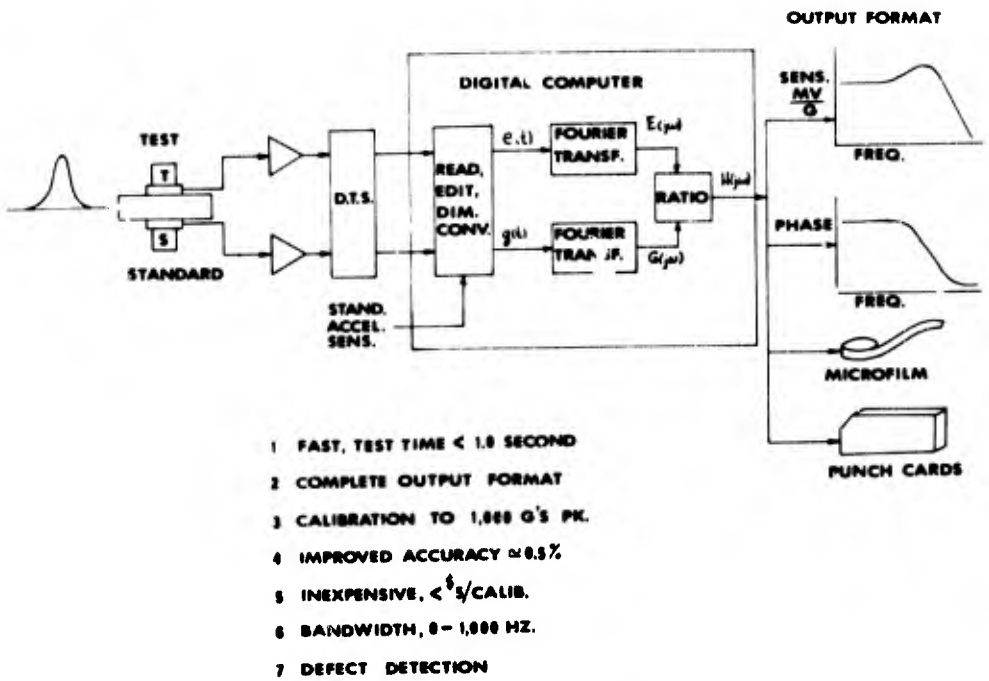

Fig. 4. New technique

accelerometer signals is sampled at a maximum of 10,400 samples per second.

The 10-bit plus-sign sample size yields 1023 counts from 0 to a full scale of +5000 mv and 1023 counts from 0 to -5000 mv. The rms sampling error is 0.03 percent [9] of full scale. Each calibration record is identified by an I.D. number placed automatically on the tape just prior to the recorded data. In this way, a large number of calibration records can be recorded and stored on a single reel of tape and analyzed during a single pass through the digital computer.

For a given calibration, the digital computer reads and edits the magnetic tape and converts the binary counts into engineering units of millivolts for the test accelerometer time history $e(t)$ and g units for the standard accelerometer time history $g(t)$. A control card with the standard accelerometer sensitivity is required to perform the latter dimensional conversion. The computer then calculates the individual Fourier integral transforms $E(j\omega)$ and $G(j\omega)$ according to Eq. (8). Following this, the computer ratios the two transforms to produce a frequency function $H(j\omega)$:

$$\frac{E(j\omega)}{G(j\omega)} \quad H(j\omega) \qquad (9)$$

$H(j\omega)$ is the calibrated sensitivity of the test accelerometer, in units of millivolts per g, as a function of frequency over the bandwidth of interest. It also contains the phase shift characteristic as a function of frequency.

Finally, the computer outputs all this calibration information in the form of graphs for documentation, microfilm for storage, computer punch cards for future data analysis work, and a listing for checking.

Pulse Shape

In the application of this technique, one must be concerned with the type or shape of pulse applied to the accelerometers. The Fourier integral transform of the pulse must fully saturate the calibration bandwidth. A square pulse, as shown in Fig. 3, would not be satisfactory because it contains no frequency content or energy at integer multiples of $2\pi/\tau$. Also, the transform of the applied pulse must not contain any energy beyond the Nyquist limit or the frequency which is numerically one half of the sampling rate. For the DTS sampling at 10,400 samples per second (per channel), the Nyquist limit is 5200 Hz. Also, in accordance with the restrictions on Eq. (8), the pulse must equal

before pulse initiation (t 0) and zero after pulse completion (t T).

Using the above restrictions as design criteria, we chose a pulse that is Gaussian in form (see Fig. 5). The unique thing about a Gaussian time function is that its Fourier integral transform is also Gaussian [10]. When plotted on log-log paper, a Guassian transform is very flat from dc to some corner frequency and then rolls off at an ever-increasing slope. However, the best reason for using a Guassian-type pulse is that in reality it is quite easy to create, to a close degree of approximation.

TESTING

Hand Hammer Accuracy Test

One of the first tests performed using the digital computer program was designed to produce an indication of the accuracy of the entire digital system (which includes the DTS, software, and hardware of the digital computer) in the quickest and simplest manner. A hammer was built from 1.5-in. round stock steel with a Plexiglas handle attached. On one end was mounted a single accelerometer, and on the other end a nylon cap screw was inserted to act as an impact medium (see Fig. 6). To define the system accuracy, the output signal from the single accelerometer and signal conditioning unit was paralleled into both the test and standard accelerometer channels of the DTS. The computer then read two sets of data, multiplexed from the same single pulse, and effectively ratioed the two transforms derived from the same pulse. Since this is calibrating the same pulse against itself, the ratio should be unity, and any deviation from unity would be an indication of system error.

The hammer was impacted onto a phenolic table six times, and six records were made. A resulting typical pulse was "nearly" Gaussian, of about 2.5 msec duration and 95-g peak. The Fourier integral transform rolled off steeply (22 db/octave) beyond 400 Hz (see Fig. 7). Figure 8 is an envelope of the results of all six accuracy calibrations plotted in terms of percentage of deviation from unity. The results were excellent. The system error remained less than 0.2 percent out to 400 Hz and diverged with increasing frequency. The reason for the loss of accuracy beyond 400 Hz is the frequency content of the transform becoming very small and the computer ratioing two small numbers.

Drop Ball Test

A second test series was set up using a commercially available "drop-ball shock calibrator" as an exciting device. The testing was designed (a) to provide an actual calibration and compare it with a calibration performed on an electromagnetic exciter, (b) to test again for the system accuracy as in the previous tests, (c) to get a reasonable estimate of the time required, and (d) to get a reasonable cost estimate on a production basis.

Two identical model piezoelectric accelerometers and associated charge amplifiers were sinusoidally calibrated at 1, 10, and 20 g levels from 10 to 1000 Hz. One accelerometer was considered the test accelerometer, the other the standard. The calibrated sensitivity of the test accelerometer as calibrated against the standard is plotted in Fig. 9. The wave shape developed by the drop-ball shock calibrator was nearly Gaussian, of about 1.0-msec pulse duration and 36-g peak acceleration. There was one major and serious difference in the wave shape. Before the dropping ball impacts the anvil on which the accelerometers are mounted, the anvil is held in position by a magnetic clamp. After impact, the anvil is freed from the magnetic clamp and allowed to fall freely so that the pulse does not terminate back at zero g where it started but displays an overall

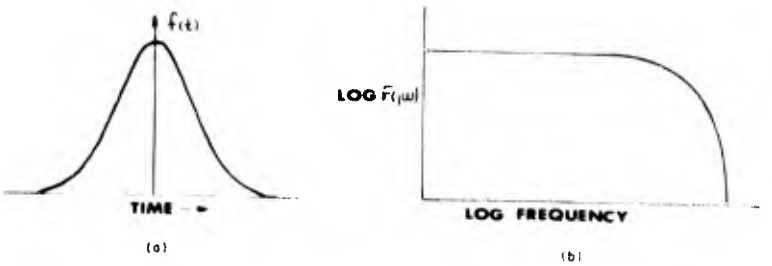

Fig. 5. (a) Gaussian time function; (b) Gaussian Fourier transform

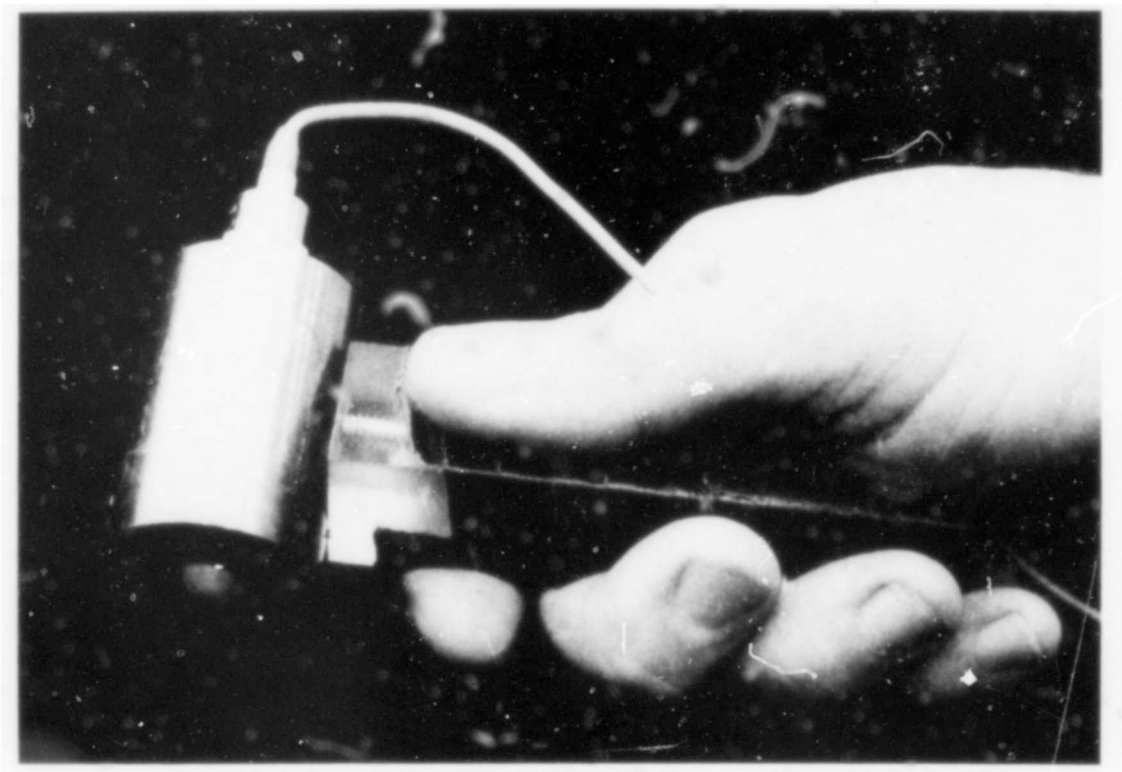

Fig. 6. Hand hammer

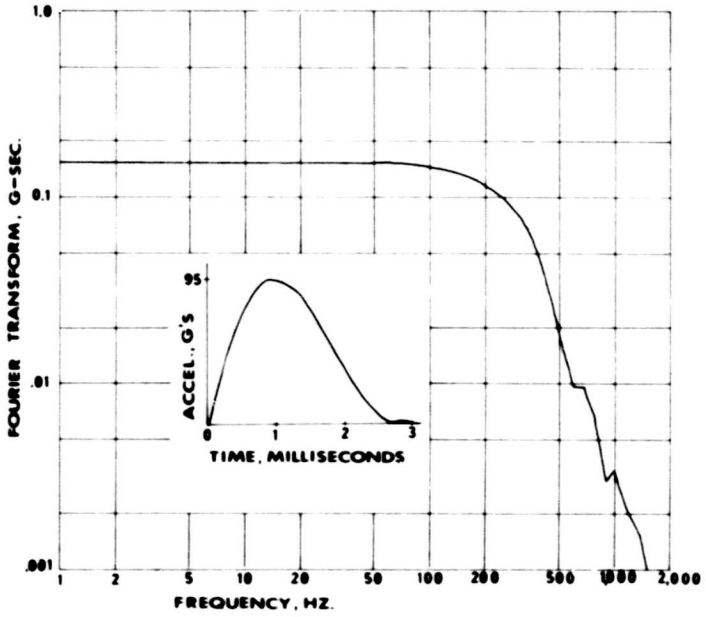

Fig. 7. Hammer impulse and Fourier transform

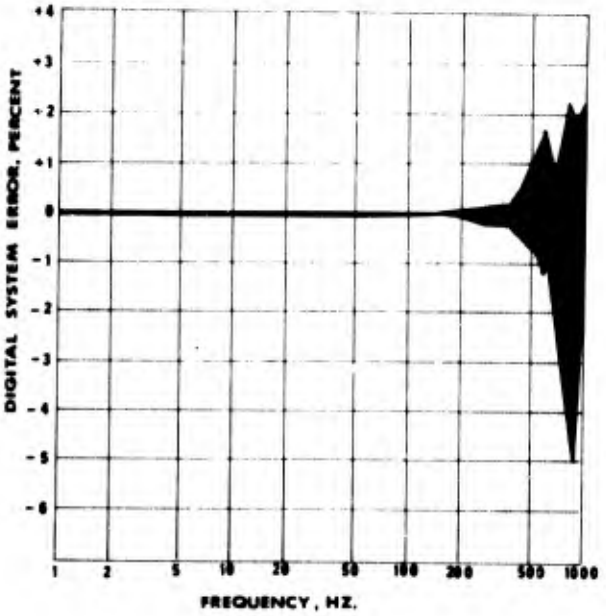

Fig. 8. Digital system error

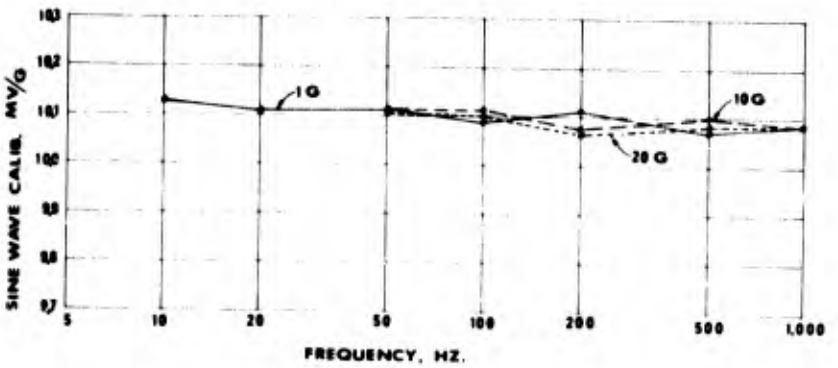

Fig. 9. Sine wave calibration

1-g shift. This violates one of the restrictions of Eq. (8) and forces wave shape truncation at some arbitrary point in time.

A total of 24 impulse calibrations plus 5 additional accuracy calibrations were recorded within 1 hr. (This time did not include mounting and dismounting the test accelerometer. This must be done in any production calibration simulation and general requires 4-5 min.) The resulting envelope of the 24 impulse calibration runs is illustrated in Fig. 10. The obvious error divergence in the low-frequency domain is attributed to the 1-g shift and necessary truncation plus the quantization error at that level. However, it should be noted that even with the obvious violation of one of the restrictions of Eq. (8), the errors or differences from the sinusoidal calibration were approximately ±1 percent. The 5 accuracy calibrations indicated digital system accuracy of ±0.2 percent over the entire bandwidth.

The estimated time to perform these 29 calibrations, including mounting and dismounting the test accelerometers, is about 3.5 hr. The actual computer time to analyze the 29 calibrations was 4.02 min. At a computer charge of $200 per hour, this amounts to $0.46 per calibration (output in listing form only; plotting and card punching increases the cost slightly). All things considered, the per calibration cost estimate is between $2 and $5.

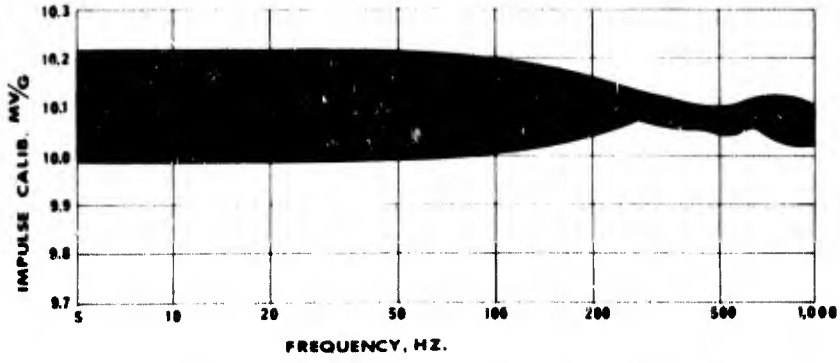

Fig. 10. Envelope of impulse calibrations

DESIGN OF AN IMPULSE EXCITER

Specifications

The following specifications were chosen as criteria for designing a device to produce an acceleration impulse to a standard and one or more test accelerometers to be calibrated by the described technique above. (With higher sampling rates of A/D converters available in the future, it will be possible to excite and record signals from several test accelerometers simultaneously.)

1. The acceleration pulse should be Gaussian or a good approximation of a Guassian time function. The resulting Fourier transform should be flat to some corner frequency and then roll off at better than 20-db/octave slope. The pulse duration should be adjustable down to 1.0 msec. The pulse shall start at 0 g and terminate at 0 g.

2. Because of the wide variety of test requirements, the peak acceleration level must be fully adjustable from near 0 g to 1000 g.

3. Crosstalk or transverse motion shall be less than 2 percent of the peak acceleration level.

4. The mounting area for the test accelerometer shall be large enough to accommodate servo force-balance type accelerometers.

5. The device should be simple in design and inexpensive to fabricate, and should require a minimum of maintenance.

Description of Impulse Accelerometer Calibration Table

The impulse exciter that evolved out of the specifications listed above is illustrated in Fig. 11. It is basically a round, laminated table 30 in. in diameter. It has two protruding cleats 180 deg apart that impact against steel stops bolted to the fixture base. Convex rubber pads are fixed to the cleats as impact media to shape the pulse. The acceleration impulse direction is horizontal and tangent to the outer edge of the table.

The procedure is to back up the table against the opposite stop, thereby lifting a bucket of lead (variable) via cord wrapped around the hub and passed over two sheaves. Releasing the wheel allows the weighted bucket to accelerate the table at a low, constant level. About 30 deg before impact, the bucket bottoms out, the cord goes slack and the table coasts, with negligible deceleration (bearing friction is so small that restrictions on Eq. (8) are satisfied) into the stops to create the desired pulse. Just prior to impact, the DTS recording is started and continues for a given period of time. After impact, the table rebounds with negligible deceleration for the 30 deg required to take up slack in the cord. By this time, the DTS has stopped recording the transducer output signals.

This design was chosen for the following reasons:

1. The radial crosstalk acceleration is proportional to the angular velocity of the table, which is the integral of the angular acceleration.

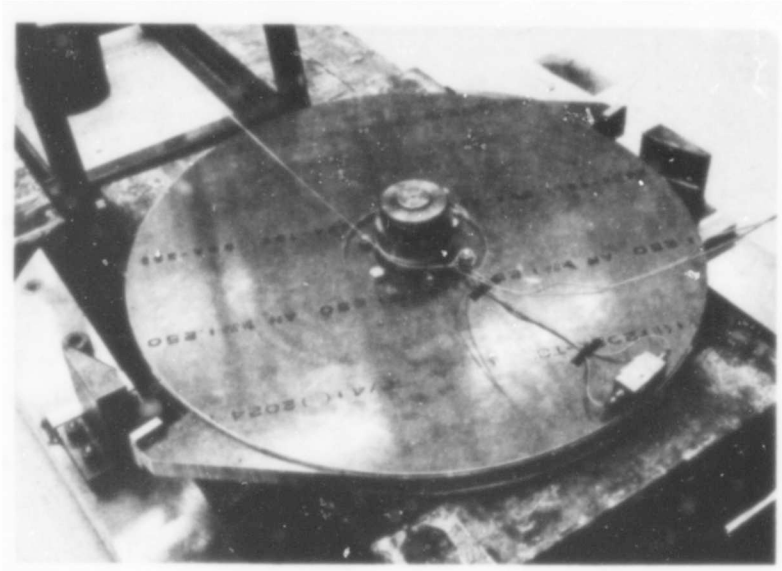

Fig. 11. Accelerometer calibration table

The table diameter of 30 in. was chosen to insure that the radial crosstalk be less than 2 percent of the peak tangential acceleration.

2. The table yields an overall velocity change and thereby produces acceleration energy down to 0 Hz.

3. The peak acceleration level is easily adjustable by adjusting the bucket weight and yields no rebound problems for very low acceleration pulses.

4. The first tangential resonance is due to a "shear-moment of inertia" relationship of the table and is predictable at about 3000 Hz. By proper design of the impact pads, a minimum of energy is produced at that frequency. Further, the laminated construction is such that the laminating adhesive will mechanically filter out the 3000-Hz resonance.

5. The table offers a larger, easily accessible area for mounting transducers.

6. The dual impact design eliminates any reaction load at the center bearing.

7. With the design of a stable mounting platform centered over the bearing housing, the device could be adapted to calibrate angular accelerometers.

8. Finally, and probably most important for the present, it is simple and inexpensive to build, and it requires negligible maintenance.

Initial Testing

Evaluation of the impulse calibration table was very encouraging; however, some design errors did show up. The base plate (2-in.-thick aluminum), upon which the stops are mounted, was not stiff enough and, consequently, the stop reactions dynamically warp the base and excite the bearing shaft. The result is that the vertical crosstalk is 6-10 percent of the impulse peak level. The cleats, upon which the rubber pads are mounted, and the stops did not have enough contacting surface area, and the resulting impulse is too long in duration to maintain required system accuracy to 1000 Hz. Corrective modifications are presently in work.

While the parts required for modification of the calibration table were in work, the computer program, developed by a Boeing programming group, was being tested for acceptance. The fundamental acceptance criteria are that the program must do the processing as required and that it be adequately documented so that engineering aides can efficiently service the program without extensive training or knowledge of the mathematics. Acceptance was made when an engineering aide was able to process a tape, with many calibrations, and get the proper results. An accelerometer calibration produced from the computer plot routine during this acceptance testing is shown in Fig. 12. It is the calibration of a ±25-g, strain-gaged accelerometer with a natural frequency of 650 Hz.

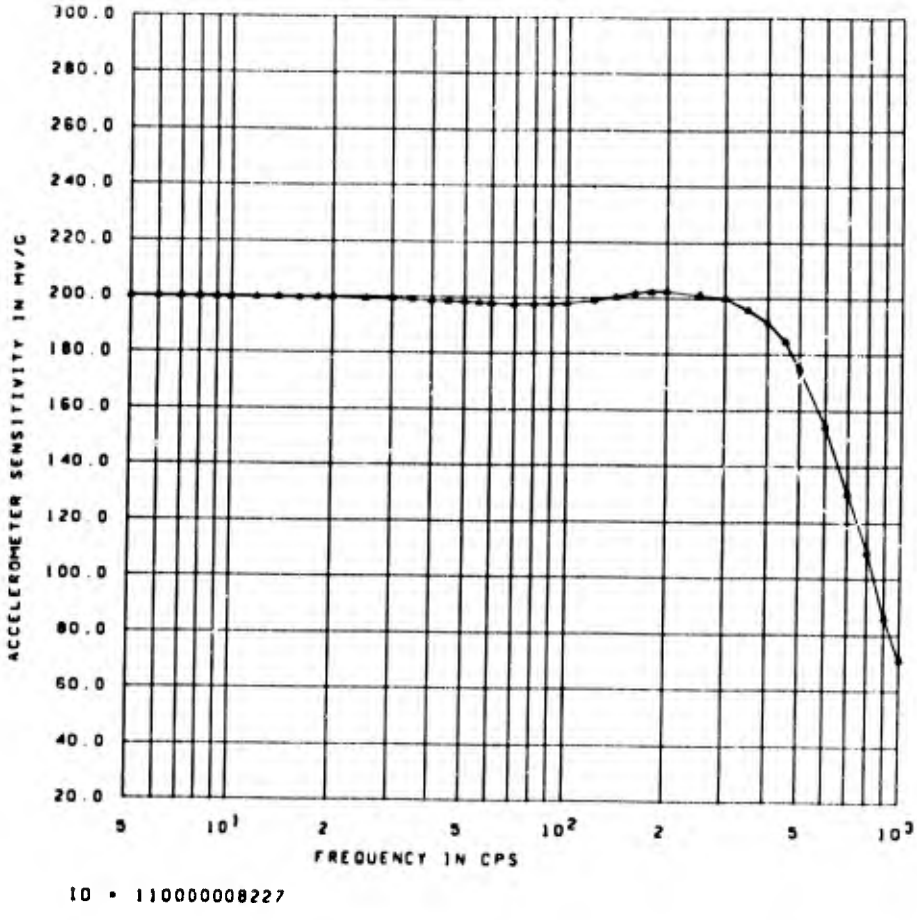

Fig. 12. Accelerometer calibration from computer plot routine

CONCLUSIONS

For the production calibration of accelerometers for aerospace testing, the present technique of sinusoidal excitation by electromagnetic exciter has been shown to be slow, limited, inaccurate, and expensive. The modern digital computer has made the accurate computation of Fourier integral transforms from transient or impulse types of time functions an economic reality. Because of this, a new technique for the calibration of accelerometers has been developed that is faster, cheaper, more accurate, and more versatile than the present technique. Basic ground rules for the application of the technique have been discussed and integrated into the design and fabrication of an accelerometer calibration table.

ACKNOWLEDGMENTS

The author wishes to thank the following members of Boeing Space Division Staff Management for their support in the development of this technique: D. R. Harting, J. J. Sheppard, D. G. DeCourcey, A. T. Snyder, and C. J. Adriance.

REFERENCES

1. R. R. Bouche, "The Absolute Calibration of Pickups on a Drop-Ball Shock Machine of the Ballistic Type," Proc. IES Annual Meeting, pp. 115-121, Apr. 1961

2. R. R. Bouche, "The Calibration of Shock and Vibration Pickups," The Magazine of Standards, Mar. 1960

3. J. E. Rhodes, "Piezoelectric Transducer Calibration Simulation Method by Series Voltage Insertion," Environmental Quarterly, Vol. 8, No. 1, pp. 30-33 (1962)

4. S. Levy, and R. R. Bouche, "Calibration of Vibration Pickups by the Reciprocity Methods," J. Res. Nat. Bur. Standards, 57(4) pp. 227-243, Oct, 1956

5. J. Favour and J. LeBrun, The Boeing Co., Seattle, Wash., "Measurement of System Dynamics by Impulse Techniques," unpublished notes

6. J. Favour, "Transient Data Distortion Compensation," Shock and Vibration Bull. 35, Pt. 5, pp. 231-238, Feb. 1966

7. G. E. Dreifke, and J. O. Hougen, "Experimental Determination of System Dynamics by Pulse Methods," paper presented at the Fourth Joint Automatic Control Conference, June 1963

8. M. Schwartz, Ch. 2 in Information Transmission Modulation and Noise (McGraw-Hill, New York), 1956

9. J. S. Bendat, and A. G. Piersol, Measurement and Analysis of Random Data (Wiley, New York), 1966

10. B. M. Oliver, "Square Wave and Pulse Testing of Linear Systems," Hewlett-Packard Co., Application Note 17

* * *

BLANK PAGE

BIDIRECTIONAL SHOCK AND HIGH-IMPACT EFFECTS ON SHOCK TRANSDUCERS

V. F. DeVost and P. S. Hughes
Naval Ordnance Laboratory
Silver Spring, Maryland

Naval Ordnance Laboratory has observed frequent signal errors in recordings of shock produced by underwater explosions, firing of artillery projectiles, and actuation of pyrotechnic devices. Similar errors have been observed in recordings of shock produced by laboratory testers used to simulate the effects of shipboard shock, hard-target impact, and projectile setback.

A laboratory investigation of the problem has traced the source of signal error to the piezoelectric shock transducer and has identified some of the characteristics of shock which adversely affect transducer response: the shocks contain very high frequencies and some are bidirectional.

INTRODUCTION

The troublesome shock areas discussed in this paper are relatively few, considering the wide variety of shocks associated with weapons and test facilities. This limited investigation of the problem of signal error in no way is intended to rate or disqualify current shock transducers; overall, transducers have done and continue to do a good job. None of the transducers used at NOL have been discarded because of signal error problems, except those which were damaged; however, the experience has taught us to screen transducers carefully before using them to measure severe and complex shocks. This paper is intended to move others to investigate the problem and work toward its solution.

Despite the fact that many shocks encountered by new weapons and shock facilities are within the rated range of most high-g transducers, it has been rarely possible to measure them accurately. Signal error in recordings of bidirectional shocks and high impacts have been encountered using transducers rated at 20,000 to 100,000 g and having natural frequencies of 60 to 100 kHz. This paper discusses the characteristics of shocks which adversely affect transducer response and identifies, where possible, the kinds of signal error that occur in shock recordings. The paper also briefly describes mechanical filtering for shock transducers and discusses the response of single-degree-of-freedom systems subject to complex shock.

Bidirectional Shock

The term "bidirectional" is used to characterize shocks that excite the monitoring transducer along its transverse as well as its longitudinal axis. Not all bidirectional shocks cause signal error; significant errors were found only with shocks that contain high frequencies in the direction of the transverse axis of the transducer.

High Impact

The term "high impact" is used to characterize very severe shocks that excite the monitoring transducer, usually along its longitudinal axis, at frequencies approaching the transducer natural frequency. Generally, these shocks are of very short duration or have an extremely short rise time – of the order of microseconds. Some of the high-impact shocks discussed contain significant transverse components; others are unidirectional.

Signal Error

As discussed here, signal error is attributable to transducer malfunction only. Expressed in terms of transducer response, it is the error that results from transducer signals which are not proportional to the shock being measured. Other possible sources of signal error were investigated to make certain that the problem was

in fact a transducer problem. This was essential since in recording shock, signal errors can arise from many sources; the following are some of the more common ones:

1. Overmodulation resulting from input signals greater than the dynamic range of tape recorders;

2. Clipping resulting from overload of signal-conditioning amplifiers;

3. Spurious noise generated by the signal conditioners as a result of shock (more common in missile-borne devices than in laboratory devices);

4. Signal distortion by the transducer cables;

5. Noise from chatter of transducer connectors;

6. Phase distortion resulting from improper filtering.

Measures taken to eliminate or minimize the above signal errors consisted of the following:

1. The gain settings of the tape recorder and signal conditioners were set well within their dynamic ranges (only bench model charge amplifiers were used). In addition, the signal conditioners were shock isolated.

2. Low noise transducer cables were used. Tests to the breaking point of the cables were made, and the cables were found to be essentially noiseless.

3. During several severe tests, the outputs of two transducers, one potted in hard epoxy and one unpotted, were compared. The outputs were virtually the same, indicating that connector chatter was not a source of signal error for the transducers used.

4. The transducer outputs were recorded on magnetic tape and played back for shock spectral analyses. The spectra were then compared with spectra obtained from real-time analogs [1] and found to differ by less than 5 percent at frequencies up to 15 kHz. This indicates that the tape recorder filters are a negligible source of signal error.

FIELD TEST RECORDINGS

Pyrotechnic Shock

Naval Ordnance Laboratory's first attempt to record explosive-separation shock was in support of the development of the Blue Rock vehicle. Separation of the canisters from the vehicle was accomplished in two stages. In the first stage, capsule doors were cut open with Primacord; in the second stage, canisters were ejected from the capsule with SR 4990 propellant actuators.

Primacord-produced shocks contained very high frequencies and violently excited adjacent structures in every direction. Figure 1 shows several recordings of explosive-separation shock taped with a 10-kHz flat response system. Transients of the shock observed on an oscilloscope showed that the shock contained frequencies somewhat higher than those recorded on tape; initial pulse rise times may have been shorter than the Fig. 1 recordings indicate. The combined effects of shocks in the transverse and longitudinal direction of the transducers apparently resulted in the loss of transducer preset or in crystal damage.

Separately run ejection tests in which the canisters were ejected from the capsule were made using early model actuators. These tests resulted in damage to the transducers which were rated at 100,000 g – this damage occurred even at ejection velocities as low as 25 fps. Shock recordings of ejections made with lower-g actuators contained signal errors very similar to those shown in Fig. 1.

Signal error in other pyrotechnic shock measurements has been reported and observed in several recent shock and vibration papers on the subject (2 through 5). Admittedly, we cannot say for certain that the source of error in the tests reported was the transducer; however, some of the recordings look very similar to those described in this paper, especially those showing baseline shift.

Underwater-Explosion Shock

Signal errors were observed in recordings of shocks produced by close-in underwater explosions against a submerged 3-ton platform supporting an instrumentation buoy. During this series, the velocity change of shock ranged from about 35 to 55 fps. Because of the size and complexity of the test apparatus, the explosions excited shocks in every direction. Transducers were mounted inside the buoy and on the buoy antenna. The effect of the shock on transducers in many cases was similar to the effects observed in pyrotechnic shock tests. Figure 2 shows representative recordings in which signal error was present. Other examples of the Fig. 2A shock are shown in Fig. 3, transducer G. The most frequent error observed during

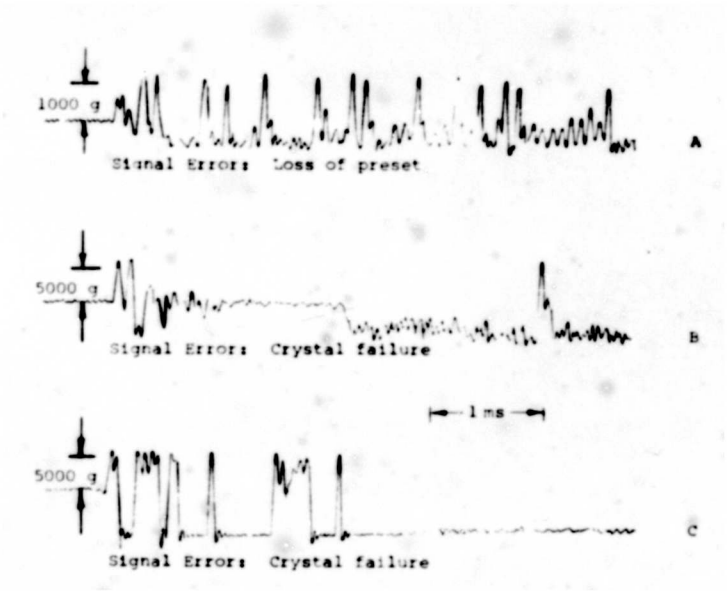

Fig. 1. Signal error in pyrotechnic shock recordings (Blue Rock instrument capsule)

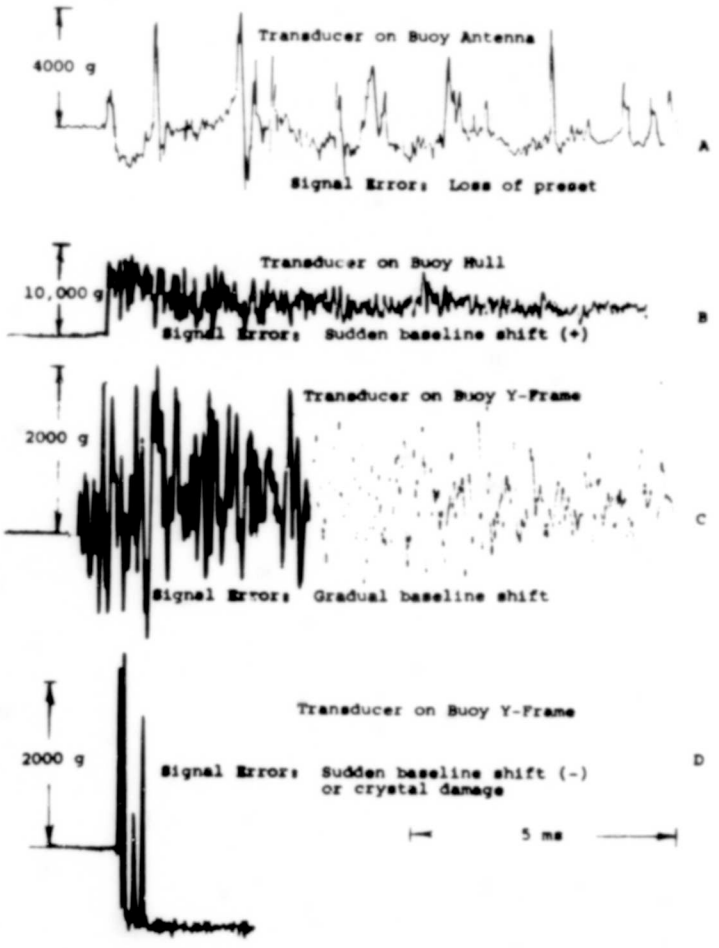

Fig. 2. Signal error in underwater explosion shock recordings

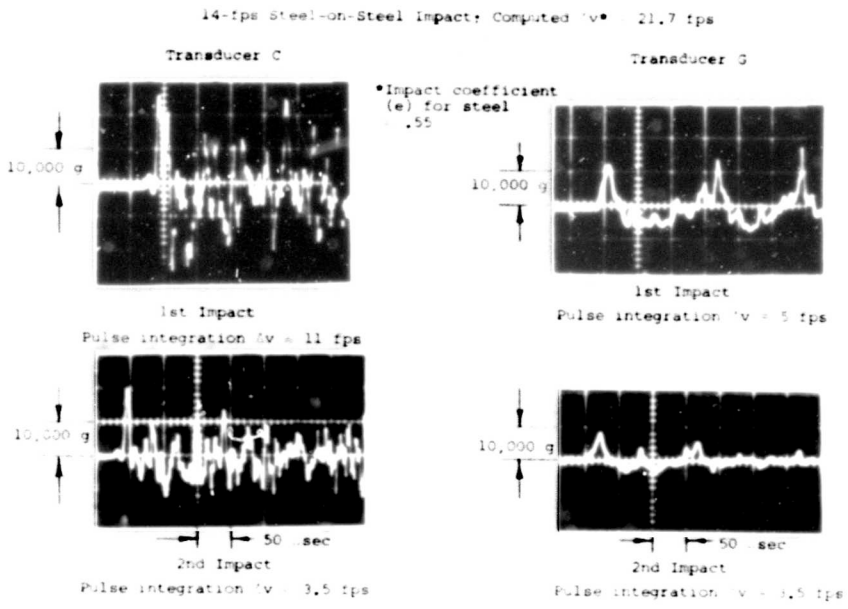

Fig. 3. Signal error in high-impact shock tester recordings (NOL 40-ft free-fall drop tester)

recordings of underwater explosion tests was that of baseline shift, traces B. and C.

Gun Shock

The most severe shocks recorded in the field were those produced in 5"/54 cartridge cases during automatic ramming and in artillery projectiles fired at service pressure. Signal error during ramming shock resulted from very high axial impacts, 30- to 32-fps velocity change, containing frequencies near the natural frequencies of the transducers. The errors during gun firings resulted primarily from transverse impacts of the projectiles against the barrel wall, which accounted for the sudden and high signal overshoot. Figure 4 shows recordings of both types of shocks [6]. The recording system used in the gun tests was flat to 20 kHz.

LABORATORY TEST RECORDINGS

Air Gun Shock

Several testers used at NOL produce shocks that adversely affect shock transducer response. Signal error has been detected in recordings of air gun [7] shock in which transverse impacts occur at levels of 10 to 40 percent of the longitudinal shock levels. Figure 5 shows recordings of shocks produced by the NOL 15-in. and 5-in. air guns and identifies the signal errors present.

Drop Tester Shocks

Transducers subjected to relatively mild steel-on-steel impacts using the NOL 40-ft drop tester [7] were able to withstand only three or four impacts before they became inoperative. Free-fall drops were made at a height of 3 ft. Figure 3 illustrates how the shock transducers of two different manufacturers responded to shocks containing frequencies estimated to be in the range of 80 to 100 kHz. Because the transducers read low (the indicated velocity change was considerably less than that computed), crystal damage under this kind of impact apparently occurs during the rise portion of the initial pulse. Also, since the signal level continued to drop off with repeated impacts, damage was apparently progressive.

Transducers were subjected to shock tests using the Mk 7 drop tester [8]. The impacts were of greater velocity change but lower frequency content than the previously described 40-ft drop tester pulses. The transducers survived the shock but produced substantial signal errors, such as baseline shift, signal overshoot, and loss of preset, as shown in Fig. 6. These

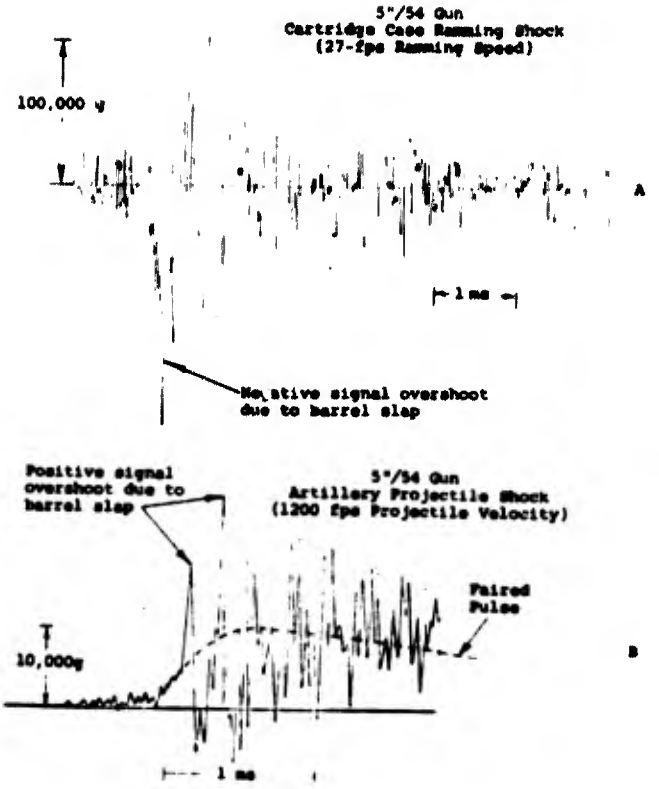

Fig. 4. Signal error in 5"/54 gun shock recordings

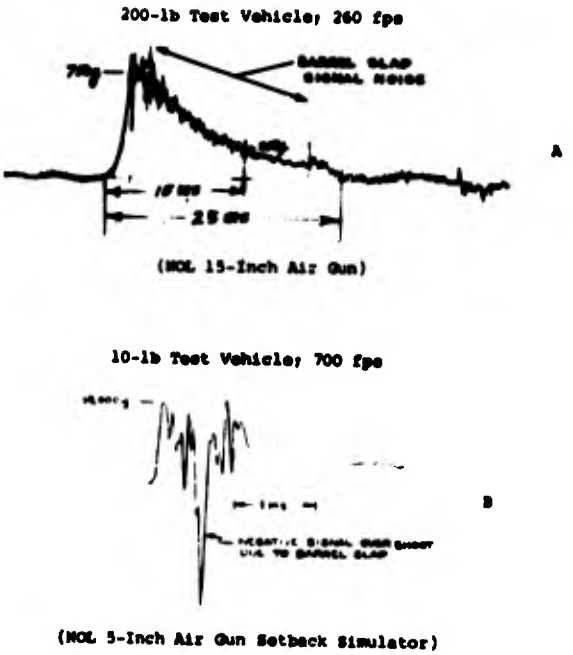

Fig. 5. Signal error in air gun shock recordings

errors appear to have been caused by the high frequencies (about 50 kHz) present in the shock; resonances may have occurred in the transducer case or mass-crystal element.

BIDIRECTIONAL SHOCK TESTS

In the field tests described previously and in some of the laboratory tests, it was impossible to determine with desired accuracy the actual directions, velocity, and characteristics of the shocks which adversely affected transducer response. To investigate the effect of bidirectional shock under controlled conditions, laboratory tests were performed on transducers in which a high-frequency transverse impact was superimposed on an axial shock pulse.

To perform the tests, special apparatus was set up using a free-fall drop tester, the WOX-126A [9]; the apparatus is represented in Fig. 7. The carriage is dropped onto a standard shock pad to produce a smooth shock pulse in the axial direction. The axial shock inertially drives a hammer against a horizontal rod to

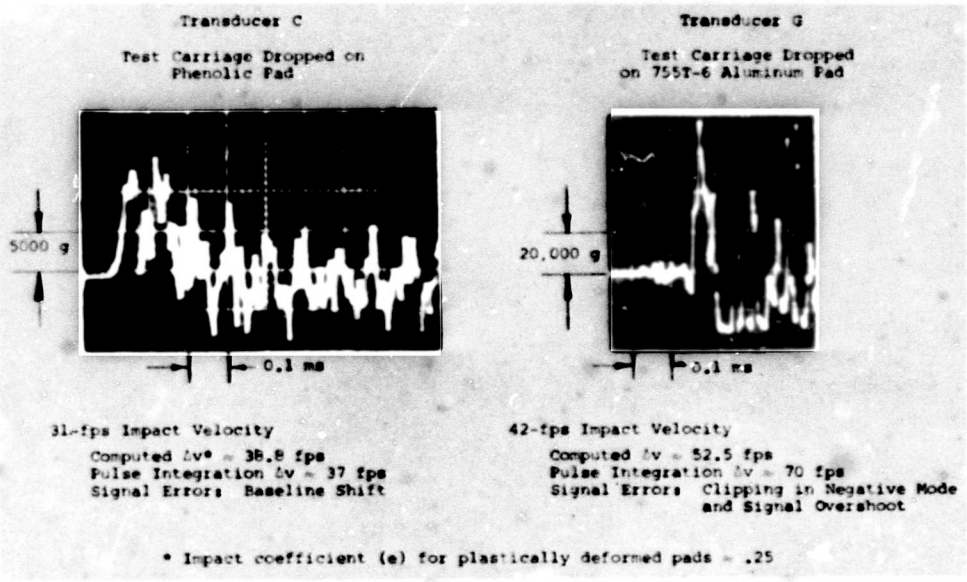

Fig. 6. Signal error in high-impact shock tester recordings (Mk 7 explosive component shock tester)

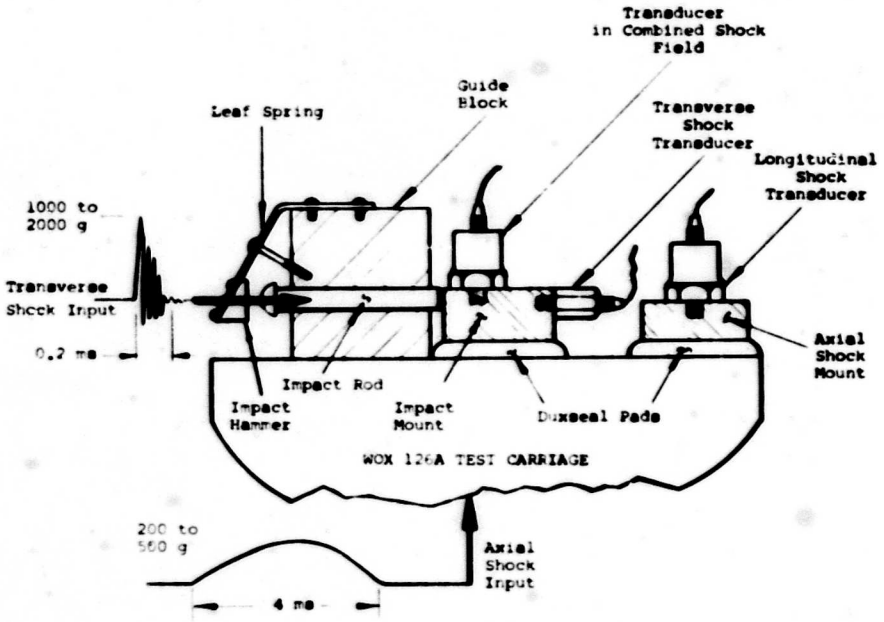

Fig. 7. Bidirectional shock test apparatus

produce an impact against one of the mounts in a direction normal to that of the axial shock. Duxseal pads are used to prevent the transverse shock from exciting the impact mount in the axial direction and to isolate the axial shock mount from the transverse shock. Duxseal, a nonhardening, nonresilient putty, is stiff enough in compression to withstand low-frequency shock, but soft enough in shear to attenuate impact shock – its behavior under impact loading is discussed later.

Eight different high-g, piezoelectric shock transducer models were tested for response to bidirectional shock. Three gages were early models, no longer in production. The gages responded to transverse impacts by superimposing signals on the axial pulse of 10.2 percent to 65 percent of the peak transverse input. Oscillograms of the applied shocks and the response of transducers to bidirectional shock are presented in Figs. 8, 9, and 10. The transducers are not identified by name since, as indicated above, it is not the object of this paper to rate transducers for particular shock applications. The screening methods employed in this investigation should prove useful to the users of transducers for determining whether a particular transducer is adequate for a particular job. Other tests can be performed to check the impact transverse sensitivity of transducers. The appendix describes a ball peening test frequently used to determine unmounted transducer natural frequency.

Several methods were studied to reduce signal error, but with limited success. Electronic low-pass filters proved ineffective because they could not correct distorted pulses or distinguish between real high-frequency signal and signal error. Use of low-frequency, resilient transducer mounts to prevent transducer overload merely introduced another source of resonance in complex shock; also, the mounts were ineffective in reducing signal error produced by transverse shock.

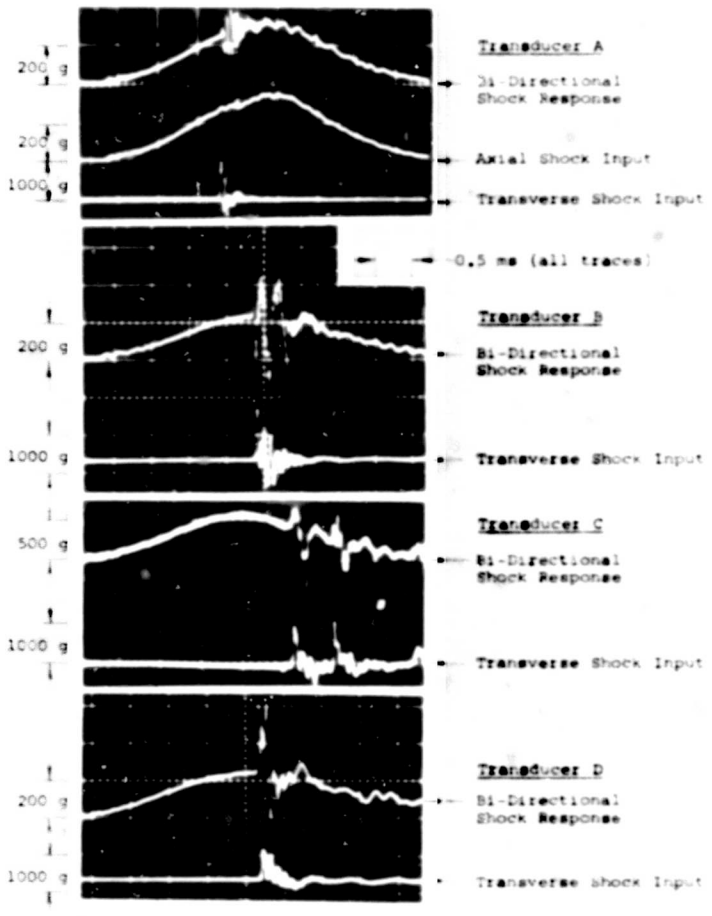

Fig. 8. Response of group 1 shock transducers to bidirectional shock

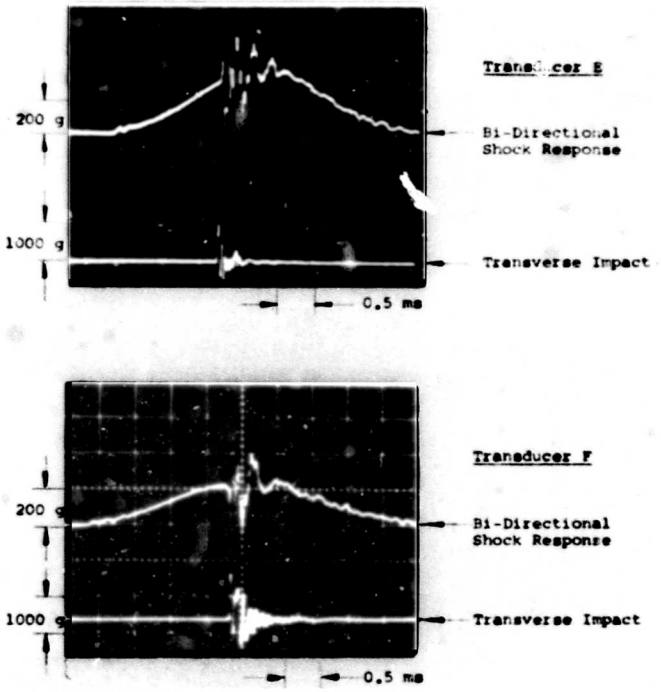

Fig. 9. Response of group 2 shock transducers to bidirectional shock

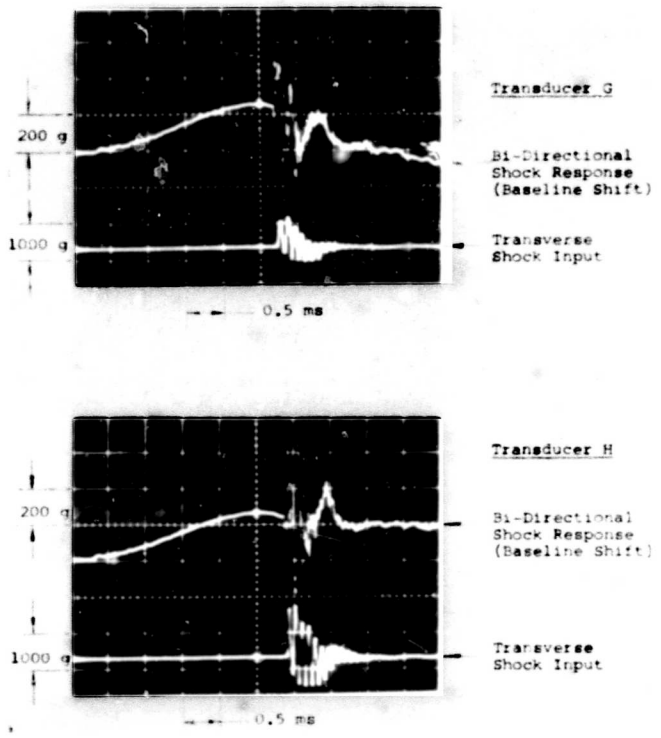

Fig. 10. Response of group 3 shock transducers to bidirectional shock

In several tests in which the shock was known to be lethal to transducers and in which the high-frequency content of shock was not considered critical, potted transducers were used to advantage. The Duxseal used to isolate the transducer mounts in the bidirectional shock tests (Fig. 7) was similarly used to isolate the transducers from the components of shock known to adversely affect transducer response. This filter consisted simply of a housing in which a shock transducer was potted in a nonresilient, nonhardening putty. The material, as demonstrated earlier, is stiff enough to transmit relatively smooth shocks but not resilient enough to respond to very high frequencies. The assembly is shown in Fig. 11.

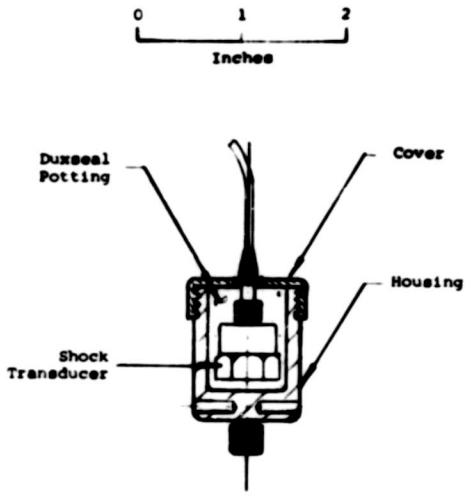

Fig. 11. Mechanical filter for shock transducers

The mechanically filtered transducer was tested for response to high axial impacts and to bidirectional shock with the same apparatus as that shown in Fig. 7. Oscillograms of filtered and unfiltered high-frequency impacts are presented in Fig. 12 to demonstrate how the filter performed when subjected to relatively noisy axial shocks. Performance of the filter for isolating the transducer from the effects of bidirectional shock is illustrated in Fig. 13.

Results of the tests show that for severe axial impacts, 22,000 g and 45-fps velocity change, the filter performed well. The highest frequency passed was approximately 11 kHz; unfiltered shocks contained frequencies from about 30 to 80 kHz. The filter did not appear to distort the principal shock pulse. In the bidirectional shock tests, the filter reduced

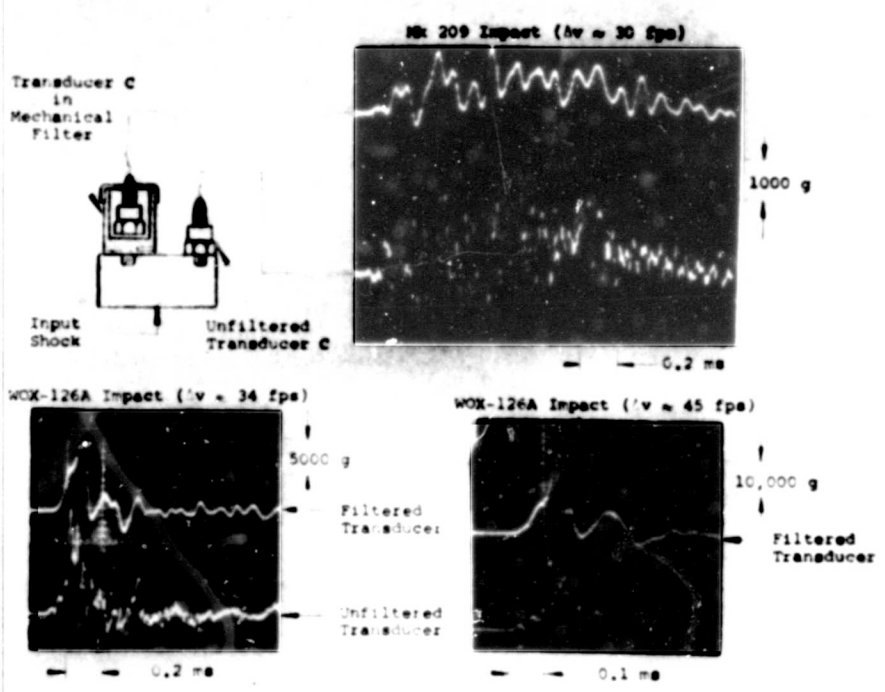

Fig. 12. Performance of mechanical filter subjected to high-impact shock

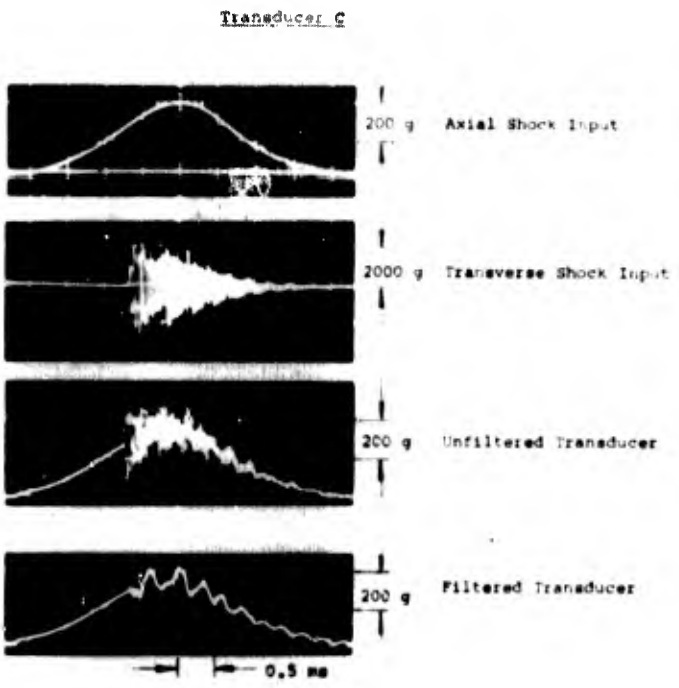

Fig. 13. Performance of mechanical filter subjected to bidirectional shock

transverse signal error to 2.5 percent of the input shock.

EFFECT OF SIGNAL ERRORS ON SHOCK SPECTRAL ANALYSIS

Undetected signal errors in shock recordings can make analysis misleading or meaningless. In the case of the 5"/54 gun shock shown in Fig. 4B, electronic integration of the acceleration record indicated a velocity change that was in error by nearly 100 percent. Also an attempt to analyze the shock spectrally proved completely futile. It is obvious that analysis of many of the shock recordings illustrated here would be equally meaningless. Gross errors in the analysis of this type of shock resulted from a combination of signal errors. To illustrate how signal error can affect interpretation and analysis of shock data, several hypothetical shock transients containing signal error were spectrally analyzed using the digital computer. For simplicity, errors were grouped into two forms: baseline shift and pulse distortion.

To simulate a complex shock containing baseline error, a 10-cycle, linearly damped, sinusoidal transient was generated by the computer, and baseline shifts were introduced by adding a positive or negative step to the entire transient. Figure 14 illustrates the damped sinusoidal signals analyzed: shock-signal 1 contains zero shift, 2 contains 25 percent positive shift, and 3 contains 1.4 percent negative baseline shift. A shock spectrum of each transient is plotted for comparison. Plots are on four-coordinate, log-log scales to show maximum absolute acceleration response, relative velocity response, and relative displacement response of undamped oscillators from 5 to 1000 Hz. Spectrum 1 represents the spectrum for the "correct" pulse. In the low-frequency region, the spectrum becomes parallel to approximately a 5-fps constant velocity value. This corresponds to the velocity change of the input pulse. Spectrum 2 is of the transient with +25 percent baseline shift. This error shifts the low-frequency region of the spectrum toward a much larger constant-velocity line, about 80 fps. Spectrum 3 is of the transient with 1.4 percent negative baseline shift. This negative shift results in a velocity change of zero. Therefore, the spectrum is no longer parallel to a constant velocity line but instead becomes parallel to a constant displacement line of approximately 0.35 in.

These examples illustrate how the spectra of shock can be significantly modified by relatively small baseline shift errors. In the recording of a complex shock where the parameters

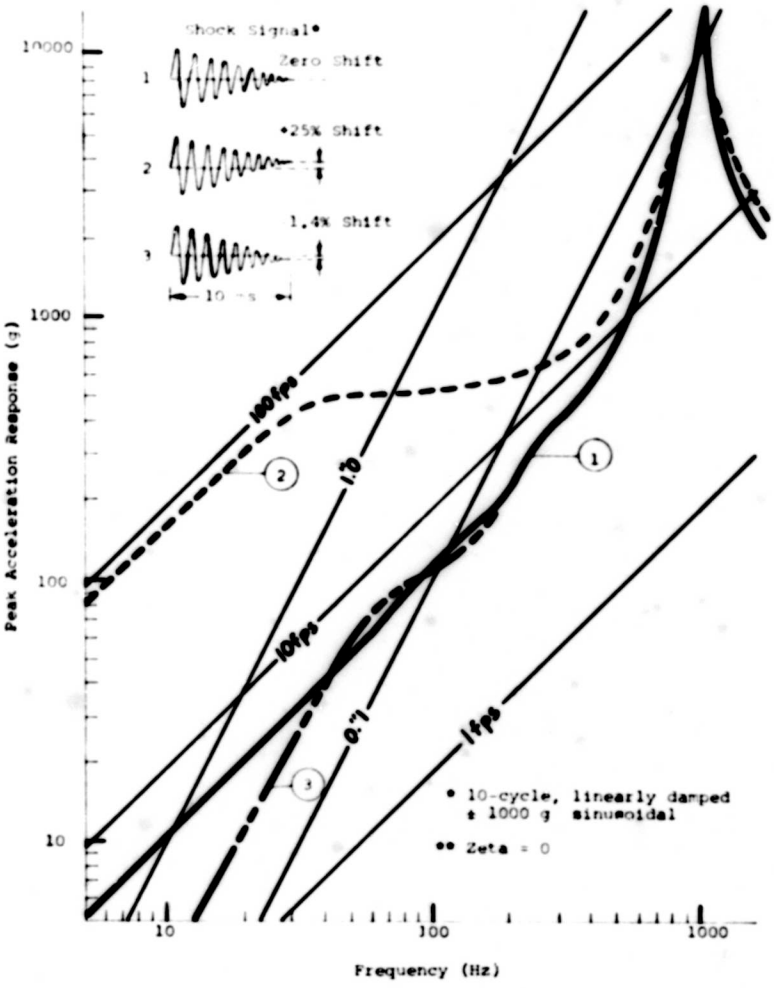

Fig. 14. Effects of baseline shift on shock spectra (zeta = 0)

of velocity change and displacement are unknown, a slight baseline shift could easily go undetected and be carried over into data analysis.

The second form of signal error, abrupt distortion at some point in the recorded shock, was simulated using simple pulses. The distortions consisted of superimposing very short duration signals on the pulses. Versed sine pulses were used as the basic shock, and a sawtooth and step pulse were used to simulate signal error. The pulses are shown in Fig. 15. The sawtooth distortion is typical of transducer responses to bidirectional shock or spurious noise; the step pulse is characteristic of some high-impact shock signal error. Spectrum 4 of the undistorted pulse is compared with spectra 5 and 6 of the two pulses containing signal error. Spectra 4 and 5 are coincident below about 230 Hz because they both have approximately the same velocity change. However, in the high-frequency region there is a marked difference between spectra; maximum error in the distorted pulse spectrum is over 400 percent. Spectrum 6, for the pulse containing an abrupt baseline shift, deviates from that of the undistorted pulse spectrum in both the low- and high-frequency regions: the velocity change indicated by the low-frequency portion of the spectrum is 20 percent low and the accelerations in the high-frequency region are about 11 percent high.

CONCLUDING COMMENTS

Without knowing precisely how the sensing elements of transducers are designed, it is difficult to say why transducers produce erroneous signals when subjected to certain complex

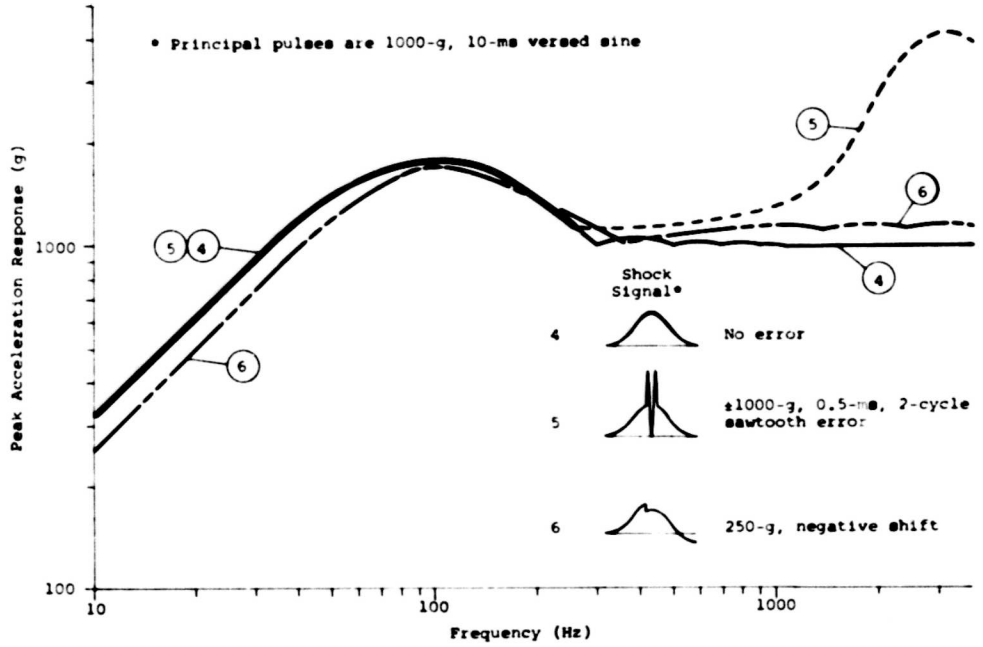

Fig. 15. Effect of pulse distortion on shock spectra

shocks. However, it is clear from the field and laboratory test data examined that the high-frequency components of shock are the principal cause of signal error. Nonresilient mechanical filters may reduce signal error or protect transducers from the damaging effects of shock; but in doing so, that portion of shock which is significant may be ignored. However, if the risk of transducer damage is great, mechanical filtering may mean the difference between getting some meaningful shock data and getting nothing. Perhaps the only practical approach to the current complex or lethal shock problem is to use a mechanically filtered transducer adjacent to one which is unfiltered or to measure shock at the higher frequencies with peak-reading mechanical devices.

Signal error is not merely a problem affecting the accuracy of shock recordings; as demonstrated by the spectra of several hypothetical shocks containing errors, the problem extends to the interpretation and analysis of shock as well.

The most desirable solution to the problems discussed here would be the development of shock transducers with lower transverse sensitivity and with a higher shock range and resonant frequency.

REFERENCES

1. W. W. Mebane, "Analog Shock-Spectrum Analyzer," NOLTR 67-97, June 1967
2. V. R. Paul, "Mechanical Shock from Frangible Joints," Shock, Vibration and Associated Environments Bull., 33(Part 4):63 (1964)
3. H. J. Roberge and J. Rybacki, "Shock Environments Generated by Pyrotechnic Devices," Shock, Vibration and Associated Environments Bull., 33(Part 4):73 (1964)
4. F. A. Ottati, "Simulation of Impulsive Environments by Use of Pyrotechnic Devices," Shock and Vibration Bull., 35(Part 1):81 (1966)
5. V. S. Noonan and W. E. Noonan, "Structural Response to Impulsive Loading (Pyrotechnic Devices)," Shock and Vibration Bull. 35(Part 6):265 (1966)

6. P. S. Hughes and L. A. Vagnoni, "Direct Measurement of 5"/54 Gun Setback Acceleration," Shock and Vibration Bull. 36(Part 2):53 (1967)

7. "U. S. Naval Ordnance Laboratory Shock-Testing Facilities," NOLR 1056 (2nd rev.), Mar. 1956, p. 36

8. V. DeVost, "Explosive Component Test Adaptor for Drop Shock Tester Mk 7 Mod 0," NOLTR 63-263, Dec. 1963

9. V. DeVost, "Test Set, Drop Shock, WOX-126A," NOLTR 61-106, Nov. 1962

Appendix

BALL PEENING TESTS

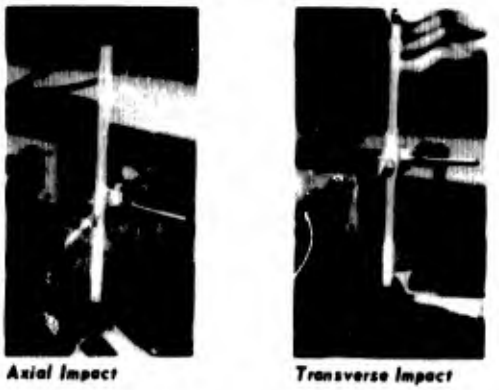

Fig. A-1. Ball peenir test apparatus

Ball peening tests consist of dropping a steel ball against the bottom or side of the transducer and monitoring its response. The transducer may be supported by the cable only or held seismically with a rubber band. The ball should weigh no more than 1 or 2 gm and be dropped about 9 in. — under these conditions no denting of the transducer surface will occur. Figure A-1 illustrates how the tests are run.

Drops are made first against the bottom of the transducer to determine the approximate impact level; then drops are made against the side of the transducer. Figure A-2 presents the results of impacts produced with a 1-gm ball against a 13-gm transducer (model C, Fig. 8). Computed transducer velocity change is about 0.5 fps.

Apparently, the transverse sensitivity of the unmounted transducer is significantly higher than that of the mounted transducer: 41 percent compared to 18 percent. While this test method may not realistically show the useful transverse impact sensitivity of a transducer, it has some merit for comparing one transducer with another to select the best instrument for measuring complex shock.

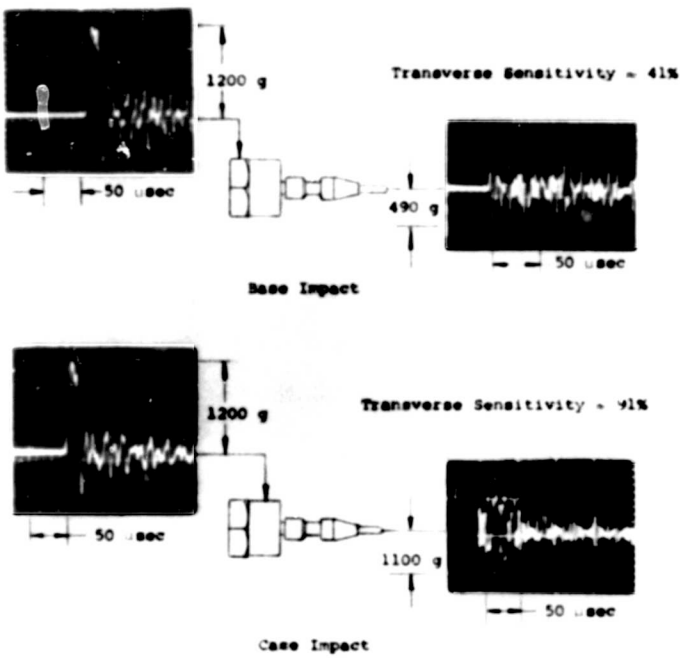

Fig. A-2. Ball peening impacts and responses (transducer C)

* * *

INFLUENCE OF FIXTURE STRESS CONCENTRATIONS ON RING ACCELEROMETERS

James A. Nagy and Charles E. Henley, Jr.
NASA Goddard Space Flight Center
Greenbelt, Maryland

Tests have revealed that the most commonly used base-strain-free accelerometer in use at the Goddard Space Flight Center is subject to a subtle source of error from strains developed in vibration fixtures. Accelerometers mounted on supposedly rigid surfaces may show errors of the order of 100 percent at the very low frequencies below any resonances.

A study to determine the nature of the fixture stress concentration and means of avoiding it was initiated. The test methods used and the results obtained are described. The test methods discussed include (a) standard accelerometer calibration techniques as well as calibrations varying torque, position, and mounting hole angle; (b) photoelastic techniques; (c) base sensitivity checks; and (d) a transducer devised to detect the presence of base strain in mounted accelerometers.

INTRODUCTION

This paper presents the results of an investigation into accelerometer base-strain sensitivity. This investigation was precipitated by anomalies experienced during lateral vibration tests of heavy spacecraft where a large moment tends to tip a circular base about a point. The load is transferred to the test fixture and produces stress concentrations around the shaker-control accelerometer mounting hole. The test fixture does not bend appreciably; however, the stress concentrations were found to produce the same spurious output obtained from the accelerometer when its base is subjected to bending on a cantilever beam. Base bending produces an erroneous accelerometer output proportional to the bending strains.

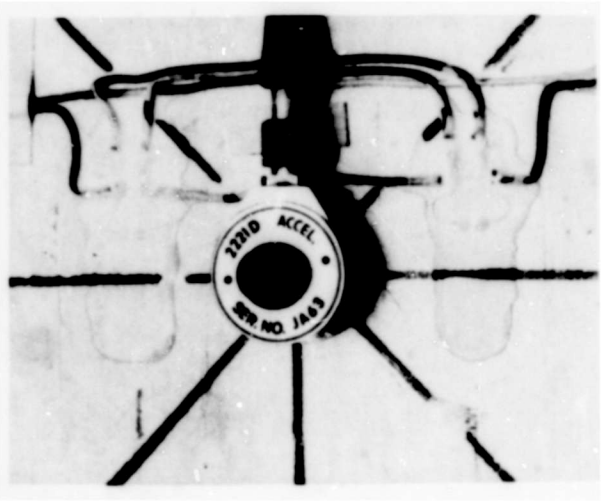

Fig. 1. Piezoelectric ring-shaped shear accelerometer

BACKGROUND

Piezoelectric ring-shaped shear accelerometers are the most commonly used at the Goddard Space Flight Center for shaker control and response measurements during vibration tests (see Fig. 1).

For shaker control, the accelerometer is screwed directly to the test fixture alongside a control monitor accelerometer. During certain spacecraft vibration tests, nonagreement had been noted between these two accelerometers at low frequencies below resonance. The cause of the problem was not understood since the fixture was not subjected to bending. Moreover, the accelerometer's shear design is intended to isolate the crystal element from base bending and case distortion. Inconsistent results from the two accelerometers frustrated early investigators, but the anomaly was circumvented by

mounting the accelerometers on a block welded to the fixture, which relieved the stress concentrations. Recent similar test inconsistencies at a contractor's facility gave rebirth to study of the problem.

The contractor's spacecraft test fixture was not available for investigation; therefore, an old Goddard fixture known to have caused erroneous accelerometer outputs was used for this investigation. The fixture is an 18-in. aluminum disk 2 in. thick; it picks up a C-125 shaker hole pattern. Figure 2 shows the simulated spacecraft lateral test setup to check the fixture control accelerometer location for base strain. The test was conducted by controlling acceleration at the shaker with a base-strain-free accelerometer to 0.5 g_p from 8 to 100 Hz while recording response at location 2, the control point used in past tests. The response accelerometer should have agreed with the control accelerometer at the low frequencies below resonance; it did not, however, as shown in Fig. 3. It was further found that its output was a function of mechanical rotation of the accelerometer about its sensitive axis, as shown by the two curves and the response marks at 20 Hz for other orientations. It was readily apparent why earlier investigators were frustrated with inconsistencies; it was not understood, however, why the accelerometer output was orientation sensitive and seemed to be frequency dependent. Still not sure that a base-strain problem existed, it was theorized that definite proof of a strain situation could be made if the accelerometer could be desensitized in such a way that it would ignore acceleration and produce an output resulting strictly from fixture stresses. When a cutaway display model of the ring accelerometer was examined, it was recognized that strain gages bonded to the accelerometer's post assembly might provide a transducer suitable for detecting base strain. Luckily, a post had been obtained from the manufacturer several years ago when these spurious outputs were first observed, and it was still available (Fig. 4). The instrumented post was installed in location 2 on the fixture. A static output was obtained during the installation of the post, and a dynamic output was obtained from 20 to 60 Hz as the simulated spacecraft mass went through resonance during a 0.5-g sine sweep. The existence of a fixture strain problem had been proved; therefore, it was decided to investigate the accelerometer's base-strain characteristics since no detailed data were available on the subject.

BASE-STRAIN SENSITIVITY TESTS

Nine ring accelerometers of the same manufacture were randomly chosen from stock and calibrated. Frequency response and amplitude linearity were carefully checked. With base-strain absent, the accelerometer's frequency response and amplitude linearity were found to be insensitive to mounting torque, orientation, and installation in misaligned holes.

The accelerometers were then tested for base-strain sensitivity, as shown in Fig. 5, using the test method described in ISA Standards RP 37.2 (1) as follows:

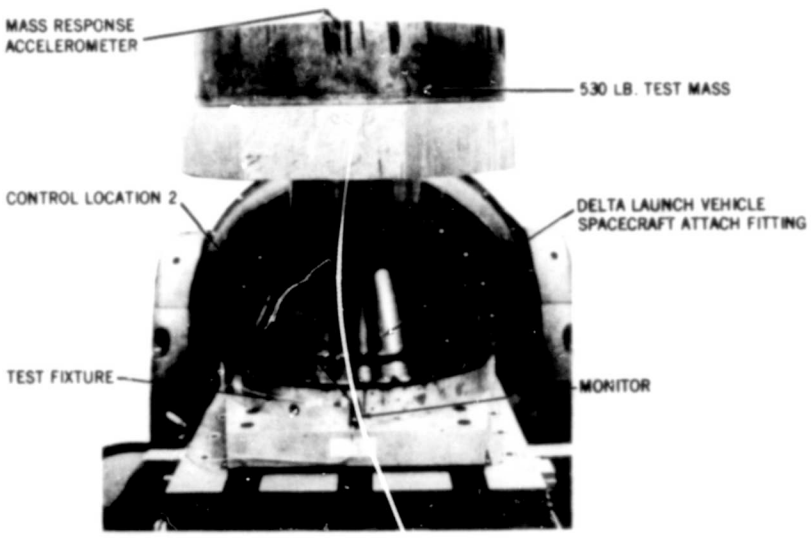

Fig. 2. Fixture mounted for lateral vibration

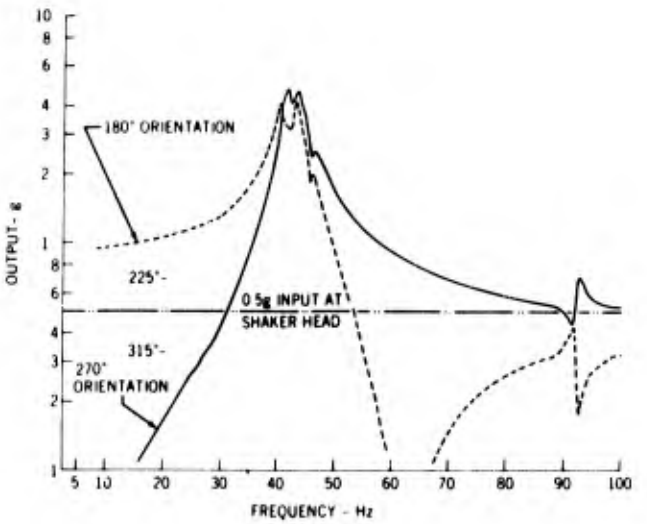

Fig. 3. Filtered composite response of 2221D at location 2

Fig. 4. Instrumented ring accelerometer post

The technique used to measure strain sensitivity of an accelerometer meets the requirement of ASA Z 24.21-1957 (General Reference C) paragraph 3.1.3.7 [Ref. 2]. The accelerometer is mounted on a simple cantilever beam. The radius of curvature at the point where the accelerometer is mounted is 1000 inches when the beam measurements are taken. A steel beam is held as a cantilever in a vice bolted to a concrete floor. The beam is 3.0 in. wide by 0.5 in. thick and 60 in. long. (The free length is approximately 57 in.) The natural frequency is very close to 5 cps. Four strain gauges are bonded to the beam adjacent to the accelerometer mounting hole (two each, top and bottom, about 1.5 in. from the edge of the clamp). A two-channel recorder is used to record the output of both the strain gauge bridge and the accelerometer under test. The system is excited by manually deflecting the free end of the

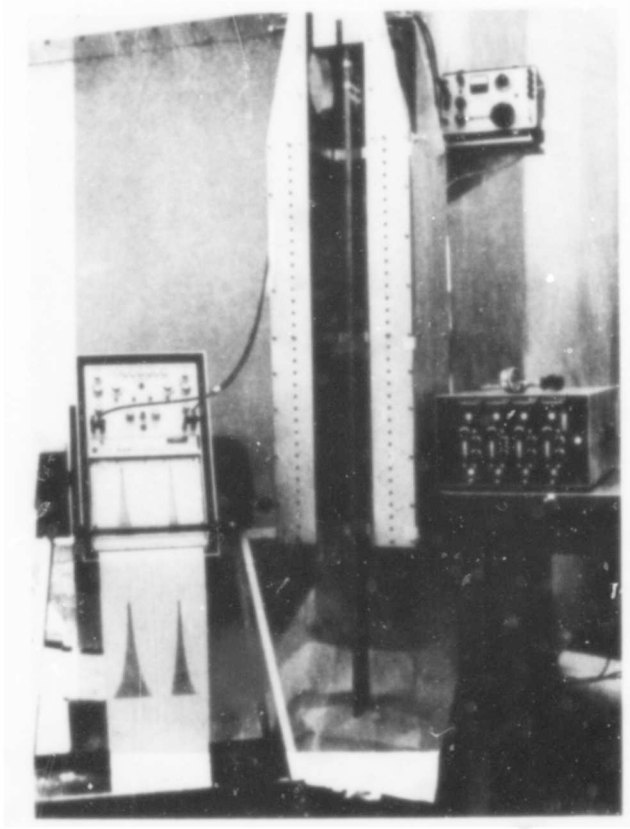

Fig. 5. Base-strain sensitivity setup

beam and allowing it to vibrate freely. The output of the accelerometer is taken from the oscillograph record at a point where the strain in the surface of the beam is 250 × 10^{-6} inch per inch. (This is equivalent to a radius of curvature of 1000 inches.) The strain sensitivity, in g's, for a strain of 10^{-6} inch per inch is found by dividing the above accelerometer output by 250 times the accelerometer sensitivity in millivolts per g.

The results, summarized in Table 1, show that the strain sensitivity for the nine accelerometers varied from an equivalent 0.008 g/μin./in. to 0.04 g/μin./in. Mounting torque was 10 in.-lb. The manufacturer recommends 8- to 12-in.-lb torque, and strain data received from the manufacturer indicates a nominal strain sensitivity for the 2221 D as 0.03 g/μin./in. The manufacturer makes no mention of torque sensitivity; however, it was found that the output of the ring accelerometer from base strain is torque sensitive.

Figure 6 shows a typical record of accelerometer output vs beam strain obtained from the beam test. Although this particular record does not show the magnitude effect of orientation, Fig. 7 does. Figure 6 does show that the accelerometer's output polarity changes with

TABLE 1
Strain Sensitivity Summary

Model	Maximum Strain Sensitivity[a] (Equivalent g/μin./in.)	Mounting Torque Effect on Strain Sensitivity (Equivalent g/μin./in.)[b]		
		5 in.-lb	10 in.-lb	15 in.-lb
2221 C	0.02	0.008	0.02	0.03
2221 C	0.04	0.02	0.03	0.04
2221 D	0.008	0.003	0.006	0.008
2221 D	0.03	0.01	0.02	0.03
2221 D	0.02	0.02	0.02	0.02
2221 D	0.04	0.02	0.03	0.04
2221 E	0.01	0.007	0.01	0.02
2221 E	0.01	0.008	0.01	0.01
2221 E	0.04	0.02	0.03	0.04

[a]Maximum strain sensitivity for 10-in.-lb mounting torque.
[b]Torque sensitivity test carried out at the approximate orientation producing maximum strain sensitivity.

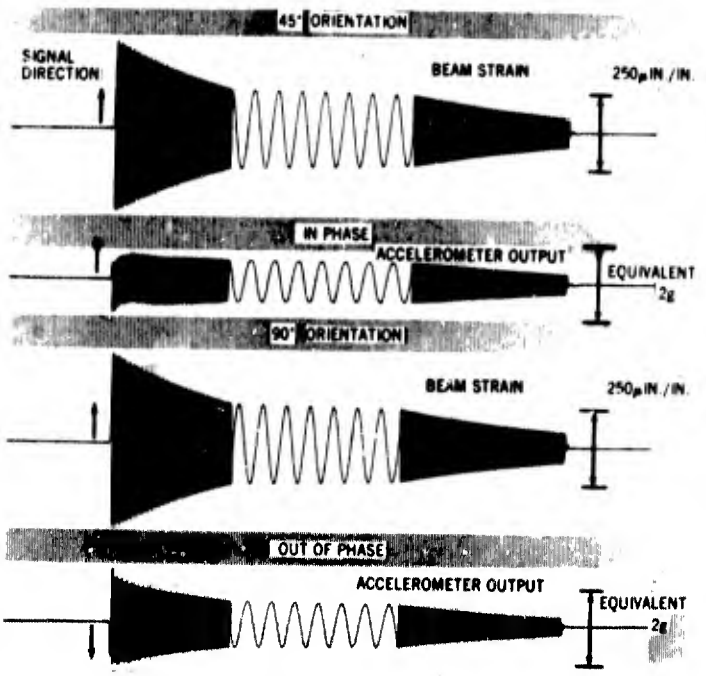

Fig. 6. Typical record for strain sensitivity determination

orientation when base strain is present. Note that the accelerometer's output is in phase with beam strain in the 45-deg position and out of phase in the 90-deg position. This can be detected with the first pull of the beam. Figure 7 shows the output of the accelerometers plotted as a function of rotation about the sensitive axis. Note that the outputs are not symmetrical about zero, that measurements were made every 45 deg, and that four measurements are required to define maximum positive and negative strain sensitivity. These plots indicate that the accelerometer is orientation sensitive to beam strains and that two cycles are generated per complete cycle of mechanical rotation. It would seem that the accelerometer is strain sensitive in two axes, 90 deg apart and perpendicular to the sensitive axis. When the beam is deflected, a strain is produced along the beam length; however, because of Poisson's effect, a strain of opposite sign is produced across the beam. As the accelerometer's x and y sensitive axes are rotated through this 90-deg strain field, a resultant sinusoidal output which produces two cycles per cycle of rotation is generated.

STRAIN-ONLY FIXTURE TEST

Although the strain sensitivity had been determined on the beam with no appreciable acceleration in the accelerometer's sensitive axis and no cross-axis acceleration, it was felt that the same absence of acceleration conditions should be duplicated with the simulated spacecraft lateral test setup. This was accomplished by rigidly fixing the fixture to the floor of the shaker cell, as shown in Fig. 8. The shaker armature was attached to the top of the mass and driven at 7 Hz to produce the required moment. Shaker displacement was held at 0.05-in. double amplitude. A vertically oriented strain gage was mounted on the fixture plate 180 deg away from location 2 to verify strains produced in the fixture. The results from this test were the same as those obtained on the beam. The five accelerometer locations shown, as well as the two on the plate beneath, showed varying degrees of base strain. Location 2 produced the highest output because of its proximity to the attachment fitting bolt carrying the greatest load from moment. A constant displacement frequency sweep from 5 to 100 Hz was conducted;

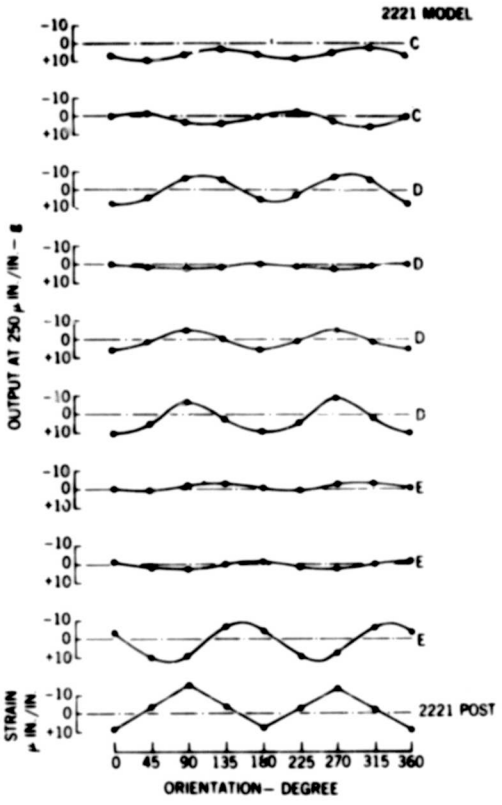

Fig. 7. Accelerometer strain output as a function of rotation about its sensitive axis

it showed that the accelerometer's strain sensitivity was not frequency dependent. It was further shown that an accelerometer could be oriented so that it would produce virtually no output from base strain on this particular fixture.

VIBRATION TEST

It was now felt that enough information was available to return to the lateral vibration test of Fig. 2 and understand the results, and that with an understanding of base strain, we could produce an overtest or undertest at will on the simulated spacecraft. To illustrate the effect on base-strain-free control for this test, a 2224C top connector shear accelerometer was tested on the beam to confirm the manufacturer's nominal figure of 0.0005 g/μin./in. The accelerometer's maximum strain sensitivity was determined to be 0.0005 g/μin./in. It was then mounted to the beam with a model 2986 insulated stud and showed no measurable output for a beam strain as high as 400 μin./in.

The plots of Fig. 9 show the response at the top of the mass for three separate tests when controlling the shaker at location 2 with strained and strain-free accelerometers. The first run was made with the strain-free 2224C mounted on the stud at location 2 to show the simulated spacecraft response with a true input. All sweeps were made at 0.5 g. The next run was made with the base-strained ring accelerometer mounted at location 2 and oriented at 180 deg to produce a positive strain signal, thereby adding to the acceleration signal and resulting in an undertest. The last run attempted was to prove that an overtest would result. The ring accelerometer was reoriented to 270 deg to produce a negative strain signal which canceled out the acceleration signal.

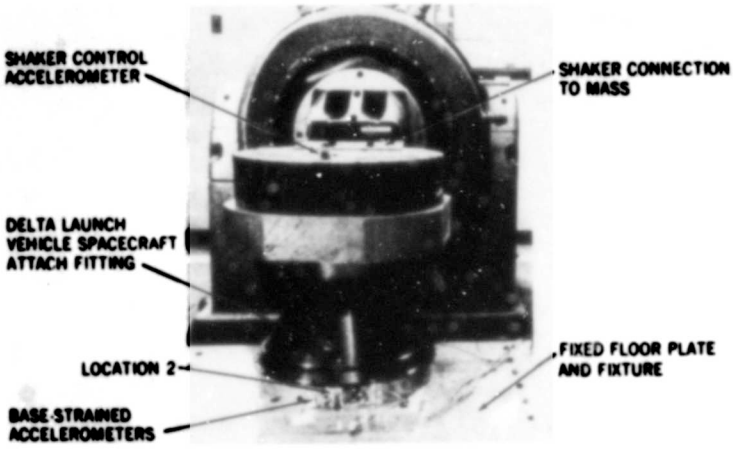

Fig. 8. Test setup for fixture strain verification

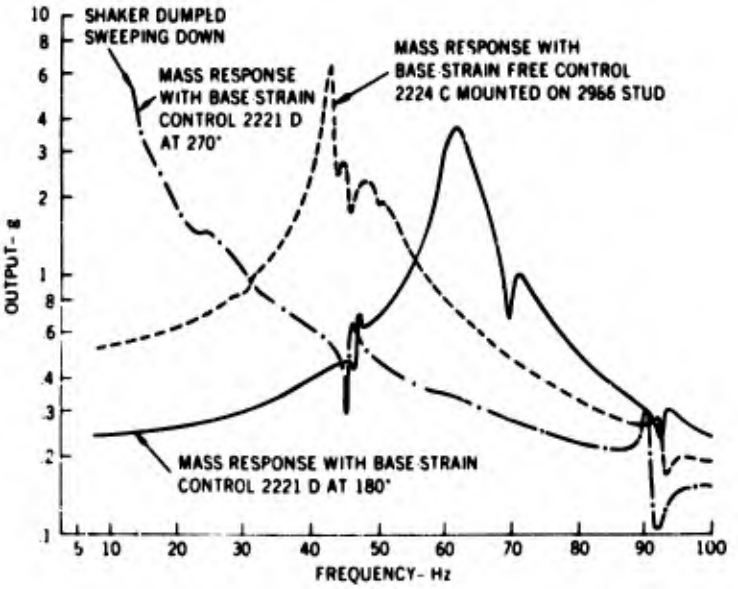

Fig. 9. Filtered mass response with strained and strain-free shaker control accelerometer mounted at location 2

When the shaker-control system was turned on at 7 Hz, the servo system saw no acceleration signal, with the result that it increased the shaker level until the amplitude protector was energized and a dump occurred. The test was then conducted by sweeping down from 100 Hz until the amplitude protector dumped. It is suspected that this response may not be as it should, since it was found that the spacecraft attachment fitting had cracked in many places in the vicinity of location 2 and at 180 deg away. In examining Fig. 9, note that at the true resonance frequency of 45 Hz, the mass will change phase approximately 180 deg with respect to the control accelerometer. The result is that if acceleration and strain are in phase below resonance, they will be out of phase above resonance and vice versa. In addition, note the false spacecraft resonant frequency indicated when the shaker control accelerometer is subjected to base strain.

ADDITIONAL OBSERVATIONS

Several other observations were made during the course of this investigation:

1. Accelerometer screws were made from four different materials to determine their effect on strain sensitivity. Beryllium copper screws decrease strain sensitivity, but the difference was not of practical significance.

2. The ASA technique for determining strain sensitivity should be modified since it is possible that the accelerometer's strain-sensitive axes could be aligned in such a way as to produce no output from base strain. The ASA technique should state that at least four measurements are required to define maximum strain sensitivity. The accelerometer should be mechanically rotated 45 deg for each measurement.

3. Manufacturers' quoted figures on base-strain sensitivity should be suspected of being incorrect, unless it is stated that the maximum strain sensitivity has been determined by the rotation technique.

4. Photoelasticity was attempted as a means to study the stress pattern around the accelerometer mounting hole; the stresses were so low, however, that the photoelastic material's threshold was reached and the results were unsuccessful.

5. Local stress concentrations exist around the hole in the bending beam, which means that the accelerometer is not witnessing the same strain as indicated by the strain gage. The problem is only of academic interest if all laboratories follow the ASA test method.

6. These results show that correlation between two accelerometers mounted side by side

does not prove that they are free of base-strain effects.

7. The results from this investigation point out that base strain could be the answer to the following vibration test anomalies: (a) the same or similar test item passes a vibration test on one shaker and fails on another; (b) the same or similar test item passes a vibration test one time and fails the next on the same shaker; (c) shaker dumps occur at low frequencies or at resonance; (d) accelerometers mounted side by side do not agree at low frequencies or at resonance; (e) poor shaker control exists during low-frequency resonances with an apparent lack of sufficient shaker compressor speed and a loss of signal at the shaker console; (f) random equalization of resonances is difficult or impossible; (g) resonances of the same or similar item seemingly shift frequency and change transmissibility under similar test conditions.

CONCLUSION

Piezoelectric ring-type shear accelerometers produce a spurious output because of accelerometer mounting hole stress concentrations as well as from a bending surface. All accelerometers should be suspected of being base-strain sensitive until proved not. Extra care should be given to the mounting location and use of a shaker control accelerometer if reliable test results are expected.

Since some accelerometer manufacturers' data sheets state that the ring accelerometer provides complete mechanical isolation of the sensing element from mounting strains, we should like to reiterate Mangolds' recommendation:

> ... It is recommended that the accelerometer suppliers because of their unique qualifications, update their data sheets to include information concerning base-strain sensitivity, temperature-transient sensitivity, and any other properties heretofore unpublished which may be of considerable value to the accelerometer users [Ref. 3].

It would be helpful if the manufacturer's product sheets and sales literature on the general subject of shear accelerometers would clearly state the base-strain sensitivity.

ACKNOWLEDGMENT

The authors extend their gratitude to Seymour Edelman of the National Bureau of Standards for reviewing the manuscript and discussing the base-strain matter. Appreciation is given to Robert Sanford of the Naval Research Laboratory for his discussion of photoelasticity.

REFERENCES

1. "Guide for Specifications and Tests for Piezoelectric Acceleration Transducers for Aero-Space Testing," ISA Recommended Practice RP 37.2, par. 6.6 (1964)
2. Specifying the Characteristics for Pickups for Shock and Vibration Measurement ASA Standard Z 24.21, para. 3.1.3.7. (1957)
3. B. Mangolds, "Unpublished Accelerometer Characteristics," Shock and Vibration Bull. 35 (Part 4): p. 37 (1966)

* * *

SONAR TRANSDUCER VIBRATION REQUIREMENTS AND MEASUREMENT TECHNIQUES

Gerald M. Mayer and Edward G. Marsh
Navy Underwater Sound Laboratory
New London, Connecticut

Vibration characteristics of passive sonar transducer elements have been investigated, and a standard series of measurements has been devised to isolate various portions of the vibration response. The hydrophone vibration response measured at the output terminals of a sonar transducer is composed of an acceleration-induced component, a velocity-induced component, and component resulting from the water-coupled energy radiated from nearby vibrating structural elements. Techniques for experimentally determining the relative contribution of each are discussed.

The experimental equipment used at the Underwater Sound Laboratory is briefly outlined, and graphical representations of each of the vibration response components discussed are given for a typical piezoelectric ceramic hydrophone.

INTRODUCTION

By its very nature, a sonar transducer has a multitude of vibration problems not present in other types of equipment. These problems dictate the use of isolation concepts and measurement techniques basically different from those used in conventional vibration work.

A sonar transducer is a device for transforming a time-varying pressure signal into an electrical signal at the output terminals, or conversely, creating a time-varying pressure field from an electrical input. This is usually accomplished by means of a piezoelectric ceramic element arranged to give the desired projecting or receiving characteristics. Since the receiving characteristics are far more sensitive to vibration phenomena, all subsequent discussion is directed to passive hydrophones or projectors operated in a passive mode.

VIBRATION RESPONSE; MEASUREMENT DIFFICULTIES

In a basic hydrophone consisting of a hollow piezoelectric ceramic cylinder, the ceramic is polarized in such a way that any induced strain in the ceramic will cause a potential across the output terminals. If this hydrophone is placed in a time-varying acoustic field or pressure field, an electrical signal proportional to the field can be detected at the output terminals. However, since the ceramic has finite mass, any motion of the ceramic causes inertial loading and the hydrophone also acts as an accelerometer. Signals resulting from the acceleration effect constitute a part of the hydrophone's undesirable characteristics.

Since a vibrating hydrophone moves in a fluid such as water, there will be a force exerted on the ceramic proportional to the velocity of the motion. This force, which is called radiation pressure, results from the relative motion between the fluid and the hydrophone and produces a second component of undersirable background noise.

Noise may also be induced from any booting material placed over the ceramic for protection, since it, too, has inertial loading which causes a strain in the ceramic and therefore an output voltage. This booting effect is very difficult to separate from a pure accelerometer effect of the ceramic, but it is nonetheless part of the total noise signal.

There may be noise radiated from the mounting points of the hydrophone and received as acoustic noise at the ceramic. This is a major problem in designing a hydrophone mount, since any radiated noise is very close to the hydrophone and is easily detected.

In theory, the accelerometer effect can be canceled by another cylinder positioned inside the existing cylinder with equivalent sensitivity but opposite polarity. The resonant frequencies of the ceramic mountings must be held very nearly equal so that the two signals are always 180 deg out of phase and of equal amplitude. This is an unsolved problem, since any small phase shift in one ceramic but not in the other results in a signal impossible to cancel.

The next alternative would be to isolate the hydrophone from any vibration at its mounting point. The hydrophone would remain motionless in the acoustic field and measure only the time-varying pressure signal. This approach would eliminate the accelerometer effect and the radiation pressure effect. The problem now is that the acoustic energy from near structure is worse since the relative motion between the hydrophone and the near structure has been increased. The increased relative motion can only be eliminated by eliminating the ship's vibration or by adding pressure release material on any surface that could radiate sound to the hydrophone, the latter technique being only partially successful.

HYDROPHONE VIBRATION RESPONSE MEASUREMENT TECHNIQUE

To compare hydrophones for vibration response, whether they are hydrophones of the same type or otherwise, a standard measurement technique was developed. The quantity measured is known as hydrophone vibration response (HVR). This is the ratio in decibels of the hydrophone output to the acceleration input referred to the mounting point. The units are in terms of sound pressure levels (microbars) to acceleration units (g). The final curve is a normalized vibration response curve.

Hydrophones subjected to this test are operated in air and water. The acceleration input levels are maintained as nearly as possible to actual ship vibration levels measured in the vicinity of the transducer mounting point. These levels are usually very low and on the order of -60 db//1 g-peak (0.001 g) or less.

The hydrophone and its mounting bracket are attached to a fixture which is attached to a small, low-level vibration exciter such as that shown in Fig. 1. The input acceleration is monitored by the accelerometer on the fixture.

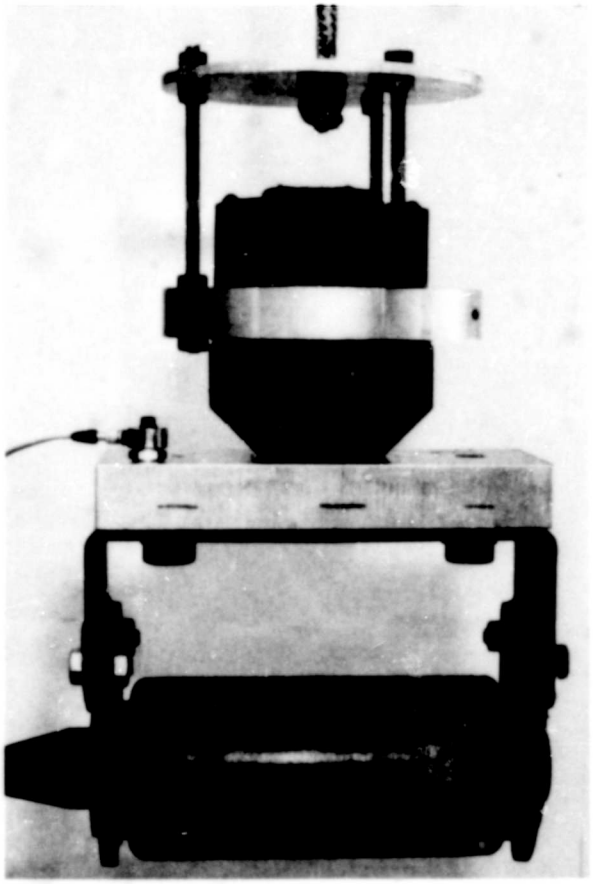

Fig. 1. Hydrophone set up for vibration measurements

Three HVR Test Curves

Hydrophone in Air — For a normal sine-sweep test, the entire setup is run in air, and curves of acceleration input, hydrophone output, and the ratio of hydrophone output to acceleration input are taken. This procedure establishes the acceleration response of the hydrophone. The radiation pressure is very low in air, and the sound radiated from near structure is not picked up, so that the air test shows the pure acceleration response. This test shows any resonances in the hydrophone itself or in its mounting. Internal resonances in the hydrophone will not change when the hydrophone is in water, but bracket resonances will be lowered because of the increase in apparent mass of the bracket. If acceleration canceling has been added, the air test will show how well the canceling effect is

working. With acceleration canceling added, a decrease in level of about 20 db might be expected during the air test.

Hydrophone in Water – The next test to be performed would be a test with the hydrophone alone in water. The water surface should be maintained between the hydrophone and the bracket. This test adds the radiation pressure signal in the resulting HVR curve. The acoustic energy radiated from the bracket is not detected by the hydrophone because of the impedance mismatch between air and water. At some frequencies the resulting curve may be lower than the pure acceleration response because of destructive interference between the acceleration effect and the radiation pressure effect.

Hydrophone with Mount in Water – The last curve and most important curve is taken with the bracket and hydrophone under water. This curve now includes all the components of the hydrophone's vibration response. The radiated noise from the bracket is now water coupled, and the hydrophone output is approximately the same as it would be on the side of a ship. The curve does not include, however, the sound radiated from the ship's structure near the hydrophone, which is, in fact, a major source of interfering signal. Curves from each of the three tests are shown in Fig. 2. The substantial increase in level when the bracket is underwater with the hydrophone indicates that the sound pressure level seen by the hydrophone is actually water-coupled radiated noise.

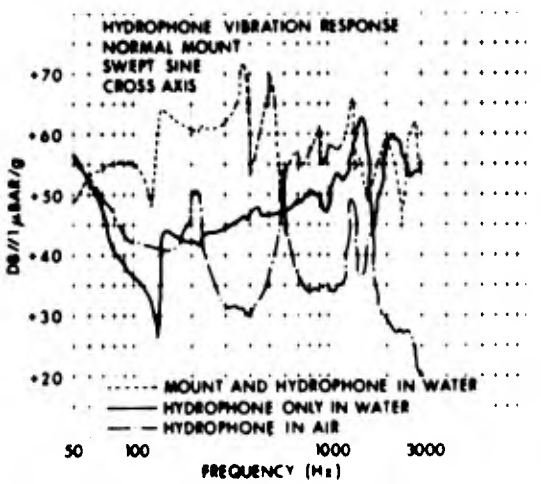

Fig. 2. Hydrophone vibration response in air, water, and water with mount

With the three different HVR curves, the sources of vibration problems are more easily isolated. An acceleration response problem would show up in the first curve, whereas a geometry-dependent radiation pressure problem should be detected in the second curve. The problem of bracket-generated noise would be seen in the third curve.

Mounting Conditions

The example shown is only one of many types and shapes. The radiation pressure was not a large problem with the cylindrical shape. The problem with this hydrophone, as far as its vibration response is concerned, is its bracket. The nearness to the hydrophone allows any vibratory motion of the bracket to be water coupled directly. Perfect isolation from the bracket does not improve the overall response, as can be seen in Fig. 3. Perfect isolation in this case is achieved by suspending the hydrophone on shock cord and positioning the bracket over the hydrophone with no physical connection. The energy received by the hydrophone is now entirely water coupled. The curve shows that the average level of the perfectly isolated hydrophone is very nearly the same as that of the hydrophone in its normal mount.

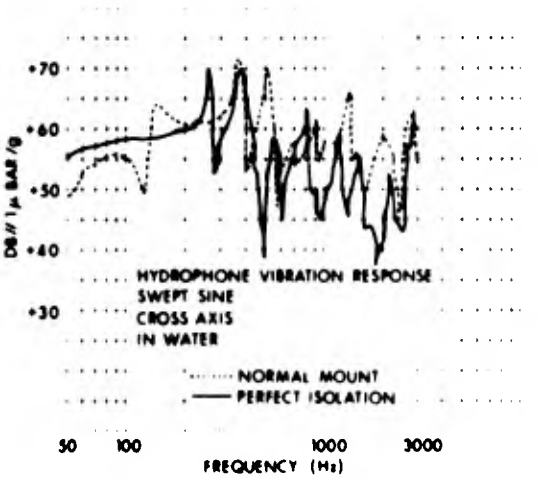

Fig. 3. Hydrophone vibration response in water with normal mount and perfect isolation

The next possible alternative for the particular mounting condition would be a rigid mount. This approach would eliminate the

isolation provided by the normal mount, which resulted in relative motion between the bracket and the hydrophone.

For the hydrophone referred to in the example, a rigid bracket was constructed of 0.5-in.-thick aluminum plate. The distance from the hydrophone to the bracket was the same as with the normal mount. The resulting curves indicate that for some frequency bands, a rigid mount for this hydrophone would be the best choice. A comparison of the curves is shown in Fig. 4.

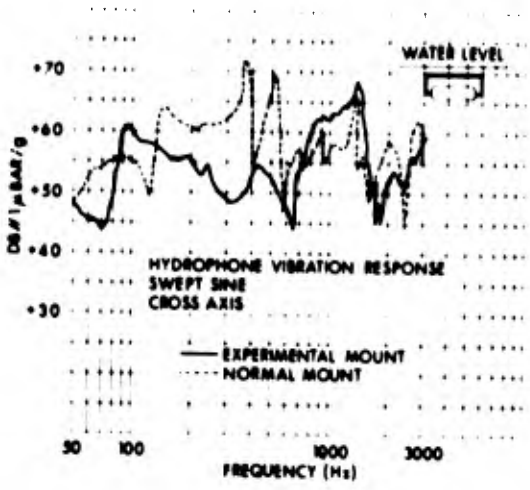

Fig. 4. Hydrophone vibration response in water, with normal mount and rigid experimental mount

The decision as to which bracket would be more suitable would depend on several conditions. For example, the bracket and hydrophone also have to meet shock requirements. A rigid bracket might result in mechanical damage to the ceramic, whereas a very compliant bracket may not possess sufficient strength to retain the hydrophone during shock.

Another important consideration is the frequency range of interest for the hydrophone. It might be that one bracket is clearly better than another over the range of interest for the hydrophone, but is much worse in other frequency bands. Since in the actual environment the excitation is random, the desired signal may be difficult to distinguish with high noise levels present in other frequency bands. If, for example, the hydrophone was used for frequencies between 100 and 600 Hz, the rigid bracket might be the best choice.

USL Measurement and Analysis System

Since random excitation is characteristic of the shipboard environment, HVR curves may be taken with shaped random excitation. The spectrum of the input acceleration can be matched to an actual ship vibration spectrum taken from sea tests. Since the output of the hydrophone is quite linear with input acceleration, the results of a swept sine test and a random test compare favorably. It is therefore possible to conduct laboratory tests by using the swept sine technique, providing the test input levels are maintained fairly near the actual input levels. It is necessary to maintain a realistic input, because the bracket mounting points are somewhat nonlinear with input amplitude.

In our case, the HVR curves are taken at the USL Transducer Vibration Laboratory. The hydrophone and bracket under test are fixtured and excited by a small reaction-type shaker. The control accelerometer is either servo controlled or equalized to provide a response similar to actual sea test acceleration levels.

The hydrophone and acceleration signals are then analyzed by narrow-band tracking filters. The ratio of the two amplitudes is taken by what is basically a mechanical impedance and power spectral density (PSD) analysis system. The log of the dc voltage proportional to each signal is taken, and the difference between the hydrophone and acceleration signal is plotted as the ratio of hydrophone output to acceleration input. The units are microbars per peak g when the sensitivities of each device are accounted for.

The system used in the Transducer Vibration Laboratory is a Spectral Dynamics PSD and mechanical impedance analog analyzer. There is additional capability of four simultaneous-analysis channels with constant bandwidth filters. The available filter bandwidths are 2, 5, 10, 20, 50, and 100 Hz, which may be automatically switched at predetermined frequencies. Available also is variable time averaging and bandwidth correction shift for PSD analysis. In the impedance mode, phase angle and artificial integration may be performed on incoming signals to find mechanical impedance, or mobility, apparent mass, compliance, etc.

Adjacent to the analysis equipment is a large elliptical wooden test tank for underwater tests. The tank, 10 ft by 12 ft by 9 ft deep, is isolated on low-frequency air mounts to attenuate ground-induced vibration.

This facility has been established at the Underwater Sound Laboratory specifically for the purpose of investigating sonar transducer vibration characteristics. Only sporadic work has been done in the past in this investigative area, and the understanding gained through present efforts is expected to yield significant improvements in the performance of transducers.

• • •

BLANK PAGE

AUTOMATED VIBRATION ANALYSIS

R. Pabich and W. H. Sellers
Raytheon Company
Bedford, Massachusetts

Automated vibration analysis, which utilizes the well-known principles of dynamic analogies, consists of two essential steps: (a) composition of an analogous electrical circuit for the corresponding mechanical system, and (b) preparation of a routine electronic circuit analysis program (ECAP) input data sheet for the digital computer (ECAP, from International Business Machines Corp., is an integrated system of programs for the design and analysis of circuits, which an engineer can use without any previous knowledge of computer programming).

The essentials for using automated vibration analysis are presented by explaining the coding techniques of ECAP and illustrating the details of the method through three completed examples. The examples include the simple oscillator and conclude with a vibrating beam problem. The examples also illustrate the directness and simplicity of the method in finding transient responses and natural frequencies. The automated vibration analysis method eliminates solving a set of differential equations when a transient solution is required and eliminates establishing and solving the determinantal or frequency polynomial in a frequency analysis.

INTRODUCTION

Analytical studies of vibration systems normally consist of frequency and transient analyses. Various numerical methods are required to carry out these studies. The principal limitation on the extent of the vibration analysis is the complexity and time requirement involved in obtaining detailed results from the analyses. A multi-degree-of-freedom system often will be evaluated only for the lowest natural frequencies because of the time required to calculate higher modes of vibration. Even with the advent of electronic computers, standard methods of analyses require many hours of tedious algebraic manipulations and computer programming time. An answer that relieves much of the time consumed in standard methods of vibration analysis is the approach of automated vibration analysis.

Automated vibration analysis, which utilizes the well-known principles of dynamic analogies, consists of two essential steps: (1) composing an analogous electrical circuit for the corresponding mechanical system, and (2) preparing a routine electronic circuit analysis program (ECAP) input data sheet for the digital computer (ECAP, from the International Business Machine Corp. is an integrated system of programs for the design and analysis of circuits, which an engineer can use without any previous knowledge of computer programming). The details for use of ECAP consist of numbering all nodes and branches of the analogous electric circuit, assigning a positive current flow direction for each branch, and programming the input which consists of only six types of code statements. The complete details of coding the ECAP program are found in Ref. [1] and are summarized in this paper.

The essentials for using automated vibration analysis are presented by first explaining the coding techniques of ECAP, and illustrating the details of the method through three completed examples. The examples, which include the simple oscillator and conclude with a vibrating beam problem, illustrate the directness and simplicity of the method in finding natural frequencies and transient responses. With this method there is little or no need of solving algebraic polynomials for frequencies by any of the classical numerical procedures and no requirement to solve the set of governing differential equations for a system when a transient analysis is required.

SINGLE-DEGREE-OF-FREEDOM VIBRATION SYSTEM

The general single-degree-of-freedom system with lumped parameters can be modeled by the second-order linear differential equation with constant coefficients (Fig. 1, Eq. (1)). Equation (1) is the governing equation of motion for the single-degree-of-freedom system.

The complete analysis of a system requires the displacement x, the velocity v = dx/dt, the steady-state motion of mass M when subjected to a periodic forcing function F(t), frequency response of M to varying frequencies of F(t), and the transient solution of M when subjected to various forcing functions. The complete analysis of this system is found by utilizing ECAP. The application of ECAP to the single-degree-of-freedom problem is presented in a step-by-step procedure and a summary of input-output results is included in Fig. 1.

Step 1

By application of dynamic analogies [2], develop the equivalent electric circuit. The mechanical configuration is shown with an appropriate electrical equivalent in Fig. 1. For the mass-inductance analogy the analogous parameters are listed below.

Mechanical System

M, Mass
C, Damping coefficient
K, Spring constant
F(t), Force function
dx/dt = v, Velocity
x, Displacement

Electrical System

L, Inductance
R, Resistance
1/C, Reciprocal of capacitance

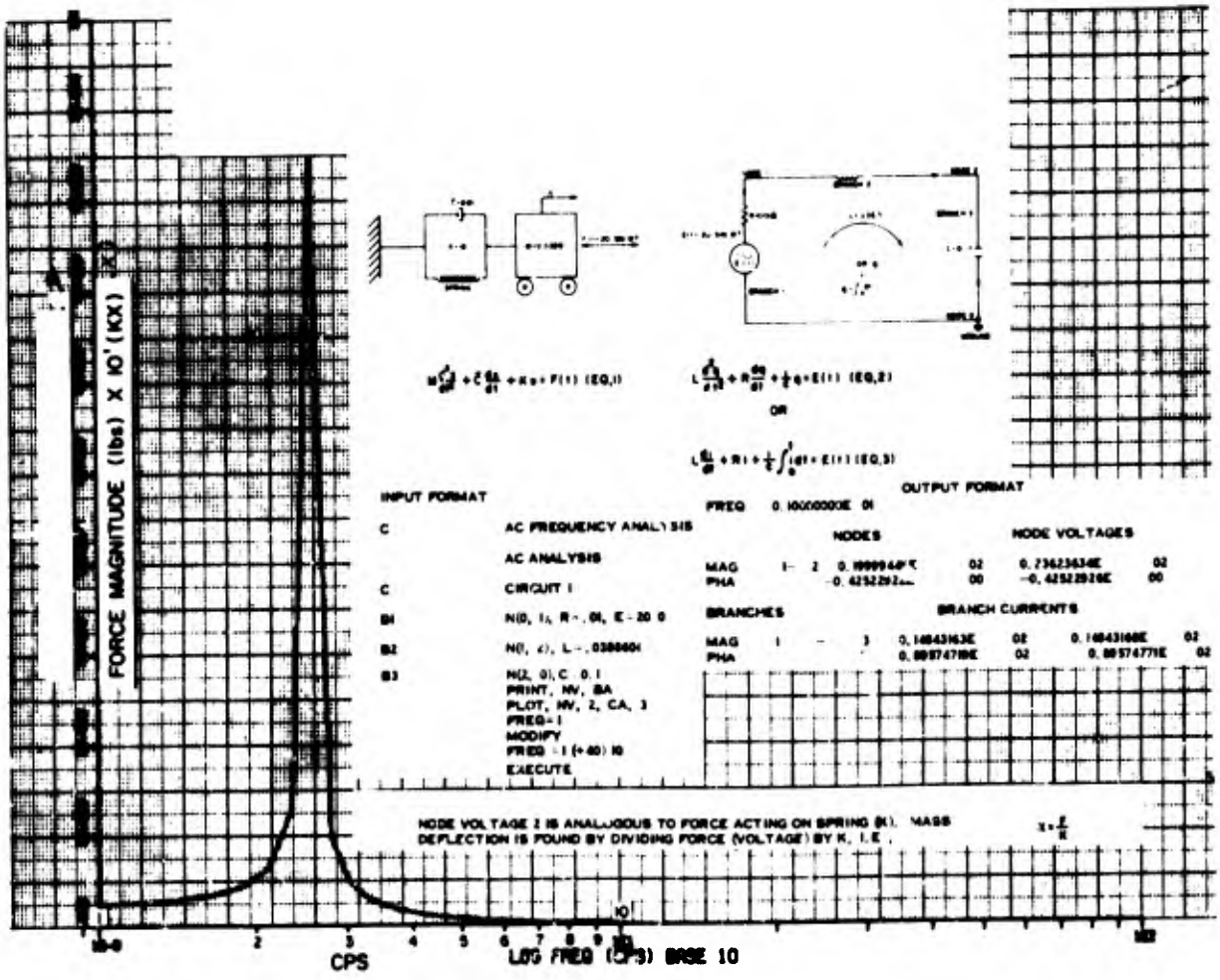

Fig. 1. Spring force magnitude vs frequency

$\Sigma(t)$, Electromotive force, EMF
$dq/dt = i$, Current
$q = \int i dt$, Electric charge

Step 2

Prepare the input data for computer program, as shown in Fig. 1. The analogous electical circuit to be analyzed by ECAP is also shown in Fig. 1.

1. Number all nodes. A node is defined as a junction of two or more electrical components. All ground nodes are designated as zero. Nodes must be numbered in a continuous sequence from 1 to N. Nodes can be numbered, however, in any order desired.

2. Label and designate positive current flow for each branch of the circuit. A branch is defined as the conducting path between two nodes. The current direction in most cases can be selected arbitrarily. The current directions in Fig. 1 are positive in the direction of the arrows. Branches must be numbered consecutively from 1 to N but can be arranged in any order.

3. Prepare data input information. The circuit topology is described in the computer program by writing a punch card for each branch of the circuit to be analyzed. This is accomplished by defining the electrical element, its value, and the location of the branch to which it belongs. The format for doing this is illustrated as follows for branch 1:

Branch Identification	Branch Location - Between Node 0 and 1	Parameter values of circuit elements in Branch 1
B1	N(0, 1)	R = 0.01, E = 20/0

All branches are defined in this manner: each is identified by number (B1), location (joins nodes 0 and 1: N(0, 1)), and values of the parameters on B1 (R = 0.01, and E = 20/0). By defining each branch of the circuit in the format as given, the complete description of the circuit is defined for computer calculation as input data.

4. Prepare the complete input sheet, illustrated in Fig. 1. Note that the format for the ECAP input program must be followed exactly.

5. Obtain interpretation of results (circuit analysis calculations). Voltages and currents from the computer program are given in terms of magnitudes and phase angles (Fig. 1: MAG, PHA) for the frequency analysis. The voltages and currents are equivalent and equal, respectively, to the forces and velocities of the pertinent components of the mechanical system. Figure 1 depicts a plot of the force acting on the spring (node voltage 2) as plotted directly from the computer plotting system; if desired a hand plot can be obtained from the output computer sheet.

MULTI-DEGREE-OF-FREEDOM SYSTEM

The simplicity, depth, and convenience of automated vibration analysis is illustrated by analysis of a three-degree-of-freedom system. The steps involved in this analysis consist only of deriving an equivalent electrical circuit for the mechanical system and coding the input for the ECAP program. A real value of the method lies in the economy of time and cost involved in applying the automated vibration analysis, compared with the classical methods of analysis, such as Holtzer's method for frequency analysis.

The automated vibration analysis of the system will consist of a frequency analysis and a transient analysis. The equivalent mechanical system and an analogous electrical circuit utilizing the mass-inductance analogy are shown in Fig. 2.

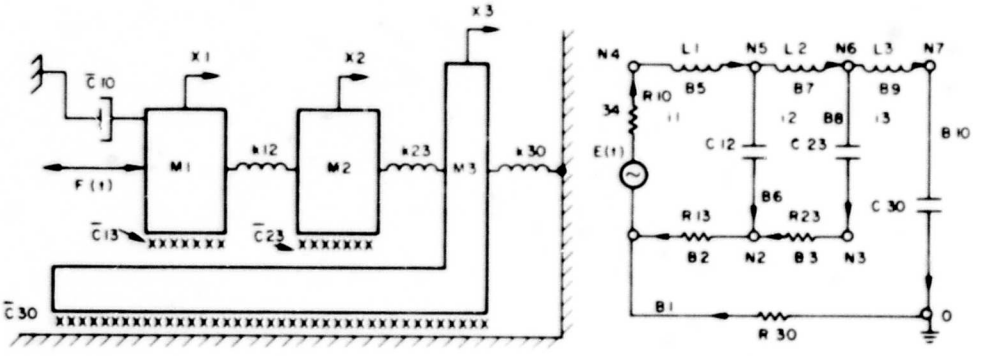

Fig. 2. Three-degree-of-freedom dynamic analogy (N = node, B = branch; arrows show direction of current flow, assigned arbitrarily)

Values for the parameters of the mechanical system are:

M_1 0.00388 lb-sec^2/in.

$\bar{C}_{10}$ 0.01 lb-sec/in.

M_2 0.00518 lb-sec^2/in.

C_{13} 0.001 lb-sec/in.

M_3 0.013986 lb-sec^2/in.

$\bar{C}_{23}$ 0.001 lb-sec/in.

$\bar{C}_{30}$ 0.001 lb-sec/in.

K_{12} 25 lb/in.

K_{23} 75 lb/in.

K_{30} 75 lb/in.

The ECAP inputs for the transient and frequency analysis are listed and illustrated in Figs. 3 and 4. The inpute data is keypunched and fed directly to the computer. Figure 3 depicts the frequency analysis; the damped natural frequencies are read directly from the computerized plot.

The output from the computer program is displayed in graphical form in Fig. 3. The graph gives the voltage at node 7 vs input frequency. The analogous quantity here is the force acting across the K_{30} spring of the mechanical system. Voltage is directly related to

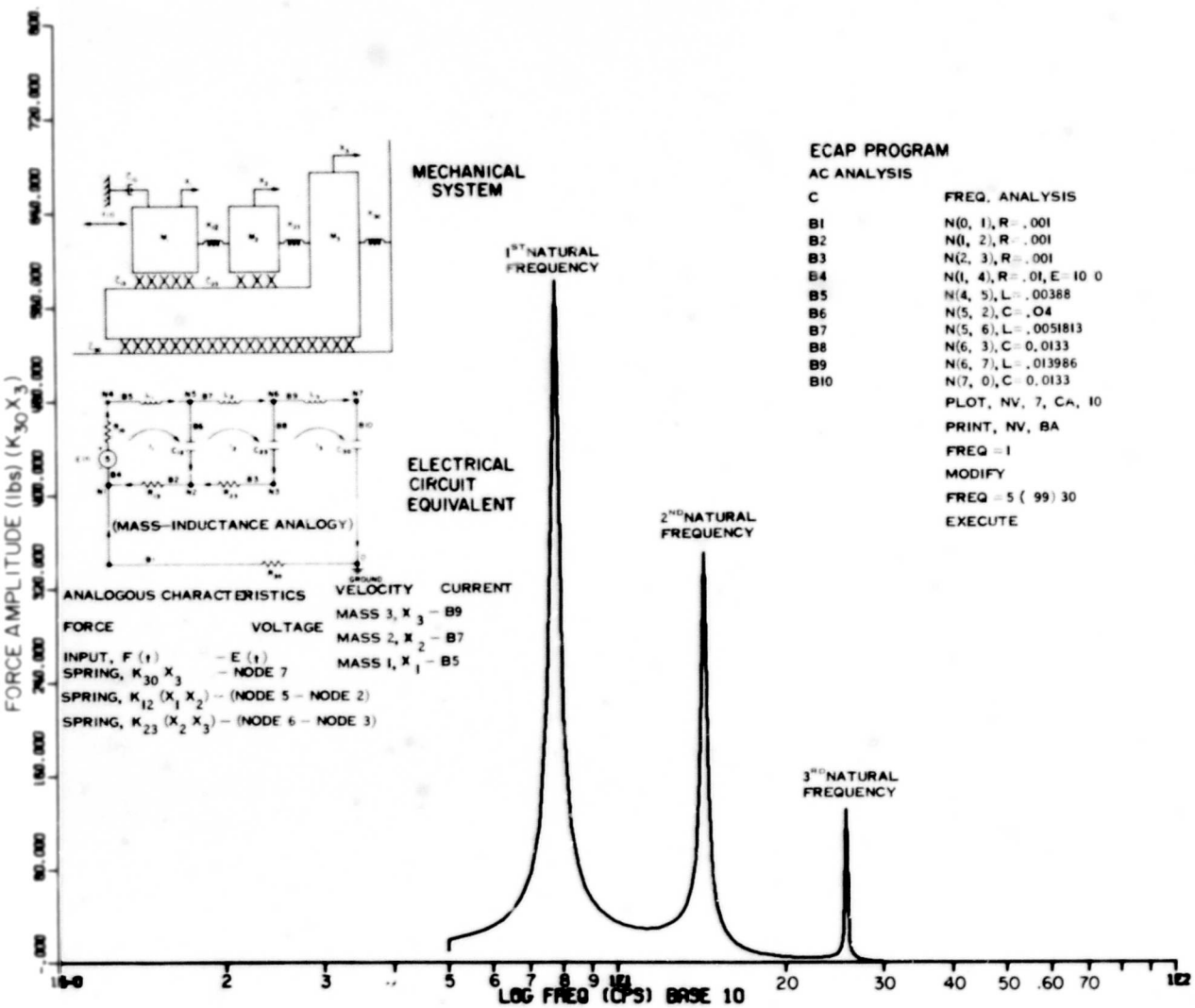

Fig. 3. Spring force magnitude vs frequency for the three-degree-of-freedom case (K_{30} spring force)

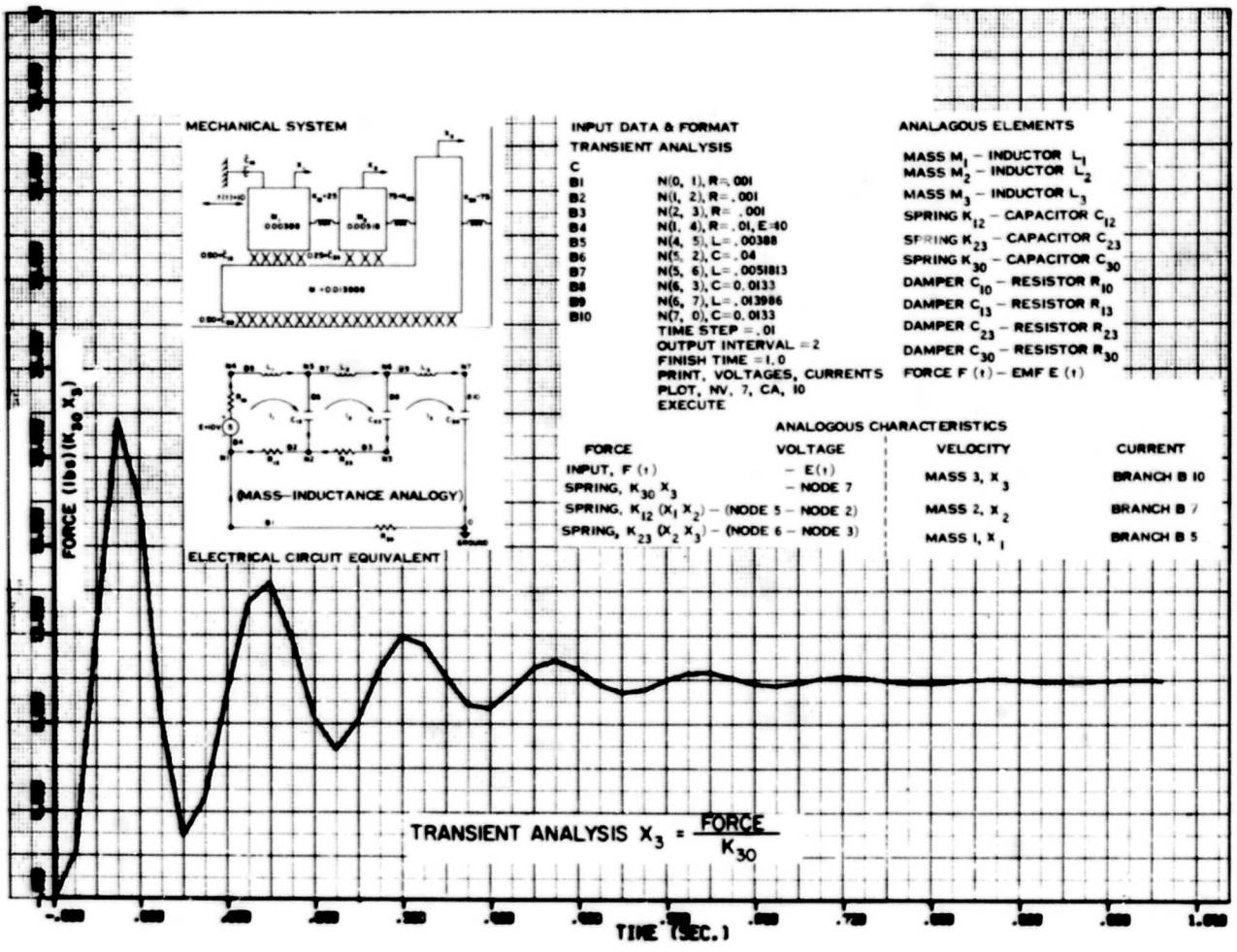

Fig. 4. Transient analysis for three-degree-of-freedom case

force, i.e., 1 v is equal to a force of 1 lb. The three damped natural frequencies are readily determined by inspection of the graph.

The transient analysis was solved for the motion of mass 3 subject to a constant force of 10 lb acting at $t = 0$. The input for the transient analysis and the motion is displayed in Fig. 4. The graph is plotted in terms of node 7 voltage and this is equal to the force across the spring K_{30} of mass 3. The displacement is found by dividing the spring force (node 7 voltage) by K_{30}.

MASS-CAPACITANCE ANALOGY OF MULTI-DEGREE-OF-FREEDOM SYSTEM (VIBRATING BEAM)

The analogous electric circuit for many vibration systems may be handled more conveniently if the mass-capacitance dynamic analogy [2] is utilized. This method is illustrated by the following example of a beam problem. Consider the cantilever beam by lumped-mass approximation (Fig. 5). The beam is a distributed mass system, but it will be approximated by a lumped-mass system with stiffness characteristics treated as influence coefficients [3].

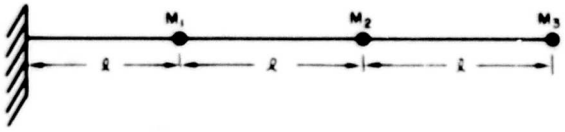

Fig. 5. Lumped-mass approximation for cantilever beam

Influence coefficients for the cantilever beam are

$$a_{11} = \frac{\ell^3}{3EI}, \quad a_{12} = a_{21} = \frac{5\ell^3}{6EI}, \quad a_{13} = a_{31} = \frac{4\ell^3}{3EI},$$

$$a_{22} = \frac{8\ell^3}{3EI}, \quad a_{23} = a_{32} = \frac{14\ell^3}{3EI}, \quad a_{33} = \frac{9\ell^3}{EI},$$

where a_{ij} (i = 1 to 3, j = 1 to 3) are the influence coefficients and ℓ = length, E = Young's modulus, and I = moment of inertia.

The corresponding spring constants are given as

$$K_{11} = \frac{138EI}{13\ell^3}, \quad K_{12} = K_{21} = \frac{138EI}{13\ell^3},$$

$$K_{13} = K_{31} = -\frac{36EI}{13\ell^3}, \quad K_{22} = -\frac{54EI}{13\ell^3},$$

$$K_{23} = K_{32} = \frac{48EI}{13\ell^3}, \quad K_{33} = \frac{9EI}{13\ell^3}.$$

The analogous mass-capacitance circuit is shown in Fig. 6.

The mass-capacitance mechanical-electrical analogy is defined by the dual of the mass-inductance analogy. That is, the analogous parameters are dually related, as shown by the following differential equation for each circuit type.

In the mass-inductance analogy for a loop circuit we have

$$\frac{Ldi}{dt} + Ri + \frac{1}{C}\int i\,dt = E(t),$$

and in the mass-capacitance analogy for a nodal circuit we have

$$\frac{Cde}{dt} + Ge + \frac{1}{L}\int e\,dt = I(t).$$

The analogous quantities are

Mechanical

M, Mass
C, Damping coefficient
K, Spring constant
v, Velocity
F, Force

Mass Inductance

L, Inductance
R, Resistance
1/C, Reciprocal of capacitance
i, Current
E, Supply voltage

Mass Capacitance

C, Capacitance
G, Conductance = 1/R
1/L, Reciprocal of inductance
e, Voltage
I, Supply current

The input for the ECAP analysis of the analogous electric circuit for the beam is presented in Fig. 7 with a computer plot of mass 3 velocity vs frequency. The first two natural frequencies of the bending beam are shown; the third natural frequency could be obtained by simply extending the computed frequency limit.

CONCLUDING REMARKS

The automated vibration analysis can be extended to many and various types of vibration problems. It is quite general for linear vibration analysis, and it can be utilized for nonlinear vibration analyses by using the switching techniques presented in Ref. [1]. With use of ECAP, automated vibration analysis could exert a great influence upon the present methods of teaching vibration analysis.

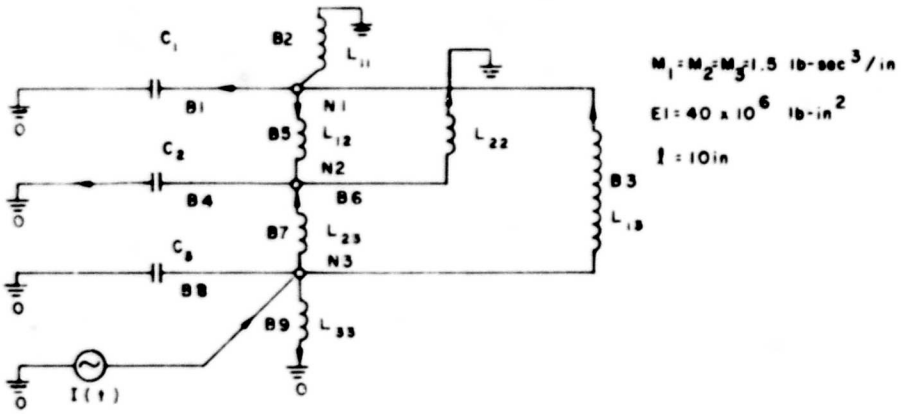

Fig. 6. Analogous mass-capacitance circuit for beam

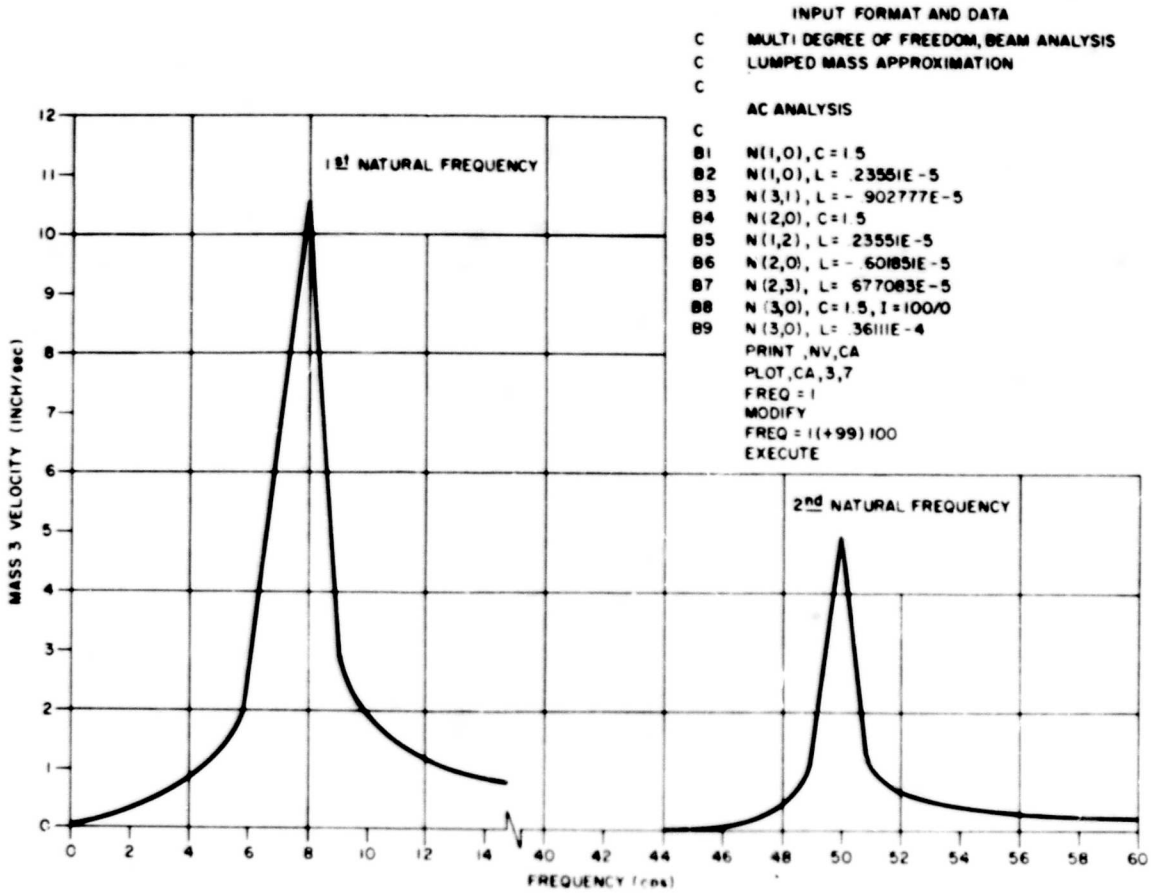

Fig. 7. Beam bending frequency analysis

REFERENCES

1. International Business Machines Corp. 1620 Electronic Circuit Analysis Program (ECAP) (1620-EE-02X) User's Manual, 1965

2. W. W. Soroka, Analog Methods in Computation and Simulation (McGraw-Hill, New York) 1954

3. R. L. Bisplinghoff, H. Ashley, and R. L. Halfman, Aeroelasticity (Addison-Wesley, Reading, Mass.) 1955

* * *

BLANK PAGE

A COMPACT, LOW-COST SHOCK-SPECTRUM ANALYZER*

William W. Mebane
Naval Ordnance Laboratory
Silver Spring, Maryland

A low-cost, portable shock-spectrum analyzer was designed and built at the Naval Ordnance Laboratory for use in the laboratory and in the field. The analyzer contains three electrical low-pass filters that simulate three single-degree-of-freedom mechanical systems. Each filter has one operational amplifier with associated resistors and capacitors. The natural frequencies and damping coefficients are varied by switching combinations of preselected resistors and capacitors. Twenty-four single-degree-of-freedom systems with natural frequencies from 3.04 to 625 Hz in about one-third octave steps are simulated.

The unit is normally used in conjunction with a magnetic tape recorder and a direct-writing oscillograph. A shock pulse to be analyzed is recorded on a magnetic tape recorder and then played through the analyzer with appropriate tape speed changes to produce single-degree-of-freedom responses over the frequency range of 3.04 to 20,000 Hz. The responses are recorded on an oscillograph and the maxima are measured and plotted vs frequency.

Design and operational details of the analyzer are described. A brief development of the one-amplifier, low-pass electrical filter and its application to the mechanical single-degree-of-freedom system is given. The formulas used in selecting network elements are presented. Normal operational procedures, including frequency, damping, and accuracy limitations, are shown. Finally, the spectra from analyzed and theoretical pulses are compared.

INTRODUCTION

This paper describes a low-cost, compact, analog shock-spectrum analyzer (Fig. 1) that was designed and built at the Naval Ordnance Laboratory. The analyzer's principal function is to produce the analog responses of a series of single-degree-of-freedom systems to a given shock excitation. Usually the responses are displayed on an oscillographic record and the maxima are selected and plotted as functions of the frequencies of the responding systems. Other response characteristics can be obtained in a similar manner. This paper discusses the operational and design details of the analyzer and compares the performance of the analyzer with the shock spectra of several pulses.

BACKGROUND

The shock spectrum as used in this report is defined as the plot of the maximum absolute values of the acceleration responses experienced by a series of single-degree-of-freedom systems, as a function of the frequencies of the systems, to a given shock pulse [1]. It is assumed that

$$A_{max} = \omega_n^2 x_{max}$$

where A_{max} is the maximum acceleration response, ω_n is the angular natural frequency of the single-degree-of-freedom system, and x_{max} is the maximum deflection. Although this relationship is true only with no damping, the error is negligible for lightly damped systems.

Use of the shock spectrum concept for specifying shock tests has increased in recent years, presenting a need for a compact easy-to-use shock-spectrum analyzer that can be used both in the field and in the laboratory. It is believed that the unit described meets the requirements desired in such an analyzer. The performance aspects are discussed below.

Most laboratory shock-producing equipment can produce a large number of pulse shapes, each with its unique shock spectrum. Since the measuring and cataloging of all the possible shock spectra is impractical, only the most frequently used pulses from each tester are analyzed and filed. Therefore, when a new spectrum is required, experimentation is almost always necessary to achieve an acceptable pulse. The analyzer described helps speed

*This paper was not presented at the Symposium.

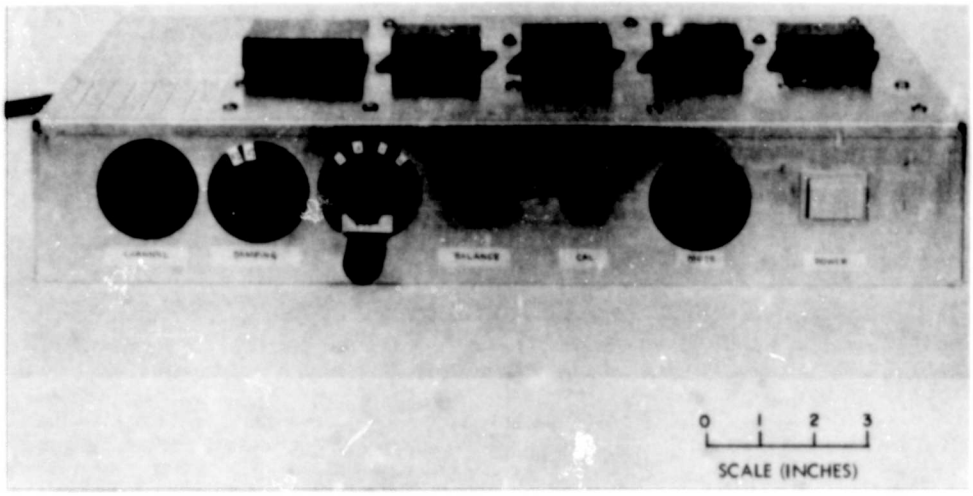

Fig. 1. Analog shock-spectrum analyzer

the experimentation by providing on-the-spot shock-spectrum analysis.

GENERAL DESCRIPTION

The analyzer, which provides three simultaneous frequency response channels and an input monitor, is housed in a 10- by 17- by 3-in. chassis and contains only five operational amplifiers. A ±15-v dc regulated power supply and assorted resistors, capacitors, potentiometers, and switches are included. Twenty-four mechanical single-degree-of-freedom systems with natural frequencies from 3.04 to 625 Hz in about one-third octave steps are simulated. The desired frequencies are selected in groups of 3 by a switch on the front panel of the analyzer. Damping coefficients of 2 and 5.35 percent of critical are provided. The input gain is adjusted by the variable resistor R_2 (Fig. 2) in the feedback of the input amplifier. A 1.35-v battery is provided for step calibration, and a mode-selection switch provides single selected channel output when desired.

BASIC PRINCIPLE

The basic principle used in this analyzer was the application of the one-amplifier, resistance-capacitance (RC) electrical network to simulate the mechanical single-degree-of-freedom system. The mechanical system is illustrated in Fig. 3. The dynamic equation for this system is

$$m\ddot{z} + C(\dot{z} - \dot{y}) + k(z - y) = 0 . \qquad (1)$$

Define

$$x = z - y ,$$

then

$$\dot{x} = \dot{z} - \dot{y}$$

and

$$\ddot{x} = \ddot{z} - \ddot{y} .$$

With these substitutions, Eq. (1) becomes

$$\ddot{x} + \frac{C}{m}\dot{x} + \frac{k}{m}x = -\ddot{y} . \qquad (2)$$

Let

$$\omega_n = \sqrt{k/m} ,$$

$$C_c = 2\sqrt{km} ,$$

$$\xi = C/C_c ,$$

and designate the Laplace transform of $x = \mathfrak{L}[x]$. In Laplace transform notation, Eq. (2) becomes

$$\left[s^2\mathfrak{L}[x] - sx_o - v_o\right] + 2\xi\omega_n\left[s\mathfrak{L}[x] - x_o\right] + \omega_n^2\mathfrak{L}[x] = \mathfrak{L}[-y] \qquad (3)$$

In shock-spectrum computations, the initial velocity and displacement are zero; therefore

$$v_o = x_o = 0 \qquad (4)$$

and

$$\frac{\mathfrak{L}[x]}{\mathfrak{L}[-\ddot{y}]} = \frac{1}{s^2 + 2\xi\omega_n s + \omega_n^2} .$$

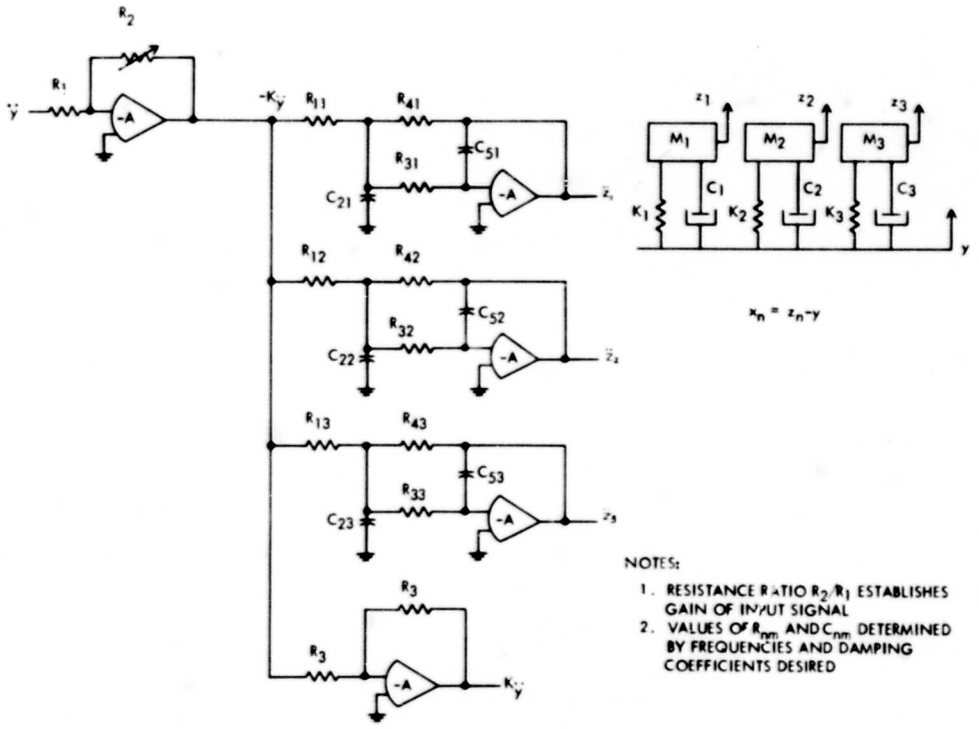

Fig. 2. Functional diagram of shock-spectrum analyzer

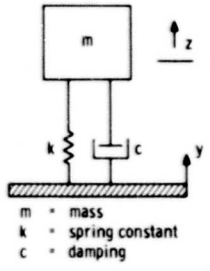

Fig. 3. Mechanical spring-mass system

Make the approximation $\omega_n^2 x = \ddot{z}$. This results in a maximum error of less than 1 percent for systems with damping factors up to 0.0535 [2]. Then

$$\frac{\mathfrak{L}[\ddot{z}]}{\mathfrak{L}[-\ddot{y}]} = \frac{\omega_n^2}{s^2 + 2\zeta\omega_n s + \omega_n^2} \tag{5}$$

The one-operational-amplifier electrical network that simulates the mechanical single-degree-of-freedom system is shown in Fig. 4. From Fig. 4:

$$e_i = I_1/Y_1 + E_0 . \tag{6}$$

$$I_1 = I_2 + I_3 + I_4 . \tag{7}$$

$$I_2 = Y_2 E_0 . \tag{8}$$

$$I_3 = Y_3(E_0 - E_g) . \tag{9}$$

$$I_4 = Y_4(E_0 - e_o) . \tag{10}$$

Since the amplifier gain approaches infinity, E_g approaches 0 (virtual ground), and

$$I_3 \cong I_5 .$$

Through the use of Eqs. (6) through (10) the following relationship is established:

$$\frac{e_o}{-e_i} = \frac{Y_1 Y_3}{(Y_1 + Y_2 + Y_3 + Y_4) Y_5 + Y_3 Y_4} \tag{11}$$

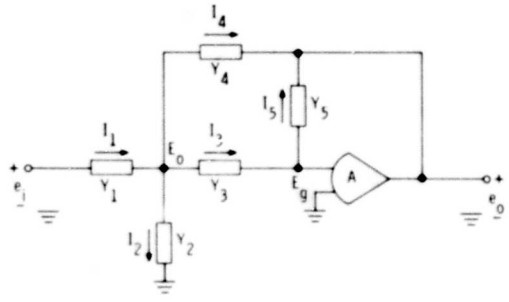

Fig. 4. Electrical network

To simulate a spring-mass system, let

$$Y_1 = G_1,\ Y_3 = G_3,\ Y_5 = sC_5,\ Y_2 = sC_2,\ \text{and}\ Y_4 = G_4.$$

By substituting these values in Eq. (11), we have

$$\frac{E_o}{-E_i} = \frac{G_1G_3/C_2C_5}{s^2 + (1/C_2)(G_1 + G_3 + G_4)s + G_3G_4/C_2C_5}. \quad (12)$$

By equating the like coefficients of Eqs. (5) and (12), the following relationships result:

$$G_1 = G_4, \quad (13)$$

$$\frac{1}{C_2}(2G_1 + G_3) = 2\xi\omega_n, \quad (14)$$

$$G_1G_3/C_2C_5 = \omega_n^2, \quad (15)$$

and letting $\gamma = \omega_n C_5$,

$$2G_1 + G_3 = 2\xi\omega_n C_2, \quad (16)$$

$$G_1G_3 = \gamma\omega_n C_2. \quad (17)$$

There is no unique solution to Eqs. (16) and (17); however, if $G_1 = \gamma/\xi$ [3], then:

$$R_1 = \frac{\xi}{\gamma} = \frac{1}{G_1}, \quad (18)$$

$$R_3 = \frac{\xi}{2\gamma} = \frac{1}{G_3}, \quad (19)$$

$$R_1 = R_4 = \frac{1}{G_4}, \quad (20)$$

$$C_2 = 2\gamma/\xi^2\omega_n, \quad (21)$$

$$C_5 = \gamma/\omega_n. \quad (22)$$

The resulting electrical network is shown in Fig. 5.

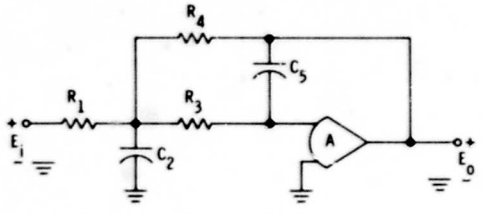

Fig. 5. Electrical circuit

Three of these active RC network circuits were combined with an input monitor channel and an input gain amplifier to form the shock-spectrum analyzer (Fig. 2). Frequencies are varied by switching the three resistors to each network simultaneously (i.e., R_{11}, R_{41}, R_{31} in Fig. 2) and the damping coefficients by switching capacitors (C_{21}, C_{51}).

TYPICAL OPERATION

The analyzer was designed primarily to be used in conjunction with a tape recorder and oscillograph. The shock pulse to be analyzed is recorded on magnetic tape operating at 60 ips. This pulse is played back several times into the analyzer at recorded speed and at 1-7/8 ips (32:1 reduction). This combination of playback speeds produces the effective frequency range of 3.04 to 20,000 Hz (Table 1). A typical operation of the analyzer is as follows.

1. A shock pulse is recorded on a magnetic tape recorder operating at 60 ips.

2. The magnetic tape record is played into the analyzer, which has four outputs: input monitor, and three channels of analog output at preselected frequencies.

3. The analyzer outputs are recorded on an oscillograph using galvanometers with flat frequency responses of 650 Hz or more, to cover the entire range.

4. The maximum response (usual criterion) of each channel is measured and plotted vs the natural frequency of the single-degree-of-freedom system to obtain the desired shock spectrum.

Other modes of operation are sometimes used. Occasionally, when the maximum frequency response requirement does not exceed 625 Hz and repeated shock pulse generation is possible, the spectrum can be obtained directly without the use of the tape recorder. This mode of operation was used to analyze the standard pulses described below. In any event, the outputs of the analyzer can be recorded on any suitable recorder with proper sensitivity and frequency response. A desirable monitoring scheme appears to be the use of peak readers on the output of the analyzer. This method would eliminate the necessity of an oscillograph, and would allow the maximum responses to be monitored on panel meters or digital voltmeters, or possibly even printed on digital printouts.

TABLE 1
Analog Shock-Spectrum Analyzer Frequencies

Switch S_1 Position[a]	Output 1		Output 2		Output 3	
	f_n (Hz)	$32 \cdot f_n$[b] (Hz)	f_n (Hz)	$32 \cdot f_n$[b] (Hz)	f_n (Hz)	$32 \cdot f_n$[b] (Hz)
1	3.04	97.3	3.78	121	4.89	156.4
2	5.98	192.0	7.66	245	9.74	311.0
3	12.1	387.0	15.1	484	19.5	624.0
4	24.5	784.0	30.3	970	38.3	1230.0
5	49.0	1570.0	61.4	1960	78.4	2510.0
6	96.6	3090.0	121.2	3880	155.0	4960.0
7	192.0	6150.0	241.0	7710	309.0	9880.0
8	386.0	12,400.0	488.0	15,600	625.0	20,000.0

[a]See Fig. 6.
[b]Natural frequencies with 32:1 (three significant figures) tape speed reduction.

ANALYZER PERFORMANCE CHARACTERISTICS

Accuracy

The accuracy obtained by use of this analyzer in conjunction with a recording oscillograph is about ±5 percent for amplitude measurements (excluding tape recorder). The frequency values were measured to ±1 percent. The 5 percent accuracy can be obtained by using nominal care in calibration and operation. For purposes of obtaining this accuracy figure, it was estimated that:

1. The overall analyzer accuracy = ±2 percent.

2. The repeatability and linearity of the recording system = ±1 percent.

3. Accuracy in physical measurements of values off the oscillogram = ±4.5 percent.

The rms combination of these values gives an estimated system accuracy of ±5 percent. These are worst-case figures. The results shown below, where electrical pulses were analyzed by the analog system and compared with mathematical solutions, show that in most instances the system accuracy is better than ±5 percent.

Frequency Range

The real-time frequency range of the analyzer is from 3.04 to 625 Hz in 24 steps at approximately one-third octave per step. A complete list of the frequencies is given in Table 1. These frequencies were obtained by calibration after construction and are slightly different from the calculated values. These differences are believed to be caused primarily by nondefinite gain of the operational amplifiers, which was assumed in the derivation. The 3.04-Hz to 625-Hz real-time frequency range was selected because: (a) only one tape speed reduction is required (32:1 speed reduction) to cover the frequency range of 3.04 to 20,000 Hz, and (b) a 625-Hz signal is about the limiting frequency that can be easily measured from data recorded on standard oscillograph paper. In fact, the RC active networks used in this design are not limited by the higher frequencies. Experimental circuits were constructed and operated satisfactorily at frequencies up to and above 20,000 Hz.

Output Channels

Three output channels and an input monitor are incorporated in the analyzer. This was an arbitrary selection, based on availability of recording equipment. In this design, the use of 7-in. oscillographs was anticipated. The recorded responses of four signals on 7-in. oscillograph paper was considered optimum for maximum sensitivity without interference between adjacent channels.

Damping

Damping coefficients (ratios of actual damping to critical damping) of 2 and 5.35 percent are provided, although other damping coefficients above 2 percent could be incorporated by changes in the capacitors. The use of

damping below 2 percent is not recommended because of instabilities that develop in the circuit.

Maximum Voltage Outputs

The operational amplifiers used in this design are limited to ±10-v dc maximum output. This limitation has been completely satisfactory when used with taped records that are in themselves limited to approximately ±2 v dc. However, if use of the analyzer with higher voltages is contemplated, the use of higher voltage operational amplifiers should be considered.

DESIGN DETAILS

The analyzer (Fig. 6) contains five operational amplifiers. Amplifier A_1 controls the level of the input signal by variable feedback resistance (R_6, R_7, R_8, and R_{11}). The output voltage gain of amplifier A_1 is continuously adjustable from 0 to about 13. Other inputs to A_1 are a balance voltage through R_2 and a 1.35-v dc calibration voltage. Amplifier A_2 is an inverting amplifier used as the "accelerometer monitor" of the signal being applied to the input of three single-degree-of-freedom analogs. Amplifiers A_3, A_4, and A_5 are combined with associated RC networks to produce three electrical low-pass filters that react as single-degree-of-freedom systems with selected damping. Natural frequencies of these systems are selected by choosing the network resistors through switch S_1. Damping changes are made by selection of capacitors through switch S_2. The outputs of the three systems are connected to the mode switch S_5. In position 1, the output of amplifier A_3 is connected to output 1, A_4 to output 2, and A_5 to output 3. With S_5 in position 2, A_3 is connected to output 2, with the other outputs grounded. Successive switch positions of S_5 place the outputs of A_4 and A_5 at output 2. This allows the operator to examine one channel at a time.

The analyzer was constructed using operational amplifiers and a relatively expensive regulated power supply at a material cost below $500. The resistors were formed from combinations of 5 percent carbon resistors, using a Wheatstone bridge to obtain the desired values. The same procedure was used in the selection of capacitors, using 5 percent components and an impedance bridge. One of the principal reasons for the low cost was the use of active RC networks to simulate the single-degree-of-freedom systems [3,4]. These RC networks included only one operational amplifier each, with associated resistors and capacitors. This procedure gave completely satisfactory results with less expense and complexity than the standard three-operational-amplifier analog simulation technique [5].

EXPERIMENTAL ANALYSES

The analyzer was used to produce the shock spectra of half-sine, sawtooth, and triangular pulses. Damping of 5.35 percent was used. The pulses were generated electrically and played into the analyzer, which produced three channels of response data. This procedure was repeated eight times for each pulse, while the response frequencies were varied to obtain the data shown in Table 2. The analyzer outputs were recorded on an oscillograph and the peak amplitudes scaled. The spectra were then generated mathematically for theoretical half-sine, sawtooth, and triangular pulses, and these are also shown in Table 2. The equations were solved by Laplace transform methods, and numerical solutions were obtained on a Multi-Access Computing facility using BASIC compiler language. The equations and an example of the BASIC program are given in the Appendix.

As shown in Table 2, the analyzer and analytical results compare favorably. In every instance, the difference between the two methods was ±5 percent or less. The maximum differences appear to be in the middle frequency (or transient) region of the half-sine pulse analysis. It is believed that these differences were primarily caused by an imperfectly generated half-sine pulse used with the analog analyzer.

CONCLUDING REMARKS

A prototype of the analyzer has been used satisfactorily during the last six months both in the laboratory and in the field. After analyses of the theoretical pulses, the analyzer was used to analyze a complex shock generated by one of the drop testers at NOL. The results compared favorably with mechanical oscillator and copper-ball analyses of the same pulse. Later, two laboratory shock facilities were calibrated to a specified shock spectrum for an ordnance requirement. These were complex, pyrotechnic-type shocks which required extensive experimentation during the calibrations of the shock facility. Also, the analyzer has been used in the field for analysis of shock pulses either from taped records or directly from accelerometer amplifiers on a real-time basis. Compactness and ease of operation make the analyzer a useful shock analyzer for laboratory and field applications.

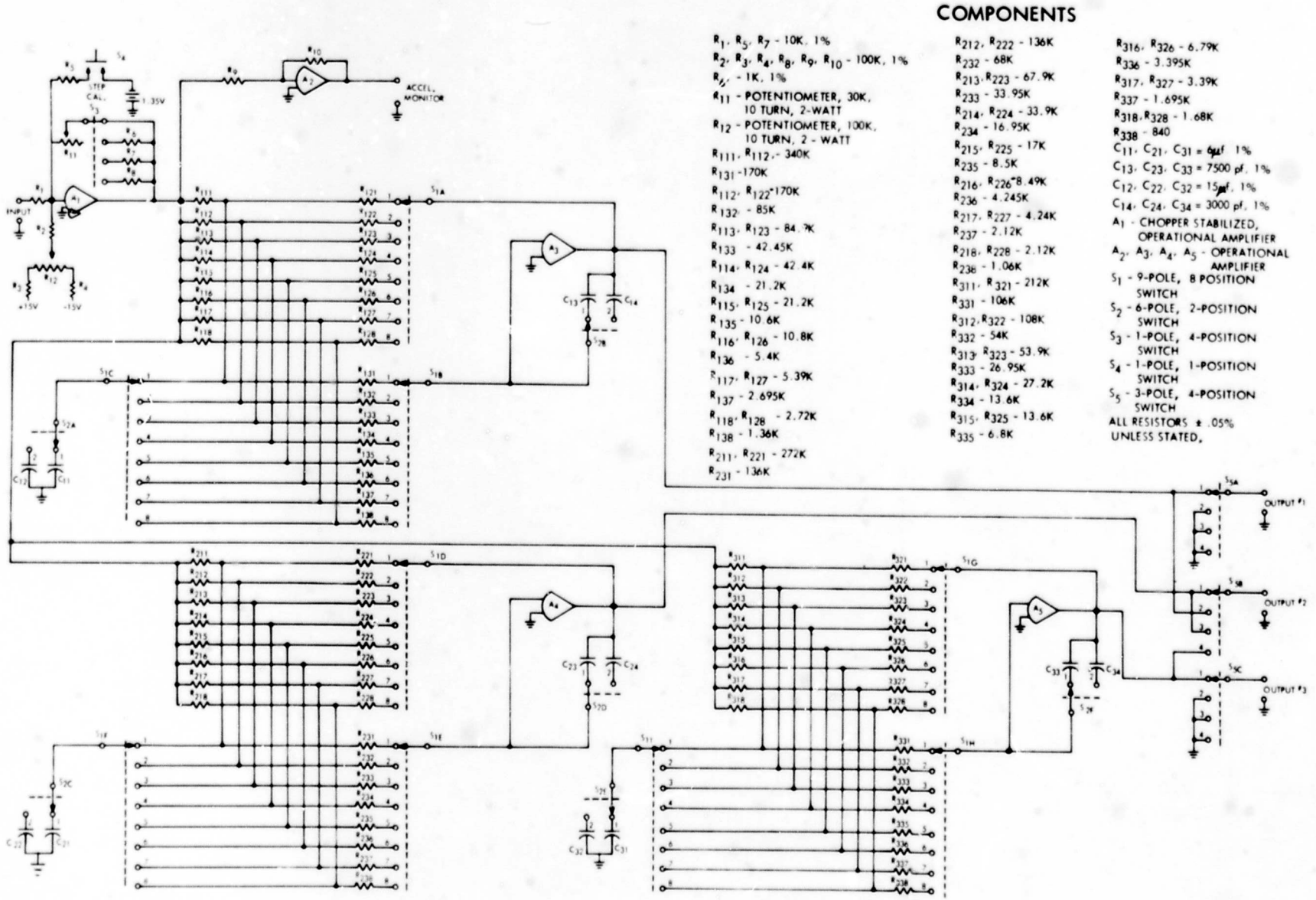

Fig. 6. Detailed electrical schematic of the shock-spectrum analyzer

TABLE 2

Comparison of Results from Analyzer with Analytical Results with 0.0535 Damping

Response Frequency (Hz)	Half-Sine Pulse			Sawtooth Pulse			Isosceles-Triangle Pulse		
	Analog Analyzer Amplitude[a]	Analytical Amplitude[a]	Pulse Period Times Response Frequency ($Tf_{(n)}$)	Analog Analyzer Amplitude[a]	Analytical Amplitude[a]	Pulse Period Times Response Frequency ($Tf_{(n)}$)	Analog Analyzer Amplitude[a]	Analytical Amplitude[a]	Pulse Period Times Response Frequency ($Tf_{(n)}$)
3.04	0.197	0.206	0.056	0.157	0.158	0.055	0.164	0.175	0.061
3.78	0.250	0.257	0.070	0.198	0.196	0.068	0.216	0.218	0.076
4.89	0.328	0.331	0.090	0.255	0.253	0.088	0.276	0.280	0.098
5.98	0.410	0.403	0.111	0.314	0.307	0.108	0.317	0.342	0.120
7.66	0.498	0.513	0.142	0.397	0.391	0.138	0.441	0.435	0.153
9.74	0.647	0.644	0.180	0.511	0.491	0.175	0.551	0.547	0.195
12.1	0.786	0.787	0.224	0.605	0.598	0.218	0.670	0.667	0.242
15.1	0.959	0.957	0.279	0.716	0.725	0.272	0.822	0.810	0.302
19.5	1.200	1.175	0.361	0.920	0.888	0.351	1.020	0.995	0.39
24.5	1.374	1.371	0.453	1.023	1.030	0.441	1.145	1.158	0.49
30.3	1.475	1.523	0.561	1.127	1.136	0.545	1.298	1.289	0.606
38.3	1.630	1.620	0.709	1.180	1.175	0.689	1.416	1.382	0.766
49.0	1.580	1.632	0.907	1.024	1.085	0.882	1.382	1.408	0.98
61.4	—	1.568	1.136	—	0.933	1.105	—	1.351	1.228
78.4	1.385	1.436	1.450	0.960	0.958	1.411	1.200	1.202	1.568
96.6	1.252	1.290	1.787	1.045	1.040	1.739	1.007	1.039	1.932
121.2	1.058	1.121	2.242	0.962	0.962	2.182	1.042	1.021	2.424
155.0	1.075	1.084	2.868	1.021	1.016	2.79	1.130	1.116	3.1
192.0	1.082	1.099	3.552	1.002	0.989	3.456	1.007	1.035	3.84
241.0	1.020	1.026	4.459	1.002	0.988	4.338	1.055	1.051	4.82
309.0	1.010	1.039	5.716	0.990	0.998	5.562	1.010	1.011	6.18
386.0	1.008	1.022	7.141	0.990	0.999	6.948	1.013	1.025	7.72
488.0	1.008	1.115	9.028	0.990	0.999	8.784	1.012	1.017	9.76
625.0	1.004	1.008	11.563	1.010	0.998	11.25	1.010	1.009	12.5

[a]Ratio of output amplitude to input amplitude.

REFERENCES

1. C. M. Harris and C. E. Crede, Shock and Vibration Handbook, Vol. 1 (McGraw-Hill, New York), 1961

2. P. S. Hughes, "Shock Spectra and an Application to Artillery Projectile Shock," Master's thesis, University of Cincinnati, 1967

3. Handbook of Operational Amplifier Active RC Networks, Applications Engineering Section, Burr-Brown Research Corp., 1966

4. L. K. Wadhwa, "Simulation of Third-Order Systems with One Operational Amplifier," IRE Proc., Feb. 1962

5. A. Carlson, G. Hannauer, T. Carey, P. J. Holsberg (eds.), EAI Handbook of Analog Computation 1965

Appendix

ANALYTICAL SHOCK-SPECTRA SOLUTIONS FOR HALF-SINE, SAWTOOTH, AND ISOSCELES-TRIANGLE PULSES

HALF-SINE PULSE (FIGURE A-1)

The general dynamic equation for a mechanical system such as that of Fig. 3 is

$$m\ddot{x} + 2\xi\omega_n\dot{x} + \omega_n^2 x = a(t) \qquad \text{(A-1)}$$

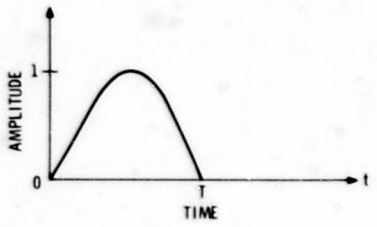

Fig. A-1. Half-sine input pulse

If

$$a(t) = \sin \omega t, \quad 0 \le t \le T,$$

and

$$a(t) = 0, \quad t \ge T,$$

then assuming that the initial displacement and velocity are zero, the Laplace transform of Eq. (A-1) is

$$\mathcal{L}[x] = \frac{\omega(1 + e^{-sT})}{(s^2 + \omega^2)(s^2 + 2\xi\omega_n s + \omega_n^2)}. \qquad \text{(A-2)}$$

Let $\ddot{z} = \omega_n^2 x$ and take the inverse transform of Eq. (A-2), which gives

$$\ddot{z} = \frac{\omega_n^2}{R_1}\left\{\left[\cos\Phi \sin\omega t + \sin\Phi\cos\omega t + \frac{\omega e^{-\xi\omega_n t}}{\omega_n\sqrt{1-\xi^2}}\left(\cos\Phi_n \sin\omega_n\sqrt{1-\xi^2}\, t + \sin\Phi_n \cos\omega_n\sqrt{1-\xi^2}\, t\right)\right] u(t) + \left[\cos\Phi \sin\omega(t-T) + \sin\Phi\cos\omega(t-T) + \frac{\omega e^{-\xi\omega_n(t-T)}}{\omega_n\sqrt{1-\xi^2}}\left(\cos\Phi_n \sin\left(\omega_n\sqrt{1-\xi^2}\,(t-T)\right) + \sin\Phi_n\cos\left(\omega_n\sqrt{1-\xi^2}\,(t-T)\right)\right)\right] u(t-T)\right\} \qquad \text{(A-3)}$$

where

$$\omega_n = \sqrt{k/m},$$

$$\omega = \Pi/T,$$

$$\xi = C/C_c \text{ and } C_c = 2\sqrt{km},$$

$$R_1 = \sqrt{(\omega_n^2 - \omega^2)^2 + 4\xi^2\omega^2\omega_n^2},$$

$$\cos\Phi = (\omega_n^2 - \omega^2)/R_1,$$

$$\sin\Phi = -2\xi\omega\omega_n/R_1,$$

$$\cos\Phi_n = (\omega^2 - \omega_n^2 + 2\xi^2\omega_n^2)/R_1,$$

$$\sin\Phi_n = 2\omega_n^2\xi\sqrt{1-\xi^2}/R_1,$$

$$u(t) = 1 \qquad t > 0$$

$$u(t - T) = \begin{cases} 0 & t < T \\ 1 & t \geq T \end{cases}$$

Equation (A-3) was solved on a Multi-Access Computing facility using BASIC compiler language. The frequencies listed in Table 1 corresponding to those solved by the analog analyzer were selected. The BASIC program for the half-sine pulse is shown in Fig. A-2. The peak positive response results are shown in Table 2.

SAWTOOTH PULSE (FIGURE A-3)

Again, the dynamic equation is

$$m\ddot{x} + 2\xi\omega_n\dot{x} + \omega_n^2 x = a(t)$$

```
100 PRINT "THIS PROGRAM FINDS THE MAX POSITIVE AND"
110 PRINT "NEGATIVE RESPONSE OF S-D-O-F SYSTEMS TO A"
120 PRINT "HALF SINE PULSE"
130 REM INPUTS ARE AS FOLLOWS: T1=PERIOD OF INPUT PULSE
140 REM 'T3' AND 'T4' DEFINE THE RESPONSE TIME INTERVAL,
160 REM 'T5'=TIME OF EACH INCREMENT, C=DAMPING, AND
180 REM F=FREQUENCY OF S-D-O-F SYSTEM.
200 READ T1,C
220 PRINT "INPUT PULSE PERIOD ="T1" SECS. DAMPING="C
230 PRINT "EVALUATED FROM T3 TO T4 AT (T4-T3)/100 INTERVALS."
250 PRINT
260 PRINT "F(N)","+A MAX","-A MAX","T1/T2"
270 PRINT
280 READ T3
290 LET A3=0
292 LET H1=0
294 LET H2=0
300 READ F
310 LET G1=2/F
320 LET G2=2*T1
330 IF G1>G2 THEN 380
340 LET T4=G2
360 GOTO 400
380 LET T4=G1
400 LET T5=(T4-T3)/100
410 LET W2=6.28*F
420 FOR T=T3 TO T4 STEP T5
500 REM INPUT PULSE = HALF SINE WITH T1=18.5 MS
510 LET W=3.14/T1
520 LET R=SQR((W2↑2-W↑2)↑2+4*C↑2*W↑2*W2↑2)
530 LET X1=W2↑2/R
540 LET V1=(W2↑2-W↑2)/R
550 LET V2=(2*C*W*W2)/R
560 LET X2=V1*SIN(W*T)-V2*COS(W*T)
570 LET X3=(W/(W2*SQR(1-C↑2)))/EXP(C*W2*T)
574 LET V3=(W↑2-W2↑2+2*C↑2*W2↑2)/R
580 LET V4=(2*W2↑2*C*SQR(1-C↑2))/R
590 LET X4=V3*SIN(W2*SQR(1-C↑2)*T)+V4*COS(W2*SQR(1-C↑2)*T)
600 LET A=X1*(X2+X3*X4)
610 IF T<T1 THEN 1000
630 LET X5=V1*SIN(W*(T-T1))-V2*COS(W*(T-T1))
640 LET X6=(W/(W2*SQR(1-C↑2)))/EXP(C*W2*(T-T1))
650 LET V5=V3*SIN(W2*SQR(1-C↑2)*(T-T1))
660 LET V6=V4*COS(W2*SQR(1-C↑2)*(T-T1))
670 LET A=X1*(X2+X3*X4+X5+X6*(V5+V6))
1000 IF T=T3 THEN 1100
1020 LET A4=A
1040 IF A4=A3 THEN 1500
1060 IF A4>A3 THEN 1200
1080 IF A4<A3 THEN 1300
1100 LET A3=A
1120 GOTO 1520
1200 IF H1=0 THEN 1240
1220 IF A4<M1 THEN 1280
1240 LET M1=A4
1260 LET H1=1
1280 GOTO 1500
1300 IF H2=0 THEN 1340
1320 IF A4>M2 THEN 1380
1340 LET M2=A4
1360 LET H2=1
1380 GOTO 1500
1500 LET A3=A4
1520 NEXT T
1600 PRINT F,M1,M2,T1*F
1620 GOTO 290
2000 DATA 18.5E-3,.0535,0
2020 DATA 3.04,3.78,4.89,5.98,7.66,9.74,12.1,15.1,19.5,24.5
2022 DATA 30.3,38.3,49,61.4,78.4,96.6,121.2,155,192,241,309
2024 DATA 386,488,625
9999 END
```

Fig. A-2. Basic program for solution of the half-sine pulse

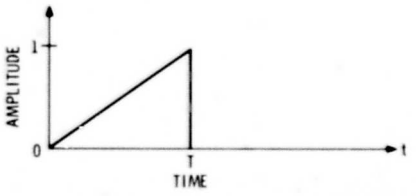

Fig. A-3. Sawtooth input pulse

where

$$a(t) = \begin{cases} t/T & 0 \le t < T \\ 0 & t > T \end{cases}$$

In shock-spectra computations, the initial velocity and displacement are zero; therefore

$$v_0 = x_0 = 0$$

$$\mathcal{L}[x] = \frac{(1 - e^{-sT})}{Ts^2(s^2 + 2\xi\omega_n s + \omega_n^2)} - \frac{e^{-sT}}{s(s^2 + 2\xi\omega_n s + \omega_n^2)} \qquad \text{(A-4)}$$

Again letting $\ddot{z} = \omega_n^2 x$, then

$$\ddot{z} = \left\{ \frac{e^{-\xi\omega_n t}}{T\omega_n\sqrt{1-\xi^2}} \left[\cos\alpha \sin \omega_n\sqrt{1-\xi^2}\, t + \sin\alpha \cos \omega_n\sqrt{1-\xi^2}\, t \right] + \frac{t}{T} - \frac{2\xi}{T\omega_n} \right\} u(t)$$

$$- \left\{ \frac{e^{-\xi\omega_n(t-T)}}{\sqrt{1-\xi^2}} \left[\left(\frac{\cos\alpha}{T\omega_n} + \cos\beta \right) \sin \omega_n\sqrt{1-\xi^2}\,(t-T) + \left(\frac{\sin\alpha}{T\omega_n} - \sin\beta \right) \cos \omega_n\sqrt{1-\xi^2}\,(t-T) \right] + \frac{(t-T)}{T} - \frac{2\xi}{T\omega_n} + 1 \right\} u(t-T), \qquad \text{(A-5)}$$

where, in addition to the previously defined terms: $\sin\alpha = 2\xi\sqrt{1-\xi^2}$; $\cos\alpha = -1 + 2\xi^2$; $\sin\beta = \sqrt{1-\xi^2}$; $\cos\beta = -\xi$.

ISOSCELES-TRIANGLE PULSE (FIGURE A-4)

The dynamic equation is

$$m\ddot{x} + 2\xi\omega_n\dot{x} + \omega_n^2 x = a(t)$$

where

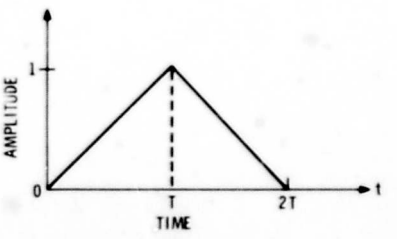

Fig. A-4. Isosceles-triangle input pulse

$$a(t) = \begin{cases} \frac{t}{T} & 0 \le t < T \\ 1 - \frac{(t-T)}{T} & T < t < 2T \\ 0 & t > 2T \end{cases}.$$

As before, letting $v_0 = x_0 = 0$,

$$\mathcal{L}[x] = \frac{1(1 - e^{-sT})^2}{Ts^2(s^2 + 2\xi\omega_n s + \omega_n^2)} \qquad \text{(A-6)}$$

and with $\omega_n^2 x = \ddot{z}$,

$$\ddot{z} = \frac{1}{T\omega_n\sqrt{1-\xi^2}} \left[\left\{ e^{-\xi\omega_n t} \left[\cos\alpha \sin \omega_n\sqrt{1-\xi^2} + \sin\alpha \cos\omega_n\sqrt{1-\xi^2}\, t \right] + \omega_n\sqrt{1-\xi^2}\, t - 2\xi\sqrt{1-\xi^2} \right\} u(t) \right.$$

$$- \left\{ 2e^{-\xi\omega_n(t-T)} \left[\cos\alpha \sin \omega_n\sqrt{1-\xi^2}\,(t-T) + \sin\alpha \cos \omega_n\sqrt{1-\xi^2}\,(t-T) \right] + 2\omega_n\sqrt{1-\xi^2}\,(t-T) - 4\xi\sqrt{1-\xi^2} \right\} u(t-T)$$

$$\left. + \left\{ e^{-\xi\omega_n(t-2T)} \left[\cos\alpha \sin \omega_n\sqrt{1-\xi^2}\,(t-2T) + \sin\alpha \cos \omega_n\sqrt{1-\xi^2}\,(t-2T) \right] + \omega_n\sqrt{1-\xi^2}\,(t-2T) - 2\xi\sqrt{1-\xi^2} \right\} u(t-2T) \right]. \qquad \text{(A-7)}$$

where, in addition to previously defined terms,

$$u(t-2T) = \begin{cases} 0 & t < 2T \\ 1 & t > 2T \end{cases}$$

Equations (A-5) and (A-7) were also solved on the computer, and the peak positive response results are shown in Table 2.

* * *

BLANK PAGE

DYNAMIC PHASE PLOTTING*†

T. E. Smart
Sandia Corporation
Albuquerque, New Mexico

In sine-wave vibration testing, continuous plotting of response amplitude vs frequency is commonly accomplished without the attendant phase information. A system for resolving accelerometer signals from sine-wave vibration tests into coincident and quadrature components for the unambiguous rendition of phase relationships is being developed.

With commercially available equipment, phase is a difficult parameter to plot on analog plotting systems. Use of complex vectors (Co and Quad phasors) eliminates many of the difficulties of phase measurement and facilitates analog plotting. Phasor information can be transformed into phase information by computer processing.

Typical results for the system at its present stage of development are illustrated and discussed.

INTRODUCTION

One of the significant, but unexploited, parameters in the measurement and analysis of sine-wave vibration test data is phase. The analysis of test data has generally been limited to acceleration response amplitudes with no indication of phase relationships. At the magnetic tape playback center for Sandia Corp.'s Environmental Test Laboratories, analog plots of acceleration vs frequency are regularly produced for sine-wave sweeps of the shakers from accelerometer responses recorded on magnetic tape. Except for mechanical impedance or mobility measurements, phase has largely been ignored.

There are several reasons for this situation. Phase is not an easy parameter to measure or process with analog equipment. The commercially available phase meter indicates phase as a function of the time between zero axis crossings by the input signals. Thus, the measurement is sensitive to amplitude, is influenced by noise, and is severely restricted in range. A discontinuity occurs when one or both inputs fall below the threshold magnitude. The scale is awkward because it covers a range of 360 deg and then repeats. An ambiguous region exists, therefore, at each end of the scale, and there is no indication of phase differences beyond a single cycle of frequency. These difficulties apply equally to analog phase plotting and make it confusing at best.

As in mathematics, and specifically in network analysis, phase relationships are described and traced by means of complex variables and phasors (vectors) which have both magnitude and direction. Applying complex notation to the vibration response amplitude, and its phase angle referred to the input, one obtains

$$g \angle \theta = C + jQ ,$$

where C is the phasor component coincident (Co) with the input, and Q is the phasor component in quadrature (Quad) with the input (or reference) (Fig. 1). These are the polar and Cartesian coordinates of the vibratory response, where

$$g = \sqrt{C^2 + Q^2}$$

and

$$\theta = \arctan Q/C .$$

Enlightened use of the Co and Quad phasors should enable one to trace phase relationships without ambiguity.

*This work was supported by the United States Atomic Energy Commission.
†This paper was not presented at the Symposium.

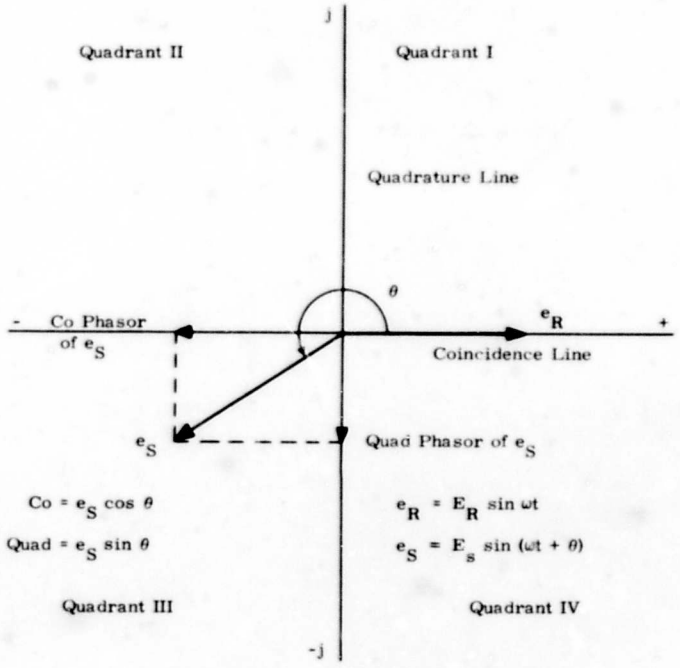

Fig. 1. Typical phasor diagram

On the basis of the foregoing, the magnetic tape playback center has abandoned efforts to plot phase directly and is developing a system whereby dynamic phase relationships can be followed by means of the Co and Quad components. In development is a subsystem which will resolve accelerometer signals into their Co and Quad phasors referred to some meaningful reference signal having the same frequency. These phasors can be plotted on the existent vibration plotting system or digitized for computer processing to obtain phase plots, transfer functions, etc. A basic phasor resolving subsystem, for 10 signal and 2 reference channels, was developed for Sandia by ADYU Electronics around the circuitry of their type 1034 synchronous filter and type 308 component resolver. The general sequence of operations for the reference channels and one signal channel is diagrammed in Fig. 2.

The frequency reference is applied to the carrier generator, and the phase reference to the input amplifier of the reference channel. Output from the carrier generator is a synchronized carrier voltage having frequency $F_C + F_R$, which is input to all balanced mixers. In the reference channel the phase reference is also input to the balanced mixer, which then outputs the three frequencies F_R, F_C, and $F_C + 2F_R$. The crystal bandpass filter passes only the carrier oscillator frequency F_C, which has the same phase as the reference input and is proportional in amplitude. After a final phase and proportionality adjustment in the next amplifier stage, the reference signal is fed to reference inputs to the coincidence resolver and, through a 90-deg phase shifter, to the quadrature resolver.

The signal input E_S is subjected to the same sequence of operations (except the 90-deg phase shift) as the phase reference E_R, and is then applied to the Co and Quad resolver inputs. The resolvers are bridges which, when excited by the Co and Quad reference voltages, allow only those components of the signal that are in phase with the exciting voltage to be rectified. Thus, the dc output of the Co resolver is proportional to $E_S \cos \theta$, and that of the Quad resolver is proportional to $E_S \sin \theta$ (see Fig. 1) when E_R is held constant within ± 1 db.

For plotting the transfer characteristics of most devices, the input voltage is normally held constant and can, therefore, be used for the phase reference as well as the frequency reference. For vibration tests, however, the input acceleration is seldom constant over the entire sweep frequency range. Therein lies the major disadvantage of the basic subsystem for direct analog plotting of the Co and Quad phasors. The frequency reference voltage derived from the

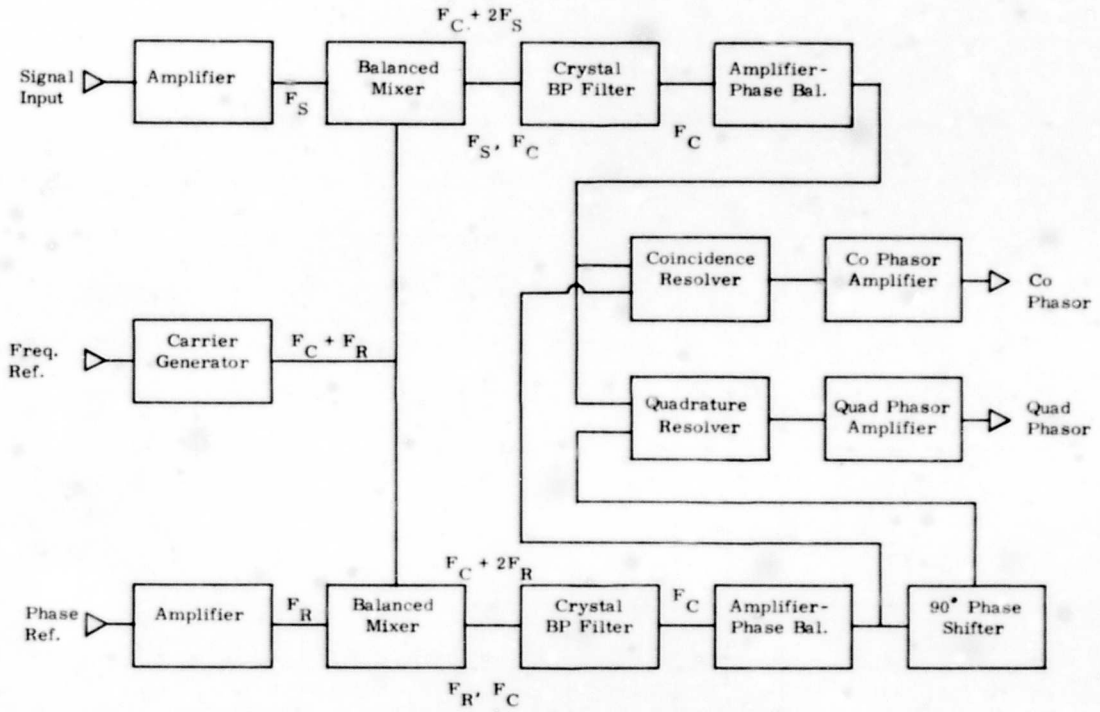

Fig. 2. Block diagram of phasor channel

shaker drive oscillator has constant amplitude and is presently being used for both frequency and phase reference. Thus, the phasor outputs are presently referred to the shaker drive voltage while efforts to achieve satisfactory automatic gain circuitry for the phase reference channel continue. This presents no particular disadvantage for computer processing of phase angles, since the phase angle between the drive voltage and the acceleration input can be subtracted out for each sample frequency.

Figures 3, 4, and 5 illustrate the phase relationships between the sweep oscillator output voltage and the acceleration input for a vibration test of a relatively simple structure. As the frequency increases, the acceleration input to the test fixture progressively lags behind the drive coil voltage in a typical normal mode, single-degree-of-freedom response. This is shown by the circular clockwise pattern of the Nyquist plot of Fig. 3, by the progressive relationship between the Co and Quad phasors of Fig. 4, and by the computed phase angle curve of Fig. 5. Input acceleration vs frequency, plotted in Fig. 6, is always equal to the square root of the sum of the squared phasors regardless of which signal is used for phase reference. On Figs. 4, 5, and 6, there is a definite noise pattern below 20 Hz. The tracking filter in the phasor subsystem has a bandpass of ±20 Hz, which will pass distortion components at frequencies below 20 Hz; the noise swings will not be damped out by the digitizer as they would be by an analog plotting system. This noise is eliminated by playing the taped record back at twice the record tape speed, which effectively reduces the filter bandpass to ±10 Hz.

Figures 7, 8, and 9 illustrate the acceleration response at a location on the test item. Figure 7 shows the Co and Quad phasors referred to the drive voltage, while Fig. 8 shows the computed phase angle of the response referred to the input. The analog plots are duplicates of these digital plots and are, therefore, not included here. A comparison of the response phasors of Fig. 7 with the input phasors of Fig. 4 clearly indicates the critical frequencies apparent on the response amplitude plot of Fig. 9 compared with the input amplitude of Fig. 6.

As users become experienced in the analysis of vibration data by means of the Co and Quad phasors, the phasor plotting system being developed should prove valuable for modal studies and as an additional tool for the evaluation of vibratory responses and transfer functions.

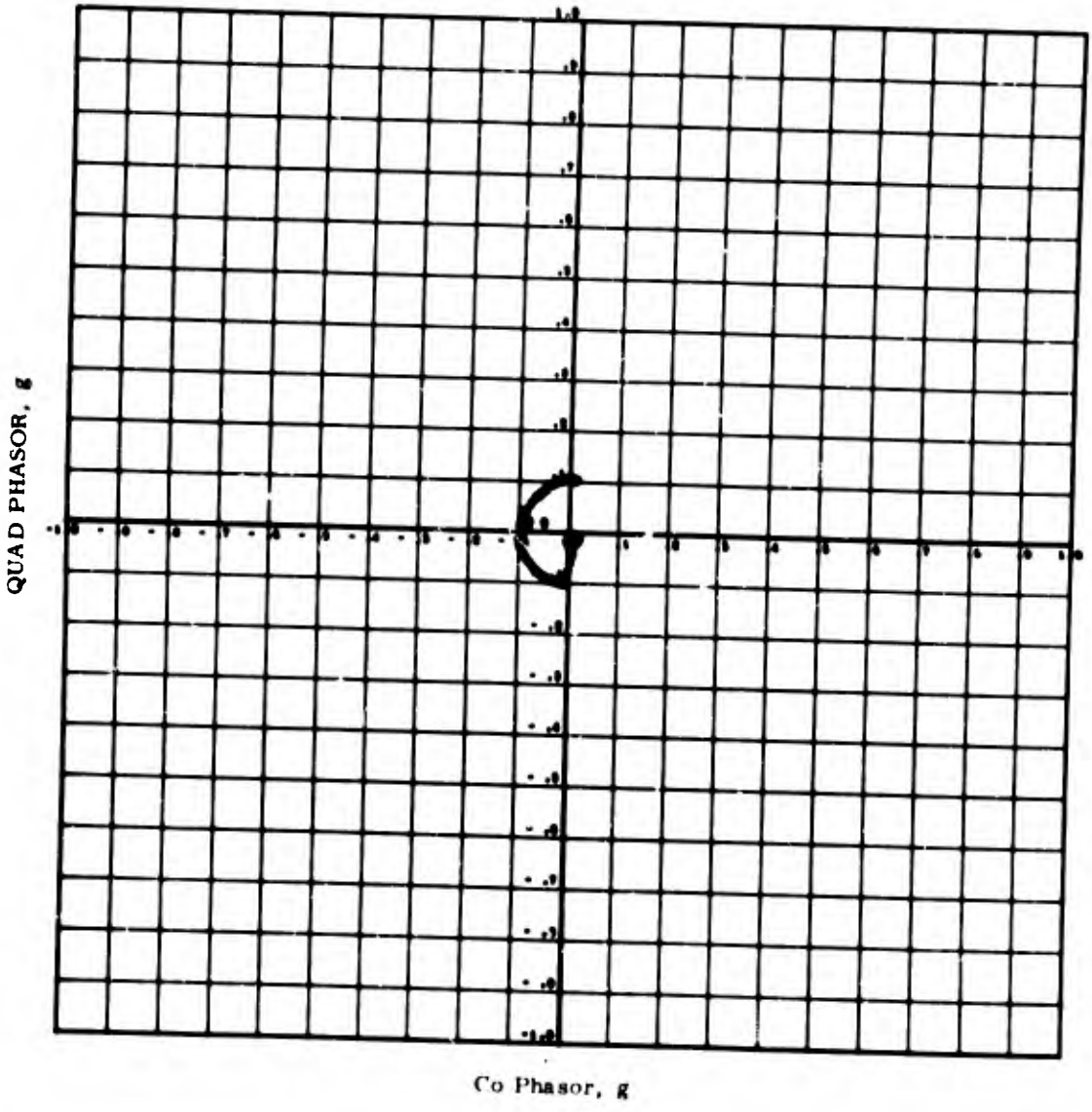

Fig. 3. Nyquist plot of input phasors

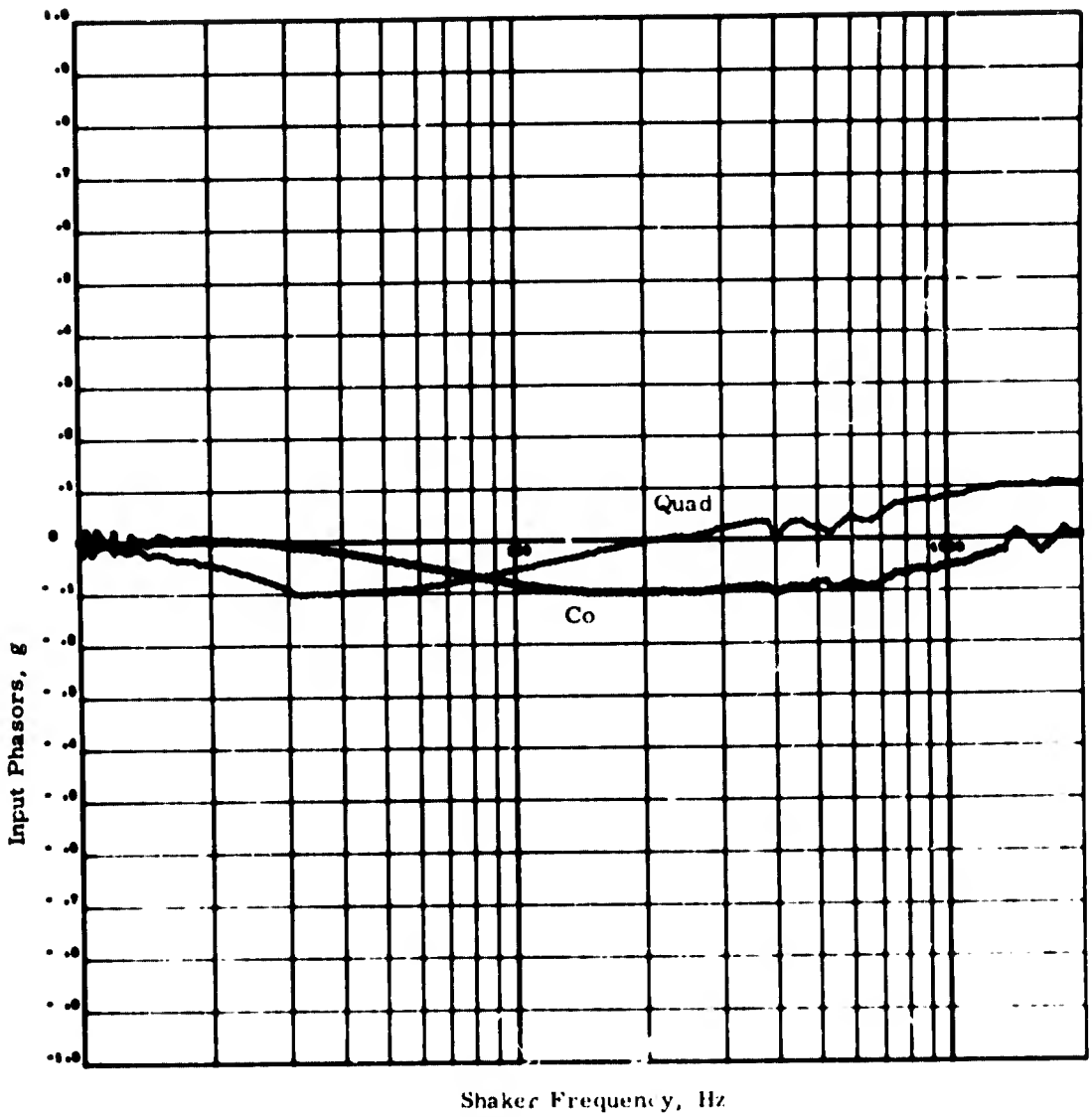

Fig. 4. Input phasor plot vs frequency

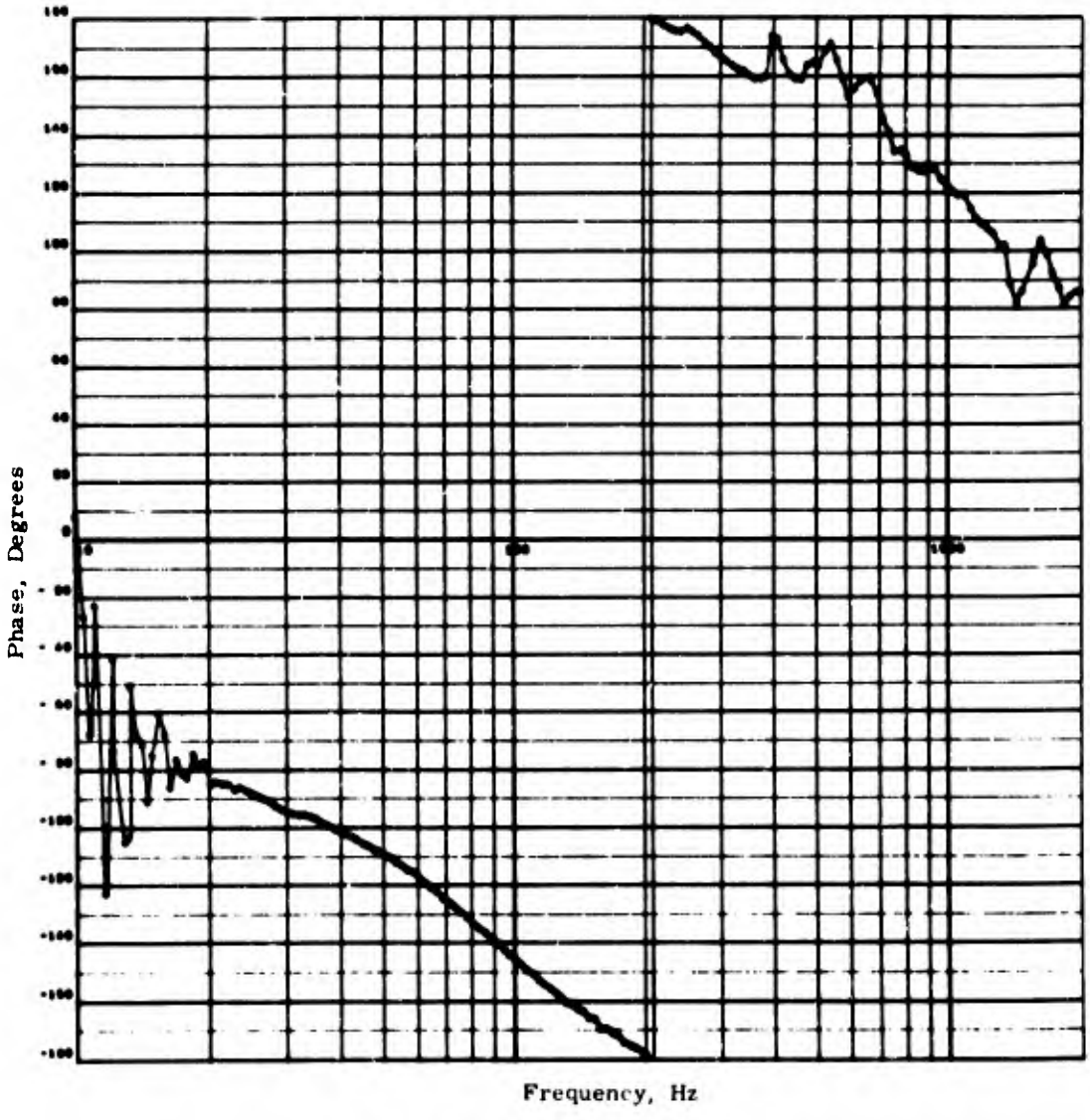

Fig. 5. Input phase plot vs frequency

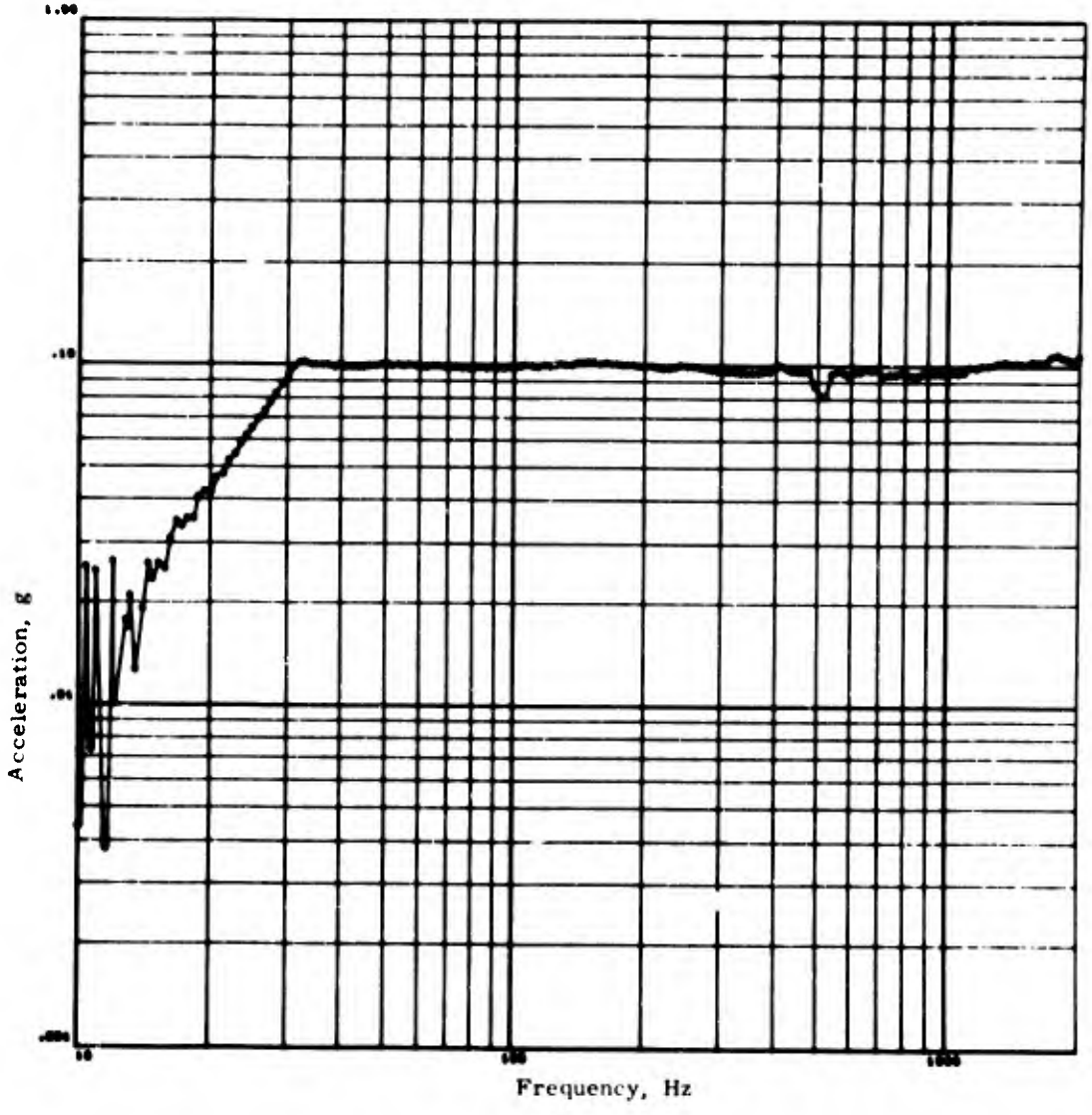

Fig. 6. Input acceleration vs frequency

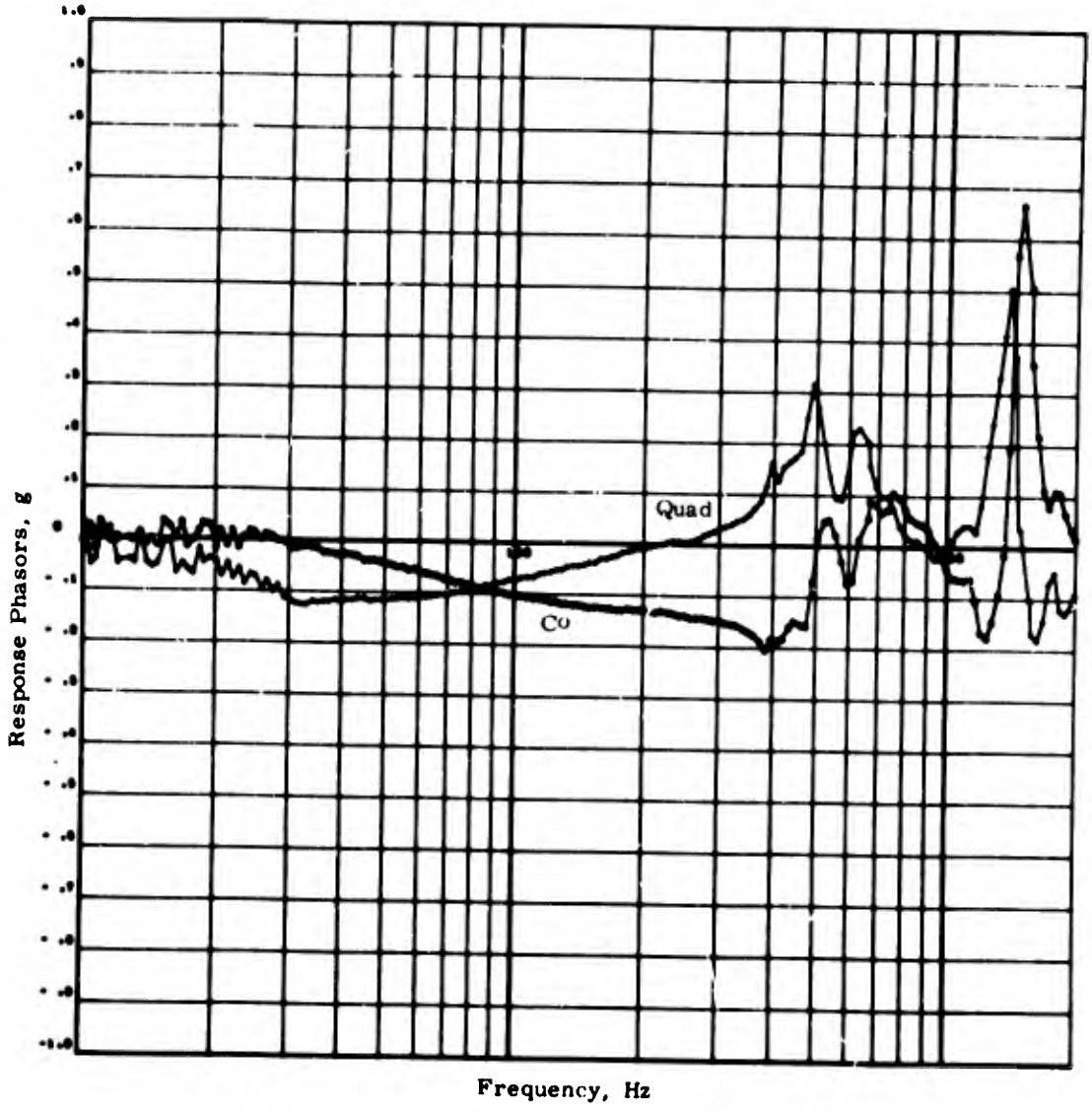

Fig. 7. Response phasor plot vs frequency

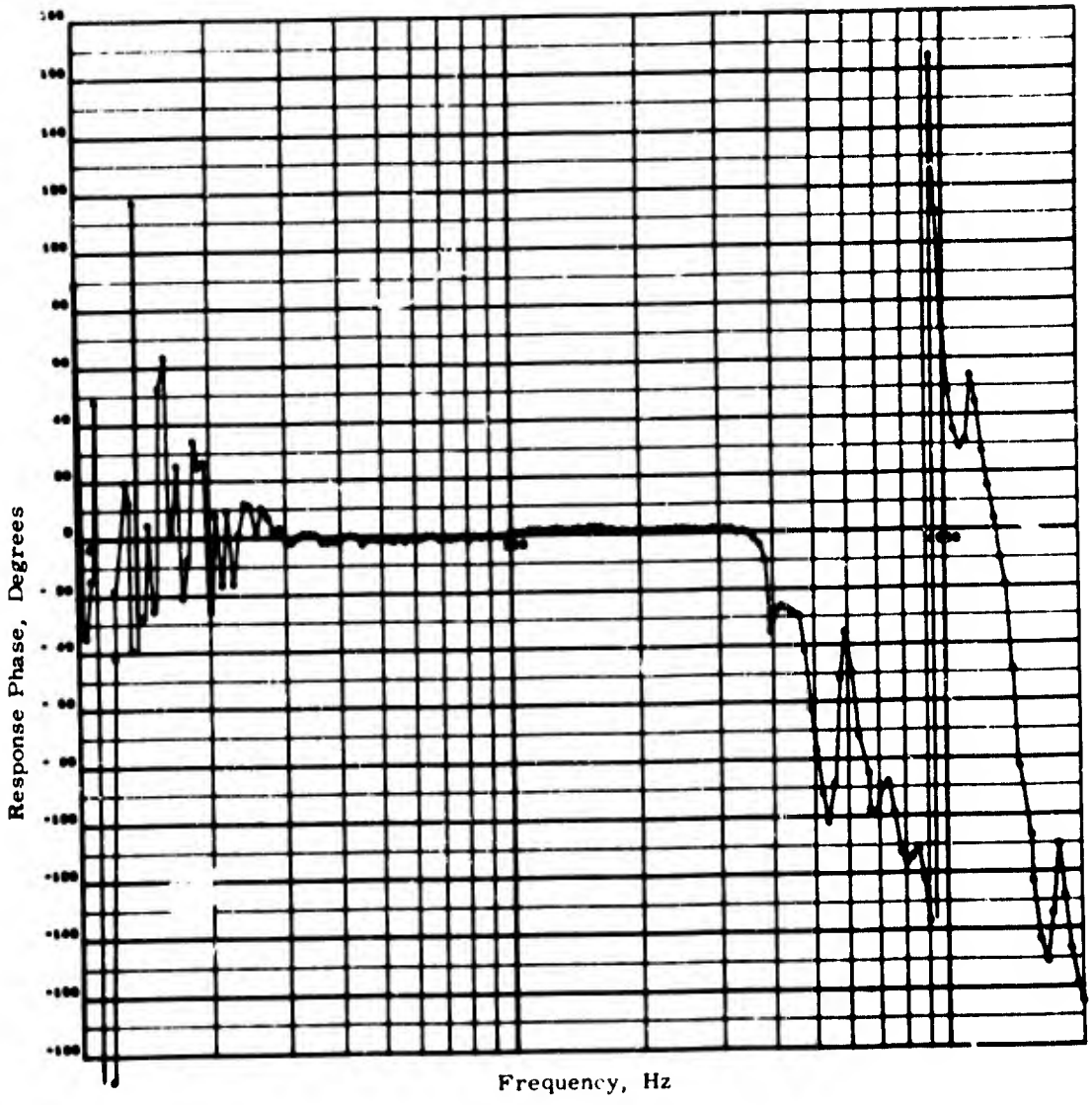

Fig. 8. Response phase referred to input

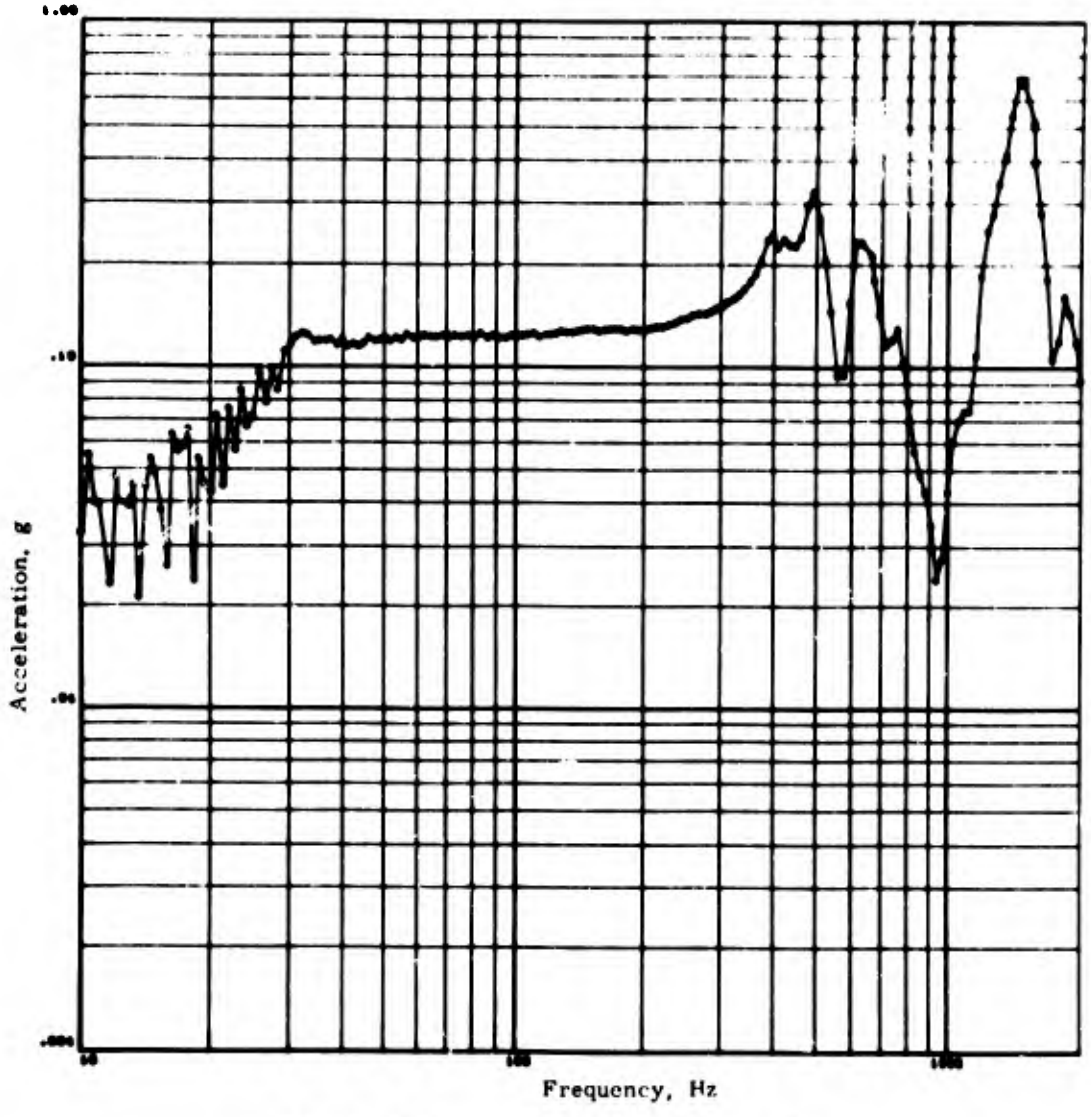

Fig. 9. Response acceleration vs frequency

* * *

RANDOM-VIBRATION-INDUCED ERRORS IN A MISSILE CAUSED BY NONLINEAR INERTIAL ACCELEROMETERS

N. A. Leifer
Bell Telephone Laboratories, Inc.
Whippany, New Jersey

When an inertial accelerometer having a nonlinear and nonsymmetrical output transducer is subjected to vibration, the mean output signal is biased. If the vibration is random, an output power spectrum can be generated which has a low-frequency portion, even though the power spectrum of the input vibration contains no low frequencies. The actual calibration curve of such an instrument can usually be approximated by two straight lines or by a quadratic curve, the former being a more severe case than actual and the latter being a less severe case than actual.

Inertial accelerometers are often used in the feedback loops of guided missiles, comparing the command signal with the response. For a linear accelerometer the error signal produced by the instrument's response to a random vibration usually has its lowest frequency content high enough to make the missile unable to respond to the instantaneous error signal. It responds instead to the mean value, which is zero error. For the nonlinear instrument the mean error is not zero but the bias mentioned above. In addition, the missile can respond to the low-frequency portion of the power spectrum of the output signal which is generated by the nonlinearity. For a sample input power spectrum and accelerometer transfer function, the output signal power spectrum is calculated for each of the two assumed curves by calculating the autocorrelation functions of the output and then taking its Fourier transform. The resulting power spectrum is then filtered through the missile's assumed transfer function, and maximum expected response is calculated.

An accelerometer was built with an intentional nonlinearity about its null point. It was then subjected to the random vibration used in the analysis, and the output was passed through a filter having the same transfer function as that assumed for the missile. The results, based on a normalized scale with the experimental data set at 1, were 0.61 for the quadratic approximation and 1.16 for the straight-line approximation.

The straight-line analysis lends itself to a quick and easy method of checking an instrument for vibration-induced error. By making a template consisting of two straight-edged sections and comparing the actual calibration curve to the template, a prediction can be made whether or not a specified error will be exceeded.

INTRODUCTION

The guidance system in many missiles contains accelerometers in servo loops to compare the actual acceleration which the missile sees with the input or command acceleration. When the missile is subjected to a random vibration, the accelerometer will in general respond and produce an oscillating error signal. If the lowest frequency of oscillation is much greater than the missile natural frequency, the missile cannot respond to the error signal but assumes the average value. If the accelerometer is linear, this average value is zero, causing no vibration-induced error. If, however, it is nonlinear, a nonzero average can result which induces an error in the missile guidance. Furthermore, a low-frequency segment of error signal can be generated to which the missile is capable of responding. Since testing the accelerometer in a combined environment of sustained acceleration and vibration would be costly and difficult, it is very desirable to be able to predict the dynamic error which will be generated simply by examining the accelerometer's static calibration curve. This paper presents a technique for doing this.

MATHEMATICAL MODELS

A typical accelerometer output characteristic is shown, exaggerated, in Fig. 1. Consider a steady-state (sustained) acceleration, G_o, being applied. If a cycle of sinusoidal vibration of amplitude g_o is superimposed upon

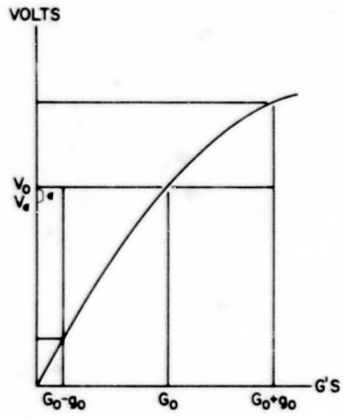

Fig. 1. Typical calibration curve

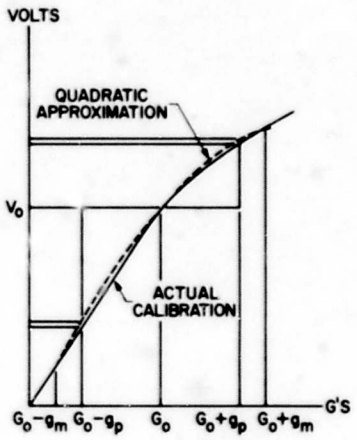

Fig. 3. Quadratic approximation

it, the resulting average output, V_ϵ, is seen to be less than V_o. The quantity $V_o - V_\epsilon$ will be called ϵ, the dynamic error. To get an idea of the magnitude of ϵ, the actual calibration will be approximated first by two straight lines as shown in Fig. 2, and then by a quadratic curve as shown in Fig. 3. Both approximate curves intersect the actual curve at G_o and at $G_o \pm g_m$, where g_m is the maximum value of vibration amplitude anticipated. As can be seen from Fig. 2, vibration along the straight-line approximation produces a greater dynamic error than the actual calibration. When the quadratic approximation lies above the actual calibration as in Fig. 3, it will produce a smaller error than the actual calibration. The errors generated by the two approximate curves will be analyzed and the results considered to be limits of the actual error.

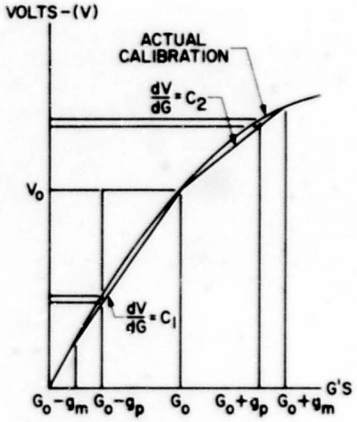

Fig. 2. Two-straight-line approximation

ERROR AS A FUNCTION OF SINUSOIDAL VIBRATION AMPLITUDE

For the straight-line approximation of Fig. 2, let the slope of the line from G_o to $G_o + g_m$ be C_2 and from $G_o - g_m$ to G_o be C_1. In one cycle of sinusoidal vibration of amplitude g_p and frequency ω, the average value of output is

$$V_\epsilon = \frac{\omega}{2\pi}\left[\int_0^{\pi/\omega} (V_o + C_2 g_p \sin \omega t)\, dt + \int_{\pi/\omega}^{2\pi/\omega} (V_o + g_p C_1 \sin \omega t)\, dt\right] \quad (1)$$

Integrating yields

$$V_\epsilon = V_o - \frac{g_p}{\pi}(C_1 - C_2) \quad (2)$$

Letting the difference in slopes $(C_1 - C_2) = C$, the error $V_o - V_\epsilon$ is

$$\epsilon_{SL} = \frac{g_p C}{\pi} \quad (3)$$

For the quadratic approximation of Fig. 3, the output is represented by the equation

$$V = Kg - K_1 g^2 + b \quad (4)$$

In one cycle of sinusoidal vibration of amplitude g_p, superimposed upon a steady-state acceleration G_o, the instantaneous acceleration is

$$g(t) = G_o + g_p \sin \omega t \quad (5)$$

The average output is then

$$V_\epsilon = \frac{\omega}{2\pi}\int_0^{2\pi/\omega}\left[KG_o + Kg_p \sin \omega t - K_1 G_o^2 - 2K_1 G_o g_p \sin \omega t - K_1 g_p^2 \sin^2 \omega t + b\right] dt \quad (6)$$

Integrating yields

$$V_\epsilon = V_o - K_1 g_p^2/2 . \quad (7)$$

Thus the error, $V_o - V_\epsilon$, for the quadratic approximation is

$$\epsilon_q = \frac{K_1 g_p^2}{2} \quad (8)$$

In both approximations the error is obviously independent of V_o. For ease of calculation and without loss of generality, all future calculations will be based on a steady-state acceleration of zero.

ASSUMPTIONS AND EQUATIONS USED FOR RANDOM ANALYSIS

The above relationships were developed for the case of sinusoidal vibration. If, instead of undergoing sinusoidal vibration, the accelerometer is subjected to random vibration, further analysis is required. The assumptions made for this analysis are as follows.

1. The nonlinearity is introduced by the transducer which converts displacement to voltage, and the spring-mass dashpot system is linear. This is not atypical, and the analysis is good if a small nonlinearity is introduced by the springs.

2. The random excitation is stationary, ergodic, and Gaussian in nature.

3. The damping factor is low enough for the accelerometer to be considered a narrow bandpass filter so that the accelerometer output motion is roughly sinusoidal at the accelerometer natural frequency.

Some of the relationships in this section are stated without proof. For more detailed derivations see Ref. [1].

If a function $\varphi_1(t)$ has a physical power spectrum $S_{\varphi_1}(f)$, and the function is operated upon by a linear device, then the resulting function $\varphi_2(t)$ has a power spectrum $S_{\varphi_2}(f)$, which is related to the input power spectrum through the equation

$$S_{\varphi_2}(f) = |H(f)|^2 S_{\varphi_1}(f) , \quad (9)$$

where $H(f)$ is the complex transfer function of the linear device. For an accelerometer with natural frequency f_n and damping factor ζ, $H(f)$ is given by the familiar relationship

$$H(f) = \frac{1}{1 - \left(\frac{f}{f_n}\right)^2 + j2\zeta\left(\frac{f}{f_n}\right)} \quad (10)$$

The autocorrelation function of some general function $\varphi(t)$ is defined by

$$\psi_\varphi(\tau) = \lim_{T\to\infty}\frac{1}{2T}\int_{-T}^{T}\varphi(t)\,\varphi(t+\tau)dt \quad (11)$$

If $\varphi(t)$ has its power spectrum $S_\varphi(f)$ halved at all frequencies, and then reflected into the negative frequency axis such that the new function $W_\varphi(f)$ has the properties $W_\varphi(-f) = W_\varphi(f)$ and $W_\varphi(f) = (1/2)\,S_\varphi(f)$; then $W(f)$ and the autocorrelation function of φ, $\psi_\varphi(\tau)$, are Fourier cosine transform pairs. In equation form this is written as

$$W_\varphi(f) = \int_{-\infty}^{\infty}\psi_\varphi(\tau)\cos 2\pi f\tau\, d\tau \quad (12)$$

and

$$\psi_\varphi(\tau) = \int_{-\infty}^{\infty} W_\varphi(f)\cos 2\pi f\tau\, df \quad (13)$$

The mean square value of φ is $\psi_\varphi(0)$. This becomes obvious by examining Eq. (11) when τ is set equal to zero. Utilizing the relationships between $W_\varphi(f)$ and $S_\varphi(f)$, and Eq. (13), the mean square value is seen to be

$$\psi_\varphi(0) = \int_0^{\infty} S_\varphi(f)\, df , \quad (14)$$

which represents the area under the power spectrum curve.

Since the input vibration is Gaussian with zero mean, the output is Gaussian with zero mean and variance $\psi_a(0)$. Combining Eqs. (9), (10), and (14),

$$\sigma_a^2 = \psi_a(0) = \int_0^{\infty}\frac{S_i(f)}{\left[1 - \left(\frac{f}{f_n}\right)^2\right]^2 + 4\zeta^2\left(\frac{f}{f_n}\right)^2} df , \quad (15)$$

where the subscript i refers to the input vibration to the accelerometer case and the subscript a refers to the output vibration of the

accelerometer's sensing element. For a general function $S_i(f)$, the analytical integration of Eq. (15) is quite difficult. Numerical integration can, however, be quite readily performed for most realistic inputs. The problem that initiated this study specified an input spectrum to be of the form shown in Fig. 4, where the frequency scale has been given in terms of the natural frequency of the accelerometer f_n. The damping factor of the accelerometer in question was $\zeta = 0.3$. Numerical integration of Eq. (15) results in a variance of $\sigma_a^2 = 367\gamma$ where γ is the maximum level of the input spectrum.

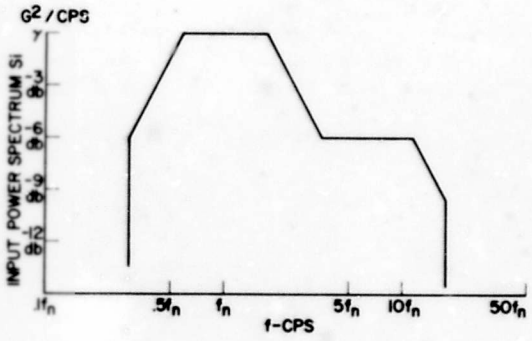

Fig. 4. Input power spectrum

The instantaneous output vibration level has a probability density function given by

$$P(g) = \frac{1}{\sqrt{2\pi}\,\sigma_a} e^{-g^2/2\sigma_a^2} \qquad (16)$$

The peak g levels of vibration (whose instantaneous values are distributed as above) can be shown to have a Rayleigh probability density function. In equation form

$$P(g_p) = \frac{g_p}{\sigma_a^2} e^{-g_p^2/2\sigma_a^2} \quad \text{for } g_p > 0$$
$$= 0 \quad \text{for } g_p < 0. \qquad (17)$$

MEAN ERROR

Equations (3) and (8) represent the average errors per cycle of vibration as functions of vibration amplitude g_p. The mean value of the error, $\overline{\epsilon(g_p)}$, is found by utilizing the relationship

$$\overline{\epsilon(g_p)} = \left[E\,\epsilon(g_p)\right] = \int_{-\infty}^{\infty} \epsilon(g_p)\,P(g_p)\,dg_p, \qquad (18)$$

where $E[\epsilon]$ is the expectation of $[\epsilon]$. Combining Eqs. (3), (17), and (18) yields

$$\bar{\epsilon}_{SL} = \int_0^{\infty} \frac{Cg_p^2}{\pi\sigma_a^2} e^{-g_p^2/2\sigma_a^2}\,dg_p. \qquad (19)$$

Integrating by parts yields

$$\bar{\epsilon}_{SL} = \frac{C\sigma_a}{\sqrt{2\pi}} \qquad (20)$$

Similarly combining Eqs. (8), (17), and (18) yields

$$\bar{\epsilon}_q = \int_0^{\infty} \frac{K_1 g_p^3}{2\sigma_a^2} e^{-g_p^2/2\sigma_a^2}\,dg_p \qquad (21)$$

Again, integrating by parts yields

$$\bar{\epsilon}_q = K_1 \sigma_a^2 \qquad (22)$$

Thus we have derived two expressions for the mean error signal, Eqs. (20) and (22), in terms of the nonlinearities C and K_1, and the mean square value of output vibration; σ_a^2 in general, or 367γ for our particular case.

To determine how much of the fluctuation of this error signal the missile can follow, the power spectrum of the output signal must be derived.

POWER SPECTRA OF OUTPUT VOLTAGE

Straight-Line Model

Consider the straight-line model of Fig. 2. With the command signal equal to zero, the instantaneous output voltage V is equal to $C_2 g$ for $g > 0$ and $C_1 g$ for $g < 0$, where g is the instantaneous g level of vibration. This can be written in the form

$$V = C_1 g - V' \qquad (23)$$

where

$$V' = 0 \quad \text{for } g < 0$$
$$V' = (C_1 - C_2)g = Cg \quad \text{for } g > 0.$$

The power spectrum of V will be found by finding the autocorrelation function of V and then taking its Fourier transform. Much of the mathematics involved in this procedure is based on work done by Rice [2].

The autocorrelation function of V, $\psi_V(\tau)$, is the average value of the product $V(t)\,V(t+\tau)$. For ease of notation, $V(t)$ and $g(t)$ will be called V_1 and g_1, respectively, and $V(t+\tau)$ and $g(t+\tau)$ will be called V_2 and g_2, respectively. $\psi_V(\tau)$ is then the average value of V_1V_2 or

$$\psi_V(\tau) = \overline{(C_1g_1 - V_1')(C_1g_2 - V_2)}. \qquad (24)$$

Combining Eqs. (23) and (24), and utilizing the fact that the expectation of a sum of random variables is the sum of the expectations of the random variables, we get

$$\psi_V(\tau) = E\left[C_1^2 g_1 g_2\right] + E\begin{bmatrix} -CC_1 g_1 g_2 & \text{for } g_2 > 0 \\ 0 & \text{for } g_2 < 0 \end{bmatrix} + E\begin{bmatrix} -CC_1 g_2 g_1 & \text{for } g_1 > 0 \\ 0 & \text{for } g_1 < 0 \end{bmatrix} + E\begin{bmatrix} C^2 g_1 g_2 & \text{for } g_1 \text{ and } g_2 > C \\ 0 & \text{all other cases} \end{bmatrix} \qquad (25)$$

The first term, by definition, is C_1^2 times the autocorrelation function of the instantaneous output vibration $\psi_a(\tau)$. This portion of the autocorrelation function transforms into a portion of the power spectrum having its lowest frequency at the lowest frequency of input vibration, 0.295 f_n in this case, as shown in Fig. 4. The missile's ability to respond to a signal is specified in terms of its time constant and overshoot in response to a step command. This can be translated into a natural frequency and damping factor of a linear second-order system. The natural frequency thus arrived at is typically much lower than the vibration input frequencies. The true missile response is in general not that of a linear second-order system, but the latter is generally a good first approximation. If better accuracy is desired, the actual transfer function of missile behavior can be used to determine missile response to error signal. In either case, for all practical purposes the missile will not respond to an error signal whose lowest frequency corresponds to input vibration frequencies.

Looking at the remaining terms, the second and third terms are identical and are found by integrating the function multiplied by the joint probability density of g_1 and g_2. Since g_1 and g_2 have equal distributions with zero mean and standard deviation σ_a, their joint probability density is

$$P(g_1, g_2) = \frac{1}{2\pi\sqrt{\sigma_a^4 - \psi_a^2(\tau)}} \exp\left[-\frac{1}{2\left(\sigma_a^4 - \psi_a^2(\tau)\right)} \times \left(\sigma_a^2 g_1^2 + \sigma_a^2 g_2^2 - 2\psi_a(\tau) g_1 g_2\right)\right] \qquad (26)$$

These integrations are performed in the Appendix. The results show that the second and third terms each integrate into $-C_1C\psi(\tau)/2$. This too transforms into a portion of the power spectrum beyond the range of interest. The last term, when integrated as shown in the Appendix, becomes

$$\psi_V(\tau) = \frac{C^2}{2\pi}\left[\sqrt{\sigma_a^4 - \psi_a^2(\tau)} + \psi_a(\tau)\cos^{-1}\left(-\frac{\psi_a(\tau)}{\sigma_a^2}\right)\right] \qquad (27)$$

Expanding Eq. (27) in an infinite series yields

$$\psi_V(\tau) = C^2\left[\frac{\psi_a(\tau)}{4} + \frac{\sigma_a^2}{2\pi} + \frac{\psi_a^2(\tau)}{4\pi\sigma_a^2} + \frac{\psi_a(\tau)^4}{48\pi\sigma_a^6} + \cdots\right] \qquad (28)$$

which converges rapidly. All terms of order $\psi_a^4(\tau)$ and higher will be neglected and the remaining three terms will be examined. Combining Eqs. (12) and (28) to get the power spectrum of the error signal yields

$$S_V(f) = 2C^2\int_{-\infty}^{\infty}\left[\frac{\psi_a(\tau)}{4} + \frac{\sigma_a^2}{2\pi} + \frac{\psi_a(\tau)^2}{4\pi\sigma_a^2}\right]\cos 2\pi f\tau\, d\tau. \qquad (29)$$

The first term under the integral integrates into a power spectrum component whose lowest frequency is that of the input power spectrum, and beyond the range of interest.

The second term of $\psi_V(\tau)$ is a constant which represents the square of the mean or "DC" value of the error signal. The mean value of error is thus found to be $C\sigma_a/\sqrt{2\pi}$. By comparing this result with the mean error arrived at by looking at the error as a function of peak g, Eq. (20), it is seen that the two expressions are identical.

The last term is evaluated by making use of the convolution theorem of the Fourier transform, which states that

"If $\mathfrak{F}[f(t)] = F(f)$ and $\mathfrak{F}[g(t)] = G(f)$;

then

$$\mathcal{F}\left[f(t) \cdot g(t)\right] = \int_{-\infty}^{\infty} F(Z)\ G(f - Z)\ dZ\ .\ ''\qquad (30)$$

Combining Eqs. (12), (29}, and (30), and the fact that

$$W_1(f) = \frac{S_V(f)}{2}\ ,$$

we finally get

$$S_V(f) = \frac{C^2}{2\pi\sigma_a^2} \int_{-\infty}^{\infty} \psi_a(\tau)^2 \cos \omega\tau\ d\tau$$

$$= \frac{C^2}{2\pi\sigma_a^2}\ \mathcal{F}\left[\psi_a^2(\tau)\right]$$

$$= \frac{C^2}{8\pi\sigma_a^2} \int_{-\infty}^{\infty} S_a(Z)\ S_a(f - Z)\ dZ \qquad (31)$$

where for computation purposes $S(-Z) = S(Z)$. The power spectrum of the error signal is thus seen to have a low-frequency component which runs all the way down to $f = 0$.

We now have the information necessary to get an expression for missile response. The mean error was found to be

$$\bar{\epsilon}_{SL} = \frac{C\sigma_a}{\sqrt{2\pi}} = 7.5\ \sqrt{\gamma}\ C\ .$$

The error signal will be assumed to be Gaussian and the missile, linear and second order. As mentioned before, while these assumptions are known to be false, they are good first approximations. The variance of the missile response is then, from Eqs. (9), (10), and (14):

$$\sigma_m^2 = \int_0^{\infty} \frac{S_V(f)}{\left[1 - \left(\frac{f}{f_n'}\right)^2\right]^2 + 4\zeta'^2 \left(\frac{f}{f_n'}\right)^2}\, df \qquad (32)$$

where f_n' is the natural frequency of the missile and ζ' is its damping factor as determined from its time constant and overshoot. Typical values of ζ' are about 0.35. To find $S_V(f)$, Eq. (31) would have to be integrated numerically and repeatedly for various values of f. In practice, however, since f_n' is so low, $S_V(f)$ is quite constant over the meaningful range of integration, and only $S_V(0)$ need be found. (For the case under study, at frequencies where the squared transfer function of missile response is down several orders of magnitude, $S_V(f)$ is only a few percent less than $S_V(0)$.) Numerical integration of Eq. (31) for $f = 0$ yields $S_V(0) = 0.146\ \gamma C^2$. Using this value for $S_V(f)$ in Eq. (32), integrating numerically, and taking the square root results in $\sigma_m = 0.74\ \sqrt{\gamma}\ C$. Setting the maximum expected error to $\bar{\epsilon}_{SL} + 3\sigma_m$,

$$\epsilon_{SL_{max}} = 9.7\ \sqrt{\gamma}\ C \qquad (33)$$

Quadratic Model

As in the case of the straight-line model, the power spectrum of the error signal produced in the quadratic model will be found through its autocorrelation function. Using the notation again that $V(t) = V_1$ and $V(t + \tau) = V_2$, the autocorrelation function of output voltage is from Eq. (4):

$$\psi_V(\tau) = \overline{\left(Kg_1 - K_1 g_1^2\right)\left(Kg_2 \quad K_1 g_2^2\right)} \qquad (34)$$

Multiplying and taking the individual expectations,

$$\psi_V(\tau) = E\left[K^2 g_1 g_2\right] - E\left[KK_1 g_1 g_2^2\right] - E\left[KK_1 g_1^2 g_2\right] + K_1\left[g_1^2 g_2^2\right] \qquad (35)$$

The first term is the by now familiar $K^2\psi_a(\tau)$ which is of no concern. The remaining three terms are immediately found from the property of the multivariate Gaussian distribution of identical variables φ_i with zero mean, sampled at different times:

$$E\left[\varphi_1\varphi_2\varphi_3\right] = 0$$

and

$$E\left[\varphi_1\varphi_2\varphi_3\varphi_4\right] = E\left[\varphi_1\varphi_2\right]\ E\left[\varphi_3\varphi_4\right] + E\left[\varphi_1\varphi_3\right]\ E\left[\varphi_2\varphi_4\right] + E\left[\varphi_1\varphi_4\right]\ E\left[\varphi_2\varphi_3\right] \qquad (36)$$

Further detail can be found in Ref. [3].

From the first half of Eq. (36), parts two and three of Eq. (35) are set to zero

$$E\left[g_1 g_1 g_2\right] = E\left[g_1 g_2 g_2\right] = 0$$

The last part of Eq. (35) becomes

$$E\left[K_1^2 g_1^2 g_2^2\right] = K_1^2 \left\{E\left[g_1^2\right]\ E\left[g_2^2\right] + \left(E\left[g_1 g_2\right]\right)^2 + \left(E\left[g_1 g_2\right]\right)^2\right\} \qquad (37)$$

Equation (35) then becomes

$$\psi_V = K_1^2\left[\sigma_a^4 + 2\psi_a(\tau)^2\right] \qquad (38)$$

The first part of Eq. (38) is the constant term which represents the square of the DC value of error signal. Thus the mean error is $K_1\sigma_a^2$ which, again, is precisely what we got with the peak g analysis, Eq. (22). The second part of Eq. (38) is integrated as shown in Eqs. (31) and (32). The result is

$$\sigma_m = 48.5\,\gamma K_1 . \tag{39}$$

The three-sigma error then becomes the mean error plus $3\sigma_m$ or

$$\epsilon_{q_{max}} = 513\,\gamma K_1 . \tag{40}$$

COMPARISON OF RESULTS BETWEEN STRAIGHT-LINE AND QUADRATIC APPROXIMATIONS

Both straight-line and quadratic approximations were set up so that the model curves and the actual curves all intersect at three points: the origin, and plus and minus g_m, where g_m is the maximum anticipated vibration level. This can be assumed to be $3\sigma_a$ or $57.3\sqrt{\gamma}$. The two models can then be equated at these points. Thus

$$C_2 g_m = K g_m - K_1 g_m^2$$

and (41)

$$-C_1 g_m = -K g_m - K_1 g_m^2 .$$

Solving Eqs. (41) and letting $g_m = 3\sigma_a$ yields

$$C = 115\sqrt{\gamma}\,K_1 . \tag{42}$$

Combining Eqs. (33), (40), and (42), the ratio of $\epsilon_{SL_{max}}$ to $\epsilon_{q_{max}}$ becomes

$$\frac{\epsilon_{SL_{max}}}{\epsilon_{q_{max}}} = 2.16 .$$

To get a somewhat smaller range for error approximation, the curve can be broken into four straight-line sections instead of two as shown in Fig. 5. With the slopes designated C_1^*, C_2^*, C_3^*, and C_4^* as shown, the average output per cycle of vibration of amplitude g_m can easily be shown to be

$$\epsilon_{C_m} = \frac{\omega}{2\pi}\left\{2\int_0^{\pi/6\omega} g_m C_1^* \sin\omega t\,dt + 2\int_{\pi/6\omega}^{\pi/2\omega}\left[\frac{g_m}{2}(C_1^* - C_2^*) + g_m C_2^* \sin\omega t\right]dt\right.$$

(Cont.)

$$\left. - 2\int_0^{\pi/6\omega} g_m C_3^* \sin\omega t\,dt - 2\int_{\pi/6\omega}^{\pi/2\omega}\left[\frac{g_m}{2}(C_3^* - C_4^*) + g_m C_4^* \sin\omega t\right]dt\right\} \tag{43}$$

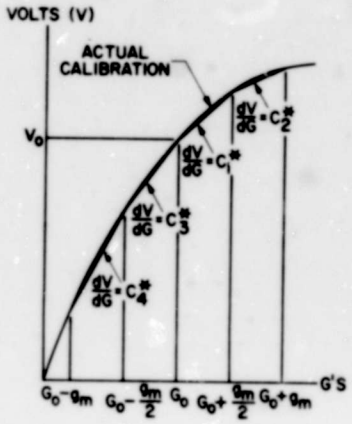

Fig. 5. Four-straight-line approximation

Integration of (43) yields

$$\epsilon_{C_m} = \frac{g_m}{\pi}\left[0.656C_3^* + 0.344C_4^* - 0.656C_1^* - 0.344C_2^*\right] \tag{44}$$

The significance of (44) is that if the slopes of Fig. 2 are redrawn such that $C_1 = 0.656\,C_3^* + 0.344C_4^*$ and $C_2 = 0.656C_1^* + 0.344\,C_2^*$, then for any amplitude of vibration g_P where $g_P < g_m$, the average error will still be less per cycle of vibration than that produced by the actual calibration curve. Thus by using the modified change in slope $C_m (C_m < C)$, a closer approach to the actual error can be made, while remaining conservative.

EXPERIMENTAL VERIFICATION

An accelerometer was built having a rather bad nonlinearity at its null point, the nonlinearity being built into the pickoff. An accurate static calibration was made by whirling the accelerometer on a precision centrifuge and feeding the output into a differential amplifier. The other input to the differential amplifier was the ideal output as measured by a very accurate reference accelerometer. The output of the differential amplifier drove the y axis of an

x-y recorder whose x axis was driven by the reference accelerometer.

The accelerometer was then subjected to random vibration whose power spectrum was shaped as in Fig. 4. A value of γ of 0.4 was chosen for the run. The accelerometer output was fed into a second-order linear electrical circuit having a damping factor of about 0.35 and a low natural frequency (such as the missile would have). The output of the circuit was recorded on a Visicorder chart. Several runs were made for a total running time sufficient to get several hundred cycles of output signal at the natural frequency of the circuit. The maximum error signal recorded was 0.75 percent of full scale (OFS) output. The values of C and K_1 were taken from the calibration curve (C being calculated by the four-line method), with the results C = 0.142% OFS/g and K_1 = 0.0022% OFS/g^2. Plugging these values into Eqs. (33) and (40) results in maximum error predictions of $\epsilon_{SL_{max}}$ = 0.87% OFS and $\epsilon_{q_{max}}$ = 0.46% OFS.

TEMPLATE CONCEPTION

The two-straight-line approach lends itself very nicely to a quick and easy way to check for vibration-induced error. Since the maximum induced error $\epsilon_{SL_{max}}$ is proportional to C, the change in slope, a maximum allowable change in slope can be derived once the vibration environment and maximum allowable error are specified. From Eq. (33)

$$C_{max} = \frac{\epsilon_{SL_{max}}}{9.7\sqrt{\gamma}} . \qquad (45)$$

The 9.7 of course holds true only for the particular system described in this paper. For other systems a new number must be derived using the techniques described. Once C_{max} is established, a template can be made consisting of two straight lines of length sufficient to cover the maximum expected excursions on the calibration curve, and of slope difference equal to C_{max}. The template is then laid against the calibration curve with its vertex at the most nonlinear point on the calibration curve. The other point of contact between the template and the curve is at the maximum expected excursion point on one of the template legs. If the other leg always remains on the same side of the calibration curve, the vibration-induced error will be within limits. Figure 6 graphically illustrates the above conception.

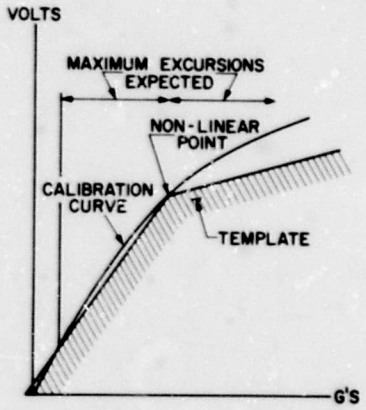

Fig. 6. Template conception

SUMMARY

The typical nonlinear accelerometer calibration can be approximated by two (or four) straight lines, or by a quadratic curve. When an instrument having the actual calibration curve is subjected to random vibration, the dynamic error generated is less than that generated in an instrument having the straight-line approximation, and more than that generated by one having the quadratic curve. The missile response to this error signal is calculated for instruments having the two approximate curves and subjected to the specified random vibration. The technique is to find the autocorrelation function of the output signal, take its Fourier transform to get its power spectrum and filter it with the missile response which is assumed to be linear and second order. The maximum response anticipated is taken to be the mean value of response plus three standard deviations.

The values thus calculated for the specific example used turn out to be 0.87 percent of full-scale output for the straight-line approximation and 0.46 percent of full-scale output for the quadratic approximation. An instrument built with an intensional nonlinearity was tested, and the result was a maximum measured simulated missile response error of 0.75 percent of full-scale output.

REFERENCES

1. Stephen H. Crandall, Ch. 4 in Random Vibration (The Technology Press of the Massachusetts Institute of Technology, Cambridge), 1958

2. S. O. Rice, "Mathematical Analysis of Random Noise," Bell System Tech. J. 24 (1945), pp. 68-69, 131-133, 152-153

3. Stephen H. Crandall and Wm. D. Mark, Random Vibration in Mechanical Systems (Academic Press, New York), 1963, p. 37

Appendix

EVALUATION OF INTEGRALS

The second and third terms of Eq. (25) are found through evaluation of the integral

$$I_1 = -CC_1 \int_{-\infty}^{\infty} dg_2 \int_0^{\infty} dg_2 \; \frac{g_1 g_2}{2\pi \sqrt{\sigma_a^4 - \psi_a(\tau)^2}}$$

$$\times \exp\left[- \frac{1}{2\left(\sigma_a^4 - \psi_a(\tau)^2\right)} \left(\sigma_a^2 g_1^2 + \sigma_a^2 g_2^2 - 2\psi_a(\tau) g_1 g_2 \right) \right]. \qquad \text{(A-1)}$$

For ease of notation, for the rest of this section σ_a will be written as σ and $\psi_a(\tau)$ will be written as ψ.

The last term of Eq. (25) is found through evaluation of the integral

$$I_2 = C^2 \int_0^{\infty} dg_2 \int_0^{\infty} dg_1 \; \frac{g_1 g_2}{2\pi \sqrt{\sigma^4 - \psi^2}}$$

$$\times \exp\left[- \frac{1}{2(\sigma^4 - \psi^2)} \left(\sigma^2 g_1^2 + \sigma^2 g_2^2 - 2\psi g_1 g_2 \right) \right] \qquad \text{(A-2)}$$

which is evaluated in Ref. [2]. The details are repeated here for convenience. Equations (A-1) and (A-2) are seen to differ only by the constant and the lower limit of integration over g_2. Operating first on Eq. (A-2), we make the following transformations:

$$g_1 = \frac{\sqrt{2(\sigma^4 - \psi^2)}}{\sigma} x$$

$$g_2 = \frac{\sqrt{2(\sigma^4 - \psi^2)}}{\sigma} y$$

This transforms Eq. (A-2) into

$$I_2 = C^2 \, \frac{2(\sigma^4 - \psi^2)^{3/2}}{\pi \sigma^4} \int_0^{\infty} dy \int_0^{\infty} dx \, xy \exp\left[-x^2 - y^2 + 2\frac{\psi}{\sigma^2} xy \right]. \qquad \text{(A-3)}$$

In order to evaluate I_2, we will first examine the integral

$$I_3 = \int_0^{\infty} dy \int_0^{\infty} dx \; \exp\left[- \left(x^2 + y^2 - 2 \frac{\psi}{\sigma^2} xy \right) \right] \qquad \text{(A-4)}$$

Let

$$x = \mu + \frac{\psi}{\sqrt{\sigma^4 - \psi^2}} v$$

$$y = \frac{\sigma^2}{\sqrt{\sigma^4 - \psi^2}} v$$

Then

$$x^2 + y^2 - 2\frac{\psi}{\sigma^2} xy = u^2 + v^2$$

and the Jacobian of the transformation equals

$$J\left(\frac{x, y}{u, v}\right) = \begin{vmatrix} 1 & \frac{\psi}{\sqrt{\sigma^4 - \psi^2}} \\ 0 & \frac{\sigma^2}{\sqrt{\sigma^4 - \psi^2}} \end{vmatrix} = \frac{\sigma^2}{\sqrt{\sigma^4 - \psi^2}}.$$

For the limits, when y runs from 0 to ∞, v runs from 0 to ∞. When x runs from 0 to ∞, u runs from $-\psi/(\sqrt{\sigma^4 - \psi^2})v$ to ∞. I_3 can then be rewritten as

$$I_3 = \frac{\sigma^2}{\sqrt{\sigma^4 - \psi^2}} \int_0^{\infty} dv \int_{\frac{-\psi}{\sqrt{\sigma^4 - \psi^2}} v}^{\infty} du \exp\left[-(u^2 + v^2) \right] \qquad \text{(A-5)}$$

Changing to polar coordinates, let

$$u = \rho \cos \theta$$

$$v = \rho \sin \theta .$$

Then the Jacobian $J(u,v/\rho,\theta) = \rho$. For u and v to range from 0 to ∞, ρ must range from 0 to ∞. To keep $v > 0$, $\sin\theta > 0$, $0 < \theta < \pi$. To keep

$$u > \frac{-\psi}{\sqrt{\sigma^4 - \psi^2}}\, v, \quad \cot\theta > \frac{-\psi}{\sqrt{\sigma^4 - \psi^2}} \text{ or } \theta < \cot^{-1}\frac{-\psi}{\sqrt{\sigma^4 - \psi^2}};$$

I_3 then becomes

$$I_3 = \frac{\sigma^2}{\sqrt{\sigma^4 - \psi^2}} \int_0^{\cot^{-1}\frac{-\psi}{\sqrt{\sigma^4-\psi^2}}} d\theta \int_0^{\infty} d\rho\, \rho\, e^{-\rho^2} \qquad \text{(A-6)}$$

Equation (A-6) is directly integrable to

$$I_3 = \frac{\sigma^2}{2\sqrt{\sigma^4 - \psi^2}} \cot^{-1}\frac{-\psi}{\sqrt{\sigma^4 - \psi^2}}. \qquad \text{(A-7)}$$

From the sketch below, it is obvious that this can be written as $I_3 = (1/2)\varphi \csc\varphi$ where $\cos\varphi = -\psi/\sigma^2$.

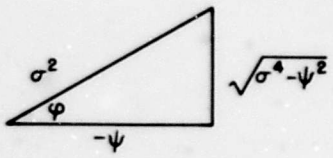

Figure A-1

Combining this result with Eq. (A-4),

$$\int_0^{\infty} dy \int_0^{\infty} dx\, \exp\left[-x^2 - y^2 - 2xy\cos\varphi\right] = \frac{1}{2}\varphi\csc\varphi \qquad \text{(A-8)}$$

Using Leibnitz's rule to differentiate under the integral yields

$$\frac{d}{d\varphi}\left(\frac{1}{2}\varphi\csc\varphi\right) = \int_0^{\infty} dy \int_0^{\infty} dx\, \frac{\partial}{\partial\varphi}\left[\exp\left(-x^2 - y^2 - 2xy\cos\varphi\right)\right]$$

Performing the above operations yields

$$\frac{1}{2}\csc\varphi(1 - \varphi\cot\varphi) = \int_0^{\infty} dy \int_0^{\infty} dx\, 2xy\sin\varphi \exp\left[-x^2 - y^2 - 2xy\cos\varphi\right]$$

or

$$\int_0^{\infty} dy \int_0^{\infty} dx\, xy\, \exp\left[-x^2 - y^2 + 2xy\frac{\psi}{\sigma^2}\right] = \frac{1}{4}\frac{\sigma^4}{(\sigma^4 - \psi^2)}\left(1 + \frac{\psi}{\sqrt{\sigma^4 - \psi^2}}\cos^{-1}\frac{-\psi}{\sigma^2}\right) \qquad \text{(A-9)}$$

Thus the integral being sought, I_2, is equal to

$$I_2 = \frac{C^2}{2\pi}\left[(\sigma^4 - \psi^2)^{1/2} + \frac{\psi}{\sqrt{\sigma^4 - \psi^2}}\cos^{-1}\frac{-\psi}{\sigma^2}\right], \qquad \text{(A-10)}$$

which is the result presented in Eq. (27).

To evaluate I_1, Eq. (A-1), the same general procedure is used. The lower limit of y in Eq. (A-3) must be changed to $-\infty$ which makes the lower limit of v equal to $-\infty$ in Eq. (A-5).

In the subsequent change to polar coordinates, ρ still ranges from 0 to ∞. The requirement that v must go from $-\infty$ to ∞ allows θ to vary from $-\pi$ to π. The requirement that

$$u > \frac{-\psi}{\sqrt{\sigma^4 - \psi^2}}\, v$$

dictates that

$$\cot\theta > \frac{-\psi}{\sqrt{\sigma^4 - \psi^2}} \quad \text{for} \quad v > 0 \ (\theta > 0)$$

and

$$\cot\theta < \frac{-\psi}{\sqrt{\sigma^4 - \psi^2}} \quad \text{for} \quad v < 0 \ (\theta < 0),$$

or

$$\cot^{-1}\frac{-\psi}{\sqrt{\sigma^4 - \psi^2}} < \theta < \cot^{-1}\frac{-\psi}{\sqrt{\sigma^4 - \psi^2}}$$

Since $\cot(\theta - \pi) = \cot\theta$, the above relationship is satisfied when θ ranges over π rad. Equation (A-6) can be rewritten as

$$I_4 = \frac{\sigma^2}{\sqrt{\sigma^4 - \psi^2}} \int_{\theta-\pi}^{\theta} d\theta \int_0^{\infty} d\rho\, \rho\, e^{-\rho^2} \qquad \text{(A-11)}$$

This integrates to

$$I_4 = \frac{\sigma^2 \pi}{2\sqrt{\sigma^4 - \psi^2}}$$

or

$$I_4 = \frac{\pi}{2} \csc \theta . \qquad \text{(A-12)}$$

Differentiating under the integral sign as before yields

$$\int_{-\infty}^{\infty} dy \int_0^{\infty} dx\ xy\ \exp\left[-x^2 - y^2 + 2xy\frac{\psi}{\sigma^2}\right]$$

$$= \frac{\pi}{2} \frac{\sigma^4 \psi}{(\sigma^4 - \psi^2)^{3/2}} . \qquad \text{(A-13)}$$

* * *

Modifying (A-3) to read

$$I_5 = -\frac{CC' 2(\sigma^4 - \psi^2)^{3/2}}{\pi\sigma^4} \int_{-\infty}^{\infty} dy \int_0^{\infty} dx\ xy$$

$$\times \exp\left[-x^2 - y^2 + 2xy\frac{\psi}{\sigma^2}\right] ,$$

and using the results of (A-13) yields

$$I_5 = -\frac{CC'\psi}{2} \qquad \text{(A-14)}$$

which is the desired result.

BLANK PAGE

VIBRATION DISTRIBUTIONS IN MULTIPANEL STRUCTURES: COMPARISON OF MEASUREMENTS WITH STATISTICAL ENERGY PREDICTIONS*

Eric E. Ungar and Nicholas Koronaios
Bolt Beranek and Newman Inc.
Cambridge, Massachusetts

The statistical energy analysis approach, as it applies to multipanel structures, is reviewed. A method is presented for determining the required power flow parameters from measurements on structural samples. Vibration distributions predicted for a point-excited planar array of panels separated by reinforcing beams and for a ring-and-stringer-reinforced cylindrical shell are found to be in generally good agreement with experimental results.

INTRODUCTION

Statistical energy analysis, the fundamentals of which are presented in Refs. [2] through [4], is an analytical tool of great potential utility, since it promises to enable one to deal relatively simply with the (multimodal) random vibrations of complex structures. This analysis approach has been applied successfully to predict the vibrational behavior of some structural and structure-fluid systems of limited complexity [5-7], although some of the basic assumptions that underlie statistical energy analysis have not been verified for the general case [1].

This paper illustrates the application of statistical energy analysis to multipanel structures and presents a comparison between analytical predictions and experimental results for two test structures.

TWO COUPLED PANELS

Statistical energy analysis permits the treatment of vibration problems that otherwise would be extremely complex in terms of simple energy balances analogous to those employed in heat transfer analyses of lumped-parameter systems. It is convenient to introduce the statistical energy approach by applying it first to a single panel, then to the two edge-joined ones (Fig. 1).

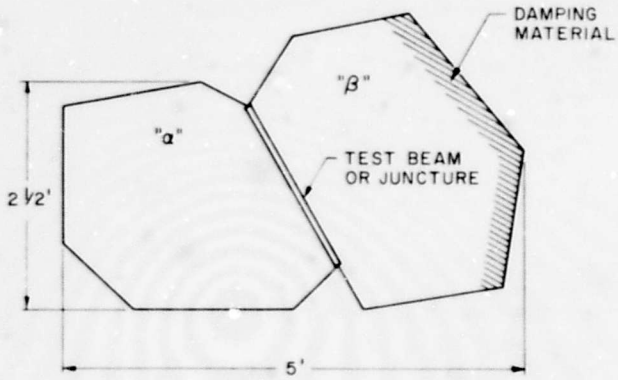

Fig. 1. Two edge-joined panels

Kinetic Energy; Power Dissipation

The total time-average kinetic energy T_{tot} in a given frequency band of a panel vibrating in a steady or stationary state is given by

$$T_{tot} = \frac{1}{2}\int_S mV^2\,dS = \frac{1}{2}M\langle V^2\rangle, \qquad (1)$$

where m denotes the mass per unit area of the panel, V^2 its mean-square velocity distribution (time averaged) in the frequency band of interest, S its total area, M its total mass, and $\langle V^2\rangle$ its mean-square velocity (averaged with respect to both time and space).

*This work was performed under sponsorship of the Air Force Flight Dynamics Laboratory, Research and Technology Division, Air Force Systems Command, and has been previously presented to the sponsor [1].

The time-average power D dissipated by the panel may be expressed [2-4] as

$$D = c\langle V^2\rangle = \eta\omega_0 M\langle V^2\rangle = 2\eta\omega_0 T_{tot} , \qquad (2)$$

where c denotes the (average) viscous damping coefficient of the panel and η its loss factor, and ω_0 represents the center (radian) frequency of the band of interest. Unlike the viscous coefficient c, the loss factor η can be defined entirely in terms of energy concepts and is not restricted to any particular energy dissipation mechanism [8]. Therefore, damping is represented by loss factors throughout the remainder of this paper.

If one knows the time-average power A that is supplied to the panel (in the frequency band $\Delta\omega$ of interest) and notes that in the steady state the energy balance A = D must be satisfied, then one may at once find the mean-square velocity of the panel (in $\Delta\omega$) as

$$\langle V^2\rangle = A/\eta\omega_0 M . \qquad (3)$$

In contrast to the classical vibration analysis approaches, one need not know the panel shape, the boundary conditions, or the panel modes to arrive at the result represented by Eq. (3).

Power Flow Between Two Panels

For two coupled panels the situation is considerably more complicated. To determine the energy balance in such a structural system, one must know not only the average power input to each panel from external sources and the average power dissipation of each panel, but also something about the average net flow of power from one panel to the other. The key relation for this power flow, as developed in Refs. [2] and [3] by generalization of results applicable to two coupled, single-degree-of-freedom systems, may be written as

$$P_{\alpha\beta} = \phi_{\alpha\beta}(T_\alpha - T_\beta) , \qquad (4)$$

where

$$T_\alpha = T_{tot\alpha}/N_\alpha \text{ and } T_\beta = T_{tot\beta}/N_\beta . \qquad (5)$$

Here N and T_{tot} represent, respectively, the number of modes whose resonances fall within the frequency band of interest and the time-average kinetic energy of the panel indicated by the subscript. Thus, T_α represents the average kinetic energy per mode of panel α (in the band $\Delta\omega$), $P_{\alpha\beta}$ denotes the time-average net power flow from panel α to panel β, and $\phi_{\alpha\beta}$ is a constant that depends on the coupling between the panels.

The conditions under which Eq. (4) is valid are not fully known. However, it appears [1,2] that one may reasonably use Eq. (4) if the coupling between the two panels is not highly nonlinear and not too strong, if the coupling itself produces relatively little damping, and if the excitations acting on the two panels are not well correlated. Thus, one may expect to obtain reasonably good results for most realistic structures that are excited, for example, by a diffuse sound field or by random forces acting on only one of the panels.

At frequencies somewhat above the fundamental resonance of a uniform panel, the number of modal resonances in a given frequency interval is independent of the boundary conditions and obeys [9]

$$N/\Delta\omega = N/2\pi\Delta f = S/4\pi\sqrt{D_p/M} \approx S\sqrt{3/2\pi t c_L} , \qquad (6)$$

where D_p denotes the flexural rigidity of the plate, t the plate thickness, and c_L the longitudinal wave velocity in the plate material. Of course, $c_L = \sqrt{E/\rho}$, where E represents Young's modulus, and ρ the density of the plate material; Δf represents the bandwidth in cycle and $\Delta\omega$ in radian units.

Statistical Energy Analysis

It is instructive now to consider the two coupled panels of Fig. 1, and to deal with the case where no external force acts on panel β, i.e., where no power is supplied to panel β from external sources: $A_\beta = 0$. For steady state conditions, an energy balance on panel β yields

$$P_{\alpha\beta} = D_\beta , \qquad (7)$$

which, by application of Eqs. (2), (4), and (5), may be rewritten as

$$\phi_{\alpha\beta}(T_\alpha - T_\beta) = d_\beta T_\beta , \qquad (8)$$

where d_β is defined as

$$d_\beta = 2\omega_0 \eta_\beta N_\beta . \qquad (9)$$

If one solves Eq. (8) for T_α/T_β, then one finds

$$1 + \frac{d_\beta}{\phi_{\alpha\beta}} = \frac{T_\alpha}{T_\beta} = \frac{\langle V_\alpha^2\rangle M_\alpha/N_\alpha}{\langle V_\beta^2\rangle M_\beta/N_\beta} . \qquad (10)$$

One may make two important observations concerning Eq. (10). The first is that the ratio $\langle V_\alpha^2\rangle/\langle V_\beta^2\rangle$ of the mean-square velocities of the panels may be determined if one knows the damping parameter d_β and the coupling coefficient $\phi_{\alpha\beta}$, and that this ratio does not depend

on the power supplied to panel α or on the damping of panel α. The second is that Eq. (10) provides a means for calculating the coupling coefficient $\phi_{\alpha\beta}$ from experimentally determined mean-square velocity ratios and damping parameters.

The energy balance of panel α may be expressed as

$$A_\alpha = D_\alpha + P_{\alpha\beta} \qquad (11)$$

and that of the complete two-plate system as

$$A_\alpha = D_\alpha + D_\beta . \qquad (12)$$

The expression of Eq. (12) may also be obtained by substituting Eq. (7) into (11); thus Eq. (12) can provide no additional information. However, Eq. (11) or (12) may be used in conjunction with Eq. (7) to check the consistency of the general analytical approach by comparing the values that these equations yield for comparable experimental data.

A series of experiments was performed on a panel configuration like that of Fig. 1, with panel α excited by a shaker, via an impedance head. These experiments involved simultaneous measurement of the mean-square velocities V_α^2 and V_β^2 (at several points on each panel, so that the spatial averages $\langle V_\alpha^2 \rangle$ and $\langle V_\beta^2 \rangle$ could be calculated) and of the time-average input power A_α. The loss factors of the two individual panels were measured separately. Values of $\phi_{\alpha\beta}$ then were calculated from Eq. (10), which involves neither A_α nor η_α, as well as from an expression which may readily be derived from Eq. (11) and which involves both A_α and η_α. Comparison of the two sets of results indicated acceptable agreement [1].

From Eqs. (2) and (8)-(11), one may also show [2] that the "apparent loss factor" $\eta_{\alpha\,app}$ of panel α, i.e., the loss factor one may measure by any of the standard techniques on panel α, with panel β attached, obeys

$$\eta_{\alpha\,app} = \frac{A_\alpha}{2\omega_0 N_\alpha T_\alpha} = \eta_\alpha + \frac{\eta_\beta \phi_{\alpha\beta}/N_\alpha}{2\omega_0 \eta_\beta + \phi_{\alpha\beta}/N_\beta} . \qquad (13)$$

Equation (13), when solved for $\phi_{\alpha\beta}$, thus provides an additional means for determining this coupling factor, which does not require tedious power-input or velocity-ratio measurements. When the results of a series of experiments, in which the apparent loss factor of panel α was obtained by the well-known decay-rate technique, were compared with corresponding results of the previously described experimental series [1], satisfactory agreement was again obtained.

MULTIPANEL STRUCTURES

General Energy Balance; Analysis

The energy balance of a typical panel (designated by subscript J) of a multipanel structure, like those of Fig. 2, may be written as

$$P_{JA} + P_{JB} + P_{JC} + \cdots + D_J = A_J , \qquad (14)$$

where the net power flow from panel J to all other panels appears on the left-hand side, in addition to the power dissipation D_J, and where the power addition A_J appears on the right-hand side. Assuming a relation like Eq. (4) for each pair of panels, and replacing D_J by $d_J T_J$ according to Eqs. (2), (5), and (9), one may rewrite Eq. (14) as

$$T_J \left[d_J + \sum_{K \neq J} \phi_{JK} \right] - \sum_{K \neq J} \phi_{JK} T_K = A_J . \qquad (15)$$

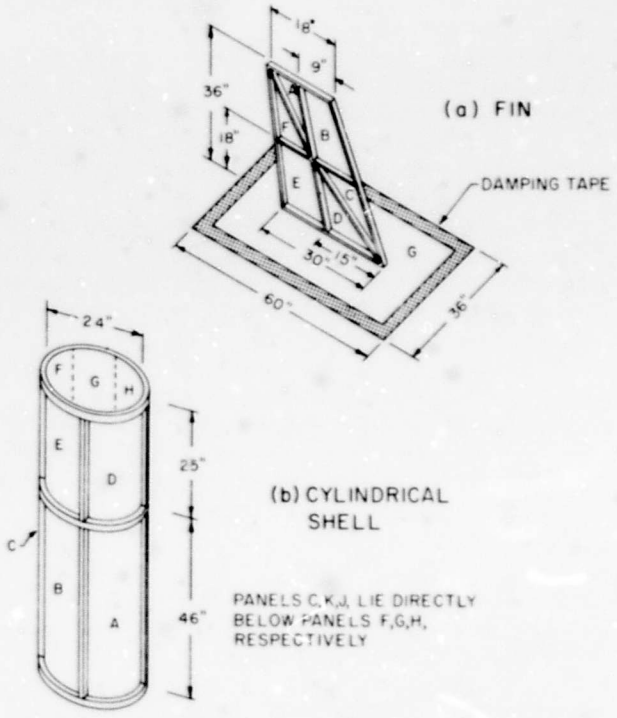

Fig. 2. Multipanel test structures

For a structure with Ω different panels, one may write Ω different equations like (15). One thus obtains a set of Ω linear equations for the

N unknown modal kinetic energies T_J, for which one may solve if given all the power inputs A_J. For structures with more than three or four panels, solution is best accomplished by numerical methods, such as those involving matrix inversion or relaxation techniques. (Note that Eq. (15) is analogous to the expression which describes heat flow in a lumped-parameter system.)

Test Structures

Two structural configurations were selected for extensive study: a finlike structure made up of beam-reinforced flat plates and a ring-and-stringer-reinforced cylindrical shell (Fig. 2). These test structures were chosen because they are reasonably realistic, yet simple enough so that their analysis does not require much computation.

Both test structures of Fig. 2 were made of 1/16-in.-thick aluminum. The reinforcing beams and rings were attached to the sheet metal skins by means of a rigid epoxy, but a weld was used to strengthen the joint between the primary fin panel and its base plate. Damping tape was applied along the edges of the fin base plate, in order to simulate the loss of vibratory energy that the fin would experience if it were attached to some larger structure.

Auxiliary Measurements

In order to provide the information required as input to the theoretical calculations, the panel loss factors and power flow coefficients were determined experimentally.

Loss factor measurements were made on each of the two separate plates that comprise the fin, before assembly and before addition of the reinforcing beams, but with the damping tape in place on the base plate. These measurements were made in 1/3-octave bands, by means of the well-known decay-rate technique. Similar measurements were also carried out on the two separate shell lengths (one 25 in., the other 46 in. long) from which the entire test shell was assembled.

Values of the power flow coefficients were obtained from a separate series of measurements, which was carried out on a two-panel configuration like that of Fig. 1, and which made use of the ideas and relations discussed in the previous section. Average values of these measured coefficients for the one beam configuration used in the test structures are presented in Fig. 3.

Measurement of Vibration Distributions and Power Output

During all measurements the test structures were suspended by long thin strings. A typical experiment consisted of exciting the test structure at one point of one of the panels with an electrodynamic shaker, and measuring the accelerations at one point on each panel. In an experimental series these measurements were repeated for different driving points on a given panel and for different measuring points on the other panels.

In all cases the mechanical power supplied to the structure was measured by an impedance head (connected between the excitation source and the driven point on the structure) and attendant electronic instrumentation. All measurements were carried out in 1/3-octave bands: the shaker was activated by a signal that was generated by a white-noise source, passed through a 1/3-octave filter, and suitably amplified; the outputs of the various accelerometers were filtered in the same 1/3-octave bands as the excitation signal before they were fed to an rms voltmeter.

Results

A series of calculations was carried out pertaining to the fin structure with only panel B excited externally. These calculations involved solution of seven simultaneous linear equations like Eq. (15) – each describing the energy balance of one of the seven fin panels – with all power input terms except A_B set equal to zero. Only those power flow terms that pertain to panel pairs sharing a common edge were retained in these equations; the rest were neglected. Loss factor, coupling coefficient, and panel area values that were obtained from auxiliary measurements were used to compute the parameters that enter these equations.

The results of these calculations are presented in Fig. 4, which shows the frequency variation of the ratio of the average kinetic energies T_J of the various panels to the input power A_B. Note that this ratio is a rather natural one to use, in view of the form of the pertinent equations. Also, if one expresses A_B as the product of the driving point resistance R and the mean-square velocity V_0^2 of the driving point, one may use Eqs. (1) and (5) to show that

$$\frac{T_J}{A_B} = \frac{\langle V_J^2 \rangle M_J / 2N_J}{V_0^2 R} \tag{16}$$

i.e., that T_J/A_B is proportional to the velocity ratio $\langle V_J^2 \rangle / V_0^2$, which is generally of primary interest.

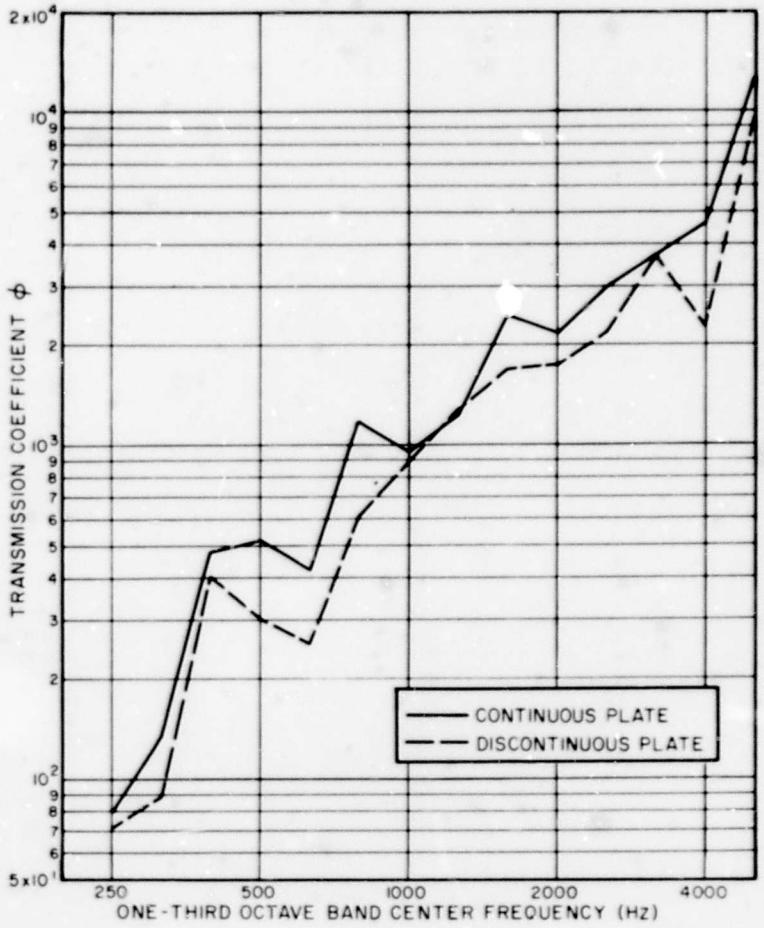

Fig. 3. Experimentally determined power transmission coefficient values for 1/2-in. by 3/4-in. aluminum beam on 1/16-in. aluminum plate

The ordering of the vibration levels of the panels apparent from Fig. 4 agrees with what one expects from energy considerations. The directly excited panel B has the highest modal energy; the highly damped panel G, which also is relatively far from the directly excited one, has a relatively low modal energy. The relative magnitudes of the energies of the other panels lie between those of B and G, with panels closer to B and farther from G having higher energies. Analogous calculations for the shell structure (analyzed as if it were a flat plate) were found to yield similar results [1]; however, because there was no single panel that was much more highly damped than the rest, the curves for the shell panels are more closely clustered.

Some typical results obtained from experimental measurements are presented in Fig. 5, together with corresponding calculated results. There exists good general agreement between the theoretical curves and experimental points; this agreement may be observed also in the more extensive information presented in Ref. [1] both for the fin and for the cylindrical shell structure, but for the shell the agreement was found to be somewhat worse than for the fin.

The scatter of the experimental results may be ascribed at least in part to the spread in the velocities measured at different points on the structure. Thus, the experimental points may not represent the spatial averages of the velocities adequately, whereas the calculations pertain only to such averages.

Driving Point Resistance

As is evident from Eq. (16), one must know the driving point resistance R, i.e., the real part of the driving point impedance, to interpret the T_J/A ratios in terms of velocity ratios

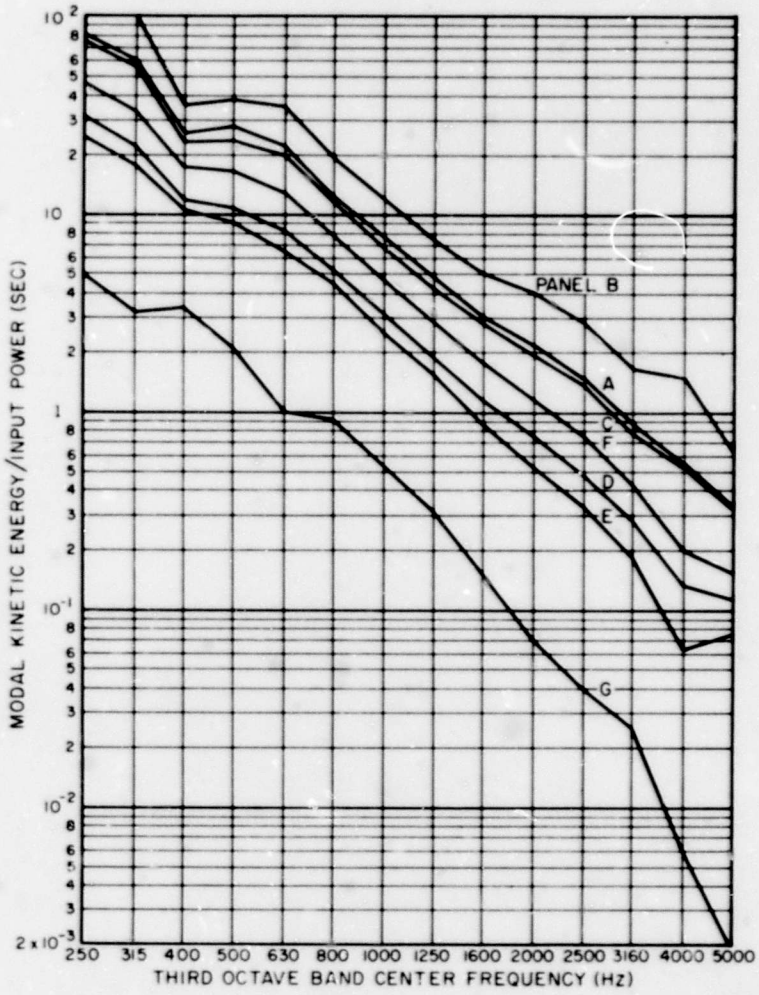

Fig. 4. Calculated responses of fin panels to excitation applied on panel B

$\langle V_J^2 \rangle / V_0^2$. Although this resistance may, at least in principle, be calculated by classical means from a complete modal analysis of the structure, such calculations are prohibitively long, and their use would negate the simplicity and brevity of the statistical energy analysis approach.

Fortunately, it has been shown [10] that at high enough frequencies the driving point impedance of any finite uniform elastic structure approaches that of a similar structure of infinite extent. The impedances of infinite structures are available in texts and handbooks (e.g., Refs. 11, 12); the driving point impedance of an infinite uniform plate is entirely resistive and is given by

$$R = 8\sqrt{D_p m} \quad . \tag{17}$$

A comparison of the driving point resistances measured on the test structures with those calculated for an infinite plate of the same material and thickness appears in Fig. 6. Observe that the experimental data here are always within an order of magnitude of the infinite-plate value, that the data points generally lie below that value, and that these points cluster more closely about that value for higher frequencies. From the fact that the experimental values generally are lower than that for the infinite plate, one can conclude that use of the infinite-plate value in calculations would result in predicted vibration levels that usually are somewhat too high, and thus conservative.

CONCLUSIONS

The results presented in this paper indicate that statistical energy analysis can be applied to obtain useful quantitative predictions of the mean-square vibratory responses of multipanel

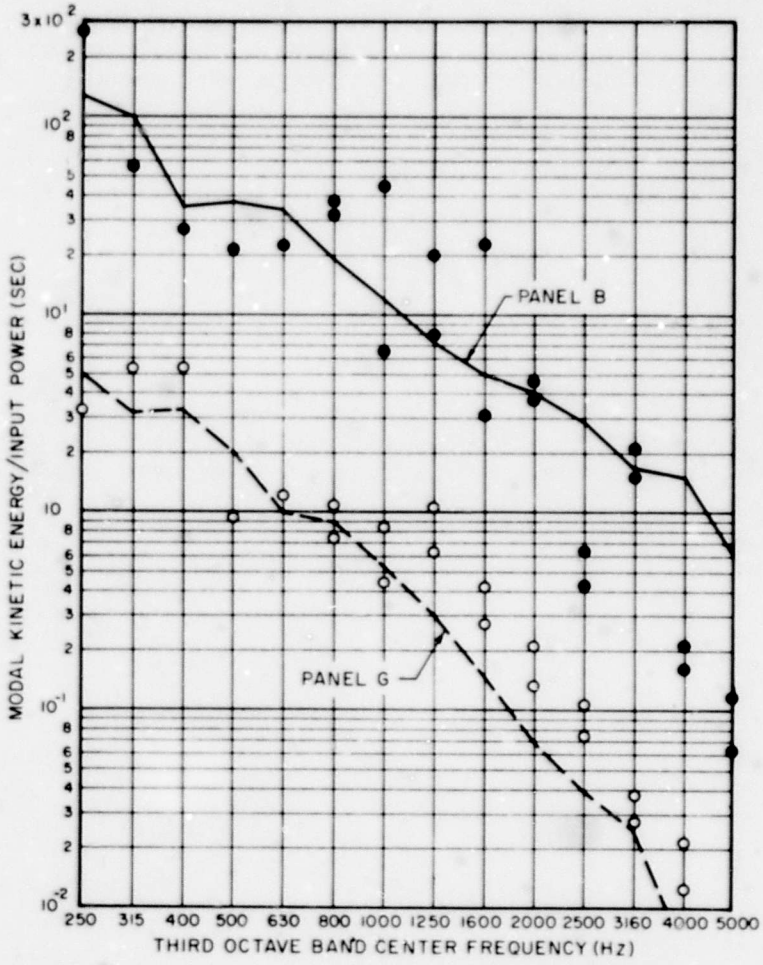

Fig. 5. Comparison of theoretical (curves) and experimental (points) results for two panels of fin

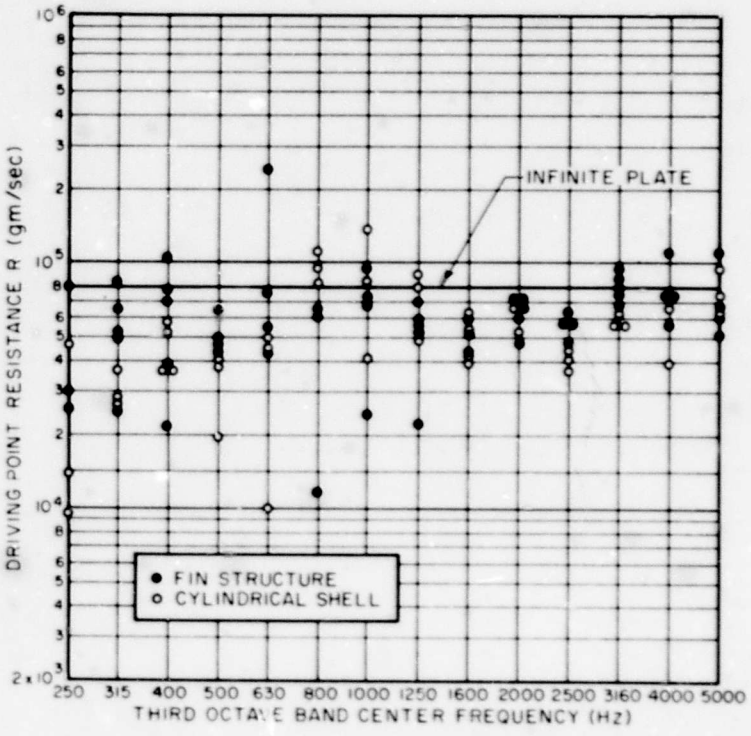

Fig. 6. Comparison of driving point resistance values measured on test structures with corresponding infinite plate resistance

structures. These predictions can be obtained without much computational effort. However, to arrive at them one must know the damping of all panels (as for classical analyses too, if resonances dominate the responses), as well as the coefficients that pertain to power flow between all adjacent pairs of panels.

The loss factors of structural components may be estimated from available information (e.g., Refs. 13, 14), or may be obtained from relatively simple measurements. No theory is as yet available from which one may calculate the coefficients pertaining to power flow between two edge-joined panels; however, a means for determining these coefficients empirically has been described here and has been shown to yield consistent results.

Although statistical energy analysis provides information on only the mean-square values of response parameters, some studies [1, 15] have been performed also on response maxima (response concentrations) and on the effect of boundary conditions on maximum stresses [16]. Much work remains to be done before the theoretical basis for statistical energy analysis is complete and before this approach can be used for obtaining all salient statistical properties of the responses of complex structures. Nevertheless, statistical energy analysis is a uniquely powerful, yet simple, tool that can provide not only a qualitative understanding of the most important aspects of the vibrations of composite systems, but also quantitative answers to complex vibration problems that cannot be attacked practically in any other way.

REFERENCES

1. E. E. Ungar, N. Koronaios, and J. E. Manning, "Application of Statistical Energy Analysis to Vibrations of Multi-panel Structures," AFFDL TR 67-74, May 1967

2. E. E. Ungar, "Fundamentals of Statistical Energy Analysis of Vibrating Systems," AFFDL TR 66-52, Apr. 1966

3. E. E. Ungar, "Statistical Energy Analysis of Vibrating Systems," ASME Paper 67-Vibr-8, Mar. 1967

4. E. E. Ungar and T. D. Scharton, "Analysis of Vibration Distributions in Complex Structures," Shock and Vibration Bull. 36(Part 5):41 (1967)

5. R. H. Lyon and E. Eichler, "Random Vibration of Connected Structures," J. Acoust. Soc. Am. 36:1344 (1964)

6. E. Eichler, "Thermal Circuit Approach to Vibrations in Coupled Systems and the Noise Reduction of a Rectangular Box," J. Acoust. Soc. Am. 37:995 (1965)

7. R. H. Lyon and T. D. Scharton, "Vibrational Energy Transmission in a Three-Element Structure," J. Acoust. Soc. Am. 38:253 (1965)

8. E. E. Ungar and E. M. Kerwin. Jr., "Loss Factors of Viscoelastic Systems in Terms of Energy Concepts," J. Acoust. Soc. Am. 34:454 (1962)

9. P. W. Smith, Jr. and R. H. Lyon, "Sound and Structural Vibration," NASA CR-160, Mar. 1965

10. E. Skudrzyk, "Vibrations of a System with a Finite or an Infinite Number of Resonances," J. Acoust. Soc. Am. 30:1140 (1958)

11. E. E. Ungar, "Mechanical Vibrations," in Mechanical Design and Systems Handbook, Sec. 6 (McGraw-Hill, New York), 1964

12. L. Cremer and M. A. Heckl, Körperschall (Springer-Verlag, Berlin), 1967

13. B. J. Lazan, "Energy Dissipation Mechanisms in Structures, with Particular Reference to Material Damping," Sec. 1 in Structural Damping (J. Ruzicka, Ed.) (American Society of Mechanical Engineers, New York), 1959

14. E. E. Ungar and J. R. Carbonell, "On Panel Vibration Damping Due to Structural Joints," AIAA J. 4:1385 (1966)

15. R. H. Lyon, "Spatial Response Concentrations in Extended Structures," Paper 67-Vibr-22, Am. Soc. Mech. Engrs. Vib. Conf., Boston, Mar. 1967

16. E. E. Ungar and K. S. Lee, "Consideration in the Design of Supports for Panels in Fatigue Tests," AFFDL-TR-67-86, June 1967

Mr. Smith (Bell Aerosystems Co.): I have three short questions, one of which I think you answered towards the end of your talk. It sounds as though the method begins by assuming that the elements behave independently as far as their modal responses are concerned. This certainly won't be true until you get up to quite high frequency which is, as you showed, up into several kc where, for example, infinite plate behavior became illustrated. So, at lower frequencies, this does seem a restriction on applicability of the method. Would you comment on that, please?

Mr. Ungar: At very low frequencies one can do modal analysis, and I advocate modal analysis. At higher frequencies where each of the subpanels has several or many modes, modal analysis becomes too cumbersome and meaningless. We can argue about that later. It does not really matter what the modes are or how they hang together. The important thing is that we know at least approximately the number of modes in a given frequency band.

Mr. Smith: The second point – you did say that you were not quite sure why the power flow should necessarily be proportional to the difference in main KE's. Perhaps it is the same thing – I am not too sure why, for example, the difference in main strains shouldn't be appropriate for certain types of power transmission between two elements. Could you comment on that again? For example, KE could obviously be significant, say, in acoustically transmitted power flow, but internally I believe the strains might be more significant.

Mr. Ungar: This method has been worked out using strain energy or kinetic energy or total energy. I do not think one is more important than the other. I happen to prefer kinetic energy because it gives us the thing I am looking for most simply.

Mr. Smith: Thirdly, do you see any prospect that having got a general idea for the response of a particular element in terms of mean square velocities, the modal properties themselves might possibly be used to determine the probable areas of failure in those elements where the mean square velocities were high?

Mr. Ungar: I think it would be a mistake to introduce modal properties. There is an approach that we have explored fairly recently and incompletely which has to do with dynamic edge effect. It permits you to determine areas of maximum stress for given reinforcements without having to bother with modes. It is incompletely developed but I think that is the way to go. We have gone through lots of contortions here to avoid messing with the modes because, as I said before, they are difficult to find and meaningless. I am still going to argue with somebody about that.

Mr. Kirkley (Martin-Marietta Corp.): It appears that the excitation you are talking about on these panels is acoustic, or a turbulent-type excitation. Is this correct?

Mr. Ungar: The excitation we used in the experiments was mechanical point excitation. Similar studies have been done with acoustic excitation, possibly also turbulent. I do not recall any turbulent data.

Mr. Kirkley: I have that point straight now. My real question is, if it is an acoustical pressure fluctuation type of disturbance, your equations do not account for the acoustic energy transmitted through the panel to an interior space. This could be added in, I assume, and not affect your results.

Mr. Ungar: The equations do account for the energy that is transmitted mechanically from one panel to the other and they do account for the energy accepted for each panel. Exactly the same formulation also applies for interior space, so you add a few more lumps to represent acoustic spaces.

* * *

BLANK PAGE

CONSTANT BANDWIDTH FM DATA SYSTEM DESIGNED FOR SATURN S-IVB/V VIBRATION TESTS*

Dean F. Redford
Thiokol Chemical Corporation
Brigham City, Utah

Thiokol's Wasatch Division was awarded a contract in January 1966 to conduct vibration tests for the Douglas Aircraft Company on the forward skirt and boattail sections of the Saturn S-IVB/V launch vehicle. The extreme size of the components tested dictated the use of a large-capacity data acquisition system to insure adequate description of the response to high-force vibration excitation. A constant bandwidth FM data acquisition system capable of recording 144 channels of wideband information was designed. The tradeoff studies conducted to evaluate available techniques are discussed, and a detailed description of the constant bandwidth FM system is presented.

INTRODUCTION

The forward skirt (Fig. 1) and boattail (Fig. 2) sections of the Saturn S-IVB/V launch vehicle were subjected to vibration tests in Thiokol's high-force-vibration facility near Brigham City, Utah. The forward skirt segment is approximately 22 ft in diameter and 12 ft long. The boattail, composed of the aft skirt segment, aft LOX bulkhead and thrust structure, is approximately 22 ft in diameter and 18 ft long. The procedure and results of these tests are being fully described in another paper presented in this symposium (see L. G. Smith of McDonnell Douglas, Inc.).

Because of the massive size of the test specimens, more than 100 data acquisition channels were required to record adequately the response to vibrational forces throughout the structures. The frequency bandwidth requirement per channel for the subject tests was 0 to 500 Hz; however, use of the constant bandwidth FM technique made it possible to obtain 0- to 2000-Hz response on all channels at no increase in data system cost, and imposed no compromise on the S-IVB/V data. The only imposition on the system to achieve the wider bandwidth was an increase in magnetic tape speed from 30 to 60 ips to increase recorder bandwidth.

This paper discusses the tradeoff studies conducted to evaluate the available data acquisition techniques and presents a detailed description of the constant bandwidth system which was designed and used for the subject tests.

BASIC CONSIDERATIONS

Three basic methods are available for recording test data: (a) analog, (b) digital, and (c) FM multiplex. Considering the variations within each of these categories, a generous assortment of techniques may be exploited for data acquisition and reduction.

The analog method, while useful for many applications such as on-line monitoring and quick look, is not suitable for a multichannel vibration data acquisition system in which the capability for automatic data reduction is required. Thus, the analog technique incorporating oscillograph recorders and oscilloscopes may be selected for backup, but the mainline data system must be digital or FM multiplex.

The digital technique was considered first because digital computers and associated equipment recently have gained such popularity that they have almost eclipsed all other methods of

*This paper was not presented at the symposium.

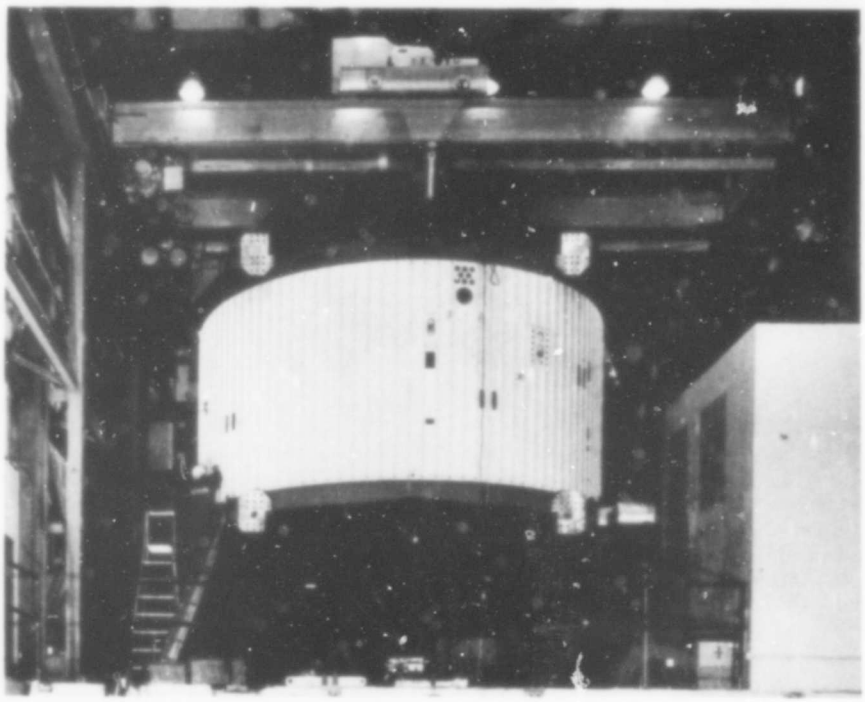

Fig. 1. Saturn S-IVB/V forward skirt section in vibration facility

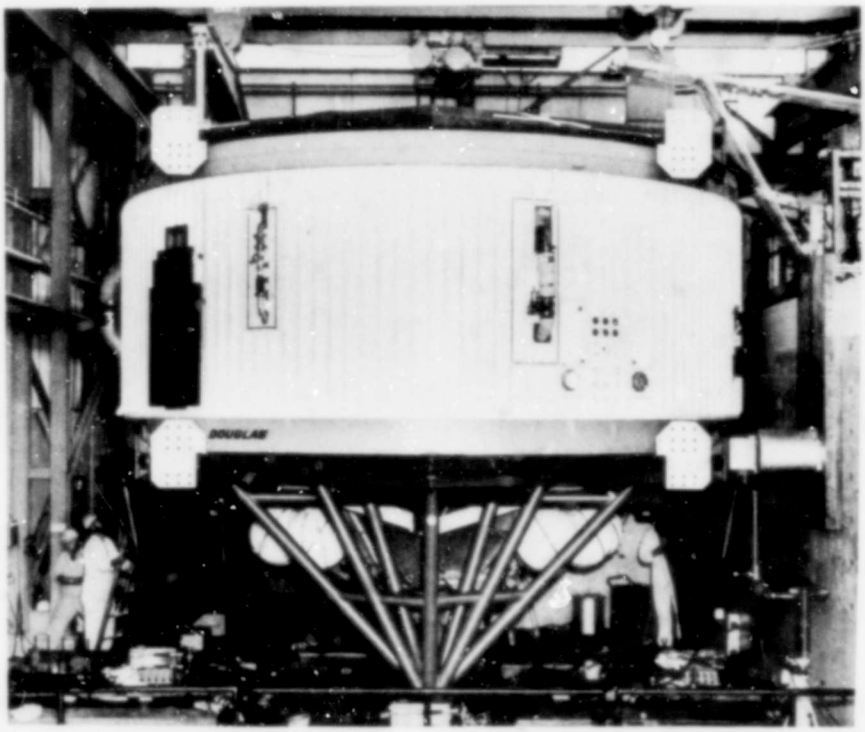

Fig. 2. Saturn S-IVB/V boattail section in vibration facility

data handling. The digital approach is desirable for many reasons, chief among which are high accuracy, low noise level, and the use of computers for data reduction. The digital computer used as a data reduction device provides virtually unlimited versatility. Through programming techniques, the computer can produce numerous types of plots from random and sinusoidal data without the necessity of modifying the data reduction system hardware.

The disadvantages of the digital approach are:

1. Time delay from program request to production of a reliable program;

2. Difficulty of determining the source of error in reduced data;

3. Problems incident to data format requirements;

4. Required data storage capacity (excessive where sample rate requirements are high, as in vibration testing).

Another data system considered was the proportional bandwidth FM system, which provides good data packing density on magnetic tape, but is limited in channel bandwidth.

Assuming a standard IRIG layout (1, Table III) for channels 1 through 19, a system can be devised to accommodate 19 channels of data on a single magnetic tape track, with frequency response from 6 to 1395 Hz. Thus, on 12 tracks, a capacity of 228 channels can be provided. However, the bandwidth restriction, while acceptable in a telemeter configuration, renders this system of limited value for vibration data acquisition.

The response restrictions of a proportional bandwidth FM system are overcome while retaining a relatively high packing density by using the constant bandwidth FM system technique. Assuming a standard IRIG layout (1, Table IV) and using 16-kHz differential frequency between carriers, the system packs up to 12 channels of wideband data on a single tape track. Again assuming 12 tape channels, a system is devised to provide 144 channels of data, a concept which offers the prospect of more nearly fulfilling the data acquisition requirements of the Saturn S-IVB/V vibration tests than the other methods investigated. One 14-channel tape recorder contains all the data on 12 tracks, allowing use of the additional tracks for system control and monitor functions such as voice annotation, shaker frequency, timing signals, and or other functions useful in the data monitoring or reduction processes.

FM SYSTEM DESCRIPTION

Systematic layout of a multichannel system is important to preclude confusion during setup thus avoiding erroneous designation of channels. With this in mind, the FM system was human engineered to provide logical groupings of 12 channels in each tape track (Fig. 3). Each 12-channel grouping is assigned a specific rack adapter position so that channels 1 through 12 in a given adapter are positioned contiguously and consecutively from left to right. Following this arrangement through the 12 sets of 12 channels in progression from top to bottom of the rack provides a layout which is at once orderly and convenient. Thus, all channels having the same center frequency are in vertical alignment throughout the rack, and all channels associated with a given tape track are in horizontal alignment from left to right in the rack. In Fig. 3, the column to the far left contains eight power supplies located strategically throughout the system — the four panels designated "B" are blank. The next 12 columns contain the 144 voltage-controlled oscillators (VCO) constituting the data input channels. The first column of this matrix contains all VCO's whose center frequency is 32 kHz, and the blocks in this column are so designated. The blocks in the succeeding columns each are designated by the appropriate VCO center frequencies. In addition to these designations, each column is identified by its channel numerical code in terms of row and column: e.g., channel 1.9 is located in row 1, column 9. The right-hand column contains 12 summing amplifiers constituting the 12 outputs of the system to the magnetic tape recorder.

An integral system calibration and monitor unit is located at approximately the vertical center of the rack for convenience in setting up and calibrating the system. To calibrate, a 12-position selector switch is used to simultaneously disconnect the input signal from a selected row of channels and connect a voltage to those channels from the calibration unit. The calibration voltage is switched manually to represent five signal levels: lower band edge, lower midrange, center (or zero), upper midrange, and upper band edge. The selected calibration signal is transmitted simultaneously to each of the 12 channels in the row or multiplex; resulting frequencies are read from test points located on the front panel of each channel using a frequency counter. An outstanding feature of this system is that any of seven input signal ranges

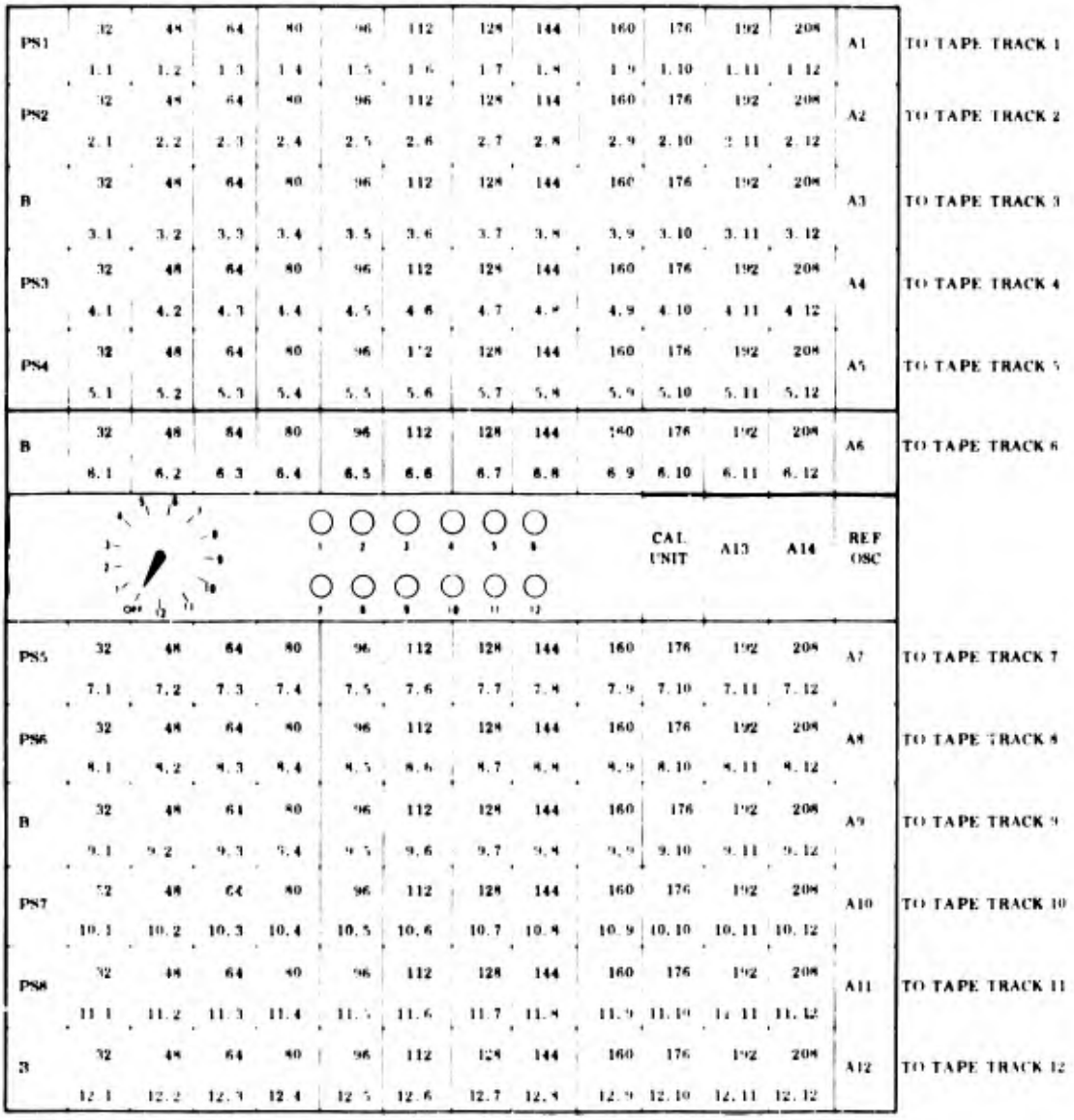

Fig. 3. FM data acquisition system layout

can be selected for full-band deviation for each channel: ±10, ±20, ±50, ±100, ±200, ±500, or ±1000 mv. Thus, the system can accommodate a wide range of input signals without requiring additional signal conditioning equipment. The input signal selector unit on each VCO provides the deviation indicated by the calibration unit, regardless of the position of the input level selector switch. This allows each channel to be set up independently for input sensitivity, regardless of its location in the system matrix. With each of the 12 channels in the first multiplex set at required sensitivity, voltage from the calibration unit causes each channel to deviate to band edge (when band edge is selected at the calibrator). After each channel in the first multiplex has been checked at upper and lower band edge (and midband if desired), the second multiplex is selected and checked in like manner. This procedure is continued until all active channels are calibrated. Each channel is reconnected to its input signal lines when the calibration selector switch is not positioned to select its multiplex. Thus, when the switch is in the OFF position, each channel is connected to its respective input signal line. Amplifiers A13 and A14 are buffers needed to eliminate loading of the calibration unit and the reference

oscillator, respectively. Twelve checkpoints are included on the monitor and calibration panel to provide quick access to the 12 multiplexed signals. The signal at this point may be viewed by oscilloscope as a multiplex, or it may be discriminated and viewed as individual analog data signals. This provides convenience in checking the data signal at the output of the system.

The technique which makes possible the multiplexing of 12 wideband channels of a given tape track is embodied in the conception of upper channel translation; i.e., the upper six center frequencies (128-208 kHz) are "translated" (heterodyned) using a 240-kHz standard frequency to beat with the carriers of these channels. Thus, 32 kHz combines with 240 kHz to generate 208 kHz and 272 kHz; through filtering, the 208-kHz value is selected and the higher value is discarded. Likewise, 48, 64, 80, 96 and 112 kHz combine with the 240-kHz standard to generate frequencies of 192, 176, 160, 144, and 128 kHz, respectively. Translation is accomplished in each instance after the basic carrier has been deviated by the intelligence or input data. This technique serves to prevent the carrier deviation ratio from diminishing to a point which makes recovery of intelligence in the discriminator difficult, if not impossible. The block diagram (Fig. 4) and frequency spectrum (Fig. 5) illustrate the system design concepts expressed above. Figure 4 shows a typical multiplex of 12 channels summed and fed to tape track 6. The six upper channels are shown with translator. The 240-kHz reference frequency is used in the translation process and is fed to tape track 6, along with the data, for future use in the detranslation process. Note that the 240-kHz reference signal is positioned well above the data frequency spectrum shown in Fig. 5, of which 208 kHz is the highest data carrier. The frequency of the reference signal is bounded by the highest data carrier and the magnetic tape bandwidth capability. Figure 5 shows that the center frequency of each channel may be deviated ±4 kHz to upper and lower band edge, and that there is an 8-kHz separation between the upper band edge frequency of one channel and the lower band edge frequency of the next higher channel. This separation represents a compromise between channel-to-channel crosstalk and frequency spectrum packing density. A further guard against data distortion is the use of a modulation index of 2, which limits the frequency to 2 kHz.

Detranslation is accomplished prior to discrimination by reversing the process employed for translation; i.e., the 240-kHz reference signal which is recorded on each tape track with the data matrix (Fig. 4) is used to translate the carrier frequencies to their pretranslated values (Fig. 6). The 240-kHz reference signal is separated from the multiplex by a reference discriminator and fed to the detranslators, where

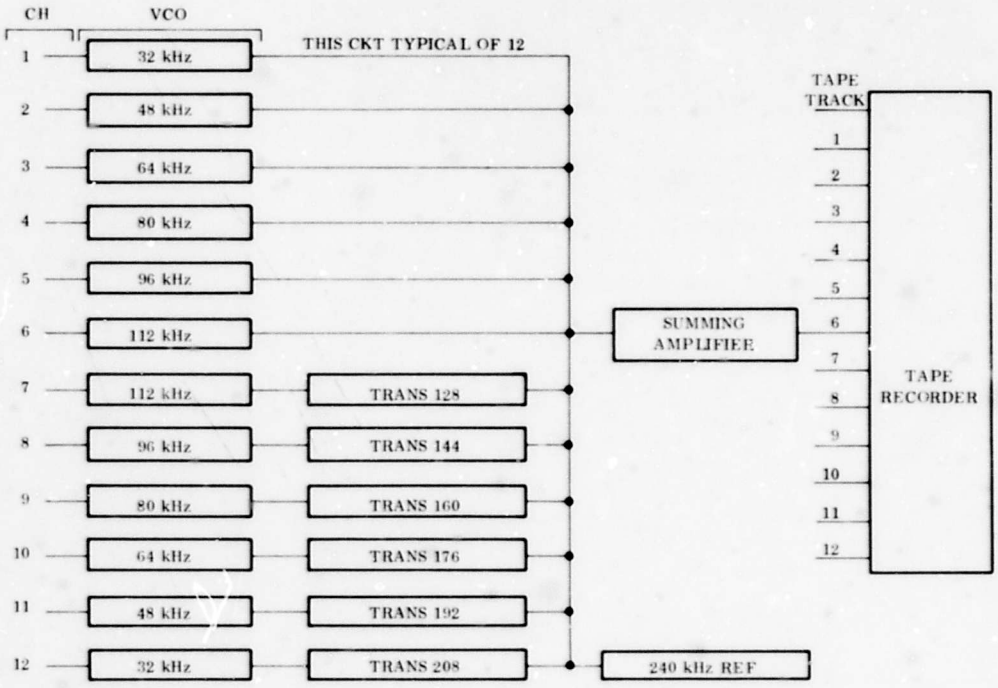

Fig. 4. FM data acquisition system block diagram

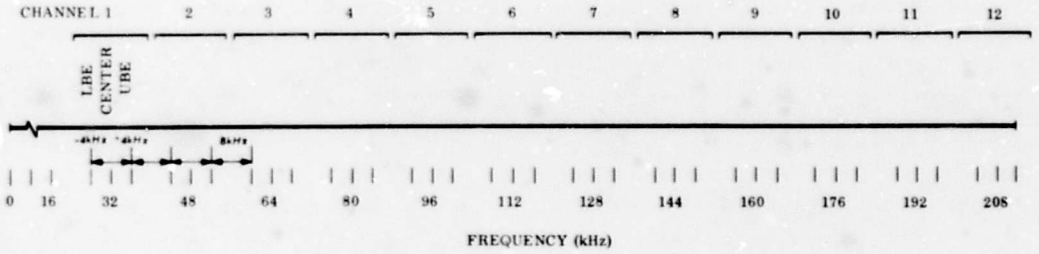

Fig. 5. FM data system frequency spectrum

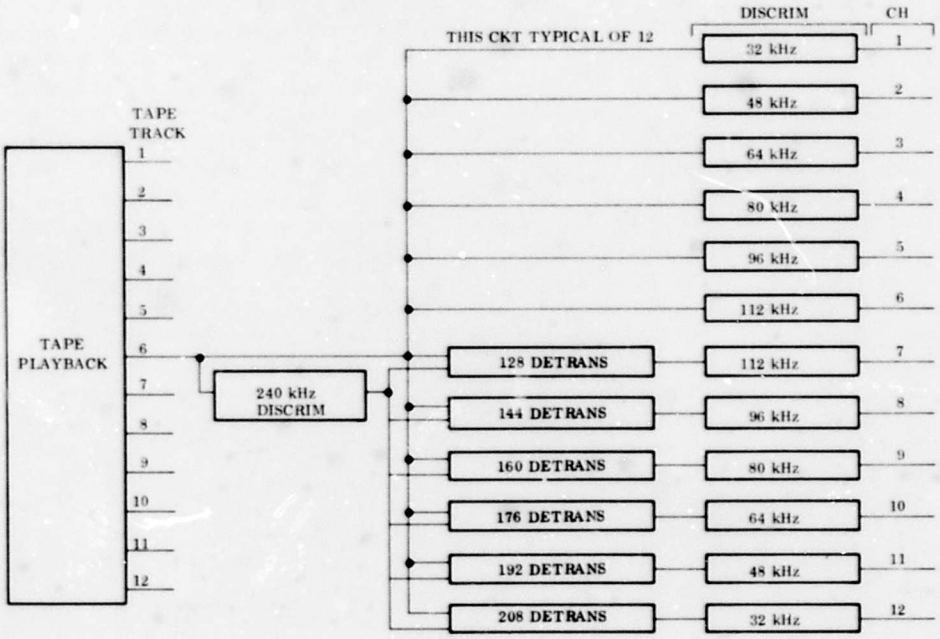

Fig. 6. Data playback system block diagram

it is used to heterodyne the translated frequencies as indicated. Each FM channel may now be discriminated to recover the original analog information. At this point, the data are fed to the oscilloscope or oscillograph for quick-look presentation, to the analog data reduction computer, or to an analog-to-digital converter for preparation for entry into a general purpose digital computer for data reduction.

The outstanding advantages of this type of data system are as follows.

1. The system provides wideband capability on each data channel.

2. Use of FM to provide multichannel packing on each tape track reduces the tape recorder requirement to a single unit for recording 144 channels, thus minimizing both tape handling and channel correlation problems.

3. Both construction and operation of the system are economical.

4. Operation is straightforward due to the systematic layout, which minimizes setup and calibration time and virtually eliminates data channel mixup.

5. The resulting data are reduced to x-y plots using rapid, low-cost data reduction methods.

6. The plots are generated efficiently in large quantities; thus there is no backlog of data awaiting reduction.

7. Recorded data may be digitized for entry into a general purpose digital computer, when special plots are required for which an analog computer is not available.

8. There is no time delay for programming the equipment.

9. It is relatively easy to determine source of error in reduced data.

10. There are no data formating problems.

11. Data storage requirements present no problem, since all data may be stored on a single 12-channel magnetic tape.

REFERENCE

1. Electromechanical Research, Inc., IRIG Telemetry Standards, April 1966, IRIG Document 106-66,

* * *

BLANK PAGE

DYNAMICS PORTION OF GEMINI AGENA TARGET VEHICLE ENGINE MODIFICATION AND TEST PROGRAM (PROJECT SURE FIRE)*

Nicholas Angelopulos
Lockheed Missiles & Space Company
Sunnyvale, California

Project Sure Fire was established to develop corrective improvements for, and demonstrate the flightworthiness of, the rocket engine designed for the Gemini Agena target vehicle; the rocket engine had failed during its first flight. There were four basic objectives for the dynamics portion of Project Sure Fire. (a) The first objective was to determine if the modified (oxidizer-lead) engine start transient dynamic characteristics are similar to or significantly different from the standard engine configuration. Dynamic measurements were recorded during acceptance testing of four YLR 81-BA-11 (standard) and three XLR 81-BA-13 (multistart) engines. (b) The second objective was to demonstrate, in shock and vibration testing of an XRM-4 engine, the structural integrity of the modified-engine installation design changes resulting from the program. (c) The third was to evaluate, in engine hot-fire tests, shock and vibration levels at specific points on the modified engine during engine start transient and ignition sequence. (d) The fourth was assessment of test results (PSD, shock spectra, rms g history, force-time plots, etc.), as well as of methods of obtaining good shock transient data (accelerometers vs strain gages).

INTRODUCTION

On November 20, 1965, following the Gemini Agena target vehicle (GATV) 5002 failure on 25 October 1965, the GATV engine modification and test program (Project Sure Fire) was established by joint action of Lockheed Missiles and Space Company (LMSC), the U.S. Air Force, Aerospace Corp., and Bell Aerospace Corp. (BAC). The program was established to develop corrective improvements for, and demonstrate the flightworthiness of, the rocket engine to assure successful missions on vehicles 5003 and those following. LMSC was technical director for the Sure Fire activity, which included subcontract effort by BAC and testing conducted at the Arnold Engineering Development Center (AEDC), Tullahoma, Tennessee.

Background

Immediately following the GATV 5002 failure, LMSC conducted an accelerated data reduction and analysis program to determine the cause. During early November 1965, flight-failure reviews were presented to the Flight Safety Review Panel, and a symposium on hypergolic rocket engine ignition at altitude was held at LMSC. The symposium was attended by 16 leading propulsion scientists and engineers representing Aerojet-General Corp., Bell Aerosystems Co., Aerospace Corp., the U.S. Air Force Rocket Propulsion Laboratory, Marquardt, Rocketdyne, Princeton University, and LMSC.

The findings and conclusions during early November were essentially: (a) the flight failure of vehicle 5002 was due to a "hard start" of the Agena primary propulsion system rocket engine; (b) the hard start was probably caused by the fuel lead into the engine thrust chamber prior to ignition (the reliable-starting standard Agena engine uses an oxidizer lead); (c) an engine modification and test program should be initiated; and (d) altitude tests must be conducted at simulated altitudes above 250,000 ft.

The combined recommendations of the study and review groups were presented by

*This paper was not presented at the Symposium.

LMSC and BAC to Air Force Space Systems Division (AFSSD), NASA, and Aerospace Corp. representatives. The final Project Sure Fire proposal was presented to NASA at Houston, Texas, on 20 November 1965. The proposal was approved and LMSC started work immediately to meet a 24 March launch date for Gemini VIII and vehicle 5003.

Objectives

There were four basic objectives for the dynamics portion of the Project Sure Fire program.

1. The first objective was that of the special engine instrumentation test program; to determine if the modified (oxidizer-lead) XLR 81-BA-13 engine start transient dynamic characteristics are similar to or significantly different from the standard YLR 81-BA-11 engine configuration. Dynamic measurements were recorded during acceptance testing of four YLR 81-BA-11 and three XLR 81-BA-13 engines at BAC (test cell H-2). For the YLR 81-BA-11 engines, there were two 60-sec firings; for the XLR 81-BA-13 engines, there were three 2-sec and two 60-sec firings.

2. The second objective was to demonstrate, in shock and vibration testing of an XRM-4 engine, the structural integrity of the modified engine installation design changes resulting from the program.

3. The third objective was to evaluate, in engine hot-fire tests, shock and vibration levels at specific points on the modified engine during engine start transient and ignition sequence.

4. The fourth objective was assessment of significant test results (PSD, shock spectra, rms g history, force-time plots, etc.), as well as methods of obtaining good shock transient data (accelerometers vs strain gages).

SPECIAL INSTRUMENTATION TESTS

Test Configuration

The test articles were production engines acceptance tested in the horizontal attitude at sea-level environment. The engine nozzle extension was replaced with a mass simulator used for engine thrust chamber gimbaling and for thrust chamber operation at sea-level atmospheric pressure. Engine configurations were in accord with the normal YLR 81-BA-11 and XLR 81-BA-13 acceptance test requirements of the respective model specifications [1].

Acceleration, force, and pressure measurements were recorded at the following locations, shown graphically in Fig. 1:

Accelerometers

Thrust chamber thrust lug - longitudinal (A-1)
Thrust chamber thrust lug - yaw (A-2)
Thrust chamber thrust lug - pitch (A-3)
Gimbal ring assembly - longitudinal, top (A-4)
Gimbal ring assembly - longitudinal, bottom (A-5)
Thrust mount structure - longitudinal, left gimbal (A-6)
Thrust mount structure - longitudinal, right gimbal (A-7)
Thrust mount structure - longitudinal, actuator top (A-8)
Thrust mount structure - longitudinal, actuator side (A-9)
Gas generator - parallel to geometric axis of generator near injector head (A-10)
Engine test rig - longitudinal (A-11)
Engine test rig - pitch (A-12)
Electronic gate box - longitudinal, in rigid area near engine attachment point (A-13)
Pressure switch relay box - longitudinal (A-14)

Thrust

Engine thrust at the four thrust mount attachment points, LC-1 through LC-4

Pressure

Engine oxidizer injector pressure
Engine thrust chamber pressure

Test Results

Test results are presented in Tables 1 and 2. Table 1 is a summary of all the vibration, force, and pressure data obtained during engine acceptance testing. Model XLR 81-BA-13 engines (803, 806, and 807) were acceptance tested early in the Sure Fire program; therefore, some of the accelerometer data (accelerometers 2 through 5, 8, and 9) were not acquired during the initial tests. Using accelerometer A-1 (mounted on the thrust chamber lug) as a reference accelerometer, the following minimum and maximum peak g's were noted during YLR 81-BA-11 and XLR 81-BA-13 engine firings:

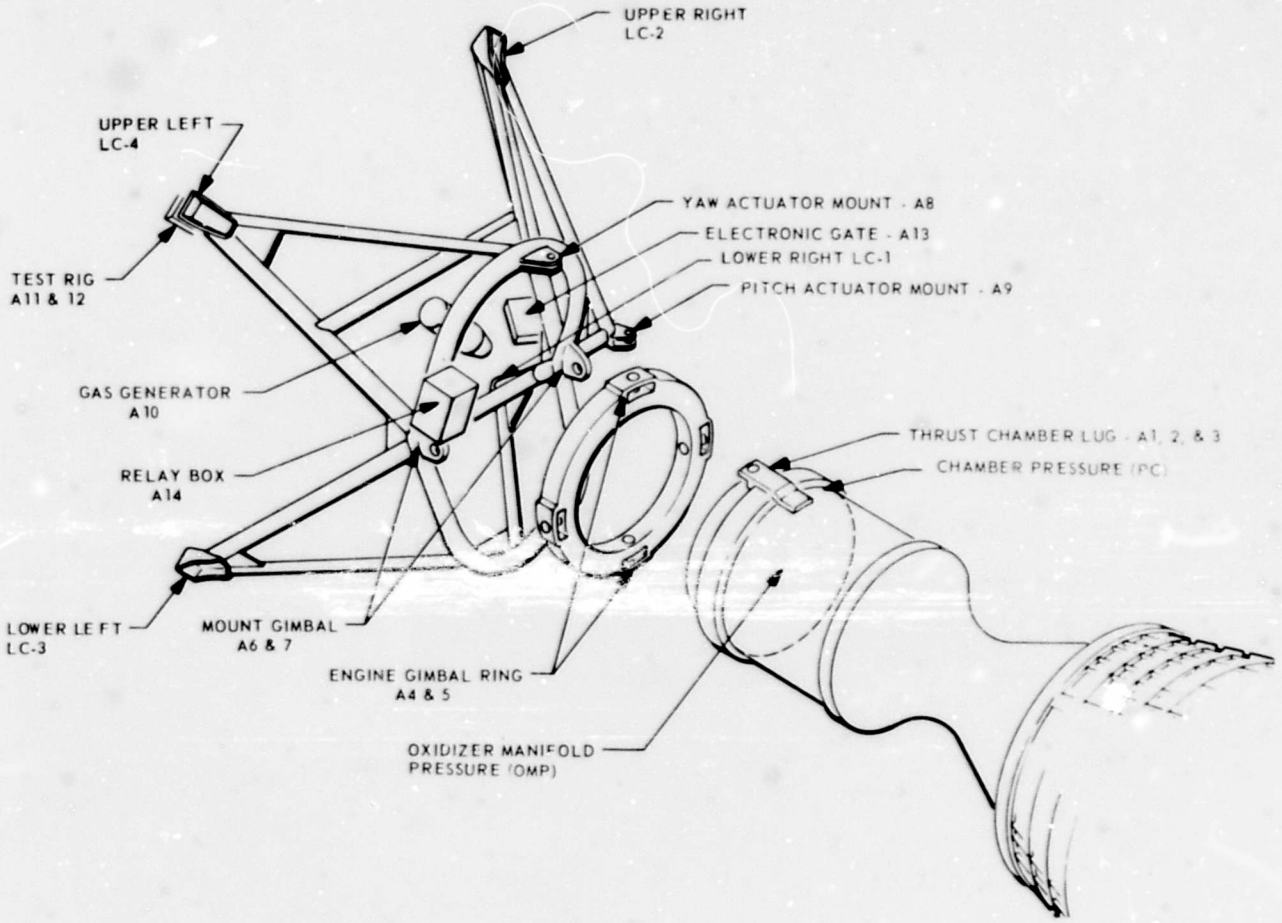

Fig. 1. Locations of dynamic measurements

TABLE 1
Engine Test Dynamic Data

Engine Model	YLR 81-BA-11						XLR 81-BA-13														
Serial Number	707		708		709		803		806		807		803			806			807		
Run Duration (sec)	60	60	60	60	60	60	60	60	60	60	60	60	2	2	2	2	2	2	2	2	2
Accelerometer	Peak g at Thrust Chamber Ignition																				
A-1	37	21	28	8	28	17	25	34	22		20	23	30	37	40				14	19	22
A-2	40	13	9	17	13	13	–	–	–	–	–	–	–	–	–	–	–	–	–	–	–
A-3	21	9	7		15	10	–	–	–	–	–	–	–	–	–	–	–	–	–	–	–
A-4	28	6	18	8	35	21	–	–	–	–	–	–	–	–	–	–	–	–	–	–	–
A-5	22	10	26	10	37	19	–	–	–	–	–	–	–	–	–	–	–	–	–	–	–
A-6	44	14	13	6	17	15	14	18	14	21	17	14	17	19	17	11	18	14	8	13	9
A-7	61	15	17	8	21	23	17	15	11	10	21	12	14	17	16	11	14	14	13	12	10
A-8	81	21	16	13	22	17	–	–	–	–	–	–	–	–	–	–	–	–	–	–	–
A-9	81	53	32	13	17	15	–	–	–	–	–	–	–	–	–	–	–	–	–	–	–
A-10	94	64			153	113	54	68	34	74	49		51	78	55	42	37	36			
A-11	8	2	9	9		7	–	–	–	–	–	–	–	–	–	–	–	–	–	–	–
A-12	13	3	3	3		5	–	–	–	–	–	–	–	–	–	–	–	–	–	–	–
A-13	–	–	–	–	–	–	18	11	19	18	23	16	15	17	14	17	16	15	14	17	19
A-14	–	–	–	–	–	–	15	17	9	15	30	27	15	15	14	8	13	13	20	28	30
Average[a]	49	23	18	9	36	26	24	27	18	28	27	18	24	30	26	18	20	18	14	18	18
Load Cell	Pounds Force																				
1	2,078	1,075	–	–	1,515	1,522	–	–	2,250	2,300	2,620	2,735	–	–	–	2,085	2,360	2,140	2,280	2,400	2,320
2	3,631	2,500	–	–	1,698	2,280	–	–	2,690	3,040	2,695	3,310	–	–	–	2,900	2,810	2,850	2 710	3,180	3,001
3	3,682	2,535	–	–	1,551	1,940	–	–	2,865	2,910	3,250	3,552	–	–	–	3,070	2,870	2,910	3,220	3,425	3,220
4	2,245	–	–	–	–	–	–	–	2,560	2,600	2,630	2,820	–	–	–	2,475	2,220	2,600	3,285	3,385	3,210
Total	11,636	–	–	–	–	–	–	–	10,365	10,850	11,195	13,417	–	–	–	10,530	10,260	10,500	11,495	12,390	11,751
Pressure Transducer	Psia																				
OMP	–	–	–	–	–	–	625	665	532	562	627	560	561	674	657	582	606	577	648	606	506
PC	321	321	468	355	453	349	440	424	484	447	425	450	407	424	433	439	453	442	375	425	375

Note. -- Blank indicates no data above the noise level; dash indicates no data because of instrumentation discrepancies or low acceleration levels.

[a]Does not include accelerometers 11 and 12.

TABLE 2
Power Spectral Density Data for YLR 81-BA-11 and XLR 81-BA-13 Engines

Engine Model	YLR 81-BA-11			XLR 81-BA-13	
Serial Number	707	708	709	803	806
Accelerometer Locations	rms g				
A-1 – TC lug, longitudinal	9	8	10	–[a]	–[a]
A-4 – Gimbal ring, top	6	4	3	–[b]	–[b]
A-6 – Thrust mount, left gimbal	–[c]	–[c]	–[c]	3	3
A-7 – Thrust mount, right gimbal	–[c]	9	11	2	3
A-8 – Thrust mount, act. top	–[c]	–[c]	20	–[b]	–[b]
A-9 – Thrust mount, act. side	28	22	–[c]	–[b]	–[b]
A-10 – Gas generator	17	–[a]	25	6	8
A-11 – Engine test rig, long.	7	6	–[c]	–[b]	–[b]
A-13 – Electronic gate	–[d]	–[d]	–[d]	8	3
A-14 – Pressure switch relay box	–[d]	–[d]	–[d]	3	3

[a]Poor data, not analyzed.
[b]Accelerometers were not mounted at these locations on engines 803 and 806.
[c]These accelerometer data were not analyzed.
[d]Not on YLR 81-BA-11 engines.

YLR 81-BA-11 engines: minimum – 8 g, maximum – 37 g
XLR 81-BA-13 engines: minimum – 14 g, maximum – 40 g

The load cell data at ignition for a nominal run of the YLR 81-BA-11 engine show 11,636 lb, compared to a nominal of 11,896 lb for the XLR 81-BA-13 engine. The load cell data for YLR 81-BA-11 engine 708 were not considered valid because of load cell calibration inaccuracies. The thrust chamber ignition pressure (P_c) measurements of the YLR 81-BA-11 and XLR 81-BA-13 engines agreed quite well. The oxidizer manifold pressure (OMP) gage was saturated during YLR 81-BA-11 engine firings, and a valid comparison was not possible; however, the XLR 81-BA-13 engine OMP transient data evaluation indicated no adverse pressure peaks.

Table 2 shows the results of the power spectral density (PSD) data. The data show a spread of 0.7 g rms measured at the test rig to 28 g rms at the thrust mount actuator side.

Figures 2 through 6 are typical PSC plots of the YLR 81-BA-11 and XLR 81-BA-13 engine firings. The area under the curves of Figs. 2 through 6 represent rms g and is equal to:

$$\text{rms g} = \left[\int_{f_1}^{f_2} G_0 \, df\right]^{1/2},$$

where G_0 = density (g^2/cps), and f = frequency (cps).

The PSD analyses were made approximately 0.4 sec after thrust chamber ignition. The PSD plots show distinct peak g (rms) values at frequencies around 900, 1600, and 1800 cps. Most of the energy represented by the area under each of the PSD plots occurs at these frequencies. These frequencies correlate with the oxidizer and fuel pump impeller blade rotational frequencies of 960 cps for the oxidizer pump and 1690 cps for the fuel pump at steady state turbine speed. The predominant 1800-cps frequency point is the first harmonic of the 900-cps frequency.

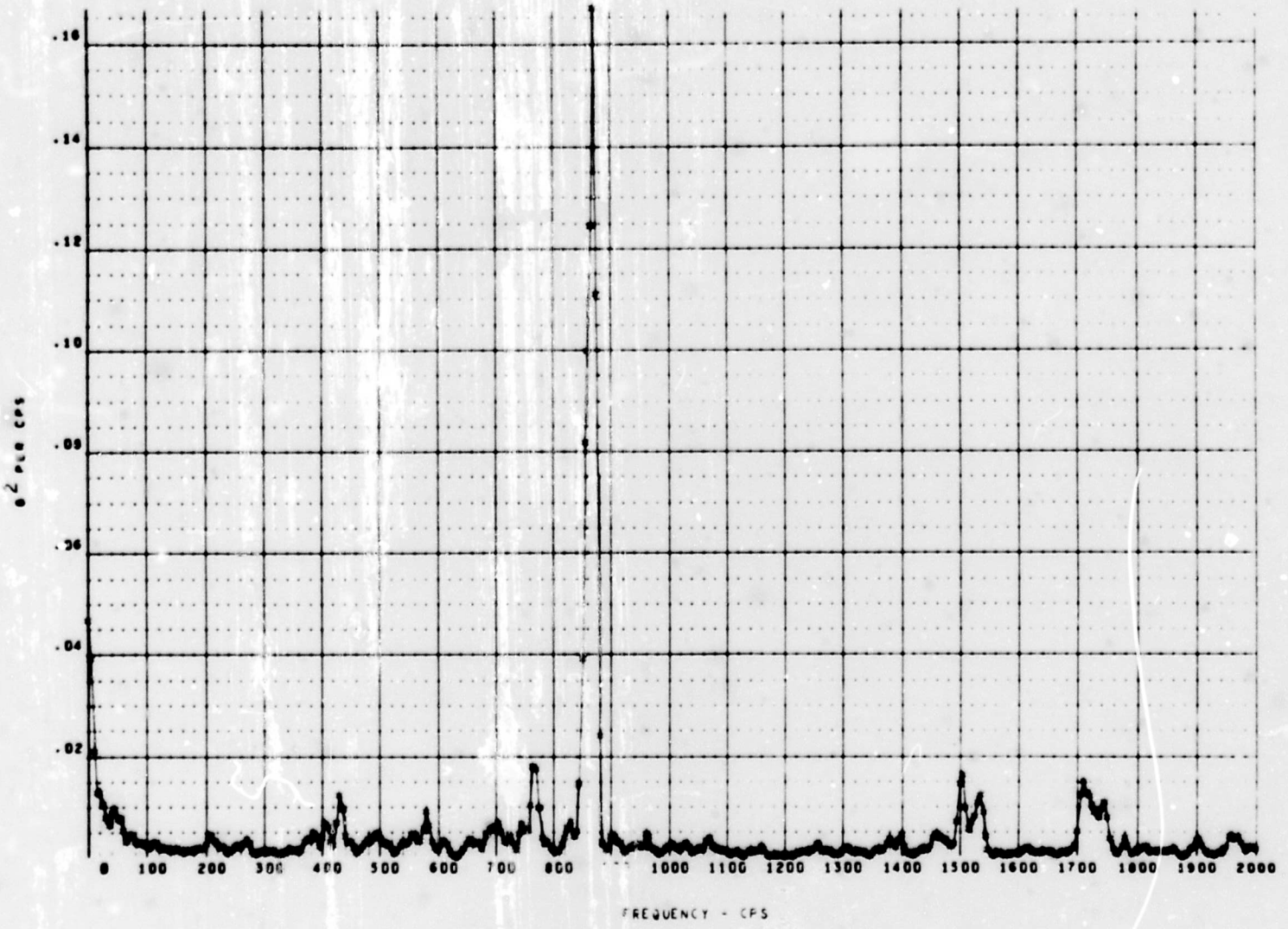

Fig. 2. PSD plot, XLR 81-BA-13 engine 803, test 435: accelerometer 6; approx. 0.4 sec after thrust chamber ignition (phase A start); rms value 3.21 g; interval, 0.5 sec

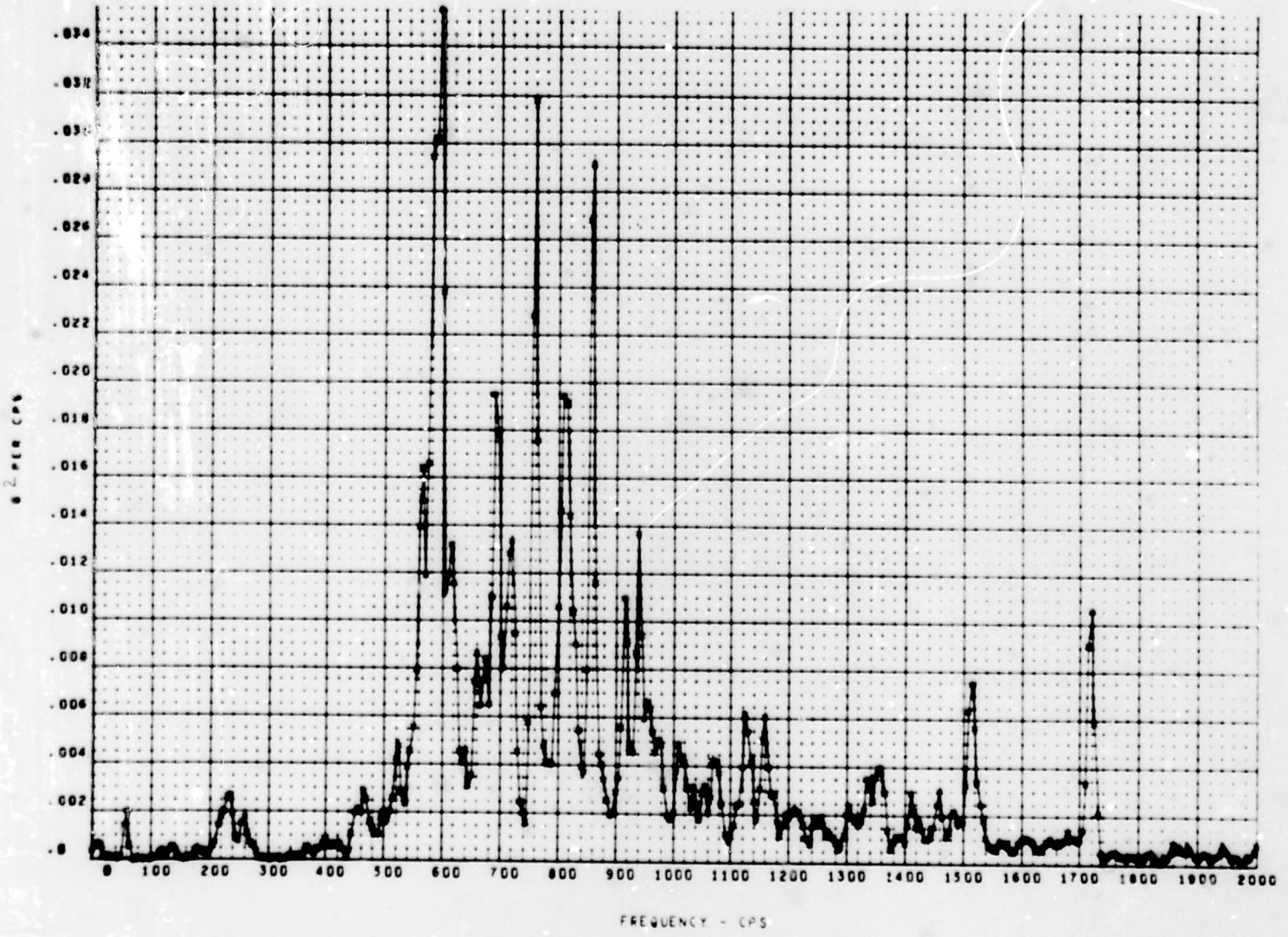

Fig. 3. PSD plot, XLR 81-BA-13 engine 806, test 436: accelerometer 13; approx. 0.4 sec after thrust chamber ignition (phase A start); rms value 2.81 g; interval, 0.5 sec

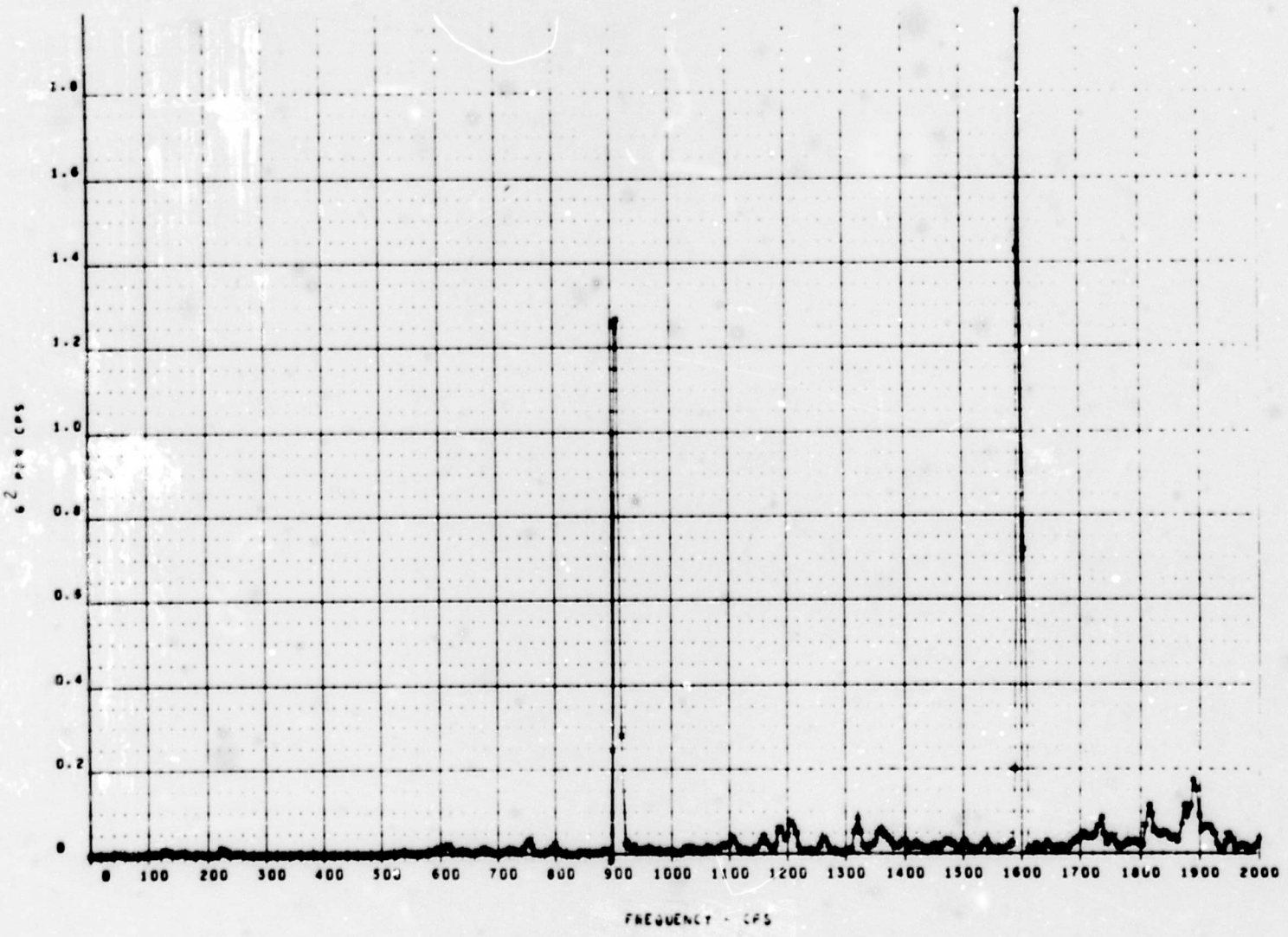

Fig. 4. PSD plot, YLR 81-BA-11 engine 707, test 438: accelerometer A-1; approx. 0.4 sec after thrust chamber ignition (phase A start); rms value 8.72 g; interval, 0.5 sec

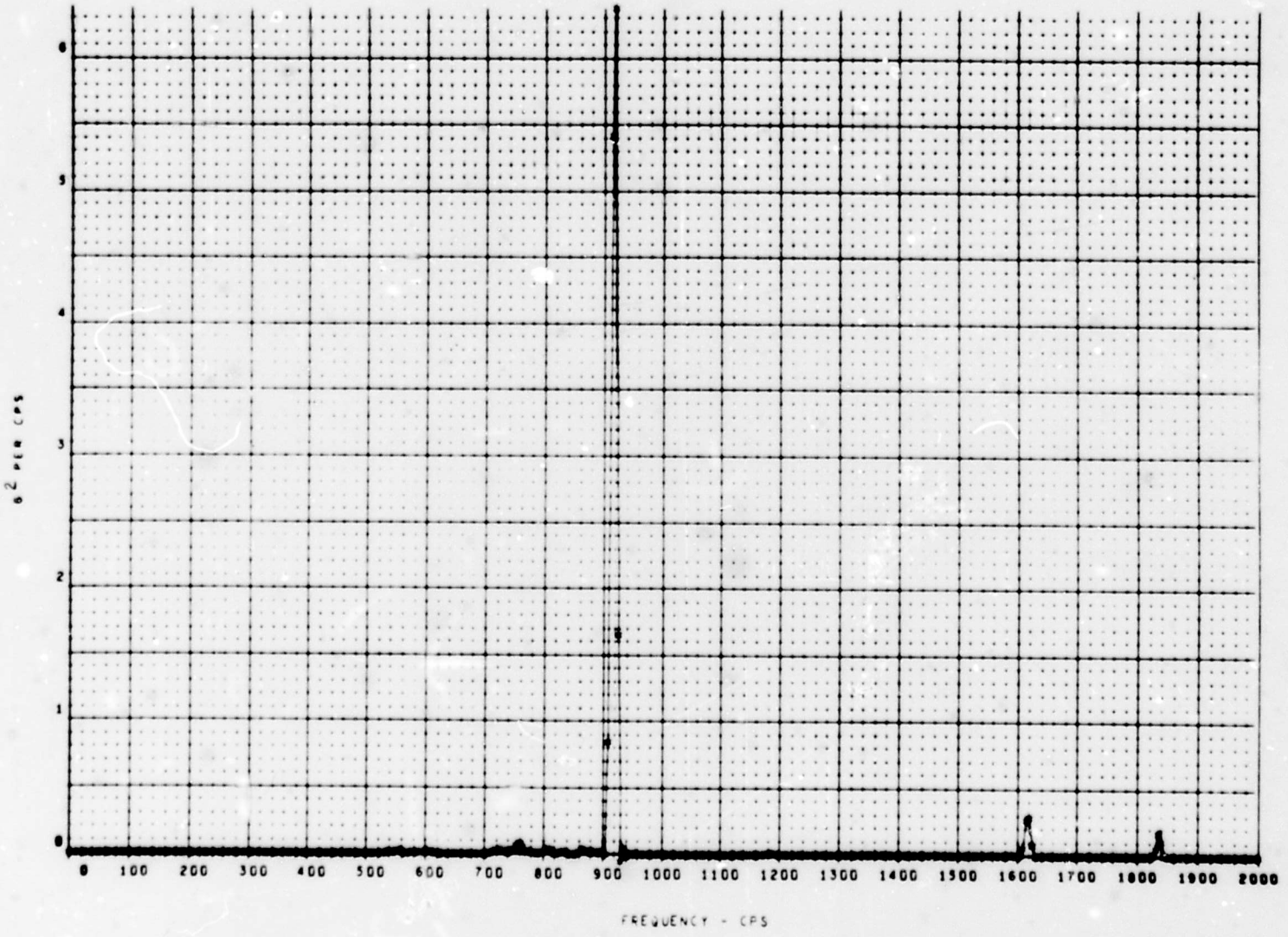

Fig. 5. PSD plot, YLR 81-BA-11 engine 708, test 439: accelerometer A-7; approx. 0.4 sec after thrust chamber ignition (phase A start); rms value 9.40 g; interval, 0.5 sec

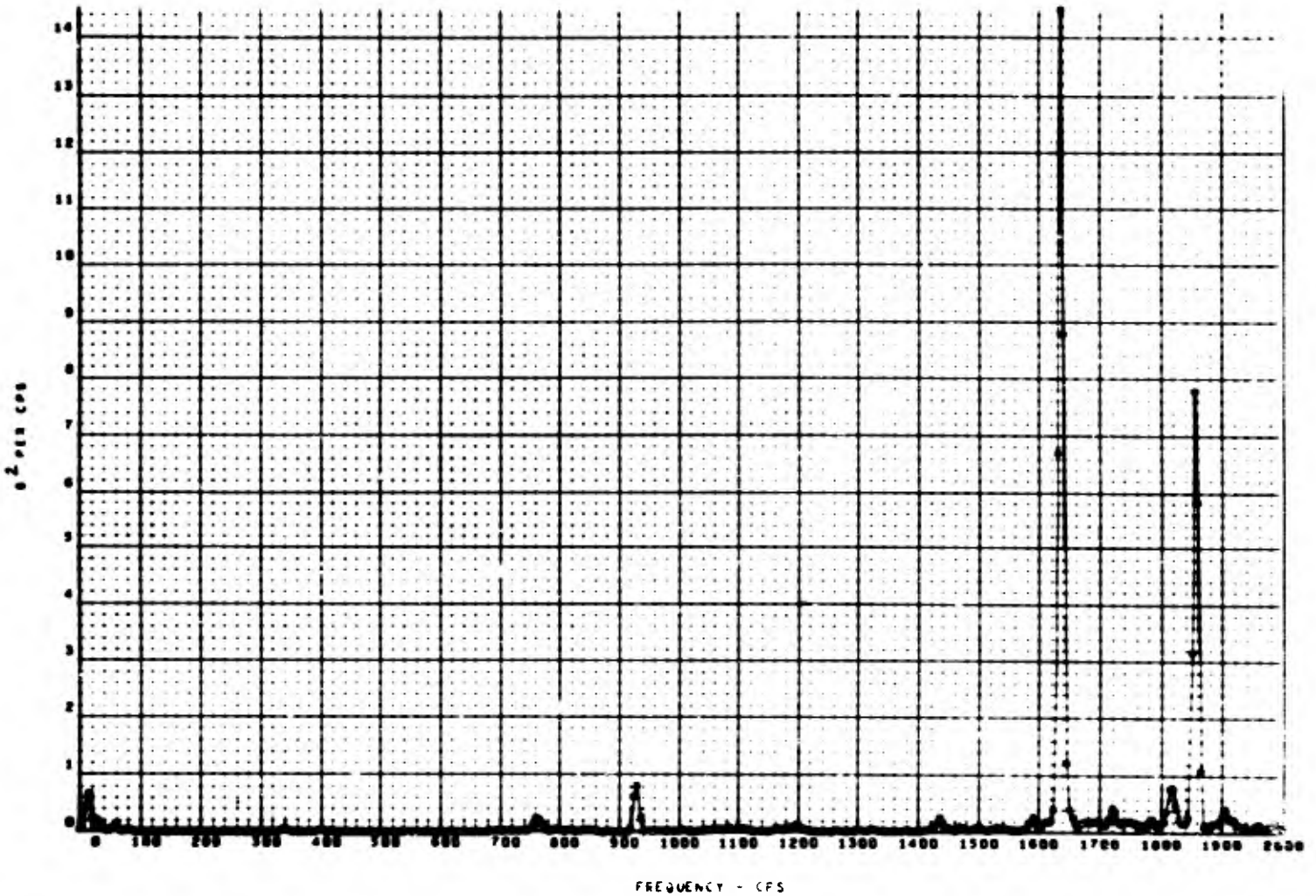

Fig. 6. PSD plot, YLR 81-BA-11 engine 709, test 440: accelerometer A-8; approx. 0.4 sec after thrust chamber ignition (phase A start); rms value 19.91 g; interval, 0.5 sec

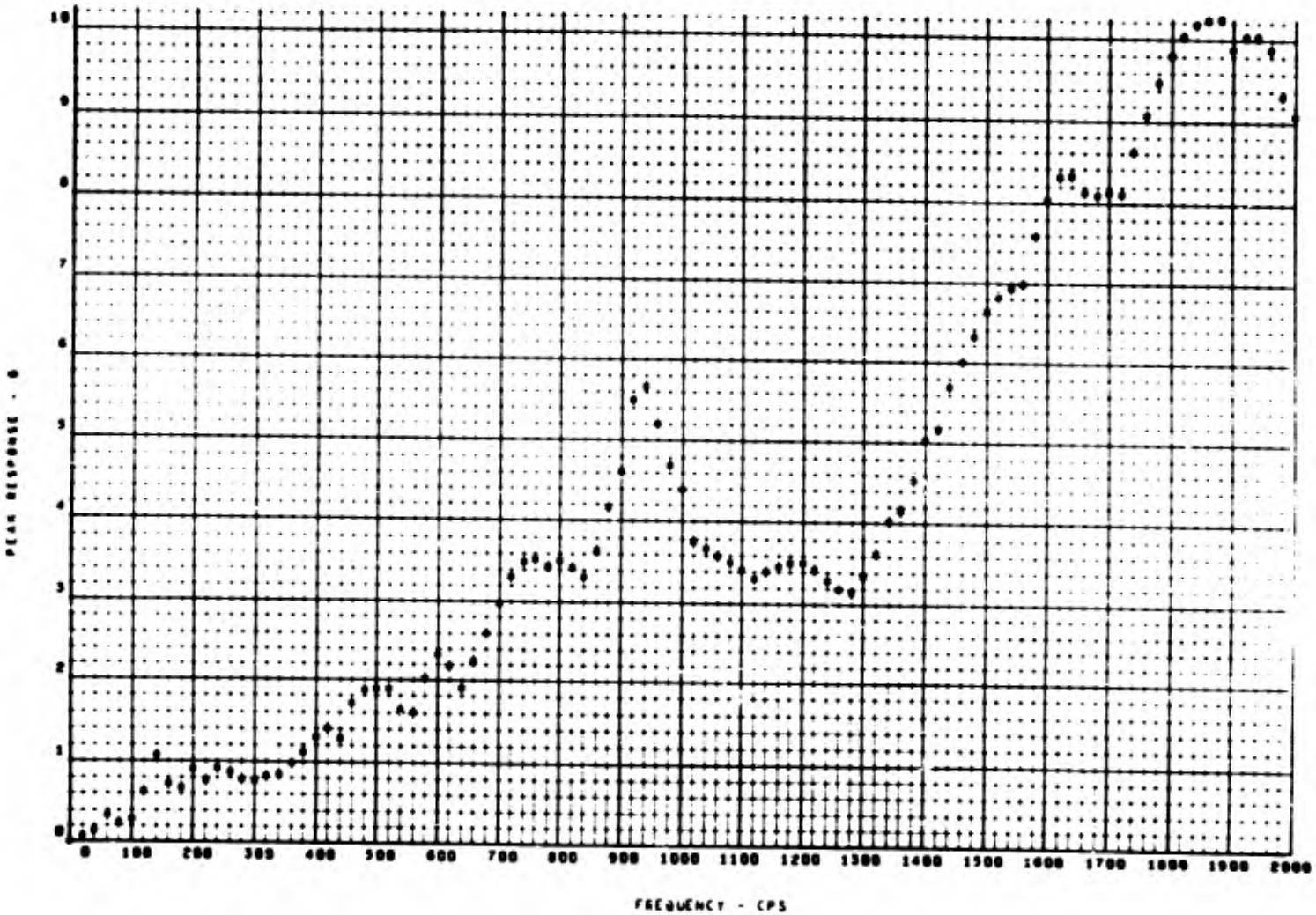

Fig. 7. Shock spectral analysis, engine 707, test 438: accelerometer A-11; thrust chamber ignition (phase A start)

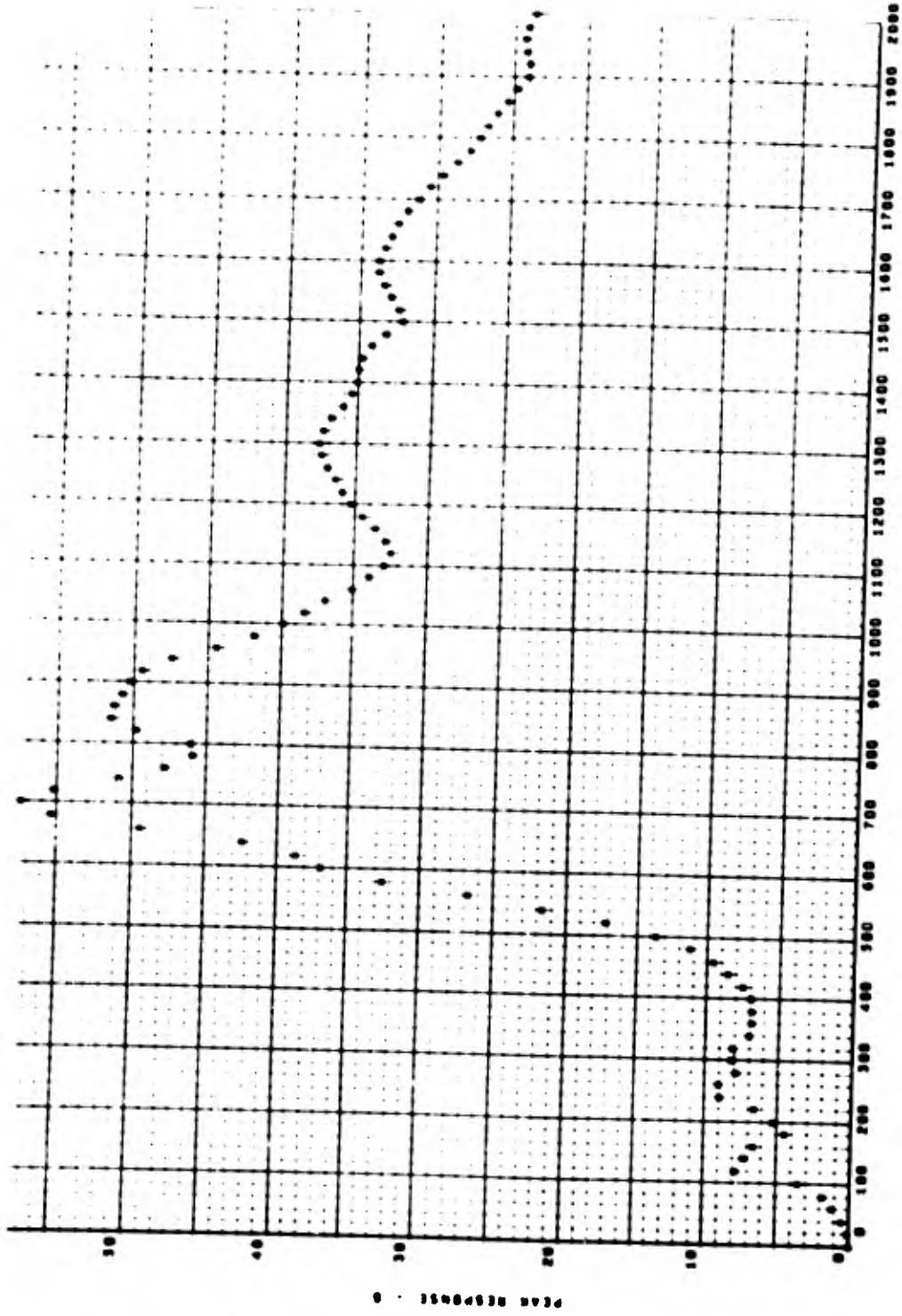

Fig. 8. Shock spectral analysis, engine 708, test 439: accelerometer A-1; thrust chamber ignition (phase A start)

Figures 7 and 8 are typical shock spectral plots showing the analysis of the accelerometer data from accelerometers A-11 for engine 707 and A-1 for engine 708. The data were reduced using an amplification factor (Q) equal to 10 where damping (') would be 0.05 from the following equation:

$$Q \quad \frac{1}{2'}$$

Damping of 0.05 is considered nominal in the Agena structure; however, sufficient data are not available to determine the damping on the BAC facility thrust stand installation. If any peak response g value is divided by the amplification factor (in this case Q = 10), it would represent the g value for steady-state vibration at that particular frequency. Figure 8 shows a peak reading of 57.5 g occurring at 700 cps. This would represent 5.75 g of steady-state vibration. The shock spectral analyses were made during the thrust chamber ignition period. The typical shock spectral plots (Figs. 7 and 8) for the YLR 81-BA-11 engine show that the peak response g levels at their resonant frequencies are within the test requirements of LMSC 6117D [1]. The dubbed tape data for the XLR 81-BA-13 engine firings were not adequate for shock spectral analysis. A dynamic analysis of the data in Table 1 indicates that the shock spectra for the XLR 81-BA-13 engine are similar to those for the YLR 81-BA-11 engine, with the possible exception of frequency content because of the difference in engine masses.

Conclusions

The data contained in Tables 1 and 2 do not indicate any significant difference in engine start transient shock severity between the YLR 81-BA-11 and XLR 81-BA-13 engines when fired at ground level. The Table 1 levels were reduced during the main engine ignition period and, therefore, generated the maximum g levels during each firing. The shock transient levels obtained during the hard-mounted engine tests at BAC compare favorably with the 40-g, 8-msec test requirements of LMSC 6117D [1] for Agena vehicle component installations.

One run of the 21-engine acceptance test produced a peak g level of 49 for a duration of approximately 3 msec. The average peak acceleration levels at ignition were less than 40 g on the remaining 20 tests. Evaluation of the steady-state vibration levels indicates that the levels were lower than the test levels specified in LMSC 6117D. During the flight operation the modified, oxidizer-lead, multistart engine is not expected to generate ignition shock levels significantly different in magnitude and character from the standard YLR 81-BA-11 engine.

ENGINE XRM-4 DYNAMIC TESTS — VIBRATION AND SHOCK

Vibration and shock flightworthiness demonstration tests were conducted at BAC laboratories to demonstrate the structural integrity of the modified engine installation design changes resulting from Project Sure Fire.

Test Plan

The installation design change of the XLR 81-BA-13 engine components was incorporated into the XRM-4 rocket engine assembly to simulate the structural mass, inertia, and dynamic characteristics of a production engine. The modified rocket engine assembly was subjected to the following tests as ordered: functional test, shock, visual inspection, functional test, vibration, visual inspection, and functional test.

The engine test assembly was vibrated along its longitudinal axis at a constant octave sweep rate for a total duration of 45 min. Input was at the engine mount attachment points in accordance with the following schedule:

5 to 10 cps at 0.25-in. amplitude
10 to 16 cps at 2.0 g peak
16 to 22 cps at 3.0 g peak
22 to 100 cps at 2.0 g peak
100 to 250 cps at 3.0 g peak
250 to 500 cps at 5.0 g peak

The engine test assembly was vibrated along its lateral and vertical axes at a constant octave sweep rate for a total duration of 45 min in each axis. Input at the engine mount attachment points accorded with the following schedule:

5 to 6.5 cps at 0.25-in. amplitude
6.5 to 100 cps at 1.0 g peak
100 to 250 cps at 2.0 g peak
250 to 500 cps at 4.0 g peak

Input at the turbine exhaust duct tab accorded with the following schedule:

5 to 6.5 cps at 0.25-in. amplitude
6.5 to 60 cps at 2 g peak
60 to 100 cps at 3.5 g peak
100 to 250 cps at 4.0 g peak
250 to 400 cps at 5.0 g peak

The engine test assembly was shock tested three times in the plus and three times in the minus direction of each of the three mutually perpendicular axes; test duration was 6 msec; level was 25 g for the longitudinal axis, 5 g for the lateral and vertical axes.

Test Configuration

The XRM-4 engine consisted of a hard mockup with mass-simulated nonfunctional parts. The functional hardware used was peculiar to the Project Sure Fire modification, since all other hardware had been previously subjected to preliminary flight rating tests (PFRT) in accordance with engine specification requirements. The sinusoidal vibration test of the engine was conducted in accordance with current LMSC engine test requirements. Figures 9 and 10 show the test article in typical setups for conducting the vibration and shock tests, respectively. Table 3 shows the location, orientation, and type of accelerometer used for the vibration and shock tests.

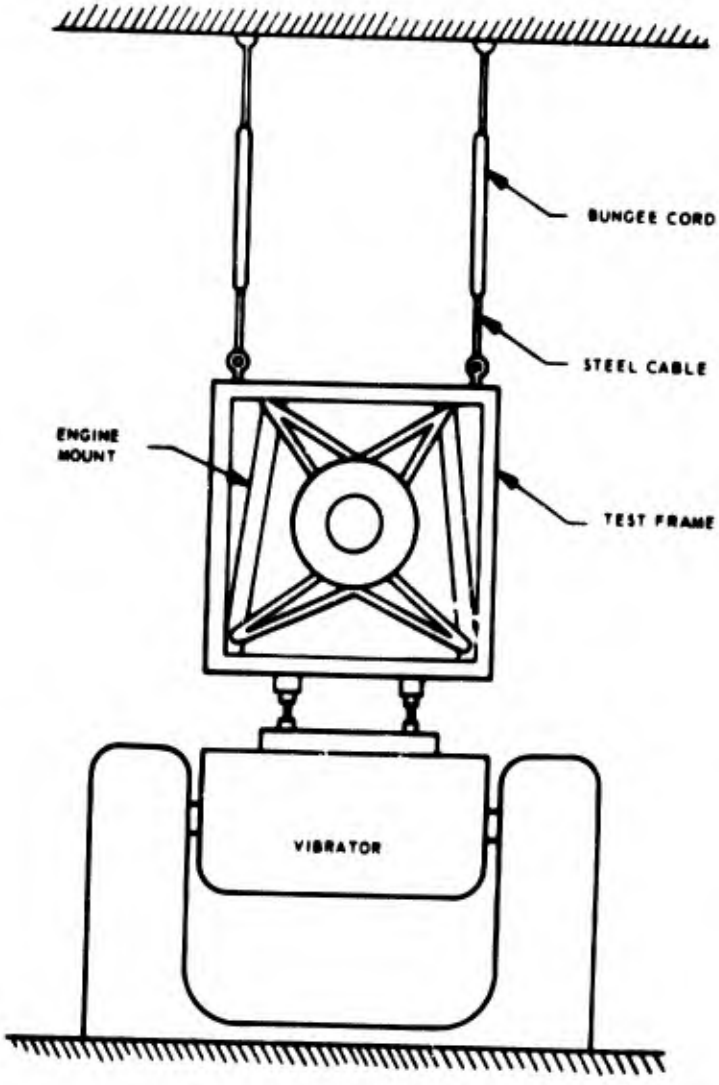

Fig. 9. Typical vibration test setup

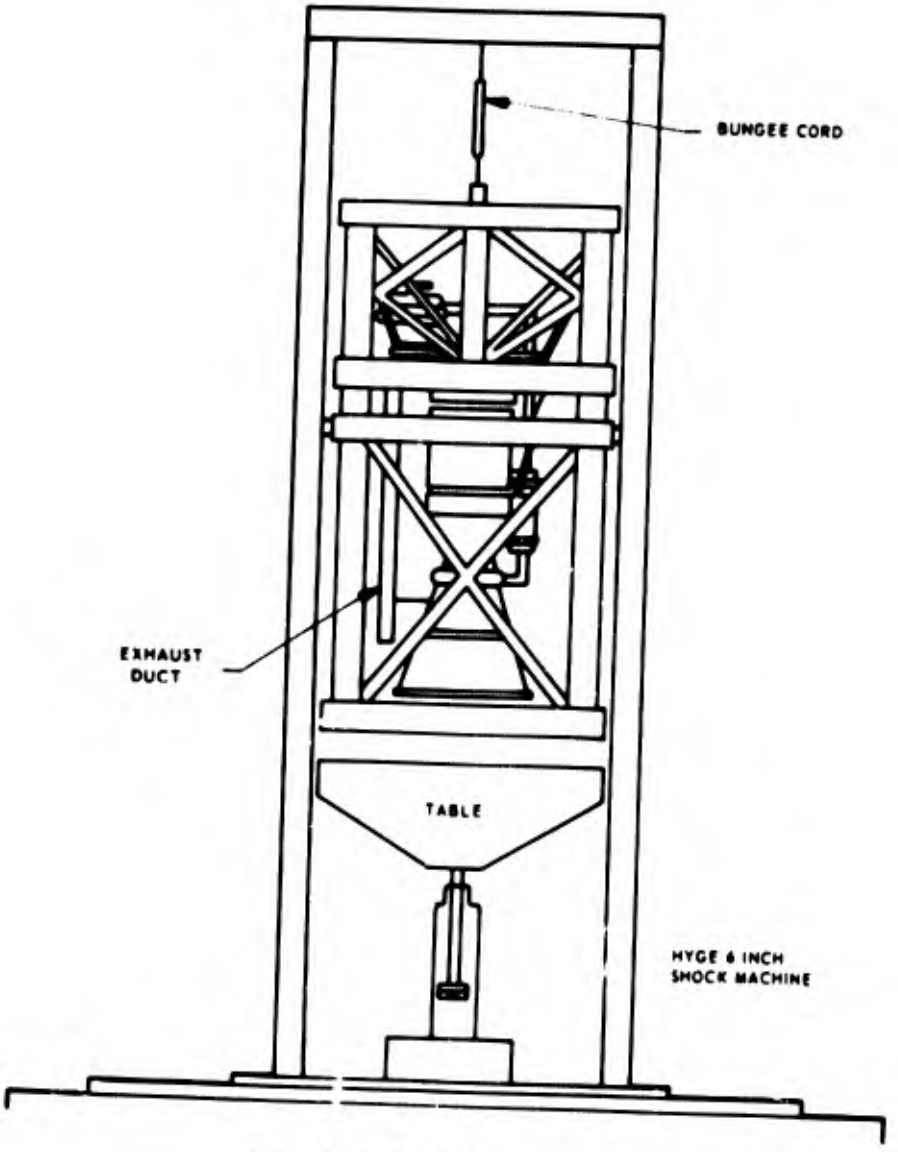

Fig. 10. Typical shock test setup

TABLE 3
Accelerometer Locations for Vibration and Shock

Acceler-ometer	Location	Orientation	Type
1	Electronic gate	Axis of vibration or direction of shock	Endevco 2226
2	Electronic gate mount		
3	Pressure switch relay box		
4	Pressure switch relay box mount		
5	Fuel start tank		
6	Oxidizer start tank		
7	OMP switch		
8	OMP switch mount		
9	OFP switch		
10	OFP switch mount	Axis of vibration or direction of shock	Endevco 2226
11	Thrust chamber lug	Longitudinal axis	Endevco 2242C with 2985 MI stud
12	Thrust chamber lug	Vertical axis	Endevco 2226
13	Thrust chamber lug	Lateral axis	
14	Gimbal ring – top	Longitudinal axis	
15	Gimbal ring – bottom		
16	Engine mount gimbal lug – left		
17	Engine mount gimbal lug – right		
18	Engine mount actuator lug – top		
19	Engine mount actuator lug – side		Endevco 2226
20	Thrust chamber lug	Longitudinal axis	Endevco 2242C with 2985 MI stud
21	Gas generator injector	Axis of injector	Endevco 2226
22	Test fixture near upper left mount	Longitudinal axis	
23	Test fixture near upper left mount	Lateral axis	
24	Gas generator solenoid valve mount	Axis of vibration (not required for shock)	
25	Fuel dual check valve	Axis of vibration (not required for shock)	
26	Oxidizer dual check valve	Axis of vibration (not required for shock)	Endevco 2226

Test Results

A resonant frequency search of the engine test fixture disclosed resonant points with transmissibility values ranging from less than 1.0 to approximately 9.1 to 1, which could yield overtest or undertest at certain frequencies. Rework of the fixture or fabrication of a new fixture was waived because of schedule limitations. To compensate for the fixture resonant frequencies, and possible overtest or undertest, a triaxial accelerometer was used for input control. The accelerometer used the total vector sum from each sensing element to control the shaker input.

Testing along the three axes of vibration was conducted with no structural or functional failures of the engine hardware, as demonstrated by posttest functional checks and inspection. The vibration test results are listed in Table 4.

Posttest inspection and functional checks revealed that no structural or functional anomalies occurred as a result of the shock tests. Figure 11 is typical shock photographs taken of the shock input pulses during the shock tests. Table 5 shows the results of the response accelerometers during each shock test.

LONGITUDINAL AXIS, 25.0g - 6.0 MS

LATERAL AXIS, 5.0g - 5.8 MS

VERTICAL AXIS, 4.7g - 6.4 MS

Fig. 11. Shock test inputs

TABLE 4
Vibration Data from Response (Output) Accelerometers

Tests	Longitudinal Axis		Lateral Axis		Vertical Axis	
	Sine Survey	Sine Test	Sine Survey	Sine Test	Sine Survey	Sine Test
Accelerometer	Vector (g)					
11	3.6	11.8	4.9	12.5	1.6	3.5
12	2.4	18.6	2.7	15.5	2.8	4.6
13	2.4	15.2	2.3	5.9	5.2	5.0
14	4.1	29.1	2.4	6.8	7.0	13.5
15	—	10.6	—	10.4	—	4.0
16	2.7	10.0	1.7	6.5	10.3	5.5
17	2.3	17.8	2.4	5.8	12.4	6.2
18	1.5	9.5	7.2	25.7	14.6	20.5
19	2.0	10.0	2.7	5.9	7.5	6.3
20	2.6	23.0	2.5	11.5	5.4	2.3
21	—	24.4	—	6.8	—	9.0
22	3.0	16.2	1.3	8.0	1.9	7.1
23	0.95	7.2	1.5	6.2	4.9	5.0

TABLE 5
Shock Data from Response (Output) Accelerometers

Tests	Longitudinal Axis						Lateral Axis						Vertical Axis					
	Plus Direction			Minus Direction			Plus Direction			Minus Direction			Plus Direction			Minus Direction		
	1	2	3	1	2	3	1	2	3	1	2	3	1	2	3	1	2	3
Accelerometer	Vector (g)																	
1	41	38	38	38	30	34	8	8	7	8	8	7	8	8	8	8	8	8
2	30	34	34	30	30	27	7	7	6	6	6	5	6	7	7	6	7	7
3	35	38	38	28	28	28	8	8	7	8	8	7	7	8	8	9	8	8
4	37	37	41	37	29	29	8	8	7	8	7	7	8	8	8	9	9	8
5	37	40	40	34	31	31	7	7	6	6	6	6	7	8	7	8	8	8
6	35	35	35	35	31	35	7	7	6	7	6	6	8	8	7	8	8	8
7	38	42	42	38	35	35	9	8	8	8	7	8	7	7	7	8	7	7
8	40	36	40	33	33	33	8	7	7	7	7	7	6	7	7	5	4	4
9	33	33	33	37	37	33	8	7	7	8	8	8	7	7	7	8	7	7
10	28	32	37	32	28	37	9	9	9	10	10	10	8	9	8	10	8	10
11	45	49	49	41	41	41	—	—	—	—	—	—	5	5	3	8	8	9
12	34	34	34	26	22	26	—	—	—	5	9	7	4	5	5	7	6	8
13	28	11	11	21	14	14	—	—	—	—	—	—	—	—	—	—	—	—
14	31	31	31	8	19	66	14	13	12	10	8	9	8	9	9	8	8	8
15	6	10	10	46	40	70	8	5	3	6	5	5	4	4	3	—	—	—
16	7	9	7	38	33	19	2	2	2	2	3	3	7	8	6	7	8	7
17	—	—	—	—	—	—	—	—	—	—	—	—	5	6	6	5	6	4
18	—	—	—	—	—	—	7	6	2	5	7	7	5	4	6	4	6	6
19	—	—	—	—	—	—	7	5	5	4	7	5	3	3	3	2	2	3
20	—	—	—	—	—	—	7	8	8	14	21	22	3	3	3	3	3	3
21	—	—	—	—	—	—	7	6	5	5	7	7	2	3	3	5	5	6

Conclusions

The engine completed vibration and shock testing with no evidence of structural or functional failures of the engine hardware as a result of test levels and durations imposed. On the basis of these test results and the correlation between past dynamics tests and flight history, the structural and functional integrity of the modified engine was validated, and the configuration was judged to be structurally flightworthy.

Future engine vibration tests should be conducted with a test fixture natural frequency above 400 cps to eliminate engine overtesting or undertesting at certain frequencies.

ENGINE HOT-FIRE TESTS

Firing tests of the Project Sure Fire modified engine were conducted to demonstrate flightworthiness (FWD) and to establish confidence in the operation and performance of the engine at sea level. Additional objectives of the tests were:

1. To verify that preliminary pump level characteristics would be assured at the maximum expected range of Gemini mission operating pressures and temperatures;

2. To certify safe engine operation at minimum and maximum voltage levels;

3. To verify that malfunction modes at sea level have not changed because of engine design modifications;

4. To evaluate shock and vibration levels at specific points on the modified engine during the engine start transient and ignition sequence.

The tests were conducted at Bell Aerospace Co. (Bell Test Center Facility), Lewiston, New York, during January and February 1966.

Test Configuration

Engine firing tests were conducted in test cell 2 DT, a vertical tower capable of supporting a maximum firing duration of 100 sec (propellant tank volume limits). Temperature conditioning of the test stand could be varied between 0° F and +160° F.

Dynamic Data Test Results

The engine and facility thrust mount were instrumented with dynamic measurement transducers as shown in Table 6 and Fig. 12. Engine vibration, force, and pressure measurements were monitored during all sea-level FWD hot-fire tests.

Test dynamic data results are presented in Tables 7 and 8. Table 7 is a summary of the dynamic data at thrust chamber ignition on engine hot-fire tests 281 and 283 through 324. Accelerometer data in Table 7 are the peak g's recorded at thrust chamber ignition. Averages of peak g's for each run are listed to give a comparison between runs for different hardware and propellant temperature conditions. Using accelerometer A-1 (mounted on the thrust chamber lug) as a reference accelerometer, the minimum and maximum peak g's from the 43 engine firings were 16 and 108 g, respectively.

The averages of peak g's for each run varied from 41 to 79. The high peak g average resulted from the malfunction test 319, which was the second pulse of a multiple power interruption test with 0.22 sec between the first shutdown signal and restart command. The start transient total force levels from the load cell data varied from 9409 to 14,105 lb. The load cell data from test 281 were not considered valid because of calibration discrepancies. The mean total force from the available data was 11,757 lb, which is near prediction for sea-level conditions.

Table 8 shows the results of the PSD data from 9 of the 43 tests that represent different propellant inlet temperature conditions from 0 to +143 F. The data show a spread of 0.5 to 17 g rms for the engine test firing for a 0.5-sec period beginning shortly after thrust chamber ignition.

The PSD data shown in Table 8 and Figs. 13, 14, and 15 are typical results of the sea-level engine FWD tests and indicate average levels significantly less than the LMSC 6117D test requirements of 18.7 g rms. These PSD plots show distinct peak frequencies occurring around 850, 1500, and 1700 cps. Most of the energy represented by the area under each PSD plot occurs at these predominant frequencies, which, as expected, correlate with the engine pump impeller frequencies.

TABLE 6
Engine Dynamic Measurements

Item	Parameter	Location and Orientation	Type of Mounting	Type of Transducer	Frequency Response	Accuracy	Range
A-1	Engine vibration	Thrust chamber lug — longitudinal	Epoxy bonded mounting block	Endevco 2242C with insulated stud	5—4000 cps	±5%	±150 g
A-2		Thrust chamber lug — yaw					±200 g
A-3		Thrust chamber lug — pitch					±200 g
A-4		Gimbal ring assembly, top — longitudinal					±100 g
A-5		Gimbal ring assembly, bottom — longitudinal					±200 g
A-6		Thrust mount, gimbal ring attachment, right side — longitudinal					±100 g
A-7		Thrust mount, gimbal ring attachment, left side — longitudinal					±200 g
A-8		Thrust mount, at yaw actuator fitting, longitudinal					±200 g
A-9		Thrust mount, at pitch actuator fitting, longitudinal					±300 g

A-10	Engine vibration	Electronic gate — longitudinal	Epoxy bonded mounting block	Endevco 2242C with insulated stud	5—4000 cps	±5%	±100 g
A-11		Pressure switch relay — longitudinal					±100 g
A-12		Thrust chamber lug — longitudinal	Threaded mounting block				±100 g
A-13		Gas generator, parallel to geometric axis of generator near injector head	Epoxy bonded mounting block				±400 g
A-14		Engine test rig — longitudinal					±50 g
A-15		Engine test rig — pitch					±50 g
16. LC-1	Engine thrust	At thrust mount attachment point upper left		Thrust washer (Kistler)			0 to 7000 lb
17. LC-2		At thrust mount attachment point lower left					
18. LC-3	Engine thrust	At thrust mount attachment point lower right	Epoxy bonded mounting block	Thrust washer (Kistler)	5—4000 cps	±5%	0 to 7000 lb
19. LC-4		At thrust mount attachment point upper right					
20	Chamber pressure			Kistler transducer			

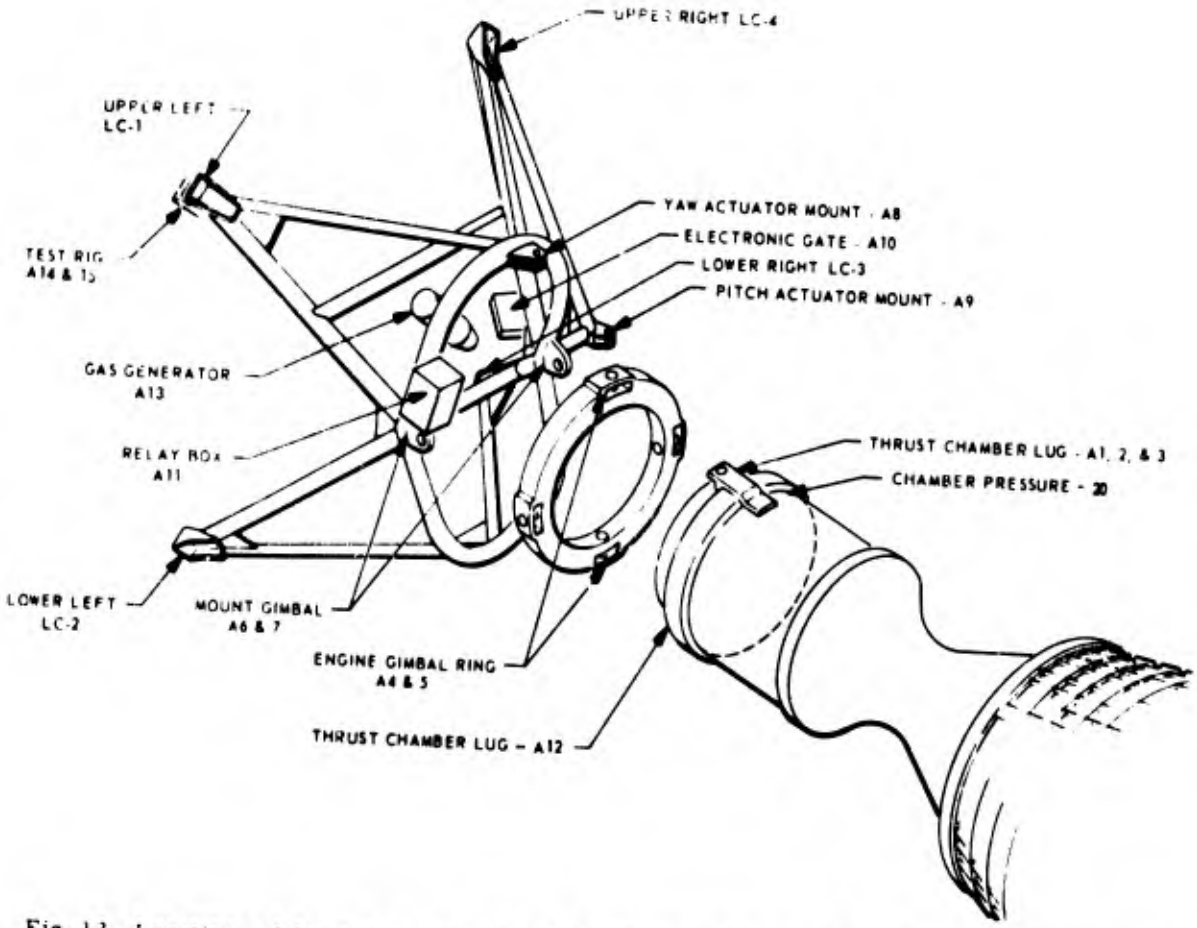

Fig. 12. Locations of dynamic measurements on engine and facility thrust mount; hot-fire tests

TABLE 7
Dynamic Data for Sea-Level FWD Tests

BAC Test No.	281	283	284	285	286	287	288	289	290	291	292	293	294	295	296	297	298	299	300	301	302	303
Temp. (°F) TMT/Prop.	40/46	46/53	604/74	526/76	511/76	459/78	456/71	84/56	96/48	215/63	329/60	367/61	96/47	97/47	212/60	33/41	35/45	2/0	519/13	468/16	18/52	484/35
Run Duration (sec)	90	31	2	2	2	2	2	2	2	2	2	2	2	2	2	2	91	30	2	2	30	2
Accelerometer	Vector (0 to peak g)																					
A-1	44	50	23	24	27	25	22	20	16	19	24	19	24	19	31	73	108	68	48	44	34	45
A-2	54	71	–	–	–	–	–	–	–	–	–	–	–	–	–	–	–	55	75	53	66	74
A-3	60	102	73	66	70	77	78	70	44	46	60	43	46	50	49	51	95	29	29	33	51	34
A-4	32	47	49	54	53	43	38	46	37	59	48	39	40	39	52	39	49	10	29	36	57	47
A-5	86	81	79	81	89	77	69	70	77	92	85	72	65	68	80	72	83	88	65	75	78	66
A-6	44	37	35	47	25	41	44	38	40	40	44	36	41	44	41	41	38	48	49	49	30	37
A-7	63	64	36	41	43	40	49	59	78	48	47	67	54	50	53	71	72	62	49	47	52	35
A-8	66	71	60	61	67	80	65	78	55	71	76	72	53	58	61	53	62	47	52	48	54	47
A-9	84	71	68	63	68	74	77	73	74	82	77	78	87	67	94	68	66	78	77	90	97	83
A-10[a]	–	–	17	15	14	9	8	14	12	16	15	18	12	12	18	17	10	14	21	25	14	20
A-11	16	6	10	6	16	12	17	10	7	15	10	11	10	7	9	14[a]	9[a]	9	17	11	15	10
A-12	45	66	72	64	76	78	53	56	51	62	75	69	55	58	76	42	64	42	44	36	53	46
A-13	71	93	120	53	–	–	–	–	–	–	–	–	–	–	–	79	67[a]	88	100	113	84	–
A-14	5	6	4	6	4	4	2	2	6	10	10	10	8	13	8	3[a]	4	3	9	8	8	5
A-15	6	8	5	8	7	3	7	2	5	10	8	6	8	8	8	16[a]	4	6	9	6	–	7
Average[b]	55	65	54	48	50	51	47	49	45	50	51	48	44	43	51	52	60	49	50	51	53	45
Average[c]	53	59	48	50	51	52	50	52	38	53	53	49	47	45	53	54	65	50	50	50	53	49
Load Cells	–										Pounds Force											
1	–	3100	2425	2340	2115	2078	1968	1892	2195	2495	2240	2280	2410	2152	2195	2200	2095	2260	2345	2490	2455	2610
2	–	–	–	–	–	–	–	–	–	–	–	–	–	–	–	2970	2886	3001	3145	3190	3150	3150
3	–	3260	3260	3220	2585	2681	2585	2325	2980	3105	3182	2980	2900	2898	2980	2940	2940	3002	3050	2825	2970	2878
4	–	–	–	–	–	–	–	–	–	–	–	–	–	–	–	2855	–	2890	3230	3180	3030	3115
Total	–	–	–	–	–	–	–	–	–	–	–	–	–	–	–	10965	–	11153	11770	11685	11605	11753
BAC Test No.	304	305	306	307	308	309	310	311	312	313	314	315	316	317	318	319	320	321	322	323	324	
Temp. (°F) TMT/Prop.	419/35	40/133	550/143	511/143	96/103	603/105	507/107	50/54	362/62	309/73	421/71	84/57	43/49	136/64	183/60	183/60	237/58	237/58	278/58	278/58	254/60	
Run Duration (sec)	2	15	2	2	31	2	2	20	20	21	20	3	30	1	1	0.5	1	0.1	1	0.4	20	
Accelerometer	Vector (0 to peak g)																					
A-1	50	83	41	43	52	36	48	40	39	42	39	31	33	37	37	60	37	40	49	55	48	
A-2	56	67	37	–	47	27	40	41	37	64	47	36	23	30	40	80	50	50	43	65	55	
A-3	40	41	27	27	33	23	23	25	27	42	32	19	27	29	27	54	29	29	34	44	54	
A-4	36	6	8	6	42	71	68	39	40	48	41	22	83	60	46	76	57	62	71	48	61	
A-5	72	118	90	95	83	94	91	61	71	83	68	57	90	71	71	125	90	61	76	78	100	
A-6	36	86	39	39	–	22	22	38	26	28	27	26	–	–	–	–	–	–	–	–	–	
A-7	41	72	40	35	39	39	41	38	40	36	35	40	45	53	48	38	50	45	50	48	53	
A-8	41	72	44	37	24	24	29	47	45	48	35	51	100	58	53	75	55	65	55	50	55	
A-9	89	97	65	98	76	64	76	95	60	72	58	60	106	78	53	71	71	67	78	53	78	
A-10[a]	12	–	–	–	17	18	6	–	–	–	–	–	–	–	–	–	–	–	–	–	–	
A-11	8	53	20	13	11	15	10	12[a]	14[a]	11	11	13	4	4	3	5	5	3	3	3	3	
A-12	41	42	56	58	64	84	43	47	36	38	45	34	55	56	44	77	44	35	48	47	77	
A-13	–	104[a]	–	–	168	–	–	116	130	114	124	114	122	146	156	205	171	200	225	239	195	
A-14	6	24	5	7	6	5	3[a]	3	6	3	6	3	7[a]	13[a]	9[a]	7[a]	7[a]	5[a]	8[a]	4[a]	5[a]	
A-15	4	43	6	8	9	5	9[a]	8	6	8	7	7	2[a]	4[a]	50[a]	3[a]	6[a]	3[a]	6[a]	9[a]	6[a]	
Average[b]	44	70	43	45	55	43	41	50	47	52	47	42	63	57	53	79	60	60	67	66	71	
Average[c]	47	71	43	48	46	42	44	47	43	51	42	38	63	52	47	72	55	52	57	55	63	
Load Cells											Pounds Force											
1	2455	3695	2820	3030				3292	3145	3056	3142	–	4240	3680	2405	2860	2830	2572	3450	2630	3280	
2	3150		2660	2345				2360	2510	2040	2474	–	3200	2412	1280	1485	2008	1310	1804	1165	2010	
3	2845	4150	4440	4420				4640	4650	4540	–	–		–	4110	3830	–	–	–	4240	4246	
4	3200	2442	2290	2105				2075	1989	1933	2392	–	2590	2305	1614	1728	2160	1902	2075	2020	2275	
Total	11650	–	12210	11900				12367	12294	11569	–			–	9409	9903	–	–	–	10055	11805	

Note.–Dashes indicate no data because of instrumentation discrepancies or low acceleration levels.
[a]60 cps noise on data; however, the data are considered valid.
[b]Does not include accelerometers 14 and 15 (test rig accelerometers).
[c]Includes accelerometers A-1 through A-10 for comparison with similar data from AEDC tests.

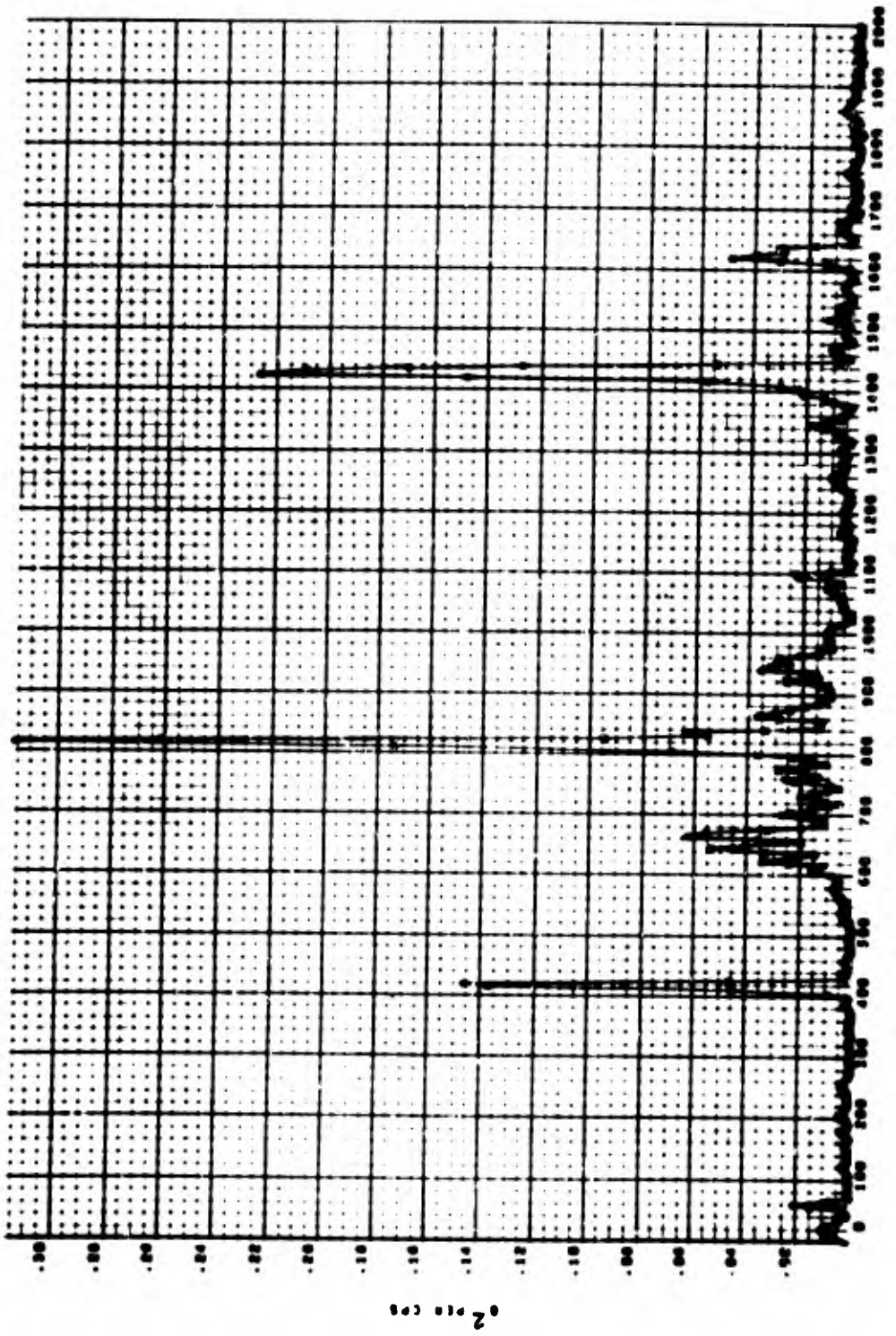

Fig. 13. PSD data, engine 803, test 297: accelerometer 6; temperature 41°F, after thrust chamber ignition; interval rms value 5.31 g

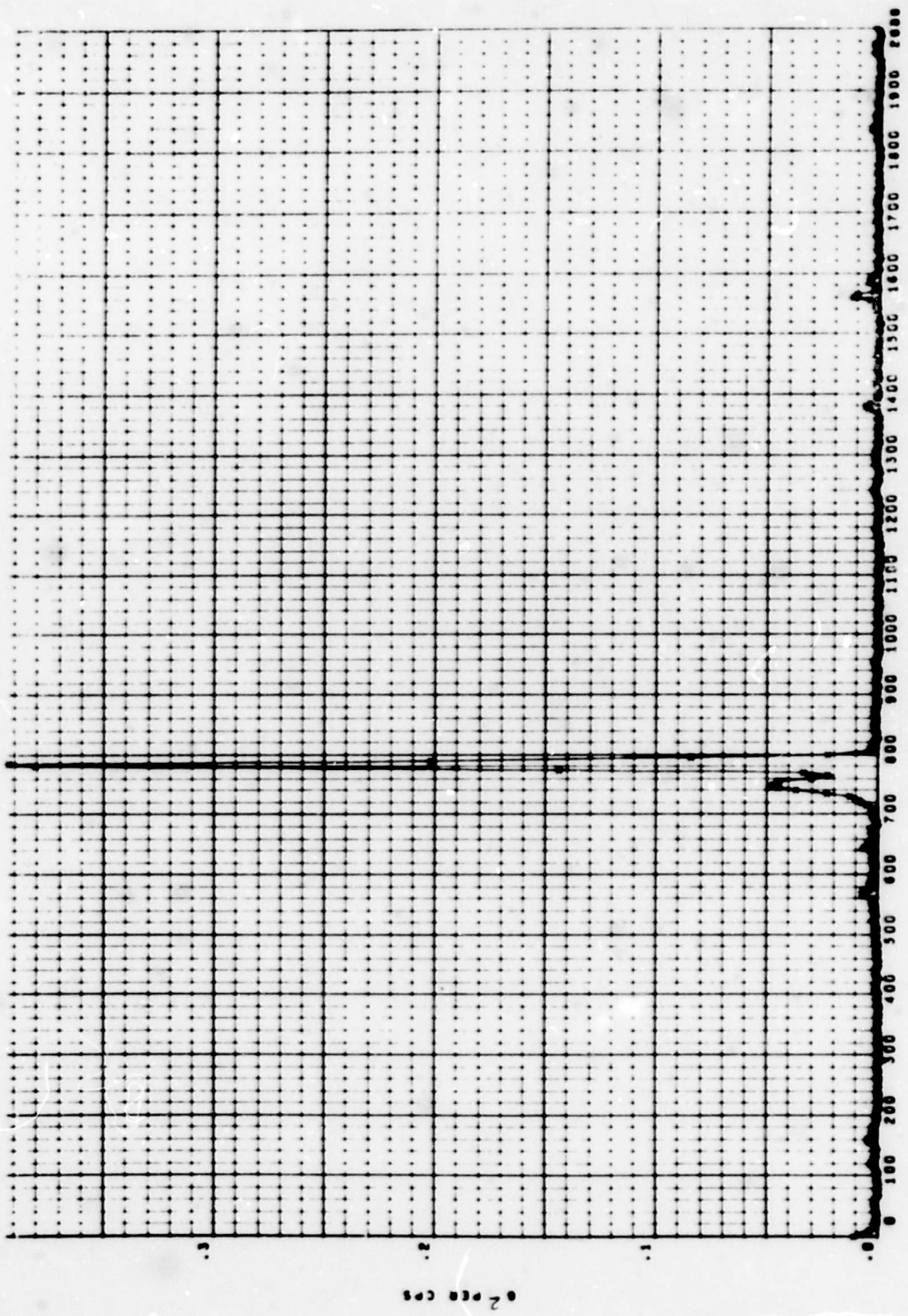

Fig. 14. PSD data, engine 803, test 299: accelerometer 3; temperature 0°F; after thrust chamber ignition; interval rms value 3.25 g

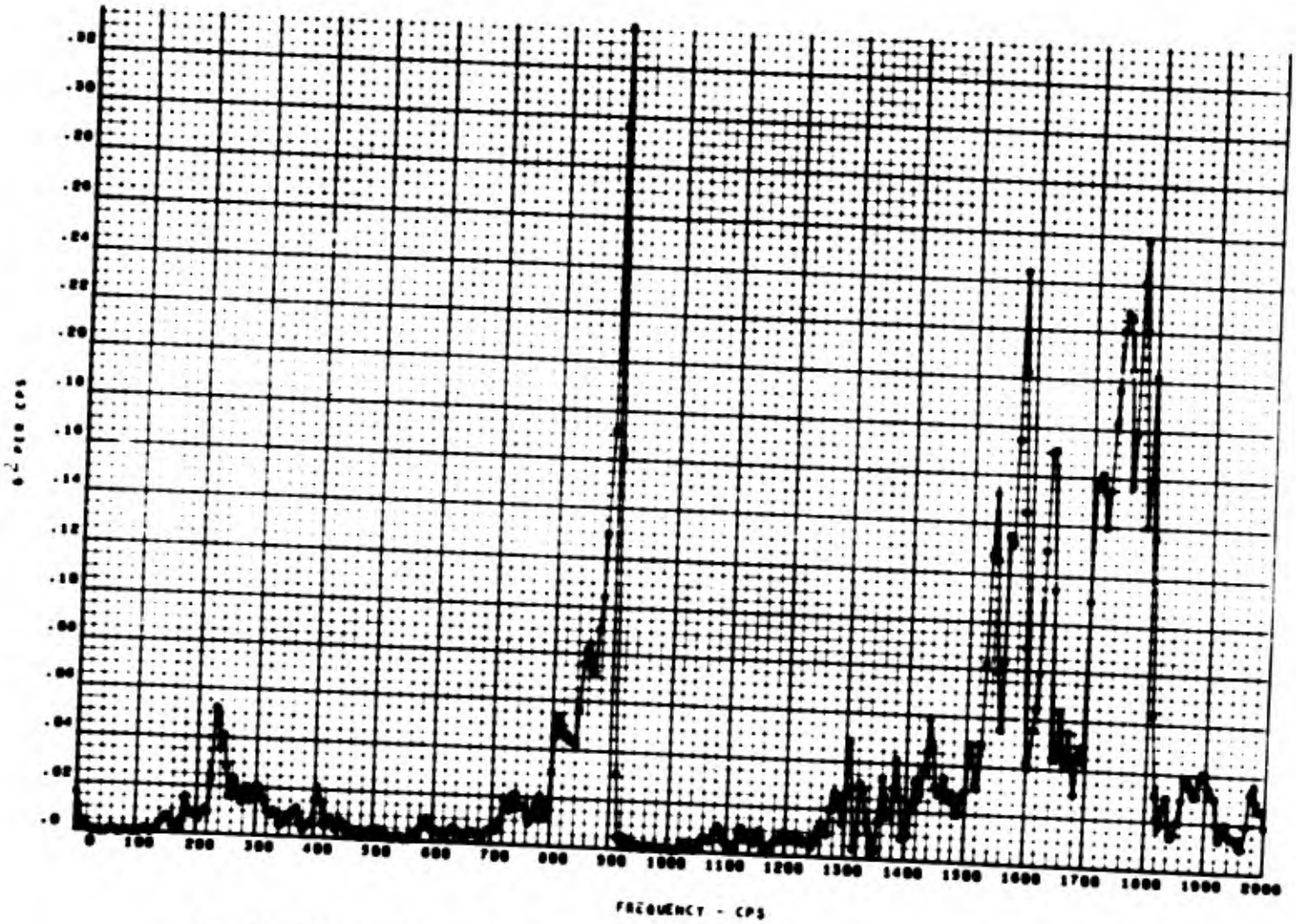

Fig. 15. PSD data, engine 803, test 306: accelerometer 9; temperature +143°F; after thrust chamber ignition; interval rms value 8.43 g

TABLE 8
Power Spectral Density Data (rms g levels) for Sea-Level FWD Tests

Test	Accelerometer															Average
	1	2	3	4	5	6	7	8	9	10	11	12	13	14	15	
287	3	–	4	6	14	6	5	7	7	12	7	14	3	4	3	7
297	6	–	3	4	9	5	5	6	5	15	8	11	11	5	4	7
299	5	3	3	2	7	–	4	5	6	5	4	3	13	2	1	5
301	4	4	17	2	1	–	1	1	0.5	3	7	2	3	5	9	4
306	7	5	5	2	12	10	7	10	8	8	5	5	4	2	1	6
307	8	5	6	1	13	8	7	10	8	10	4	3	5	2	1	6
308	7	3	3	4	9	2	6	8	6	8	4	4	11	1	1	5
310	6	5	5	6	13	4	7	10	7	7	6	17	4	2	2	7
324	5	3	3	6	5	13	4	5	5	9	4	12	17	2	2	6

Note.--Dash indicates no data for these accelerometers.

An evaluation of the dynamic test results does not indicate a trend of thrust chamber ignition shock as a function of temperature at sea-level conditions. However, the high response chamber pressure measurement indicated a more gradual initial rise rate (0.070 sec from 0 to 70 psig) at higher temperatures. Test 318 was the start for a power interruption fuel-lead start sequence, and no indication of an ignition delay and no significant difference in ignition accelerations or thrust loads were observed; however, the highest chamber pressure rise rate (0.035 sec from 0 to 70 psig) was observed on this test. The second pulse of the fuel-lead power interruption (test 319) indicated the highest average ignition peak shock levels. However, the chamber pressure characteristics, which were affected by the short coast periods wherein residual fuel is retained and reacts with the oxidizer postflow, do not permit a valid correlation of chamber pressure rise rate for this test.

Dynamic Data Test Conclusions

Throughout the range of test conditions the sea-level engine FWD dynamic test results indicate no adverse loading or accelerations during the engine start transient or operation. Therefore, within measurement and analytical capability, adverse conditions during the fuel-lead start were not observed at sea level.

The general review of steady-state engine operation vibration levels during these FWD tests indicate levels approximately equal to the LMSC 6117D test requirements.

The average thrust chamber ignition peak g's (53 g) recorded with the engine hard-mounted installation were greater than the shock test levels of 40 g specified in LMSC 6117D. An extensive analysis of each ignition accelerometer transient would be required to present the total energy levels at ignition for each accelerometer transient. However, an evaluation of the high peak accelerometer data indicates the ignition shock total levels obtained with the engine FWDT hard-mounted installation were lower than the LMSC 6117D test requirements of half sine wave, 40 g peak for 8-msec duration.

The engine FWD test ignition average peak acceleration levels are greater than the corresponding average longitudinal acceleration peak recorded during the XLR 81-BA-13 and YLR 81-BA-11 engine acceptance tests. However, the differences in facility thrust structure, engine attitude, accelerometer installation techniques, and rigidity of gimbal actuators compared with solid links prohibit a direct correlation of the accelerometer test results, even at similar test conditions.

The dynamic test results indicate that test conditions per se did not impose significant effects on engine dynamic operation over the range of the sea-level FWD conditions tested.

Accelerometer data recorded during the altitude FWD tests provided shock and vibration characteristics and levels of the modified XLR 81-BA-13 engine start transient at altitude. These data were necessary for use in evaluation and comparison with the sea-level XLR 81-BA-13 and YLR 81-BA-11 engine test data.

Test Configuration and Test Results

Figure 16 shows the dynamic measurement instrumentation locations during tests on engines 803 and 805. Table 9 presents the accelerometer locations and types of mounting used. Strain gages FSA-1 through -4 (see Fig. 16) were located at the upper left, lower left, upper right, and lower right 1.5-in. load columns of the thrust mount; specifications for each were (a) cemented mounting, (b) frequency response of 5 to 4000 cps, (c) accuracy of ±5 percent, and (d) range of 7500 μin./in. Test results are tabulated according to tests and are presented in the Tables 10 through 12 and Figs. 17 through 36. (Figures 20 through 34 are typical PSD and shock spectral plots for nominal, low-temperature, and fuel-lead conditions.) A discussion of test results is contained in the next paragraph.

Test firing CB-06 was considered a typical run and is used for comparison of the test results, since engine performance, operation, and sequencing were all nominal and representative of what would be predicted for flight.

SIGNIFICANT TEST RESULTS

As shown in Table 10, a comparison of the average peak g levels at thrust chamber ignition for each run of tests AA-01 through AA-06 showed good agreement and correlation of accelerometer data. The peak g levels of the individual accelerometers also showed good agreement, except for accelerometers AE-8 and AE-9. These accelerometers measured high g levels during tests AA-01 and AA-03. The high vertical and lateral acceleration levels (170 to 350 g) of tests AA-01 and AA-03 are attributed to turbine exhaust duct physical interference with the engine thrust chamber. The turbine exhaust duct was not restrained in the direction toward the engine thrust chamber, and with the two duct bellows acting as flexure points, the turbine exhaust pressure at ignition resulted in sufficient duct reflection to strike the thrust chamber. The turbine exhaust duct experienced a permanent set during the fire tests, and the AE-8 and AE-9 high acceleration loads were not observed during tests AA-02 or AA-04 through AA-06. After the sixth test firing, the turbine exhaust duct was restrained, and motion in the transverse axes was minimal.

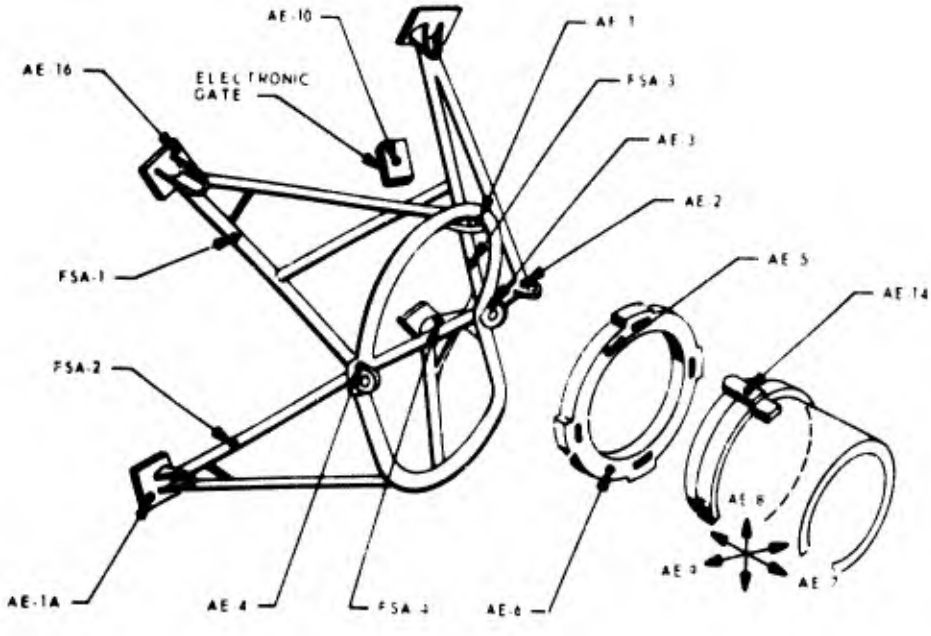

Fig. 16. Locations of dynamic measurements during tests on engines 803 and 805

TABLE 9

Engine Dynamic Measurements – Accelerometer

Accelerometer	Location and Orientation	Mounting		Range (g peak to peak)			
		Phase I & II	Phase III	AA Series	AB-01	AC & BA Series	Phase III
AE-1	Thrust mount at yaw actuator fitting – longitudinal	Epoxy	Stud	200	200	200	2000
AE-2	Thrust mount at pitch actuator fitting – longitudinal	Epoxy	Stud	200	200	200	2000
AE-3	Thrust mount gimbal ring attachment, right side – longitudinal	Epoxy	Not used	200	200	200	Not used
AE-4	Thrust mount gimbal ring attachment, left side – longitudinal	Epoxy	Stud	200	200	200	2000
AE-5	Gimbal ring assembly, top – longitudinal	Epoxy	Not used	200	200	200	Not used
AE-6	Gimbal ring assembly, bottom – longitudinal	Epoxy	Not used	200	700	2200	Not used
AE-7	Thrust chamber lug – longitudinal	Epoxy	Stud	200	400	1000	2000
AE-8	Thrust chamber lug – vertical	Epoxy	Stud	200	400	1000	2000
AE-9	Thrust chamber lug – lateral	Epoxy	Stud	200	400	1000	2000
AE-10	Electronic gate – longitudinal	Epoxy	Epoxy	200	200	200	2000
AE-1A	Engine test rig near lower left leg – longitudinal	Not used	Stud	–	–	–	400
AE-14	Thrust chamber lug – longitudinal	Not used	Stud	–	–	–	2000
AE-16	Engine test rig near upper left leg – longitudinal	Not used	Stud	–	–	–	2000

Note.--Accelerometer specifications: (a) Endevco 2242C and 2225 with insulated studs; (b) frequency response, 5 to 4000 cps; (c) accuracy, ±5%.

TABLE 10
Peak Accelerometer Levels at Thrust Chamber Ignition – Tests AA-01 through BA-22

AEDC Test No.	AA-01	AA-02	AA-03	AA-04	AA-05	AA-06	AB-01	AC-01	AC-02	AC-03	AC-04	AC-05	AC-06	AC-07	AC-08
Temp. (°F) Prop./Gen. Skin (Static)	42/42	43/41	44/64	41/102	40/41	33/107	55/71	45/52	50/63	44/83	48/152	48/78	38/51	39/114	45/174
Run Duration (sec)	5	5	5	5	5	5	5	20	5	5	5	5	5	5	5
Accelerometer	Vector (0 to peak g)														
AE-1			Open Circuit				353	42	75	66	83	41	58	75	100
AE-2	114	60	59	74	53	56	410	51	60	169	127	50	60	183	128
AE-3	46	33	26	38	41	66	385	45	63	91	82	41	59	82	100
AE-4	51	34	22	43	31	39	623	33	52	57	86	32	41	59	81
AE-5	43	43	24	61	66	77	533	55	60	100	90	45	57	95	104
AE-6	49	36	30	45	41	55	395	38	50	107	70	43	49	59	70
AE-7	61	40	26	47	42	60	387	39	47	121	87	34	55	61	80
AE-8	24[b]	75	68[c]	55	58	70	683	15	25	25	28	18	14	29	40
AE-9	28[d]	18	15	18	21	26	440	24	19	20	30	40	31	31	104
AE-10	18	20	16	22	18	24	358	28	43	56	65	28	28	44	53
Average	48	40	32	45	41	53	457	37	49	81	74	37	45	71	86

AEDC Test No.	AC-09	AC-10[a]	AC-11	AC-12	AC-13	AC-14	BA-15	BA-16	BA-17	BA-18	BA-19	BA-20	BA-21	BA-22
Temp. (°F) Prop./Gen. Skin (Static)	12/7	6/58	8/105	6/127	7/134	9/38	48/56	94/101	94/145	11/28	13/148	15/134	16/22	55/61
Run Duration (sec)	5	5	5	5	5	5	15	2	2	15	2	2	15	180
Accelerometer	Vector (0 to peak g)													
AE-1	150		100	133	100	125	42	50	25	563	45	—	—	—
AE-2	383		73	354	229	242	55	80	64	537	—	141	—	—
AE-3	191		91	141	136	132	32	50	27	280	—	—	—	—
AE-4	100		86	122	100	132	33	48	43	480	135	340	175	121
AE-5	130		138	218	157	190	45	45	35	280	135	770	240	125
AE-6	131		154	169	169	—	—	—	—	—	—	—	—	—
AE-7	84		152	210	178	195	29	39	29	312	125	717	—	—
AE-8	766		313	493	557	319	14	14	11	359	318	828	—	—
AE-9	120		42	87	97	213	15	18	15	503	65	872	—	—
AE-10	124		57	94	77	80	27	30	24	142	94	193	110	114
Average	217		120	202	180	181	32	42	30	384	102	551	175	120

Note.—Dash indicates no data because of instrumentation discrepancies or low acceleration levels.

[a]Recorder not on.
[b]170 g from the exhaust duct hitting the engine.
[c]350 g from the exhaust duct hitting the engine.
[d]336 g from the exhaust duct hitting the engine.

TABLE 11
Peak Accelerations and Loads at Thrust Chamber Ignition — Tests CA-01 through CB-16

AEDC Test No.	CA-01	CA-02[a]	CB-03	CB-04	CB-05	CB-06	CB-07	CB-08	CB-09	CB-10[a]	CB-11	CB-12	CB-13	CB-14	CB-15	CB-16
Temp. (°F) Prop./TMT	50/50	30/56	47/56	32/61	16/76	28/122	14/56	11/96	11/160	7, 59/40	59/142	1/11	3/33	-8/20	54/119	53/203
Run Duration (sec)	5.10	4.99	4.89	4.82	5.20	4.94	1.99	5.09	1.99	5.05	1.99	1.88	5.13	5.07	5.16	5.98
Accelerometer	Vector (0 to peak g)															
AE-1A	–		–	6	–	–	–	29	26		–	33	25	59	61	224
AE-2	46		42	–	–	–	–	–	–		–	–	–	–	–	–
AE-4	33		–	18	–	–	–	–	–		–	–	–	–	–	–
AE-7	46		41	41	48	71	53	190	142		64	142	103	245	705	–[b]
AE-8	–		–	–	–	–	–	35	–		31	–	–	–	P17	598
AE-9	37		–	–	–	–	–	–	–		–	–	–	–	–	721
AE-10	24		20	18	30	26	20	32	28		26	50	40	45	51	199
AE-14	–		–	–	–	–	–	–	–		–	–	–	–	–	–
AE-16			–	25	29	14	18	41	25		25	47	36	51	92	945
Average	37		34	[illegible]	36	37	30	65	55		36	68	51	100	205	503
Strain Gage	Pounds Force (calculated)															
FSA-1	6270		3695	4340	4340	3990	3695	3990	3695		3695	4340	3695	3460	3460	4002
FSA-2	5120		4430	4825	5140	4425	4140	4425	4425		4425	4430	4425	4530	4530	5230
FSA-3	5610		3695	3695	3990	3695	3695	3990	3695		3695	4340	3695	3460	3780	4002
FSA-4	–[c]		–[d]	–[d]	–[d]	–[d]	–[d]	–[d]	–[d]		–[d]	–[d]	–[d]	–[d]	–[d]	–[d]

Note.--Plain dash indicates no data because of instrumentation discrepancies or low acceleration levels.

[a]Recorder not operating.
[b]Questionable data because of DC shift and amplifier saturation.
[c]Questionable data.
[d]No data--open bridge.

TABLE 12
Power Spectral Density Data Summary for Typical Test Firings

AEDC Test No.	AA-04	AC-04	AC-14	BA-16	BA-18	CA-01	CB-04	CB-05	CB-07	CB-08	CB-11	CB-12	CB-13	CB-14	CB-15	CB-16
Accelerometer	rms g[a]															
AE-1	–	1	11	12	4	–	–	–	–	–	–	–	–	–	–	–
AE-2	22	28	23	20	1	–	–	–	–	–	–	–	–	–	–	–
AE-3	8	8	6	8	2	–[b]	–[b]	–[b]	–[b]	–[b]	–[b]	–[b]	–[b]	–[b]	–[b]	–[b]
AE-4	15	9	7	9	7	8	–	–	–	–	–	–	–	–	–	–
AE-5	11	9	11	8	3	–[b]	–[b]	–[b]	–[b]	–[b]	–[b]	–[b]	–[b]	–[b]	–[b]	–[b]
AE-6	12	6	2	3	5	–[b]	–[b]	–[b]	–[b]	–[b]	–[b]	–[b]	–[b]	–[b]	–[b]	–[b]
AE-7	8	9	5	8	4	6	5	4	4	4	6	5	6	–	10	–
AE-8	–	5	3	4	2	–	–	–	–	–	–	–	–	–	–	–
AE-9	4	7	4	4	3	–	–	–	–	–	–	–	–	–	–	311
AE-10	4	12	7	8	6	4	4	4	4	4	4	4	5	5	–	26
AE-1A	–[b]	–[b]	–[b]	–[b]	–[b]	–	–	–	–	2	–	4	4	3	3	71
AE-16	–[b]	–[b]	–[b]	–[b]	–[b]	5	6	5	–	5	–	5	8	–	8	111
Average per test	10	10	8	8	4	6	5	4	4	4	5	5	6	4	7	130

Note.—Plain dash indicates no data because of instrumentation discrepancies or low acceleration levels.

[a]Values computed for 0.5-sec time period beginning just after thrust chamber ignition, except test AA-04, where PSD's were generated during the thrust chamber ignition period.

[b]Accelerometer not used.

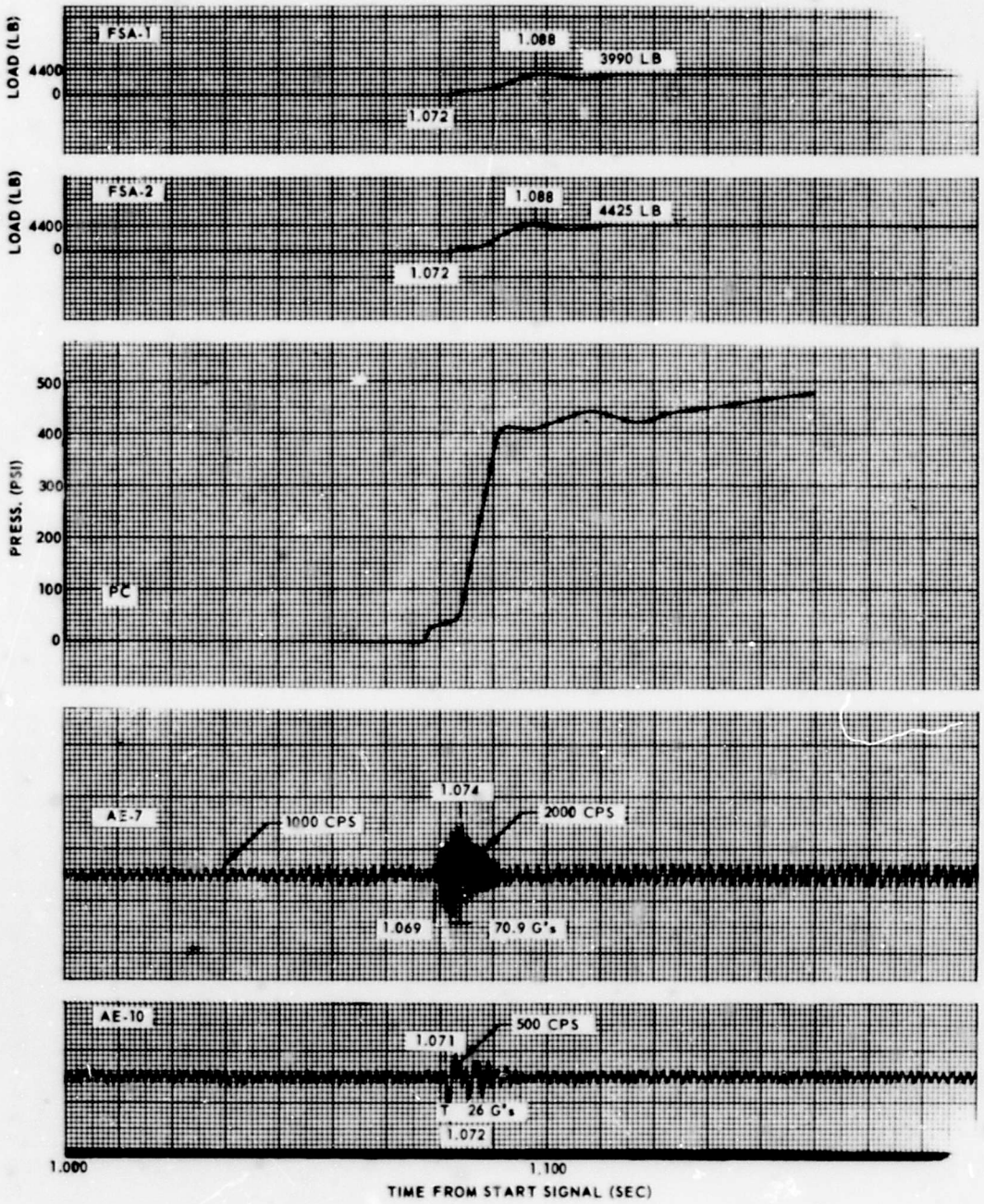

Fig. 17. Typical dynamic measurements and chamber pressure during a nominal test firing (CB-06)

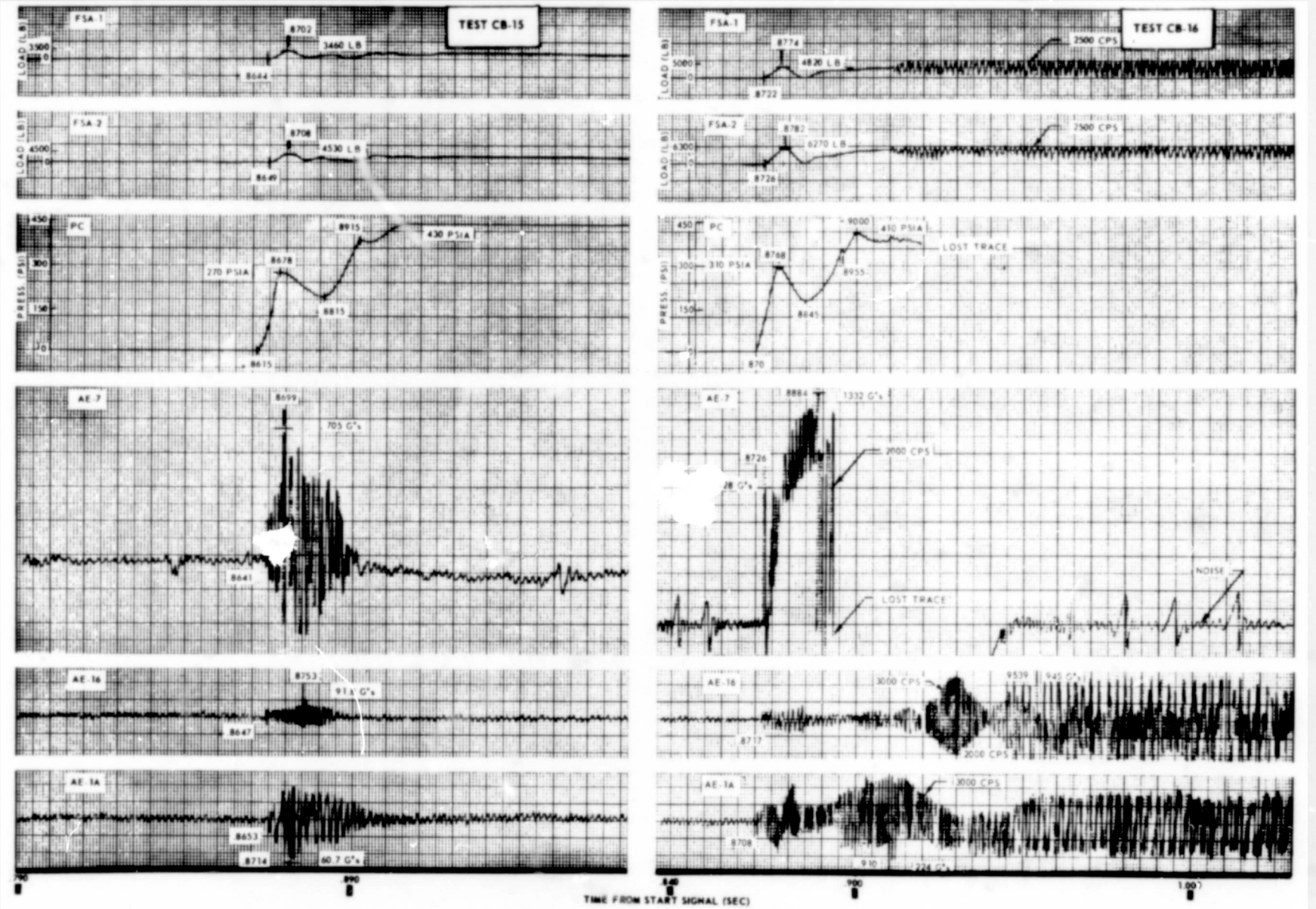

Fig. 18. Typical dynamic measurements and chamber pressure for fuel-lead starts

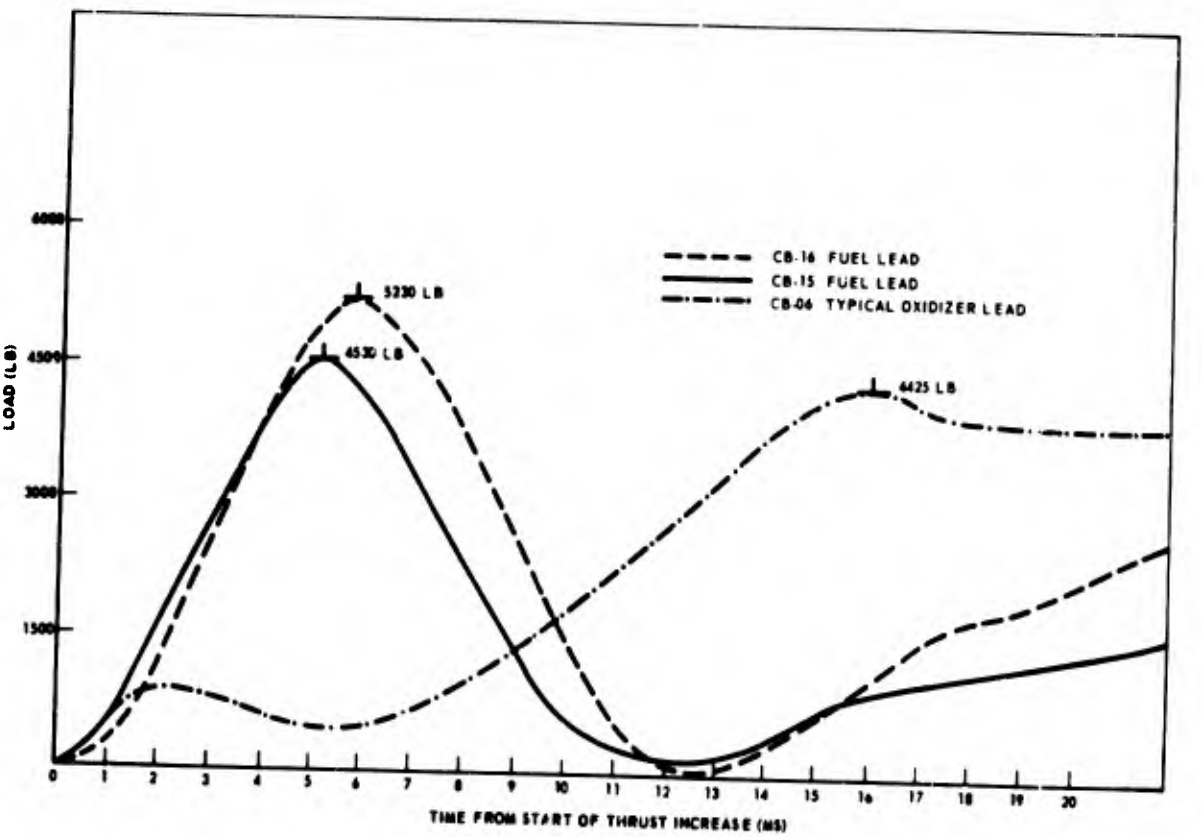

Fig. 19. Initial and peak thrust response curves for strain gage FSA-2 during tests CB-06, CB-15, and CB-16

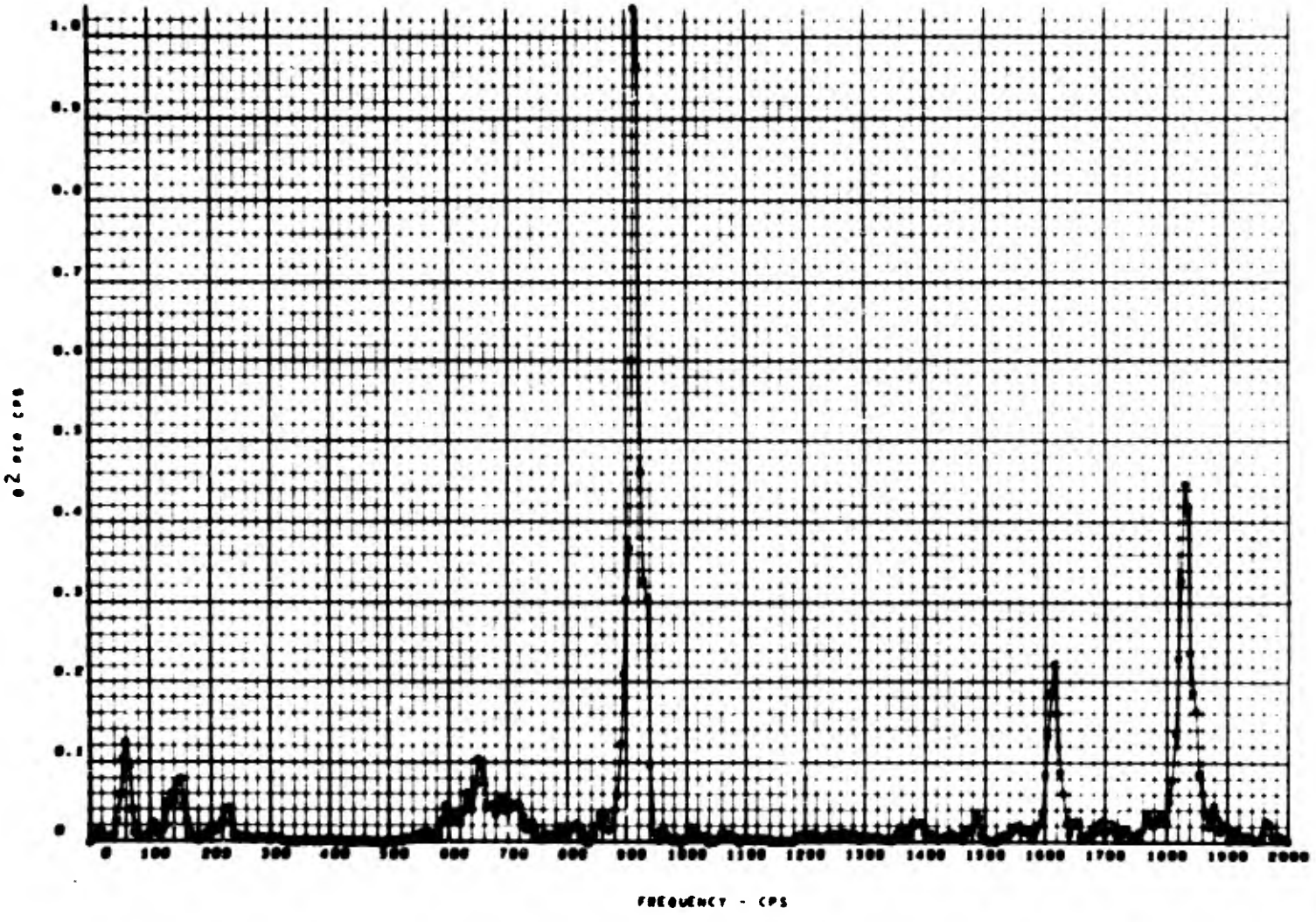

Fig. 20. PSD data, engine 805, test AA-04· accelerometer AE-07; temperature 40°F, thrust chamber ignition; interval rms value 8.34 g

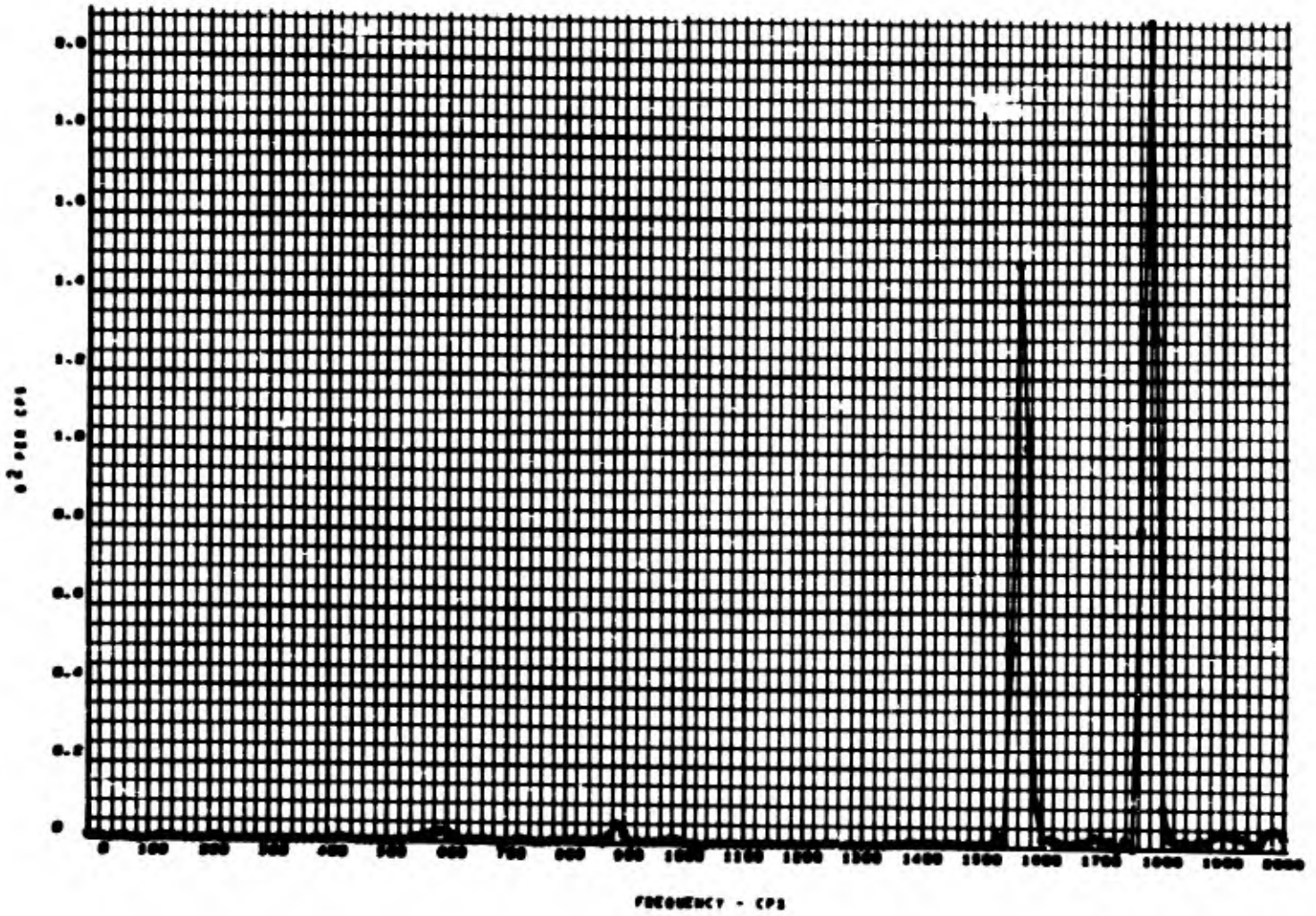

Fig. 21. PSD data, engine 803, test AC-14: accelerometer AE-5; temperature 10°F; after thrust chamber ignition; interval rms value 10.76 g

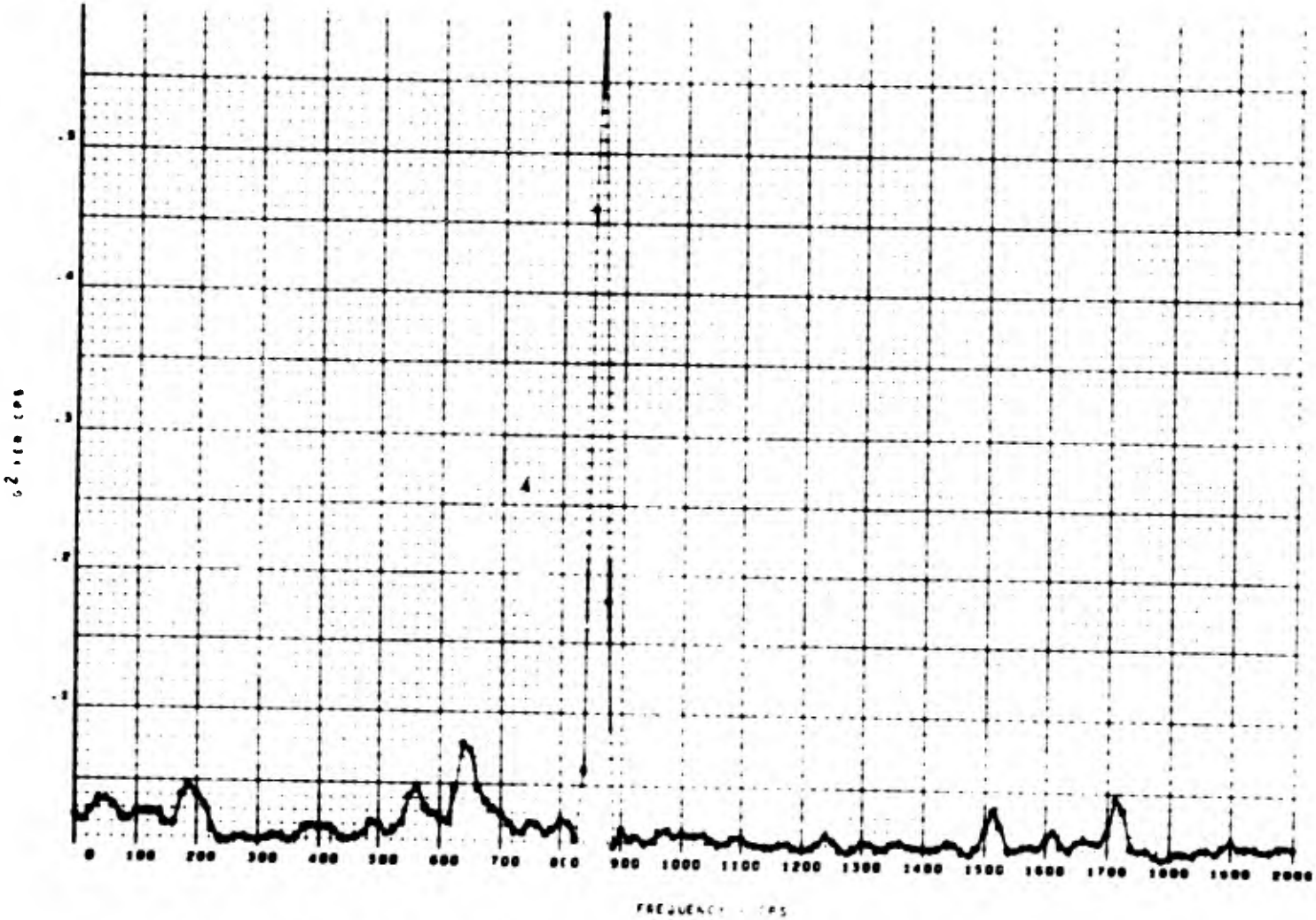

Fig. 22. PSD data, engine 803, test BA-18: accelerometer AE-4; temperature -10°F (fuel temp. -25°F); after thrust chamber ignition; interval rms value 7.29 g

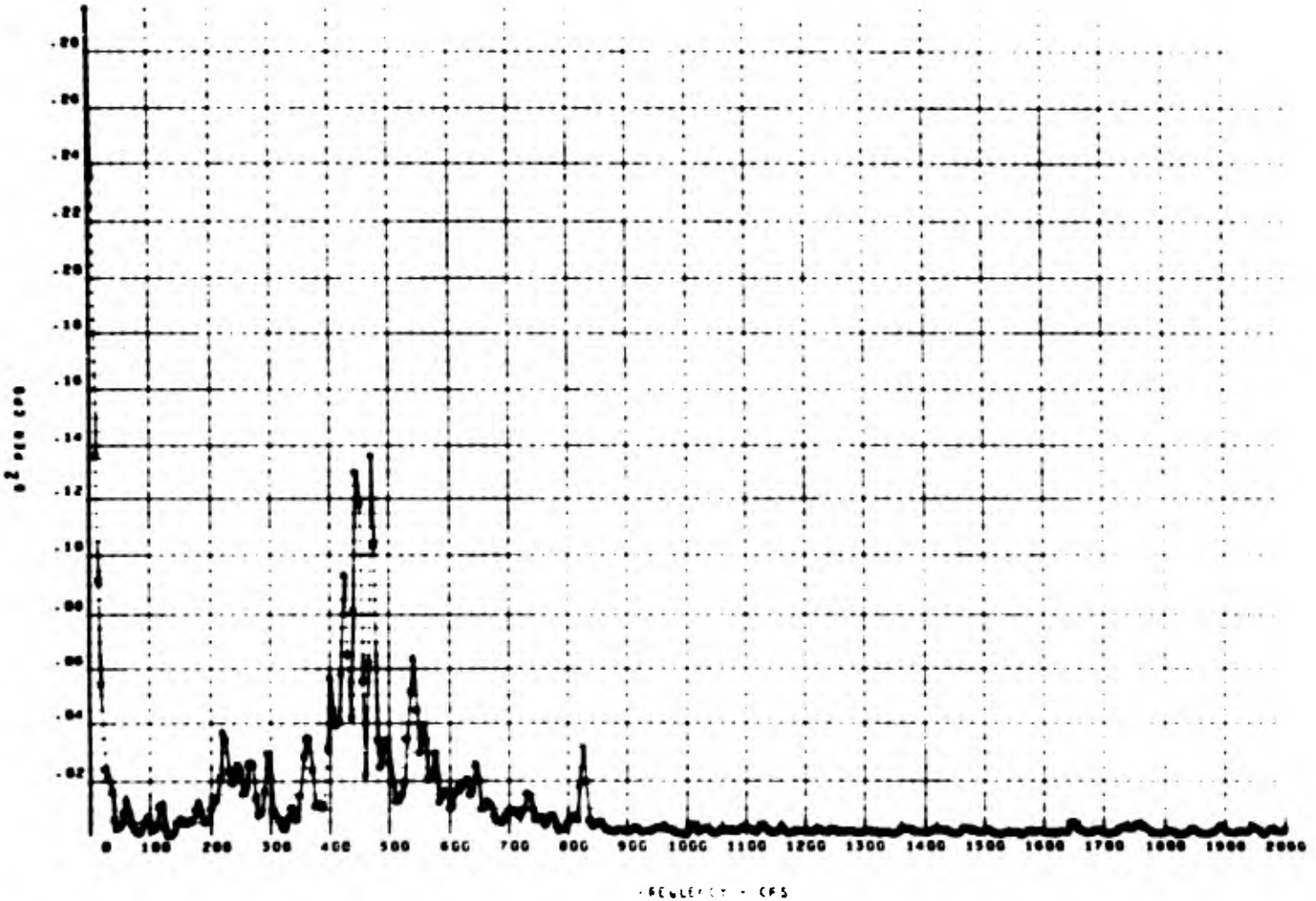

Fig. 23. PSD data, engine 803, test CB-14: accelerometer AE-10; temperature -10°F; after thrust chamber ignition; interval rms value 5.00 g

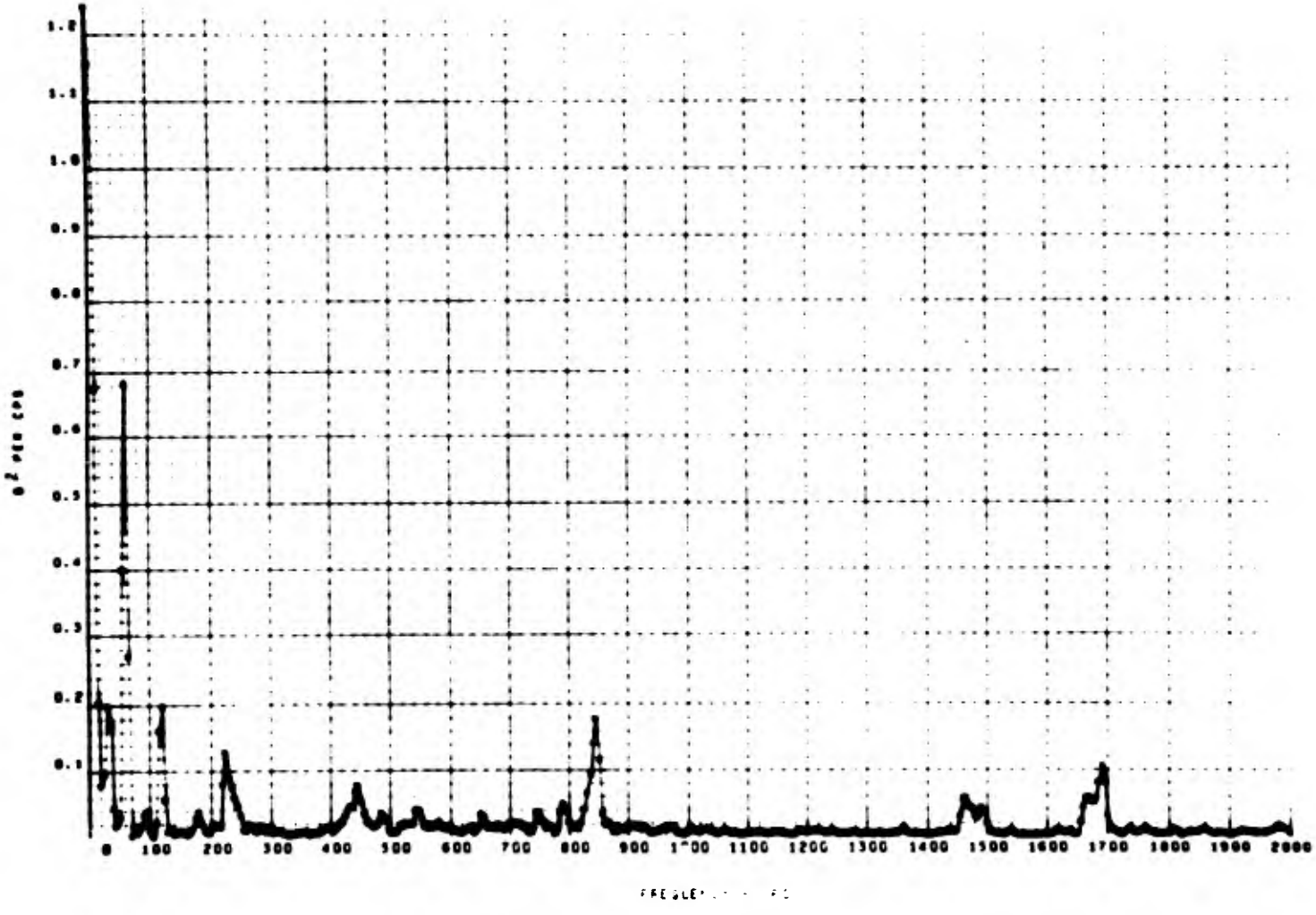

Fig. 24. PSD data, engine 803, test CB-15: accelerometer AE-16; temperature 50°F; after thrust chamber ignition; interval rms value 7.85 g

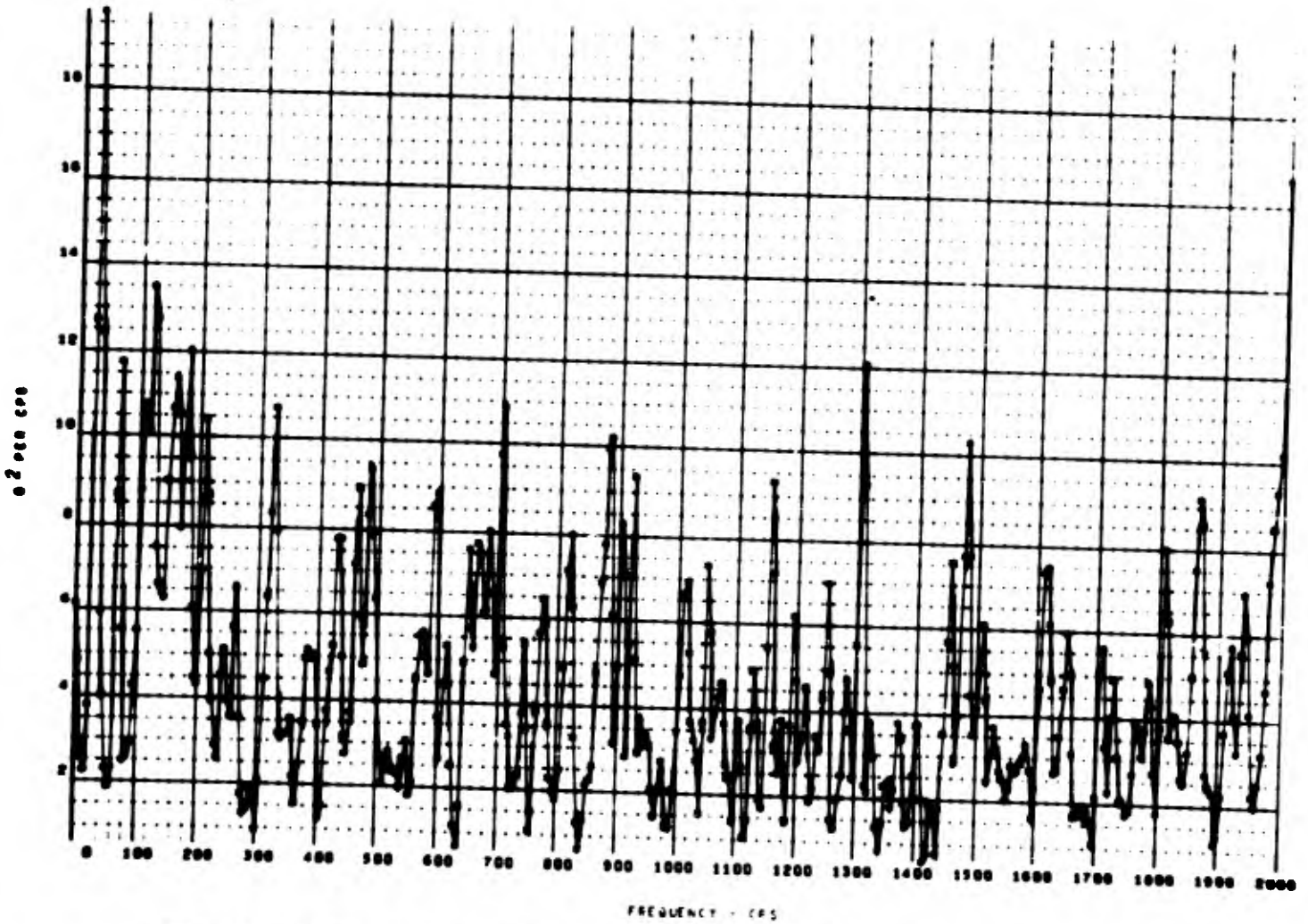

Fig. 25. PSD data, engine 803, test CB-16: accelerometer AE-16, temperature 50°F; after thrust chamber ignition; interval rms value 110.69 g

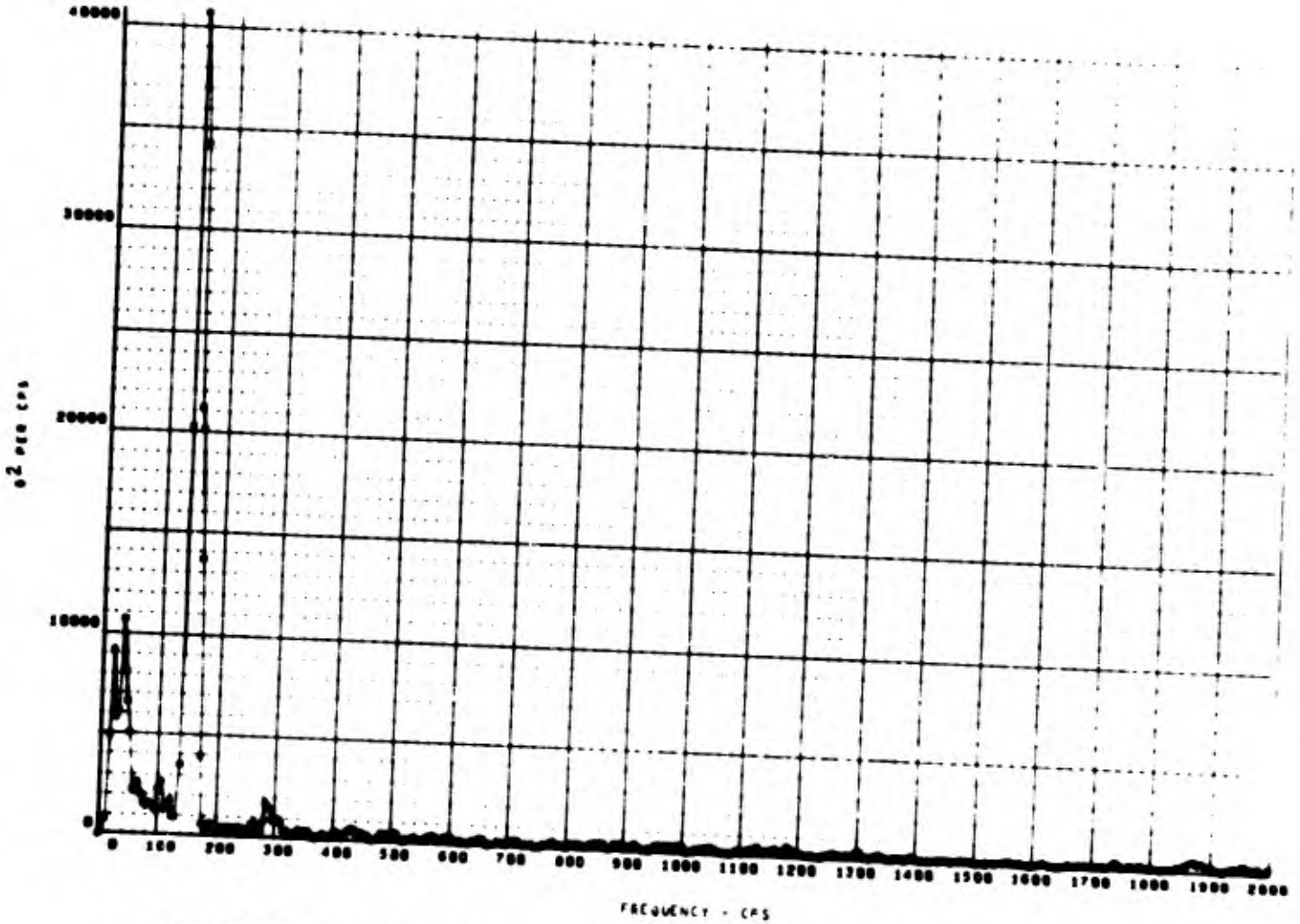

Fig. 26. PSD data, engine 803, test CB-16: accelerometer AE-9; temperature 50°F; after thrust chamber ignition; interval rms value 310.57 g

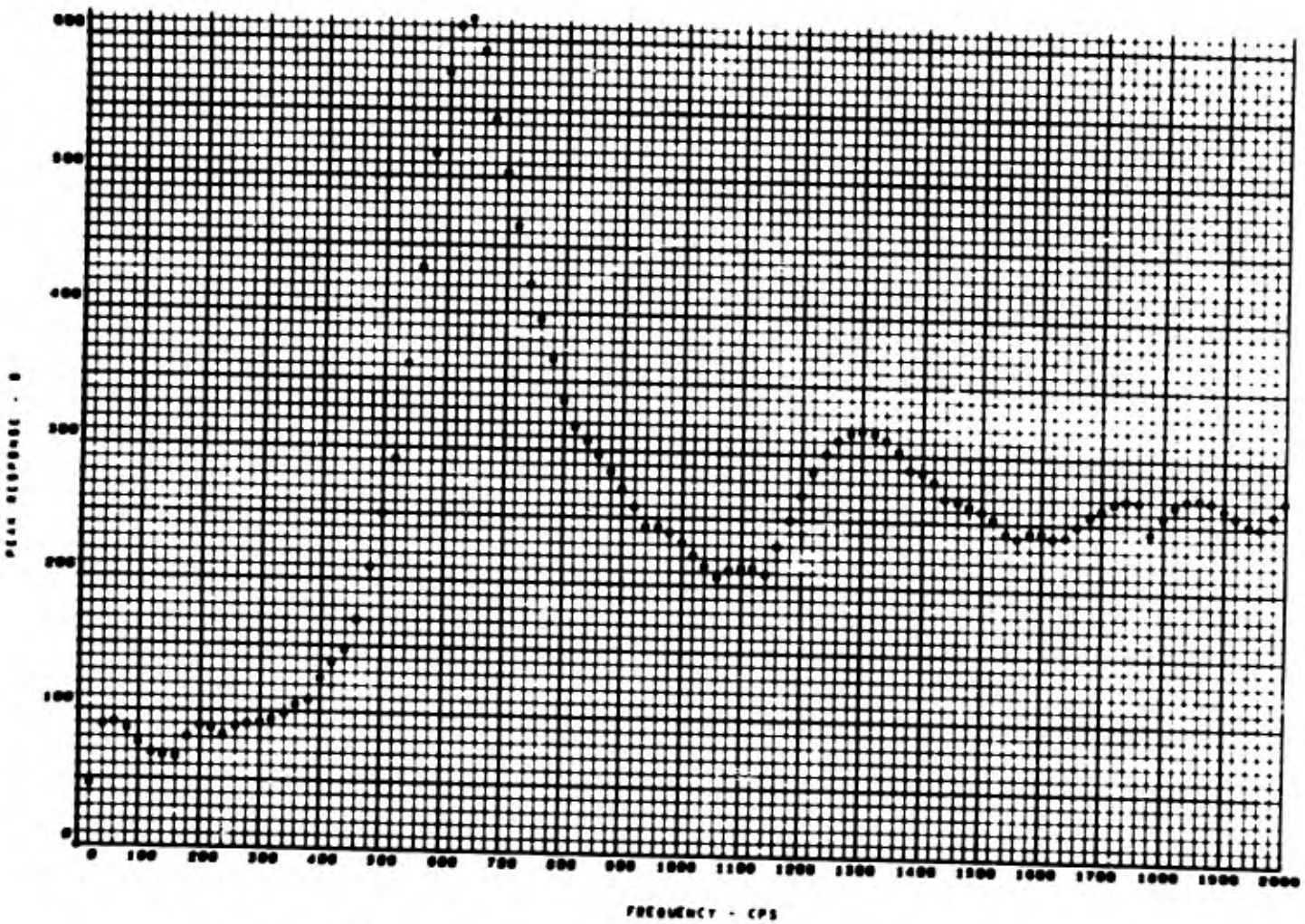

Fig. 27. Shock spectral analysis, engine 803, test AC-09: accelerometer AE-4; temperature 10°F; thrust chamber ignition; Q = 10.0

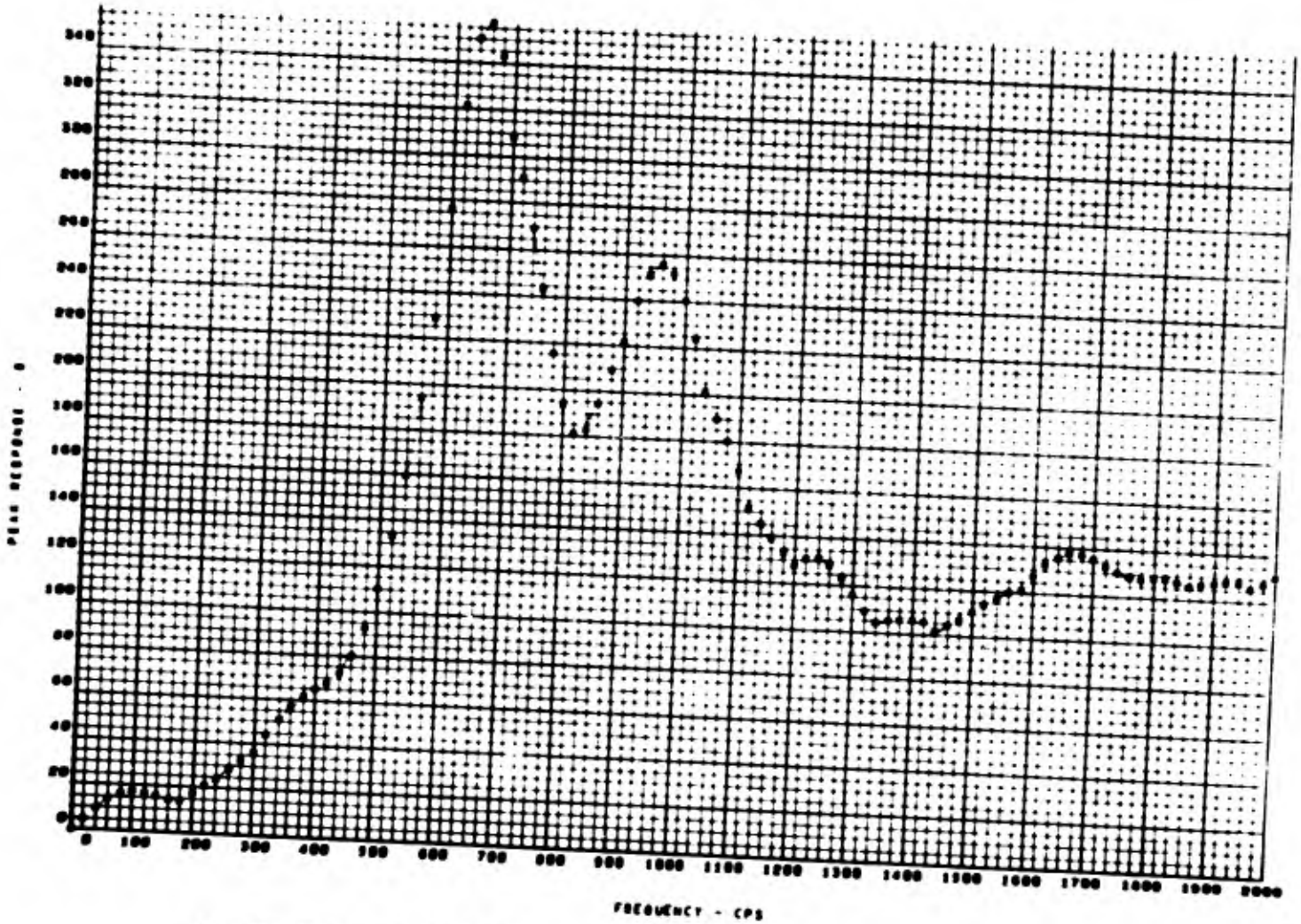

Fig. 28. Shock spectral analysis, engine 805, test AA-04: accelerometer AE-4; temperature 40°F; thrust chamber ignition; Q = 10.0

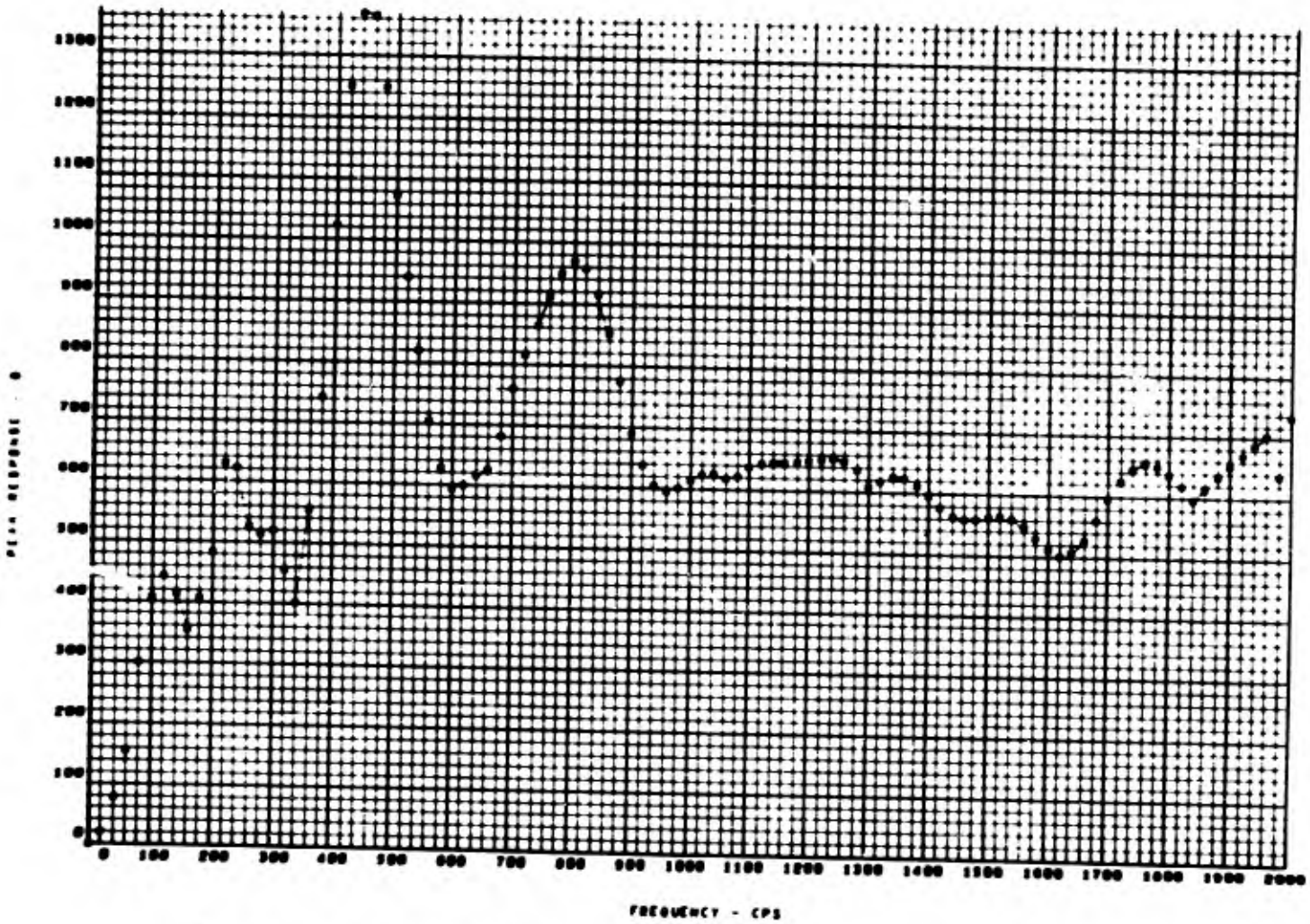

Fig. 24. Shock spectral analysis, engine 805, test AB-01: accelerometer AE-10; temperature 50°F; thrust chamber ignition; Q = 10.0

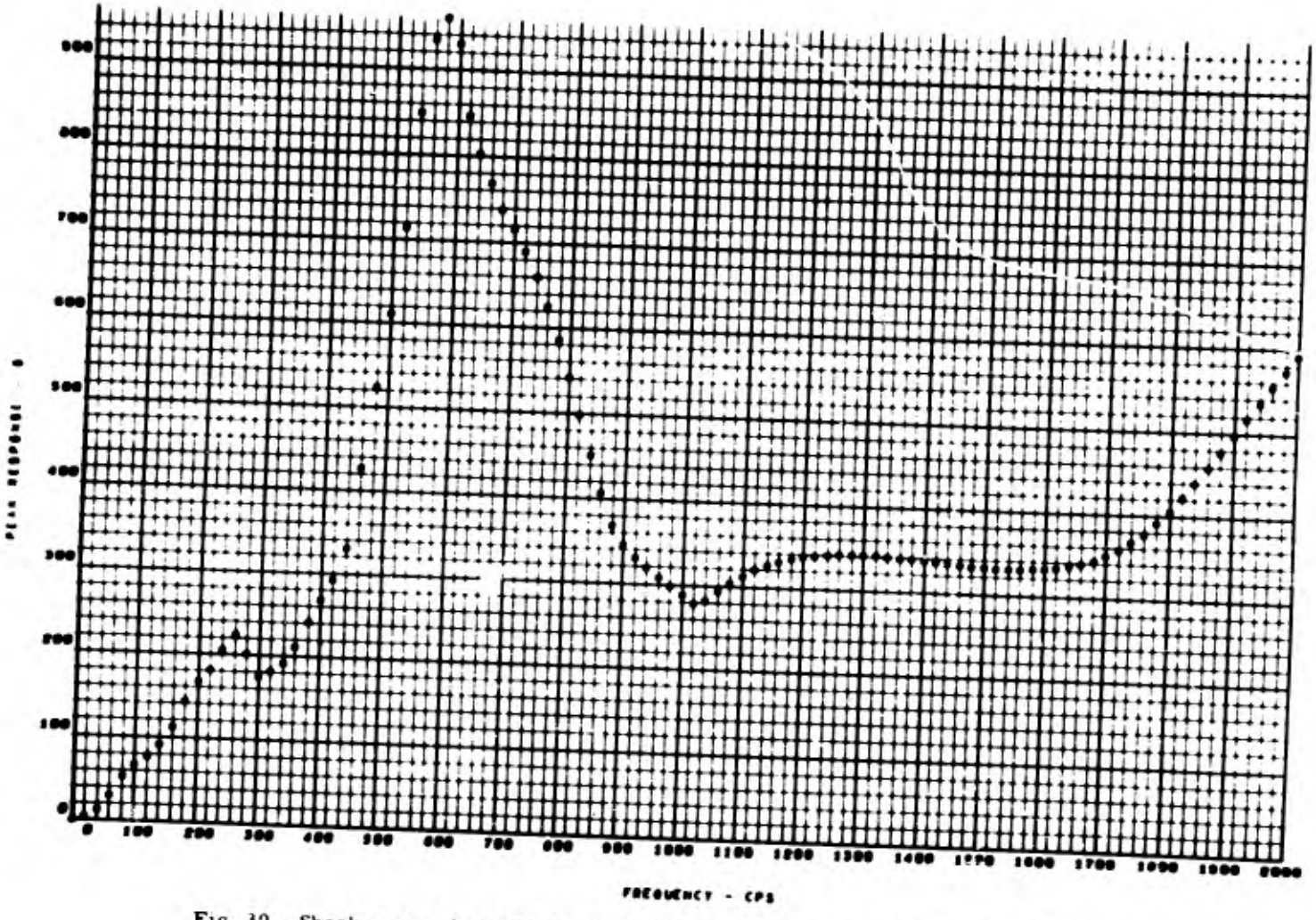

Fig. 30. Shock spectral analysis, engine 803, test BA-18: accelerometer AE-10; temperature 10°F; thrust chamber ignition; Q = 10.0

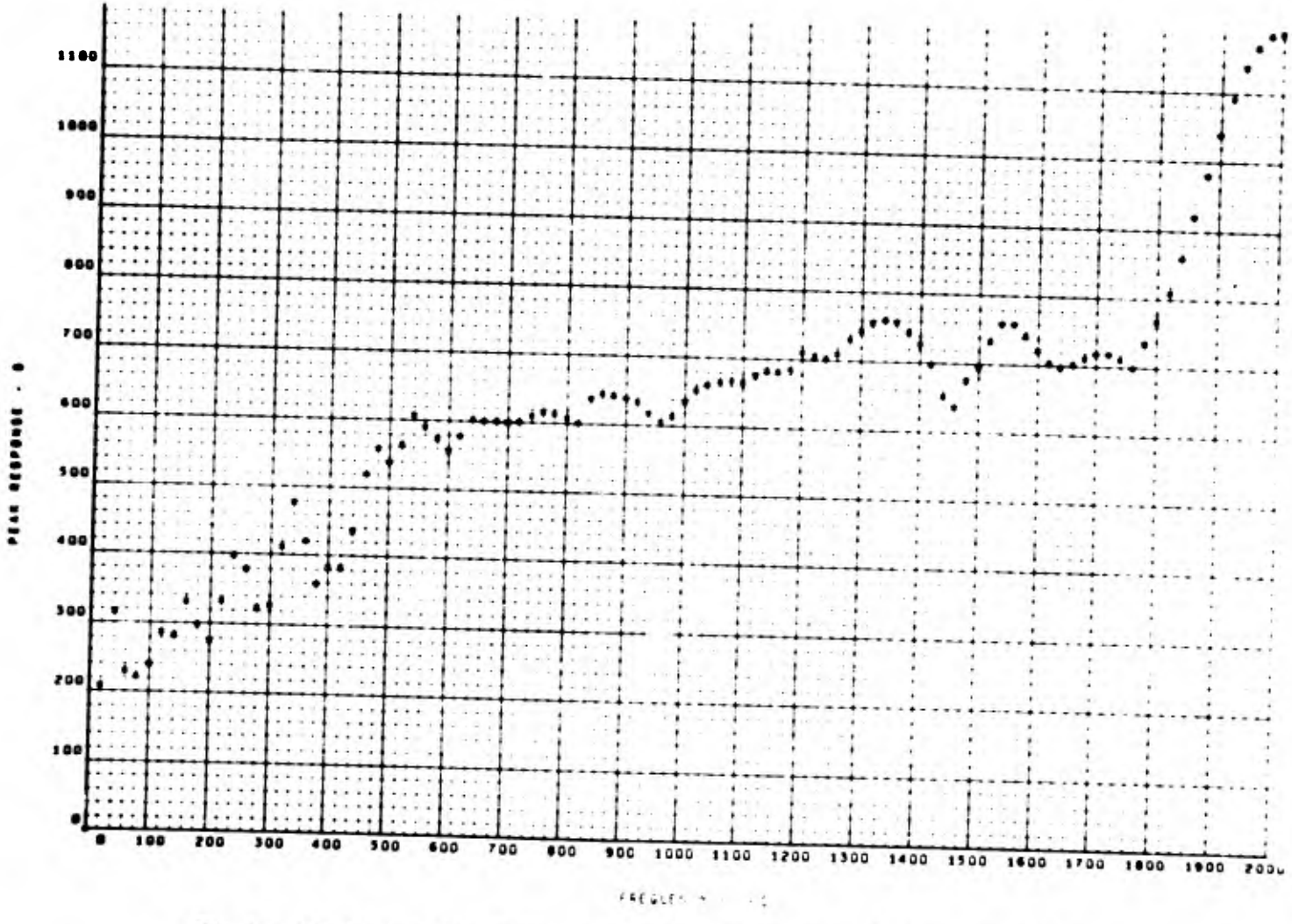

Fig. 31. Shock spectral analysis, engine 803, test CB-16: accelerometer AE-10; temperature 50°F; thrust chamber ignition; Q = 10.0

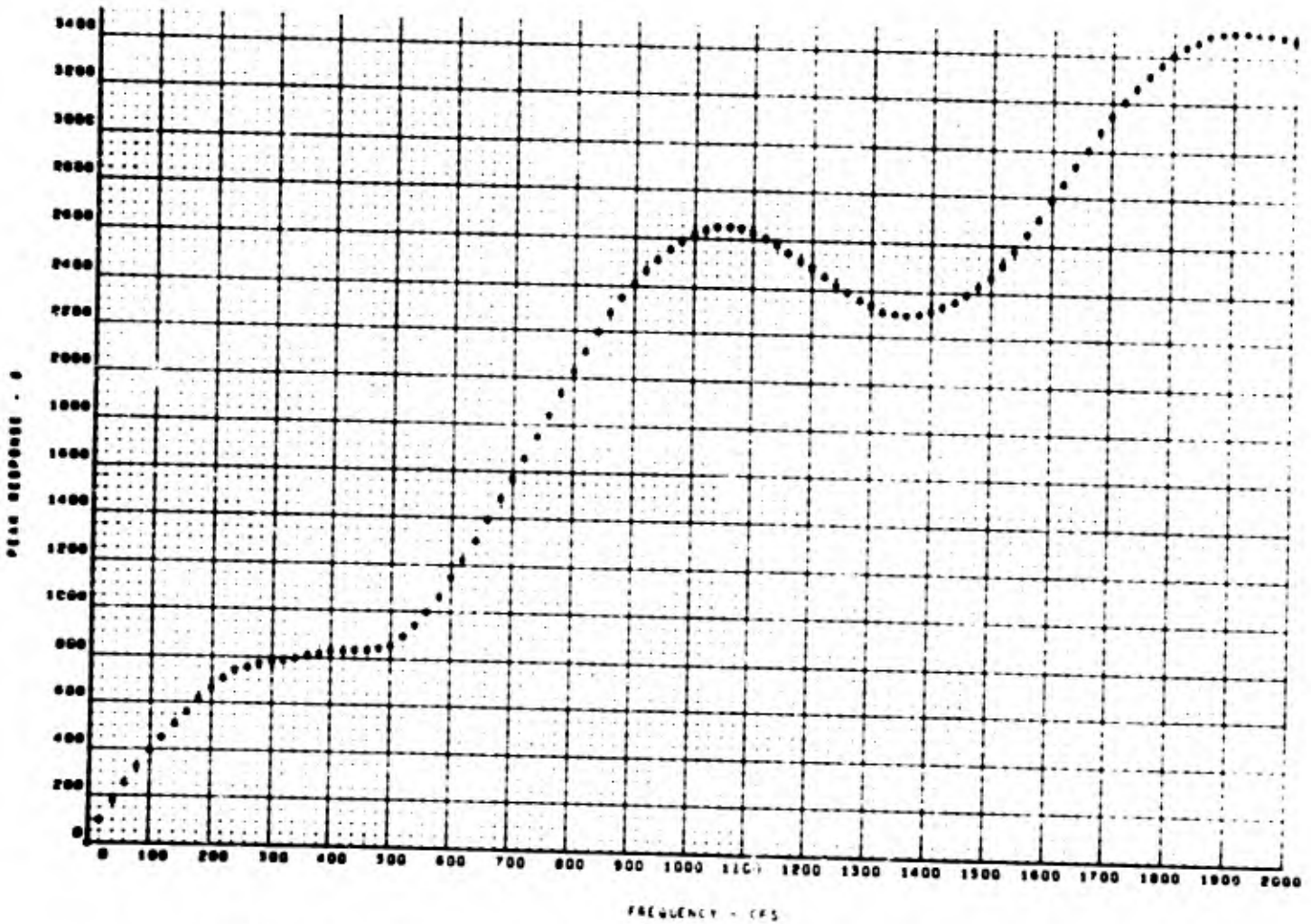

Fig. 32. Shock spectral analysis, engine 803, test CB-14: accelerometer AE-7; temperature -10°F; thrust chamber ignition; Q = 10.0

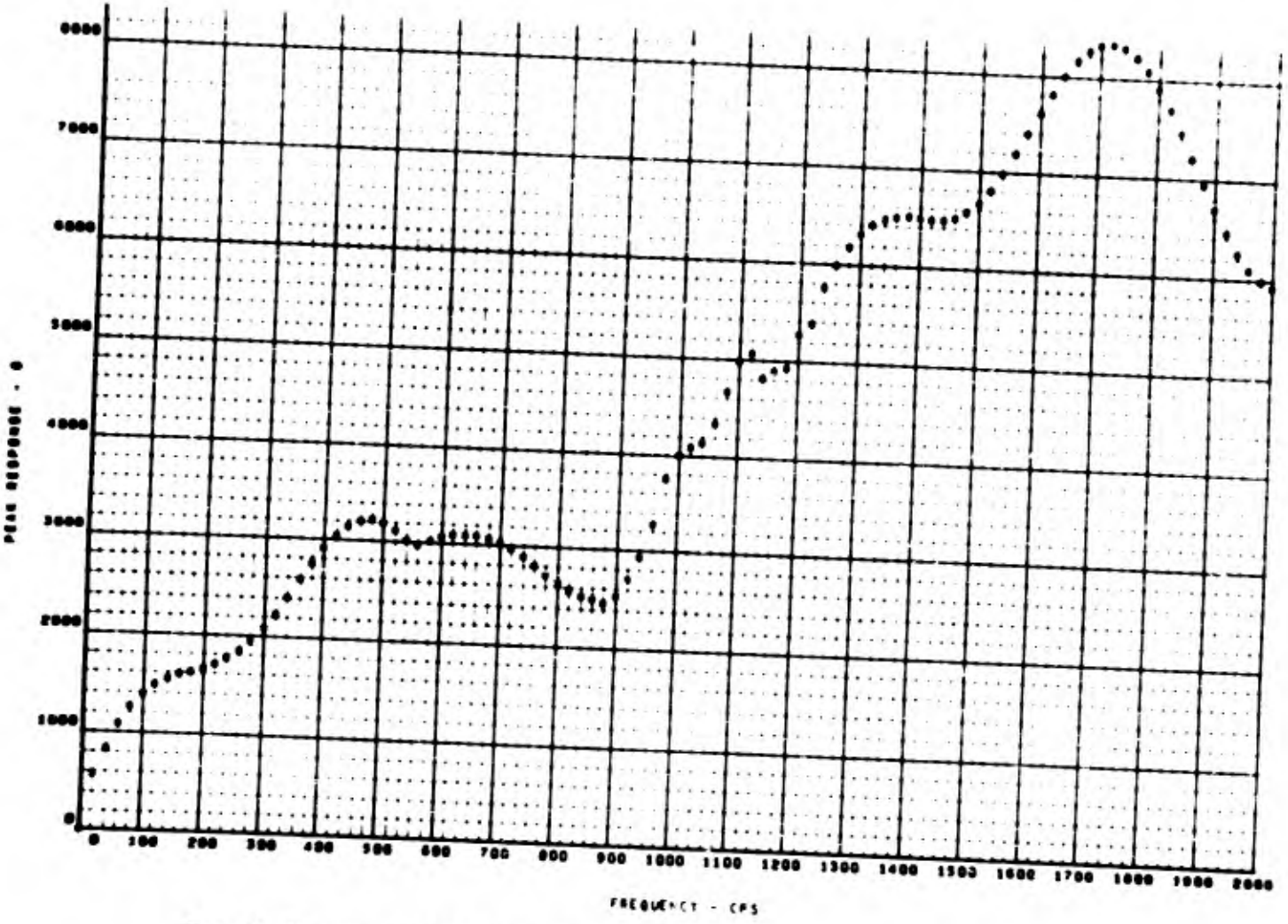

Fig. 33. Shock spectral analysis, engine 803, test CB-15: accelerometer AE-7; temperature 50°F; thrust chamber ignition; Q = 10.0

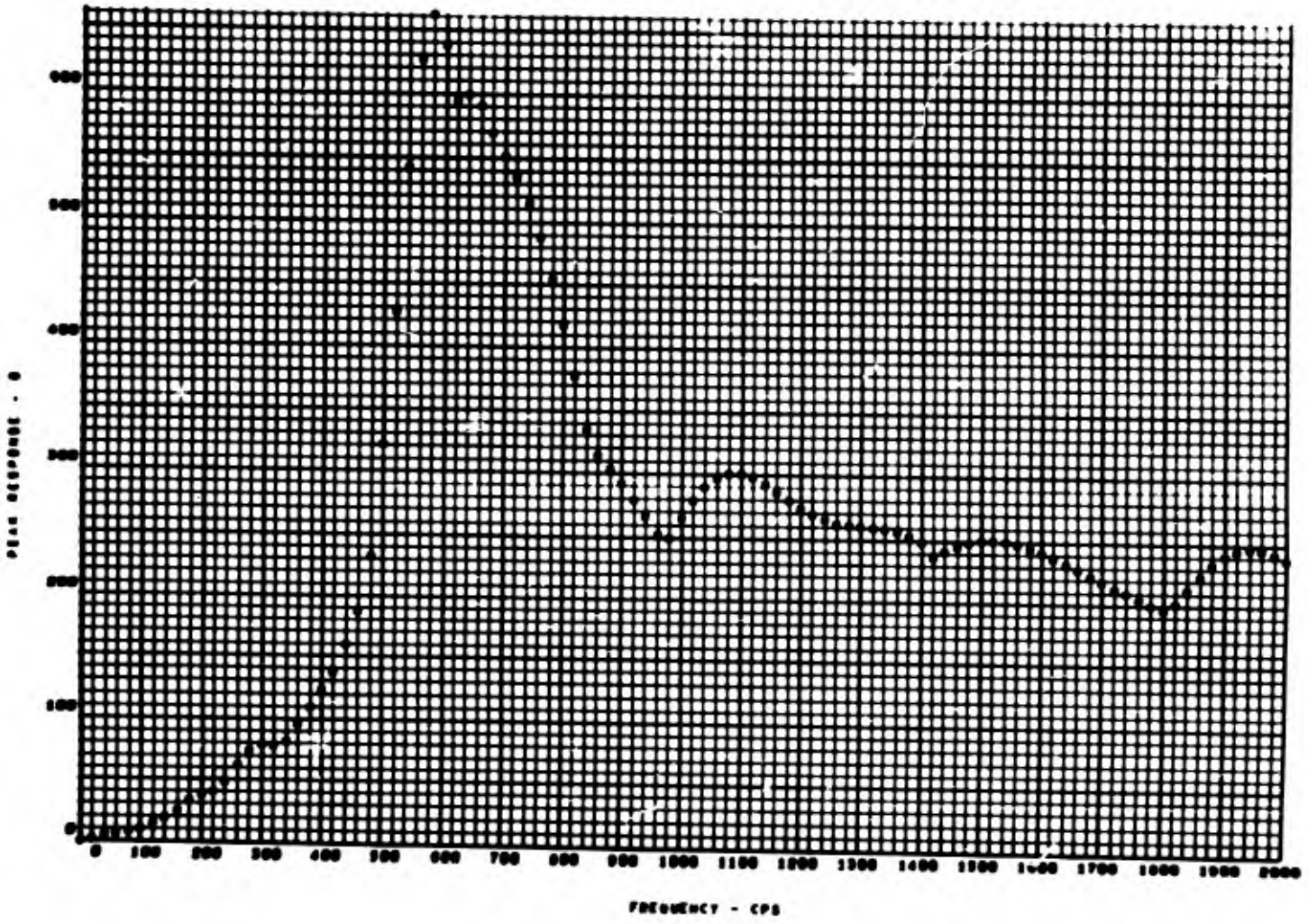

Fig. 34. Shock spectral analysis, engine 803, test AC-14: accelerometer AE-3; temperature 10°F; thrust chamber ignition; Q = 10

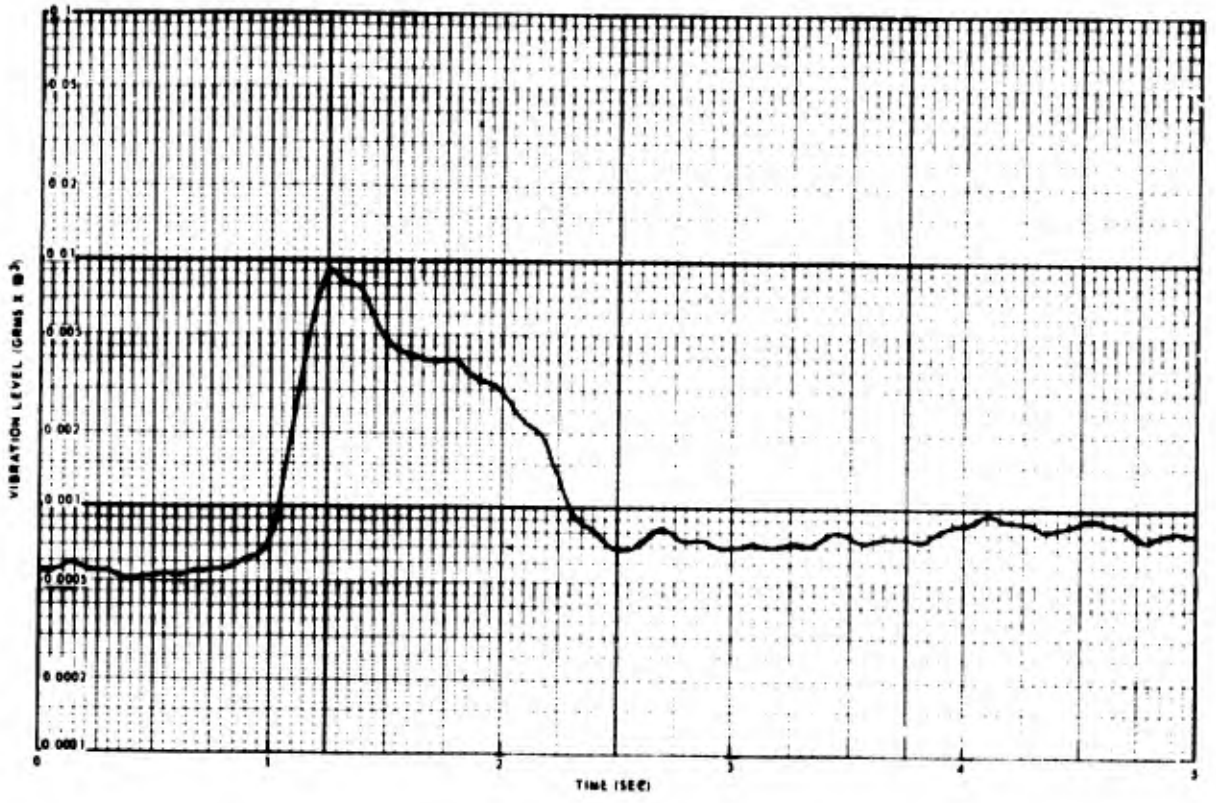

Fig. 35. Accelerometer AE-10, rms g time history plot for test CB-16

Test firing AB-01 resulted in a hard start and generated peak g acceleration levels more than 10 times greater than the first six tests. Data from 9 of the 10 accelerometers were poor because of amplifier saturation, zero shift, and fractured accelerometer mountings; however, data from accelerometer AE-10 (electronic gate) were very good.

Table 10 also shows that tests AC-09 through AC-14 of the ignition confidence tests (AC-01 through AC-14) generated peak g levels greater than tests AC-01 through AC-08 by a factor of 3. Tests AC-09 through AC-14 were conducted at lower propellant and hardware temperatures, and the test results showed a preliminary correlation of greater peak shock levels at thrust chamber ignition with decreasing temperatures.

Low-temperature tests BA-18 and BA-20 of the mission simulation tests evidenced peak g ignition shock levels significantly greater than the average ignition shock levels observed during the low-temperature tests of the AC test series. However, review of the test data revealed that the fuel and thrust chamber injector temperatures were significantly below 0 F at start for tests BA-18, BA-20, and BA-21. Only three accelerometers produced valid data during tests BA-21 and BA-22, prohibiting a comprehensive evaluation and correlation of these test accelerometer results with other AEDC test data. However, the available accelerometer data listed in Table 10 and evaluation of the engine performance data indicate test BA-21 ignition shock levels were greater than the average low-temperature test levels. Table 11 shows thrust chamber ignition peak g and force levels measured during tests CA-01 through CB-16. Test CB-06 was considered a typical run because engine performance and operation were as predicted; therefore, data for this have been used throughout the remainder of this section for comparison purposes.

Tests CB-08, CB-09, CB-12, CB-13, and CB-14 were low-temperature tests established to evaluate low-temperature ignition shocks. The results of these tests showed average ignition peak shock levels of 1.5 and 4 times the levels obtained during test CB-06. The subzero cold-test data for BA-18 and BA-20 indicated average ignition peak shock levels 10 times greater than test CB-06. Tests CB-15 and CB-16 were fuel-lea ' tests during the

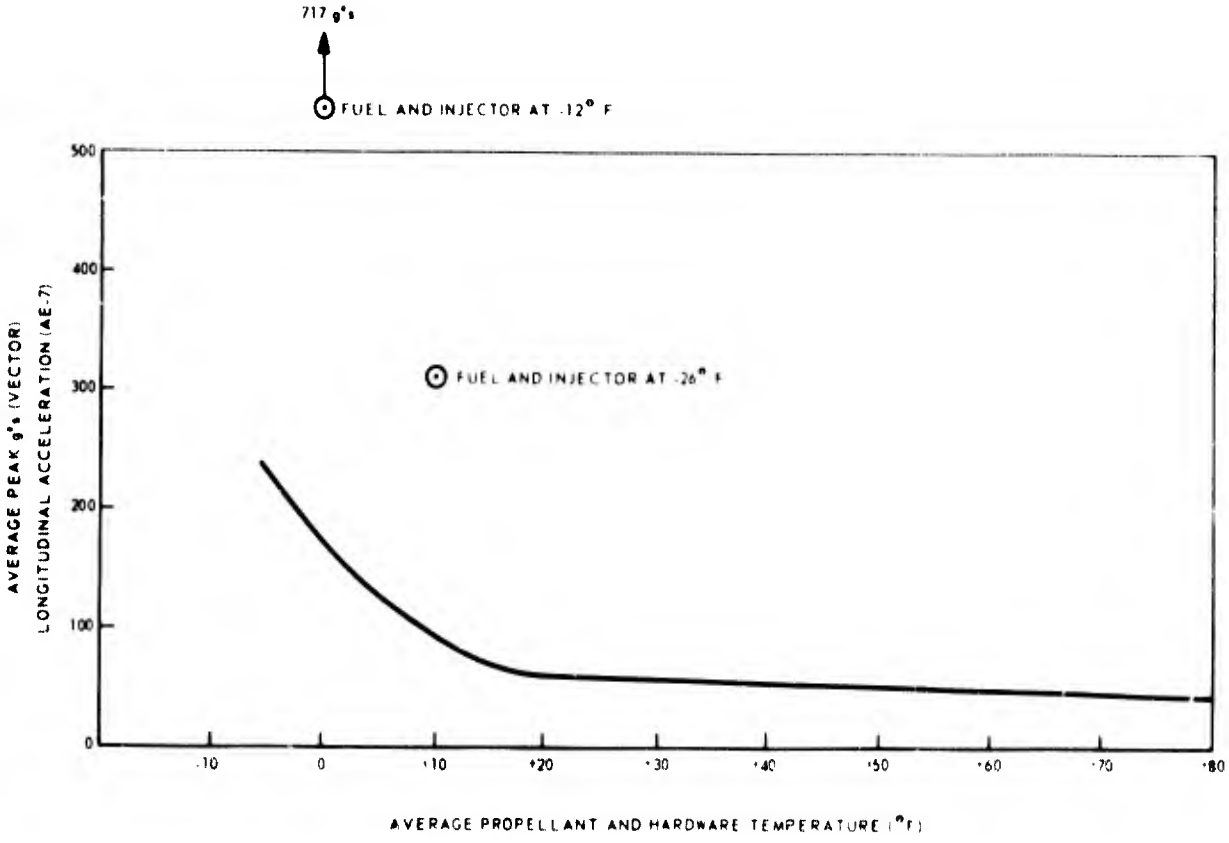

Fig. 36. Summary relation of ignition shock and propellant hardware temperature

malfunction series and resulted in hard starts. The individual accelerometers for tests CB-15 and CB-16 showed thrust chamber ignition peak g levels from 2 to 67 times the levels observed during test CB-06. A complete set of force data was not available because of strain gage FSA-4 malfunction; however, by extrapolating the available data, the computed total force loads at ignition were 15,980 lb and at least 18,464 lb for tests CB-15 and CB-16, respectively. All of the strain gage levels shown in Table 11 are the peak values recorded during the start transient. Figure 18 shows good time correlation between chamber pressure, accelerometer, and strain gage data, except for accelerometer measurement AE-7 during test CB-16. This measurement evidenced a zero shift, and the accelerometer was sheared off at the mounting stud during the test. Figure 19 shows that the thrust buildup data of strain gage FSA-2 were approximately three times faster during tests CB-15 and CB-16 than for test CB-06 (5 to 6 msec vs 16 msec). The average rms g levels for each test shown in Table 12 correlated very well, except for the fuel-lead test CB-16 where the level was 14 times greater than the average levels observed during CB-06. However, this observation is based on the very limited data shown in Table 12, since accelerometers AE-1, 2, 4, 8, 9, 1A, and 16 gave little or no data during tests CA-01 through CB-16.

The PSD plots show that the greatest acceleration density levels occur at about 900, 1600, and 1800 cps. In most of the tests, the highest level occurs at 900 cps, which correlates with the oxidizer-pump impeller rotational speed. The peak occurring at 1600 cps correlates with the fuel-pump impeller rotational speed, and the 1800-cps frequency is the first harmonic of the 900-cps peak frequency. The PSD plots are dynamic data results during a 0.5-sec period immediately after thrust chamber ignition, except the plots for test AA-04 which were made during the start transient conditions for comparative analyses. Test AA-04 is a typical test during the initial test series with dynamic data results similar to test CB-06. The PSD data shown for the electronic gate in Fig. 23 show that the predominant frequencies occurred between 400 and 500 cps. The shock mounting of the electronic gate resulted in lowering its natural frequency and damping the high

acceleration density levels (usually occurring at 900 cps) by a factor of 15. Results of the PSD analysis in Fig. 25 indicate that erratic vibration conditions were present after thrust chamber ignition for the duration of test CB-16 (about 5 sec). The acceleration density levels varied from 2 to 20 g^2/cps at no specific predominant resonant frequencies.

Shock spectral plots (Figs. 27 through 34) show typical peak response g vs frequency characteristics from accelerometer data during nominal temperature tests, hard-start test (AB-01), low-temperature tests, and fuel-lead tests. The maximum peak response g level for the same accelerometer (AE-4) during the low-temperature test (AC-09) was greater by a factor of 2 at the same frequency than for a nominal temperature test (AA-04) as shown in Figs. 27 and 28, respectively. The shock spectral analyses from the electronic gate data for tests AB-01, BA-18, and CB-16 reveal that the hard start of test AB-01 generated the high maximum peak response, 1365 g, and that the predominant frequencies occurred at 450, 580, and 2000 cps for AB-01, BA-18, and CB-16, respectively. The significant difference in the electronic gate frequency value for test CB-16 occurred because the shock transient lasted for 1.5 sec with a forcing frequency of 3000 cps. That is, the shock-mounted electronic gate assembly was being vibrated at nearly 3000 cps. At nominal temperature, the ignition during fuel-lead test CB-15 generated peak response g levels greater than twice that for the low-temperature oxidizer-lead test CB-14, and approximately 5 times greater than the level for test CB-06, as shown in Figs. 32 and 33.

Figure 35 is an rms g time history plot of the electronic gate accelerometer measurement AE-10 for test CB-16. The plot shows that the highest rms g level occurred at 1.25 sec after start signal, and the shock transient was sustained for 1.5 sec. Thrust chamber ignition occurred at 0.87 sec after start signal during test CB-16, and turbine pump operation was terminated at 5.9 sec by command shutdown.

Conclusions

The average start transient peak g levels were 48 g for the tests conducted within the temperature range +30°F to +100 F. This shock level is slightly less than the average values obtained during the sea-level FWD tests (53 g), slightly higher than the average values recorded during XLR 81-BA-13 and YLR 81-BA-11 engine acceptance tests (23 g), and slightly higher than the 40-g shock test requirements of LMSC 6117D. However, the duration (approximately 1 msec of these levels during the AEDC testing was considerably less than the 8-msec requirement in LMSC 6117D, and therefore generated less total energy.

The dynamic data showed a correlation between lower propellant and hardware temperatures and increasing ignition shock peak g levels as indicated in Fig. 36. The observed ignition shock levels with the hard-mounted engine installation at AEDC were compatible with LMSC 6117D test requirements when all hardware and propellant temperatures were maintained above +10°F. However, tests with temperatures below +10°F, and especially with the subzero fuel and thrust chamber injector temperatures experienced during AEDC tests BA-18, 20, and 21, produced ignition shocks greater than the 6117D test requirements. The engine hardware and installation demonstrated the capability of withstanding these high shock transients with no detrimental effects resulting from the adverse temperature conditions. However, the dynamic data results indicate that a lower temperature limit of 0°F at ignition should be established, considering (a) the significant increase in altitude ignition shock levels at temperatures below zero (142 peak g at 0°F to 717 maximum peak g at temperatures below 0°F), and (b) the dynamic qualification test requirements for vehicle hardware mounted in proximity to the engine. The low-temperature tests (0°F) conducted with strain gage instrumentation showed no significant change in peak thrust level at ignition, indicating that the higher peak acceleration levels observed were primarily the result of a more rapid rise in chamber pressure during propellant ignition with no indication of a significant increase in ignition peak thrust overshoot.

The highest acceleration levels recorded during the altitude FWD engine tests were observed during test AB-01; however, the levels recorded during the fuel-lead tests, especially test CB-16, were significantly greater than the LMSC 6117D test requirements.

The lowest propellant temperatures predicted for flight are not the bulk temperature in the tanks, but those injected into the thrust chamber from the pump discharge lines which are opened to vacuum during propellant venting. Analysis indicates that the probability of the temperature of propellants in the lines decreasing below 0°F is small. Therefore, ignition shocks predicted for Gemini flights should not exceed the values demonstrated on the engine during the AEDC tests.

Strain gages are a much better tool than accelerometers for evaluating engine hard starts.

SUMMARY

The original USAF model XLR 81-BA-13 rocket engine was designed and developed to provide a multistart primary propulsion system capability for the Gemini Agena target vehicle (GATV). The engine configuration was similar to the basic standard Agena model YLR 81-BA-11 engine except for (a) the start system, (b) the main propellant valve sequencing which was changed because of removal of pressure switches from the engine control circuit, and (c) associated electrical system modifications. The main propellant valve sequencing provided a fuel-lead ignition sequence in the main thrust chamber under normal operating conditions, creating a difference from the oxidizer-lead designed into the YLR 81-BA-11 engine. Extensive sea-level subassembly and engine testing and simulated altitude testing at a maximum of 120,000 ft were accomplished during development and preliminary flight rating tests (PFRT).

During the first flight of the multistart engine on GATV 5002 on 25 October 1965, premature engine shutdown occurred during the first engine start sequence. Engine shutdown caused propellant flow from the main tanks to stop, but the pressurization system continued to pressurize the small ullage volumes, eventually rupturing the tanks. Tank rupture allowed propellants to mix and react, destructing the vehicle. The postflight failure analysis resulted in the conclusion that the most probable cause of the flight failure was a hard start. In the main combustion chamber of the rocket engine, a hard start is not a detonation but a result of a reaction occurring at a very high rate. Less probable causes of the failure were pyrotechnic separation shock damage, and inadvertent engine shutdown by the engine electronic gate.

Corrective action requirements were generated on the basis of results of the postflight analysis, a propulsion system and vehicle aft rack design review, and a symposium on ignition of hypergolic propellants. It was recommended that (a) the XLR 81-BA-13 engine be converted for a thrust chamber oxidizer-lead start sequence similar to the YLR 81-BA-11 engine, (b) shock mounting be incorporated for certain engine electrical control components, and (c) the electronic gate shutdown capability be disabled during ascent burn operation. Test requirements were established to verify adequacy of the design changes and demonstrate flightworthiness of the modified engine configuration. Results of a symposium on hypergolic ignition indicated that one significant test requirement was not included in the original XLR 81-BA-13 engine development and PFRT programs. This was engine testing at an altitude which properly simulated the hard vacuum that exists during flight. Therefore, an engine modification and test program was planned; it required reliable ignition demonstration during hard vacuum simulation tests at 250,000 ft before the target launch date for GATV 5003. This required an accelerated, maximum success schedule. Consequently an Air Force, Aerospace, NASA, and industry team effort and maximum priorities were necessary to accomplish the program according to the proposed schedule. Project Sure Fire was established to manage the engine modification and test program, and activity was initiated early in November 1965.

Vibration, shock, and hot-fire tests were conducted in January and February 1966 as part of the engine sea-level flightworthiness demonstration program. Satisfactory structural design of the new and modified component installations was verified. The 42 hot-fire tests demonstrated satisfactory operation and sequencing of the modified engine configuration, and verified successful implementation and checkout of the modified engine test and servicing procedures. The sea-level FWD test program provided high confidence that the modified engine configuration provided the desired transient operating and sequencing characteristics over the range of specification temperatures, pressures, and voltages. Consequently, the simulated altitude FWD tests were allowed to proceed without further design change, with the objective of demonstrating that these transient characteristics would provide safe and reliable ignition and operation in a flight environment.

A total of 43 engine FWD tests at simulated altitudes ranging from 257,000 to 453,000 ft and two checkout firings at 85,000 ft were conducted during the period of 7 February to 2 April 1966. The ignition confidence, simulated mission, low-temperature, and malfunction tests at an average simulated altitude of 356,000 ft successfully demonstrated the high-altitude flightworthiness of the modified XLR 81-BA-13 engine. Sufficient confidence in the reliability of engine ignition had been gained from the 27 Phase I and Phase II altitude tests completed by 4 March 1966 to assure GATV 5003 flightworthiness and allow commitment of the modified engine design to flight. Significantly, the postulated

GATV 5002 flight failure mode was confirmed during the altitude malfunction tests, which showed that a fuel lead on the XLR 81-BA-13 engine would produce hard starts when tested at the proper altitude and that a reasonably high probability of hardware damage exists. Reevaluation of vehicle 5002 data indicated that the engine damage incurred during the flight was similar to that observed during the last fuel-lead test. In addition to the successful flightworthiness demonstration of the modified engine, the altitude tests provided data on altitude ignition characteristics over a temperature range of +100°F to below zero.

At the same test conditions, the XLR 81-BA-13 engine thrust chamber produced significantly different ignition characteristics for a fuel-lead start sequence as compared with an oxidizer lead. Therefore, a comparative evaluation of the differences in ignition characteristics was made on the basis of test data for the full-scale (engine) thrust chamber, subscale thruster, and the engine gas generator assembly. The hardware design factors (such as feed configuration, injector type, residence time, etc.) which can affect ignition were reviewed, and the dependent conditions existing in the chamber at ignition, i.e., mixture ratio, density, ignition delay, and ignition chemistry, were recorded or derived as the test variables of altitude, temperature, and propellant lead were changed. The requirements for a reliable ignition were considered. The proper pressure and temperature must be generated in the fuel-oxidizer mixture during the induction period just prior to ignition, and a sufficient amount of oxidizer must be present during induction to prevent long ignition delays or quenching of the reaction.

CONCLUSIONS

Significant conclusions derived from Project Sure Fire are:

1. An oxidizer-lead start sequence is optimum for the XLR 81-BA-13 engine thrust chamber, providing low and acceptable ignition shock levels over the range of required operating conditions.

2. Significant differences exist between oxidizer and fuel-lead ignition characteristics in the XLR 81-BA-13 thrust chamber.

3. The GATV 5002 flight-failure analysis conclusion that an engine hard start occurred was proved correct; the postulation that the engine hard start was due to a fuel-lead start sequence was also correct.

4. Fuel-lead hard starts yield high probability of damage to the thrust chamber assembly.

5. Testing at the proper simulated altitude to determine engine ignition reliability is a necessary and extremely important phase of spaceflight engine development.

REFERENCE

1. Lockheed Missiles and Space Company, "General Environmental Specification for Equipment of the Agena and Associated Payload," LMSC 6117D, June 1963

* * *

BLANK PAGE

DYNAMIC ANALYSIS OF COMPLEX STRUCTURES*†

M. D. Benton, G. K. Hobbs
Hughes Aircraft Company
El Segundo, California

and

J. R. Dickerson
University of Texas
Austin, Texas

A general computer program for the analysis of structures subjected to static and/or dynamic loading environments has been completed. The program includes several modeling features which are of general interest to the dynamicist and the stress analyst confronted with the problem of analyzing today's complex structures.

The general equations of motion are constructed using distributed mass and distributed stiffness characteristics of finite element models, thus providing both mass and stiffness coupling. The ability to include infinitely stiff elements allows modeling elements such as cylinders (described relative to their geometric center) which have protuberances or other elements attached to their periphery. The ability to include flexible and pinned joints as well as zero-mass coordinates in any combination at any station may be used to enhance further the ease and accuracy in modeling a complex structure.

Included in the program are routines which will generate a 12 by 12 matrix for any straight-sided body of revolution with or without longitudinal stringers and for a constant-section, symmetric or nonsymmetric beam. Any element not of those two types may be included by direct placement of externally generated stiffness matrices into the system stiffness matrix.

INTRODUCTION

Many recent spacecraft have been designed primarily by dynamically induced loads, and therefore the analytical models used in the dynamic analysis of these spacecraft must be sufficiently detailed to reflect the dynamic response load gradients. At the same time, the analysis must be sufficiently flexible to allow for rapid synthesis of design loads data and to provide for rapid and extensive parametric studies for structural optimization. As a result of these requirements, a general computer program for the analysis of structures subjected to static and/or dynamic loading environments has been completed.

The general equations of motion are constructed using distributed mass and distributed stiffness characteristics of finite element models, thus providing both mass and stiffness coupling. The distributed mass matrix developed is based on the relationship

$$m_{ij} = \int_0^{\ell} m(x)\, \varphi_i(x)\, \varphi_j(x)\, dx \,. \tag{1}$$

which is similar in form to the standard relationship

*This paper was not presented at the Symposium.

†Development of the methods presented here was sponsored by Hughes Aircraft Company, Space Systems Division, Internal Research and Development funds.

$$k_{ij} = \int_0^{\ell} EI(x)\, \varphi_i''(x)\, \varphi_j''(x)\, dx \tag{2}$$

for the stiffness characteristics of a system.

The ability to include infinitely stiff elements allows modeling elements, such as cylinders, which are described relative to their geometric center and have protuberances or other elements attached to their periphery. The ability to include flexible and pinned joints as well as zero-mass coordinates in any combination at any station may be used to enhance further ease and accuracy in modeling.

Only the available computer core limits the types of internally generated stiffness matrices Presently included is a routine which will generate a 12×12 stiffness matrix for any straight-sided body of revolution with or without variable- or constant-cross-section longitudinal stringers. An example of this type of element is a honeycomb cone, of variable facesheet thickness, and variable core thickness, with tapered longitudinal stringers. A second stiffness routine presently included is for a constant-section, symmetric or nonsymmetric beam. Any extrusion or fabricated section is an example of this type of element. Any element not of these types may be entered by direct placement of externally generated stiffness matrices into the system stiffness matrix.

In practice, the phase-oriented dynamic deflections and internal loads are rarely used properly. However, extension to modal stress analysis including complex deflections overcomes the difficulties encountered. Static deflections and loads are generated by the inversion of the system stiffness matrix when an inverse exists, and by modal techniques for singular (free-free) systems or systems subjected to dynamic loading; i.e., for a fixed system, it is not necessary to incur the expense of an eigenvalue solution unless the solution is required for dynamic loads or for modes and frequencies.

Output from the program includes (a) natural frequencies and mode shapes; (b) phase-oriented dynamic deflections, accelerations, and loads resulting from transient, correlated random, and sinusoidal excitation; (c) static deflections and loads resulting from uniform and nonuniform static loadings; and (d) fatigue information.

EQUATIONS OF MOTION

The behavior of a linear elastic system may be expressed as

$$[M]\{\ddot{q}(t)\} + [C]\{\dot{q}(t)\} + [K]\{q(t)\} = \{F(t)\} \tag{3}$$

where $[M]$, $[C]$, $[K]$ are the $n \times n$ matrices representing the mass, damping, and stiffness, respectively, $\{q(t)\}$ is an independent, or generalized, set of coordinates, and $\{F(t)\}$ is the driving force vector.

If $[C]$ is classical, i.e., a linear combination of $[M]$ and $[K]$, then stationary mode shapes will occur and the analysis is greatly simplified in terms of the size of the equations to be treated. That is, nonproportional damping requires the treatment of a $2n \times 2n$ matrix equation [1] and hence requires almost four times the storage capacity. For this reason, only classical damping will be considered here.

Since most structures of interest are lightly damped, one is justified in solving the nondamped equations of motion. (One may later modify the frequency to take into account heavy damping, since proportional damping is considered.) To solve the equations we proceed as follows: the homogenous solution

$$[M]\{\ddot{q}(t)\} + [K]\{q(t)\} = \{0\}; \tag{4}$$

anticipating a harmonic solution,

$$\{q(t)\} = \{\varphi\}\, e^{i\omega t}. \tag{5}$$

and therefore

$$([K] - \omega^2 [M])\{\varphi\} = \{0\}. \tag{6}$$

After the eigenvalues and eigenvectors are found from Eq. (6), we perform a coordinate transformation on Eq. (3). Let

$$\{q\} = [\varphi]\{\eta\}, \tag{7}$$

where $[\varphi]$ is the modal matrix from Eq. (6). Substituting into Eq. (3) and premultiplying by $[\varphi]^T$

$$[\varphi]^T[M][\varphi]\{\ddot{\eta}(t)\} + [\varphi]^T[C][\varphi]\{\dot{\eta}(t)\} + [\varphi]^T[K][\varphi]\{\eta(t)\} = [\varphi]^T\{F(t)\}. \tag{8}$$

Since the vectors $[\varphi]$ are orthogonal with respect to the mass and stiffness matrices and since we consider only classical damping, then the equations represented by Eq. (8) are uncoupled and may be written as

$$[M]\{\ddot{\eta}(t)\} + [C]\{\dot{\eta}(t)\} + [K]\{\eta(t)\} = \{F(t)\}, \tag{9}$$

which may be solved by the usual methods of differential equations. The results of this solution for $\{\eta_r(t)\}$ represent modal deflections in the rth mode as

$$\{q_r(t)\} = [\varphi]\{\eta_r(t)\}. \tag{10}$$

STIFFNESS MATRIX

The stiffness method is a means of analyzing complex structures by idealizing a structure as a set of finite structural elements connecting nodal points. The loads acting on the structure are replaced by equivalent forces acting only at the nodal points, and the deformation of the structure is defined by the displacements of the nodal points. For each element, forces and small deformations at the nodal points are linearly related to each other through a set of constants which are based on the elastic properties and the geometry of the element.

In structural mechanics, the relation between force and deflection is written

$$\{F\} = [K]\{x\}, \tag{11}$$

where $\{F\}$ is the vector of forces resulting from displacements $\{x\}$ at the nodal points. Thus, any term of the stiffness matrix $[K]$ may be found by noting that the element k_{ij} is the force on coordinate i for a unit displacement of coordinate j, with all other displacement restrained to be zero.

The stiffness matrix for the entire structure is found by superposition of each of the individual elemental stiffness matrices after the coordinate system of the element has been transformed to coincide with the coordinate system of the structure. This transformation is accomplished through a compatibility relation

$$\{q\} = [Com]\{x\}, \tag{12}$$

where $\{x\}$ is the elemental nodal displacements and $\{q\}$ is the system displacements. The construction of $[Com]$ is discussed later in this section.

Adding all of the elemental stiffness matrices by superposition results in a system force-displacement relationship

$$\{F_s\} = [K_s]\{q\}, \tag{13}$$

where $\{F_s\}$ is a vector of system nodal forces and $\{q\}$ is a vector of system nodal displacements.

The terms in the elemental stiffness matrix may be determined from energy considerations, with each term given by

$$k_{ij} = \frac{\partial^2 \nu}{\partial x_i \partial x_j} \tag{14}$$

where ν is the total strain energy. This relation is a direct consequence of the principle of least work.

Calculation of the stiffness coefficients using the strain energy approach is direct but often quite involved. Fortunately, just as the forces at the nodal points are related through conditions of equilibrium, a similar relationship holds for the stiffness coefficients. For example, in an element with two nodal points, only the coefficients at one of the nodes need be determined, for the remaining coefficients can be found by a simple transformation. The stiffness matrix can be partitioned to separate the nodal points such that

$$\left\{\frac{F_1}{F_2}\right\} = \left[\begin{array}{c:c} k_{11} & k_{12} \\ \hdashline k_{21} & k_{22} \end{array}\right] \left\{\frac{x_1}{x_2}\right\} \tag{15}$$

or

$$\{F_1\} = [k_{11}]\{x_1\} + [k_{12}]\{x_2\} \tag{16}$$

$$\{F_2\} = [k_{21}]\{x_1\} + [k_{22}]\{x_2\} \tag{17}$$

Forces at one node are related to forces at the other node through the equation

$$\{F_2\} = [\gamma]\{F_1\} \tag{18}$$

Substitution of Eq. (18) into Eq. (17) yields

$$[\gamma]\{F_1\} = [k_{21}]\{x_1\} + [k_{22}]\{x_2\} \tag{19}$$

Solving for $\{F_1\}$ and equating the coefficients of $\{x_1\}$ and $\{x_2\}$ to the corresponding coefficients in Eq. (16) and then rearranging yields

$$[k_{21}] = [\gamma][k_{11}] \tag{20}$$

$$[k_{22}] = [\gamma][k_{12}] \tag{21}$$

Since the stiffness matrix is symmetric,

$$[k_{12}] = [k_{21}]^T = [k_{11}][\gamma]^T \tag{22}$$

Substitution of Eq. (22) into Eq. (21) yields

$$[k_{22}] = [\gamma][k_{11}][\gamma]^T \tag{23}$$

The complete stiffness matrix for the element becomes

$$[k] = \left[\begin{array}{c:c} [k_{11}] & [k_{11}][\gamma]^T \\ \hdashline [\gamma][k_{11}] & [\gamma][k_{11}][\gamma]^T \end{array}\right] \tag{24}$$

Elements of k_{11} may be determined from Eq. (14) or by inverting a flexibility matrix $[\delta]_{11}$; $[\delta]_{11}$ relates displacements at node 1 for unit forces at node 1, while node 2 is restrained. Thus,

$$\{x_1\} = [\delta_{11}]\{F_1\} \tag{25}$$

The δ_{ij}'s are found from

$$\delta_{ij} = \frac{\partial^2 \nu}{\partial F_i \partial F_j} , \tag{26}$$

where ν is the total strain energy. Since the strain energy is usually easier to formulate in terms of applied forces rather than deformations, it is generally easier to determine $[\delta_{11}]$ than $[k_{11}]$.

To illustrate this technique, consider the problem of a conical beam with linearly varying sectional properties. The coordinate system and definition of positive forces and displacements are shown in Figs. 1 and 2.

Fig. 1. Representation of conical beam with linearly varying sectional properties, coordinate system and definition of positive forces and displacements

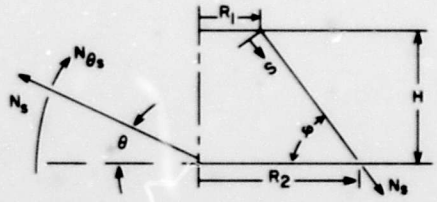

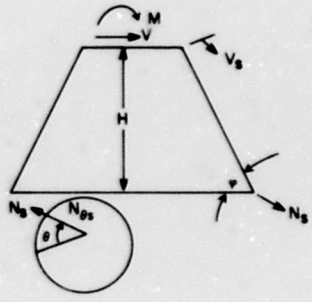

Fig. 2. Conical beam

Equilibrium equations for a general membrane shell of revolution are

$$\frac{\partial}{\partial s}(rN_{\theta s}) + \frac{\partial}{\partial \theta}(N_{\theta s}) - N_\theta \cos\varphi = 0$$

$$\frac{\partial}{\partial s}(rN_s) + \frac{\partial}{\partial \theta}(N_\theta) + N_{\theta s}\cos\varphi = 0 \tag{27}$$

$$\frac{N_s}{r_1} + \frac{N_\theta}{r_2} = 0 ,$$

where N_θ is the shear associated with $N_{\theta s}$ and N_s.

For a conical shell

$$r_1 = \infty$$

$$r_2 = \frac{r}{\sin\varphi}$$

$$r = R_1 + S\cos\varphi$$

$$0 \le S \le \frac{H}{\sin\varphi}$$

Thus, the equations of equilibrium become

$$r\frac{\partial N_s}{\partial s} + \cos\varphi N_s + \frac{\partial}{\partial\theta}(N_{\theta s}) - N_\theta \cos\varphi = 0$$

$$r\frac{\partial}{\partial s}(N_{\theta s}) + \cos\varphi N_{\theta s} + \frac{\partial}{\partial\theta}(N_\theta) + N_{\theta s}\cos\varphi = 0 \qquad (28)$$

$$N_\theta = 0$$

or

$$r\frac{\partial N_s}{\partial s} + \frac{\partial N_{\theta s}}{\partial\theta} + \cos\varphi N_s = 0$$

$$r\frac{\partial N_{\theta s}}{\partial s} + 2N_{\theta s}\cos\varphi = 0 \qquad (29)$$

For the general case where

$$N_s = \bar{N}_s \cos\varphi$$

$$N_{\theta s} = \overline{N_{\theta s}} \sin\varphi ,$$

Eqs. (29) reduce to

$$r\frac{\partial \bar{N}_s}{\partial s} = \bar{N}_s \cos\varphi + \overline{N_{\theta s}} = 0$$

$$r\frac{\partial N_{\theta s}}{\partial s} + 2\overline{N_{\theta s}}\cos\varphi = 0. \qquad (30)$$

The solution to Eqs. (30) is

$$\overline{N_{\theta s}} = \frac{A}{r^2}$$

$$N_s = \frac{1}{r}\left(\frac{A}{r\cos\varphi} + B\right) ,$$

where A and B are constants which are evaluated from end conditions.

$$V = \int_0^{2\pi} N_s \cos\phi\cos\theta r\, d\theta - \int_0^{2\pi} N_{\theta s}\sin\theta r\, d\theta$$

$$= \int_0^{2\pi}\left(\frac{A}{r\cos\phi} + B\right)\cos\phi\cos\theta r\, d\theta - \int_0^{2\pi}\frac{A}{r}\sin^2\theta\, d\theta$$

$$= \pi B\cos\phi . \qquad (31)$$

$$M = \int_0^{2\pi} N_s \sin\phi r\cos\theta r\, d\theta + \int_0^{2\pi} N_{\theta s}\sin\theta s\sin\phi r\, d\theta$$

$$= \int_0^{2\pi}\sin\phi\cos^2\theta\left(\frac{A}{R_1\cos\phi} + B\right)R_1\, d\theta$$

$$= \pi\sin\phi\left(\frac{A}{R\cos\phi} + B\right)R_1 \qquad (32)$$

Therefore, from Eqs. (31) and (32),

$$B = \frac{V}{\pi \cos \phi}$$

$$A = \left(\frac{M}{\pi \sin \phi} - \frac{VR_1}{\pi \cos \phi} \right) \cos \phi ,$$

thus

$$N_s = \frac{1}{\pi r} \left[\frac{M}{r \sin \phi} + \frac{V \left(1 - \frac{R_1}{r} \right)}{\cos \phi} \right] \cos \theta \qquad (33)$$

$$N_{\theta s} = \frac{\cos \phi}{\pi r^2} \left[\frac{M}{\sin \phi} - \frac{VR_1}{\cos \phi} \right] \sin \theta .$$

The strain energy is

$$U = \frac{1}{2} \int_0^{2\pi} \int_0^{\pi / \sin \phi} \left(\frac{N_s^2}{C_1} + \frac{N_{\theta s}^2}{C_2} \right) r \, ds \, d\theta , \qquad (34)$$

where for an isotropic case $C_1 = Et$ and $C_2 = Gt$. For sandwich shells $C_1 = 2Et_f$ and $C_2 = 2Gt_f$, where t_f = facesheet thickness, E = meridional Young's modulus. If longitudinal stringers are to be added, the thickness in C_1 only is to be increased to account for the added cross-sectional area.

For a linearly varying C_1 and C_2

$$C_1 = C_{10} + \frac{S}{S_1} (C_{11} - C_{10})$$

$$C_2 = C_{20} + \frac{S}{S_1} (C_{21} - C_{20}) ,$$

where

$$C_{10} = C_1 \text{ at } S = 0$$

$$C_{11} = C_1 \text{ at } S = S_1 = H / \sin \phi$$

$$C_{20} = C_2 \text{ at } S = 0$$

$$C_{21} = C_2 \text{ at } S = S_1 = H / \sin \phi .$$

Substituting the linearly varying set of C_i's and integrating Eq. (34) with respect to θ yields

$$U = \frac{1}{2\pi} \int_0^{S_1} \left\{ \frac{1}{rC_1} \left[\left(\frac{M^2}{r^2 \sin^2 \phi} + \frac{2VM}{r \sin \phi \cos \phi} \right) \left(1 - \frac{R_1}{r} \right) + \frac{V^2}{\cos^2 \phi} \left(1 - \frac{2R_1}{r} + \frac{R_1^2}{r^2} \right) \right] \right.$$

$$\left. + \frac{\cos^2 \phi}{r^3 C_2} \left[\frac{M^2}{\sin^2 \phi} - \frac{2MVR_1}{\sin \phi \cos \phi} + \frac{V^2 R_1^2}{\cos^2 \phi} \right] \right\} ds . \qquad (35)$$

Performing the indicated integration and substituting into Eq. (26) yields

$$f_{VV} = \frac{1}{V} \frac{\partial U}{\partial V}_{M=0}$$

$$= \frac{1}{\pi} (J_2 + R_1^2 I_6) , \qquad (36)$$

$$f_{VM} = \frac{1}{M}\left(\frac{\partial U}{\partial V}\right)_{V=0}$$

$$= \frac{1}{\pi}\left(\frac{J_i}{\sin\phi} - R_1 \cot\phi\, I_6\right) \tag{37}$$

$$f_{MM} = \frac{1}{M}\left(\frac{\partial U}{\partial M}\right)_{V=0}$$

$$= \frac{1}{\pi}\left(\frac{I_3}{\sin^2\phi} + \cot^2\phi\, I_6\right) \tag{38}$$

where, for $C_{11} = C_{10}$, $C_{21} = C_{20}$, and $R_1 = R_2$,

$$I_3 = S_1/(R_1^3 C_{11})$$

$$I_6 = S_1/(R_1^3 C_{21})$$

$$J_1 = S_1^2/(2R_1^3 C_{11})$$

$$J_2 = S_1^2/(3R_1^3 C_{11})$$

or, for $C_{11} \neq C_{10}$, $C_{21} \neq C_{20}$, and $R_1 = R_2$,

$$I_3 = \frac{S_1 \ln\left(\frac{C_{11}}{C_{10}}\right)}{R_1^3 (C_{11} - C_{10})}$$

$$I_6 = \frac{S_1 \ln\left(\frac{C_{21}}{C_{20}}\right)}{R_1^3 (C_{21} - C_{20})}$$

$$J_1 = \frac{S_1^2\left[(C_{11} - C_{10}) - C_{10} \ln\left(\frac{C_{11}}{C_{10}}\right)\right]}{R_1^3 (C_{11} - C_{10})^2}$$

$$J_2 = \frac{S_1^3\left[\frac{(C_{11}^2 - C_{10}^2)}{2} - 2C_{10}(C_{11} - C_{10}) + C_{10}^2 \ln\left(\frac{C_{11}}{C_{10}}\right)\right]}{R_1^3 (C_{11} - C_{10})^3}$$

or, for $C_{11} = C_{10}$, $C_{21} = C_{20}$, and $R_1 \neq R_2$,

$$I_3 = \frac{-\left(\frac{1}{R_2^2} - \frac{1}{R_1^2}\right)}{2C_1 \cos\phi}$$

$$I_6 = \frac{-\left(\frac{1}{R_2^2} - \frac{1}{R_1^2}\right)}{2C_2 \cos\phi}$$

$$J_1 = \frac{\left[R_1 \frac{\left(\frac{1}{R_2^2} - \frac{1}{R_1^2}\right)}{2} - \left(\frac{1}{R_2} - \frac{1}{R_1}\right)\right]}{C_1 \cos^2\phi}$$

$$J_2 = \frac{\left[\frac{R_1^2}{2}\left(\frac{1}{R_2^2} - \frac{1}{R_1^2}\right) + 2R_1\left(\frac{1}{R_2} - \frac{1}{R_1}\right) + \ell n\left(\frac{R_2}{R_1}\right)\right]}{C_1 \cos^3\phi}$$

or, for $C_{11}R_1 - C_{10}R_2 = 0$, $C_{21}R_1 - C_{20}R_2 = 0$, $R_2 \neq R_1$,

$$I_3 = \frac{-S_1\left(\frac{1}{R_2^3} - \frac{1}{R_1^3}\right)}{3(C_{11} - C_{10})}$$

$$I_6 = \frac{-S_1\left(\frac{1}{R_2^3} - \frac{1}{R_1^3}\right)}{3(C_{21} - C_{20})}$$

$$J_1 = \frac{S_1\left[\frac{R_1}{3}\left(\frac{1}{R_2^3} - \frac{1}{R_1^3}\right) - \frac{1}{2}\left(\frac{1}{R_2^2} - \frac{1}{R_1^2}\right)\right]}{\cos\phi\,(C_{11} - C_{10})}$$

$$J_2 = \frac{S_1^2\left[R_1\left(\frac{1}{R_2^2} - \frac{1}{R_1^2}\right) - \left(\frac{1}{R_2} - \frac{1}{R_1}\right) - \frac{R_1^2}{3}\left(\frac{1}{R_2^3} - \frac{1}{R_1^3}\right)\right]}{\cos\phi\,(C_{11} - C_{10})^2}$$

or otherwise let

$$\alpha = \frac{R_1}{S_1}(C_{11} - C_{10}) - C_{10}\cos\phi$$

$$\beta = \frac{R_1}{S_1}(C_{21} - C_{20}) - C_{20}\cos\phi;$$

then

$$I_1 = \frac{1}{\alpha}\ell n\left(\frac{C_{11}R_1}{C_{10}R_2}\right)$$

$$I_2 = \frac{1}{\alpha}\left[\left(\frac{1}{R_2} - \frac{1}{R_1}\right) + \left(\frac{C_{11} - C_{10}}{S_1}\right)\right]$$

$$I_3 = \frac{1}{2\alpha}\left[\left(\frac{1}{R_2^2} - \frac{1}{R_1^2}\right) + 2\left(\frac{C_{11} - C_{10}}{S_1}\right)I_2\right]$$

$$I_4 = \frac{1}{\beta}\ell n\left(\frac{C_{21}R_1}{C_{20}R_2}\right)$$

$$I_5 = \frac{1}{\beta}\left[\left(\frac{1}{R_2} - \frac{1}{R_1}\right) + \left(\frac{C_{21} - C_{20}}{S_1}\right)I_4\right]$$

$$I_6 = \frac{1}{2\beta}\left[\left(\frac{1}{R_2^2} - \frac{1}{R_1^2}\right) + 2\left(\frac{C_{21} - C_{20}}{S_1}\right) I_5\right]$$

$$J_1 = \frac{-S_1\left[\left(\frac{1}{R_2^2} - \frac{1}{R_1^2}\right) + 2C_{10}\cos\phi\, I_3\right]}{2(C_{11} - C_{10})\cos\phi}$$

$$J_2 = \frac{-S_1\left\{\frac{S_1}{R_2^2} - J_1\left[\frac{R_1}{S_1}(C_{11} - C_{10}) - C_{10}\cos\phi\right] - C_{10} R_1 I_3\right\}}{(C_{11} - C_{10})\cos\phi}.$$

Inverting $[f_{11}]$ yields $[k_{11}]$.

From static equilibrium the relation between the shear and bending moment at node 1 to the shear and bending moment at node 2 is

$$\begin{bmatrix} V_2 \\ M_2 \end{bmatrix} = \begin{bmatrix} -1 & 0 \\ -L & -1 \end{bmatrix} \begin{bmatrix} V_1 \\ M_1 \end{bmatrix} \tag{39}$$

or

$$[\gamma] = \begin{bmatrix} -1 & 0 \\ -L & -1 \end{bmatrix} \tag{40}$$

Having found $[k_{11}]$ and $[\gamma]$, the remaining coefficients can be found using Eq. (24).

It is required that a transformation matrix be generated to rotate the elemental stiffness matrix into the system coordinate system. That is, form the matrix $[C_{om}]$ such that

$$\{q\} = [C_{om}]\{x\}, \tag{41}$$

where $\{x\}$ is the elemental coordinates and $\{q\}$ is the system coordinates. The construction of $[C_{om}]$ consists of either finding the direction cosines of each elemental coordinate with respect to each system coordinate or finding the projection of each unit elemental coordinate on each system coordinate, both of which are simple problems in geometry.

JOINTS

The effects of joints on mode shapes and frequencies are well known; even so, joints are often omitted from dynamic models.

Presented here is a systematic method of including both pinned joints and spring joints in the stiffness matrix of an element. The approach used is to modify an elemental stiffness matrix by the use of influence coefficients at each end for spring joints and the static removal of degrees of freedom for pinned joints.

Spring Joints

Given the elemental stiffness matrix $[K_1]$ and the influence coefficient matrix $[a]$ of the joints on the ends of the element, the deflections including the joints are related to those not including joints by the transformation shown in Fig. 3, where

$$\{x_2 - x_1\} = [a]\{F\}, \tag{42}$$

but

$$\{F\} = [K_1]\{x_1\}. \tag{43}$$

Fig. 3. Transformation relating deflections including joints to those not including joints

Solving for x_1 in Eq. (42) and substituting into Eq. (43) yields:

$$\{F\} = [K](-[a]\{F\} + \{x_2\}) .$$

Solving for $\{F\}$ yields

$$\{F\} = ([I] + [K_1][a])^{-1}[K_1]\{x_2\} .$$

Thus, the new stiffness matrix for the element which includes spring joint flexibilities is

$$[K_2] = ([I] + [K_1][a])^{-1}[K_1] . \qquad \text{(transformation 1)}$$

Note that $[a]$ is not necessarily diagonal.

Pinned Joints

To incorporate pinned joints, it is imposed that zero external forces be applied to the degree of freedom in x_1 corresponding to the pin joint. The force deflection equation is partitioned such that

$$\left\{\begin{array}{c} F_i \\ \hline 0 \end{array}\right\} = \left[\begin{array}{c|c} K_{ii} & K_{ij} \\ \hline K_{ji} & K_{jj} \end{array}\right] \left\{\begin{array}{c} x_i \\ \hline x_j \end{array}\right\} .$$

Expanding yields

$$\{F_i\} = [K_{ii}]\{x_i\} + [K_{ij}]\{x_j\} \qquad (44)$$

$$\{0\} = [K_{ji}]\{x_i\} + [K_{jj}]\{x_j\} . \qquad (45)$$

Solving for x_j in Eq. (45) and substituting into Eq. (44),

$$\{F_i\} = [K_{ii}]\{x_i\} - [K_{ij}][K_{jj}]^{-1}[K_{ji}]\{x_i\} . \qquad (46)$$

(It must be noted that $[K_{jj}]$ may be singular unless care in modeling is taken to insure that no rigid body motion is possible.)

Rearranging Eq. (46) yields

$$\{F_i\} = ([K_{ii}] - [K_{ij}][K_{jj}]^{-1}[K_{ji}])\{x_i\} .$$

Thus, the new stiffness matrix for the element with the inclusion of pin joints is

$$[K_2] = ([K_{ii}] - [K_{ij}][K_{jj}]^{-1}[K_{ji}]) . \qquad \text{(transformation 2)}$$

For elements with both pinned and spring joints, both transformations 1 and 2 must be applied sequentially.

INFINITE STIFFNESS

In many structures, it is convenient to use infinite stiffness elements in conjunction with joint flexibilities as a means of reducing degrees of freedom without losing significance in the structure to be analyzed.

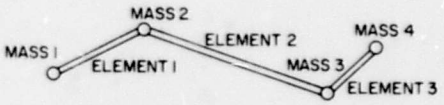

Fig. 4. Representation of three-element substructure

Consider the case where a substructure is composed of three elements as represented by Fig. 4. Suppose that it is necessary to represent this system by only two mass stations, say mass 1 and mass 4. Then elements 1 and 3 may be treated as infinitely stiff if the appropriate flexibilities are introduced as joint flexibilities at the ends of those elements. It may also be expedient to treat elements such as cylinders with protuberances as having infinitely stiff extensions from their points of description (geometric center) to the end of the protuberance. For example, consider the cylinder represented by Fig. 5. If the cylinder has stiffness properties described at station 1 and if it is required to attach the beam to station 2, this operation is accomplished by (a) making element 1 infinitely stiff and including the local flexibility of the cylinder at station 2 as joints at that station, and (b) requiring station 2 to have zero mass.

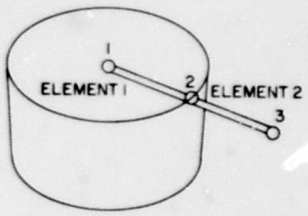

Fig. 5. Representation of cylinder with protuberance

If it is necessary to use a rigid element in the dynamic modeling of a structure, an infinite magnitude term will be present in the stiffness matrix. To avoid the implications of an infinite term in the stiffness matrix, the displacement of one end of the element possessing the infinite stiffness may be expressed in terms of the displacements at the opposite end combined with rigid body rotations.

Fig. 6. Rigid element in a dynamic model

Suppose, for example, that it is necessary to include a rigid element in a dynamic model (Fig. 6). One method of treating this problem is as follows. The displacements at end 2 (see Fig. 6) can be expressed in terms of displacements at end 1 by

$$\{x_2\} = [\beta]\{x_1\} \tag{47}$$

where $[\beta]$ is the rigid body compatibility matrix

$$\begin{Bmatrix} x_7 \\ x_8 \\ x_9 \\ x_{10} \\ x_{11} \\ x_{12} \end{Bmatrix} = \begin{bmatrix} 1 & 0 & 0 & 0 & 0 & 0 \\ 0 & 1 & 0 & 0 & 0 & L \\ 0 & 0 & 1 & 0 & -L & 0 \\ 0 & 0 & 0 & 1 & 0 & 0 \\ 0 & 0 & 0 & 0 & 1 & 0 \\ 0 & 0 & 0 & 0 & 0 & 1 \end{bmatrix} \begin{Bmatrix} x_1 \\ x_2 \\ x_3 \\ x_4 \\ x_5 \\ x_6 \end{Bmatrix} \tag{48}$$

Therefore, for the complete system consisting of many elements, some of which are infinitely stiff,

$$\left\{ \begin{array}{c} x \\ \hline x_R \end{array} \right\} \left[\begin{array}{c} I \\ \hline \beta \end{array} \right] \{x\} = [T]\{x\} \tag{49}$$

where the x_R are the redundant coordinates to be eliminated, [I] is the identity matrix, and [T] expresses the relationship between all dependent coordinates.

Operating on the equations of motion yields

$$[T]^T [m][T]\{\ddot{x}(t)\} + [T]^T [c][T]\{\dot{x}(t)\} + [T]^T [k][T]\{x(t)\} = [T]^T \{f(t)\} \tag{50}$$

or

$$[M]\{\ddot{q}(t)\} + [C]\{\dot{q}\} + [K]\{q\} = \{F(t)\} \tag{51}$$

where the $\{q\}$ are generalized coordinates.

However, if we are analyzing a structure requiring 250 degrees of freedom and use a computer that will multiply in 10 machine cycles and perform at 0.5×10^6 machine cycles per second, then approximately 55 hr is required to perform the multiplications indicated in Eq. (50). Therefore, this approach is impractical.

The generality of the above approach will be sacrificed for a more usable approach which is limited to infinitely stiff extensions and which will suffice if only one flexible member is attached to the infinitely stiff member. In practice, many members may be connected to an infinitely stiff extension by treating each member as being attached to a different extension, although the extensions are really one and the same. Care must be taken to insure that all these extensions remain coincident; i.e., there may be no joint flexibilities at the mass station where they are joined. Therefore, the only generality sacrificed is that an infinitely stiff extension must be infinitely stiff in all directions, whereas the previous approach would allow infinite stiffness in selected directions. This remaining loss may be overcome by the inclusion of the proper joint flexibilities on the ends of the extensions.

The alternate approach is as follows (see Fig. 7). Denote the coordinates at stations 2 and 3 by $\{q_{8s}\}$ and those at stations 1 and 4 by $\{q\}$, both systems being aligned with system coordinates $\{q\}$.

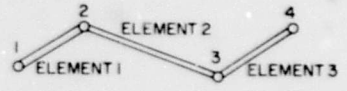

Fig. 7. Rigid element in a dynamic model

The transformation that relates forces at the $\{q\}$ coordinates in terms of forces at the $\{q_{8s}\}$ coordinates is to be found.

The strain energy of the flexible element may be expressed as

$$U = \frac{1}{2} \{q_{\theta s}\}^T [K_{\theta s}] \{q_{\theta s}\} . \tag{52}$$

Since an infinitely stiff element can possess no strain energy, and since strain energy is invariant with respect to a coordinate transformation, the system of all three elements must possess the same strain energy,

$$U = \frac{1}{2} \{q\}^T [K] \{q\} . \tag{53}$$

Redefining $[\beta]$ in Eq. (47) as

$$\{q_{\theta s}\} = [\beta] \{q\} , \tag{54}$$

and using the reversal law of transposed products,

$$\{q_{\theta s}\}^T = \{q\}^T [\beta] . \tag{55}$$

Comparing Eqs. (52) and (53) after substituting for the displacements from Eqs. (54) and (55), we see that

$$\{q\}^T [K] \{q\} = \{q\}^T [\beta]^T [K_{\theta s}] [\beta] \{q\} , \tag{56}$$

and, since this equation must hold for all $\{q\}$,

$$[K] = [\beta]^T [K_{\theta s}] [\beta] . \tag{57}$$

Defining ${}_1L_i$ as the length of the projection of the infinitely stiff element 1 on the system ith axis, and similarly for ${}_2L_i$, then it is apparent that

$$[\beta] = \left[\begin{array}{cccccc:cccccc}
1 & 0 & 0 & 0 & {}_1L_3 & -{}_1L_2 & & & & & & \\
0 & 1 & 0 & -{}_1L_3 & 0 & {}_1L_1 & & & & & & \\
0 & 0 & 1 & {}_1L_2 & -{}_1L_1 & 0 & & & & & & \\
0 & 0 & 0 & 1 & 0 & 0 & & & 0 & & & \\
0 & 0 & 0 & 0 & 1 & 0 & & & & & & \\
0 & 0 & 0 & 0 & 0 & 1 & & & & & & \\
\hdashline
 & & & & & & 1 & 0 & 0 & 0 & {}_2L_3 & -{}_2L_2 \\
 & & & & & & 0 & 1 & 0 & -{}_2L_3 & 0 & {}_2L_2 \\
 & & & & & & 0 & 0 & 1 & {}_2L_2 & -{}_2L_1 & 0 \\
 & & 0 & & & & 0 & 0 & 0 & 1 & 0 & 0 \\
 & & & & & & 0 & 0 & 0 & 0 & 1 & 0 \\
 & & & & & & 0 & 0 & 0 & 0 & 0 & 1
\end{array}\right] \tag{58}$$

The joint flexibilities associated with stations 2 and 3 must be used to modify $[K_{\theta s}]$ before performing the operation indicated in Eq. (57). The joint flexibilities associated with stations 1 and 4 are used to modify $[K]$ after using Eq. (57).

It is clear then that all of the generality of the previous method is included in the alternate approach. Since all operations are now performed on elemental stiffness matrices instead of the

system stiffness matrix, computer time is reduced to less than 1 sec for each infinitely stiff element, as compared to a total time of approximately 65 hr for the previous method.

MASS MATRIX

Much has been done on the generation of stiffness matrices for elements, but relatively little has been done on the generation of a realistic mass matrix. The old tried-and-true methods of lumping masses to generate a diagonal mass matrix may be fine for some systems, but problems occur depending on the desired results. The simple uniform cantilever beam represented as a single lump at its end is an example of such a problem structure. If it is desired to find the fundamental frequency of the beam, it is necessary to lump 34/140 of its mass at the end; but then loads at its base are in general not correct. If a different lumping is used to produce the proper shear load at a given frequency of excitation, then the natural frequency and moment will not be correct, etc.

A realistic approach to eliminate the problem of lumping mass is not to lump at all, but to generate a system mass matrix which incorporates mass coupling. The method presented here is to generate a first approximation to the elemental mass matrix and then to generate the system mass matrix by simple matrix manipulations.

By use of energy considerations it is shown [2] that a first approximation to the mass matrix for an element is

$$m_{ij} = \int_0^{\ell} m(x)\, \varphi_i(x)\, \varphi_j(x)\, dx\,, \tag{59}$$

where $m(x)$ is the mass distribution and $\varphi_k(x)$ is an assumed deflection of the element with coordinate k displaced unity and all other coordinates fixed. The $\varphi(x)$'s used for the coordinate system illustrated in Fig. 8 are as follows:

Fig. 8. Coordinate system

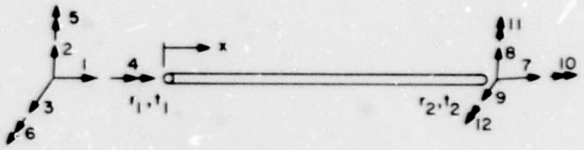

$$\varphi_1(x) = 1 - \frac{x}{\ell}$$

$$\varphi_2(x) = 1 - \frac{3x^2}{\ell^2} + \frac{2x^3}{\ell^3}$$

$$\varphi_3(x) = \varphi_2(x)$$

$$\varphi_4(x) = 1 - \frac{x}{\ell}$$

$$\varphi_5(x) = x - \frac{2x^2}{\ell} + \frac{x^3}{\ell^2}$$

$$\varphi_6(x) = \varphi_5(x)$$

$$\varphi_7(x) = \frac{x}{\ell}$$

$$\varphi_8(x) = \frac{3x^2}{\ell^2} - \frac{2x^3}{\ell^3}$$

$$\varphi_9(x) = \varphi_8(x)$$

$$\varphi_{10}(x) = \frac{x}{\ell}$$

$$\varphi_{11}(x) = \frac{-x^2}{\ell} + \frac{x^3}{\ell^2}$$

$$\varphi_{12}(x) = \varphi_{11}(x)$$

Performing the indicated integration in Eq. (59) for a mass distribution associated with a cone of linearly varying thickness yields the elemental mass matrix

$$[m] = \begin{bmatrix} m_{1,1} & & & & & & m_{1,7} & & & & & \\ & m_{2,2} & & & & m_{2,6} & & m_{2,8} & & & & m_{2,12} \\ & & m_{3,3} & & m_{3,5} & & & & m_{3,9} & & m_{3,11} & \\ & & & m_{4,4} & & & & & & m_{4,10} & & \\ & & & & m_{5,5} & & & & m_{5,9} & & m_{5,11} & \\ & & & & & m_{6,6} & & m_{6,8} & & & & m_{6,12} \\ & & & & & & m_{7,7} & & & & & m_{7,12} \\ & & & \text{SYM} & & & & m_{8,8} & & & m_{8,11} & \\ & & & & & & & & m_{9,9} & m_{9,10} & & \\ & & & & & & & & & m_{10,10} & & \\ & & & & & & & & & & m_{11,11} & \\ & & & & & & & & & & & m_{12,12} \end{bmatrix}$$

where

$$m_{1,1} = \frac{2\pi\rho\ell}{60}(12t_1r_1 + 3r_1t_2 + 3r_2t_1 + 2r_2t_2)$$

$$m_{1,7} = \frac{2\pi\rho\ell}{60}(3t_1r_1 + 2r_1t_2 + 2r_2t_1 + 3r_2t_2)$$

$$m_{2,2} = \frac{2\pi\rho\ell}{630}(145t_1r_1 + 35r_1t_2 + 35r_2t_1 + 19r_2t_2)$$

$$m_{2,6} = \frac{2\pi\rho\ell^2}{7560}(195t_1r_1 + 75t_2r_1 + 75t_1r_2 + 51t_2r_2)$$

$$m_{2,8} = \frac{2\pi\rho\ell}{420}(82t_1r_1 - 55t_2r_1 - 55t_1r_2 + 82t_2r_2)$$

$$m_{2,12} = \frac{-2\pi\rho\ell^2}{2520}(25t_1r_1 + 17t_2r_1 + 17t_1r_2 + 19t_2r_2)$$

$$m_{3,3} = \frac{2\pi\rho\ell}{630}(145t_1r_1 + 35r_1t_2 + 35r_2t_1 + 19r_2t_2)$$

$$m_{3,5} = \frac{-2\pi\rho\ell^2}{7560}(195t_1r_1 + 75t_2r_1 + 75t_1r_2 + 51t_2r_2)$$

$$m_{3,9} = \frac{2\pi\rho\ell}{420}(82t_1r_1 - 55t_2r_1 - 55t_1r_2 + 82t_2r_2)$$

$$m_{3,11} = \frac{2\pi\rho\ell^2}{2520}(25t_1r_1 + 17t_1r_2 + 17t_2r_1 + 19t_2r_2)$$

$$m_{4,4} = \frac{2\pi\rho\ell}{420}(30r_1^3t_1 + 30r_1^2r_2t_1 + 12r_1r_2^2t_1 + 3r_2^3t_1 + 10r_1^3t_2 + 12r_1^2r_2t_2 + 6r_1r_2^2t_2 + 4r_2^3t_2$$

$$m_{8,10} = \frac{2\pi\rho\ell}{240}(10r_1^3t_1 + 12r_1^2r_2t_1 + 9r_1r_2^2t_1 + 4r_2^3t_1 + 4r_1^3t_2 + 9r_1^2r_2t_2 + 12r_1r_2^2t_2 + 10r_2^3t_2$$

$$m_{5,5} = \frac{2\pi\rho\ell^3}{52920}(205t_1r_1 + 105r_1t_2 + 105r_2t_1 + 84r_2t_2)$$

$$m_{5,9} = \frac{-2\pi\rho\ell^2}{52920}(399t_1r_1 + 357r_1t_2 + 357r_2t_1 + 525r_2t_2)$$

$$m_{5,11} = \frac{-2\pi\rho\ell^3}{17640}(35r_1t_1 + 28r_1t_2 + 28r_2t_1 + 35r_2t_2)$$

$$m_{6,6} = \frac{2\pi\rho\ell}{52920}(205t_1r_1 + 105r_1t_2 + 105r_2t_1 + 84r_2t_2)$$

$$m_{6,8} = \frac{-2\pi\rho\ell^2}{52920}(399t_1r_1 + 357r_1t_2 + 357r_2t_1 + 525r_2t_2)$$

$$m_{6,2} = \frac{-2\pi\rho\ell^3}{17640}(35r_1t_1 + 28r_1t_2 + 28r_2t_1 + 35r_2t_2)$$

$$m_{7,7} = \frac{2\pi\rho\ell}{360}(12r_1t_1 + 18r_1t_2 + 18r_2t_1 + 72r_2t_2)$$

$$m_{8,8} = \frac{2\pi\rho\ell}{630}(19r_1t_1 + 35r_1t_2 + 35r_2t_1 + 145r_2t_2)$$

$$m_{8,12} = \frac{2\pi\rho\ell^2}{7560}(51r_1t_1 + 75r_2t_1 + 75r_1t_2 + 195r_2t_2)$$

$$m_{9,9} = \frac{2\pi\rho\ell}{630}(19r_1t_1 + 35r_1t_2 + 35r_2t_1 + 145r_2t_2)$$

$$m_{9,11} = \frac{2\rho\pi\ell^2}{7560}(51r_1t_1 + 75r_1t_2 + 75r_2t_1 + 195r_2t_2)$$

$$m_{10,10} = \frac{2\pi\rho\ell}{420}(4r_1^3t_1 + 6r_1^2r_2t_1 + 12r_1r_2^2t_1 + 10r_2^3t_1 + 3r_1^3t_2 + 12r_1^2r_2t_2 + 30r_1r_2^2t_2 + 60r_2^3t_2$$

$$m_{11,11} = \frac{2\pi\rho\ell^3}{52920}(84r_1t_1 + 105r_1t_2 + 105r_2t_1 + 205r_2t_2)$$

$$m_{12,12} = \frac{2\pi\rho\ell^3}{52920}(84r_1t_1 + 105r_1t_2 + 105r_2t_1 + 205r_2t_2).$$

These results degenerate exactly to the consistent masses presented in Ref. [3]. It must be noted that the above mass matrix includes only the structural mass of the elements. "Non-load-carrying" masses such as components and bracketry must be added separately.

Once the elemental mass matrices are generated, they are transformed into system coordinates and added to the system mass matrix in exactly the same manner that the elemental stiffness matrix is added to the system stiffness matrix.

TREATMENT OF A SINGULAR MASS MATRIX

If coordinates exist in the structure where there is very little mass or where it is undesirable to expend degrees of freedom, one may retain the stiffness properties of the structure by placing a zero mass at the point in question. The generalized equations of motion are then partitioned as follows:

$$\left[\begin{array}{cc} M_{11} & M_{12} \\ \hline M_{21} & M_{22} \end{array}\right] \left\{\begin{array}{c} \ddot{q}_1(t) \\ \hline \ddot{q}_2(t) \end{array}\right\} + \left[\begin{array}{cc} C_{11} & C_{12} \\ \hline C_{21} & C_{22} \end{array}\right] \left\{\begin{array}{c} \dot{q}_1(t) \\ \hline \dot{q}_2(t) \end{array}\right\} + \left[\begin{array}{cc} K_{11} & K_{12} \\ \hline K_{21} & K_{22} \end{array}\right] \left\{\begin{array}{c} q_1(t) \\ \hline q_2(t) \end{array}\right\} = \left\{\begin{array}{c} F_1(t) \\ \hline F_2(t) \end{array}\right\}, \tag{60}$$

where the q_2 refers to the zero-mass coordinates.

If it is required that no inertial forces and no damping forces are applied at the zero-mass coordinates, then the following relationship may be used to eliminate the zero-mass coordinates:

$$[K_{21}]\{q_1(t)\} + [K_{22}]\{q_2(t)\} = \{F_2(t)\}, \tag{61}$$

and

$$\{q_2(t)\} = [K_{22}]^{-1} (\{F_2(t)\} - [K_{21}]\{q_1(t)\}). \tag{62}$$

Note that $[K_{22}]$ is not singular unless there is no mass at coordinates such that the order of $[K_{22}]$ is greater than the rank of the original system stiffness matrix, or unless rigid body motion of the $q_2(t)$ coordinate can occur.

Substituting Eq. (62) into the expansion of the upper half of Eq. (60) and rearranging yields

$$[M_{11}]\{\ddot{q}_1(t)\} + [C_{11}]\{\dot{q}_1(t)\} + ([K_{11}] - [K_{12}][K_{22}]^{-1}[K_{21}])\{q_1(t)\} = \{F_1(t)\} - [K_{12}][K_{22}]^{-1}\{F_2(t)\}, \tag{63}$$

where the mass matrix is now nonsingular. When $\{q_1(t)\}$ is found, $\{q_2(t)\}$ is determined by the use of Eq. (62), and therefore internal loads and displacements at a zero-mass coordinate may still be determined.

DYNAMICAL MATRIX

Having found the final form of the system stiffness and mass matrices, it is now desired to construct a system dynamical matrix. The standard approach of

$$[D] = [M]^{-1}[K] \tag{64}$$

or

$$[\tilde{D}] = [K]^{-1}[M], \tag{65}$$

in general, develops a nonsymmetric dynamical matrix. It is often necessary, however, to generate a symmetrical dynamical matrix for the use of most eigenvalue-eigenvector computer programs. With some of these computer programs, an added advantage is that only half the dynamical matrix need be generated, thus minimizing storage requirements. A standard procedure for generating a symmetrical dynamical matrix is to perform a coordinate transformation by mass weighting the system coordinates, thus:

$$\{\tau\} = [M]^{1/2}\{q\}\,, \tag{66}$$

where $\{\tau\}$ is the new coordinate system, $[M]$ is the system mass matrix, and $\{q\}$ is the initial coordinate system. The dynamical matrix is now formed as

$$[D] = [M]^{-T/2}[K][M]^{-1/2} \tag{67}$$

yielding a symmetric dynamical matrix $[D]$. When $[M]$ is a diagonal matrix, the formation of $[M]^{1/2}$ is simply

$$[M]^{1/2} = \begin{bmatrix} M_{1,1}^{1/2} & & & 0 \\ & M_{2,2}^{1/2} & & \\ & & \ddots & \\ 0 & & & M_{m,m}^{1/2} \end{bmatrix} \tag{68}$$

But, when $[M]$ is not a diagonal matrix because of mass coupling, the generation of $[M]^{1/2}$ is much more difficult. An effective way to produce a pseudo $[M]^{1/2}$ is found in Ref. [4]. A matrix $[B]$ is found such that

$$[M] = [B]^T[B]\,, \tag{69}$$

where $[B]$ is a triangular matrix and is generated by the algorithm

$$B_{ii} = \left(M_{ii} - \sum_{k=1}^{i-1} B_{ik}^2\right)^{1/2} \quad \text{for } i = j\,,$$

and

$$B_{ij} = \frac{\left(M_{ij} - \sum_{k=1}^{i-1} B_{ik}B_{jk}\right)}{B_{jj}} \quad \text{for } i \neq j\,. \tag{70}$$

Thus the new dynamical matrix becomes

$$[D] = [B]^{-1}[K][B]^{-T}\,, \tag{71}$$

which is symmetric. The eigenvalues of the system have not been changed from the original system coordinates, and the eigenvectors may be transformed back into the nonmass-weighted system by the inverse of Eq. (66). Thus eigenvectors of Eq. (71) as $\{\xi\}$ are converted to eigenvectors of Eq. (64) as $\{\eta\}$ by

$$\{\eta\} = [B]^{-1}\{\xi\}\,. \tag{72}$$

CONCLUSIONS

The procedures described above are presently used by Hughes Aircraft Company, Space Systems Division, in the computer program Matrix Analysis Routine for Structures (MARS) on a G.E. 635 computer. Present size limits are 246 degrees of freedom, 100 zero-mass coordinates, and 100 mass stations. There are no restrictions on the number of elements. Most computations are performed in double precision, including the eigenvalue and eigenvector solution which is a modification of the Share program BIGMAT SDA 3202-01. A model of a dual-spin spacecraft consisting of 44 masses, 55 elements, 96 zero-mass coordinates, 38 infinite stiffness extensions, and 82 sets of joint flexibilities required 12 min of computer time to generate the system dynamical matrix and to solve for 50 modes and frequencies.

For a 246-degree-of-freedom system of known solution, the results generated by MARS agree with the theoretical modes and frequencies to at leat five significant figures.

REFERENCES

1. R. A. Frazer, W. J. Duncan, and A. R. Collar, Elementary Matrices (Macmillan, New York), 1946

2. W. C. Hurty and M. F. Rubinstein, Dynamics of Structures (Prentice Hall, Englewood Cliffs, N.J.), 1965

3. J. S. Archer, "Consistent Mass Matrix for Distributed Mass System," Space Technology Laboratories EM-13-4, Feb. 1963

4. B. Wendroff, Theoretical Numerical Analysis (Academic Press, New York), 1966, p. 126

BIBLIOGRAPHY

J. S. Archer, "Consistent Matrix Formulation for Structural Analysis Using Influence Coefficient Techniques," Space Technology Laboratories EM 13-24, Nov. 1963

S. H. Crandall and W. D. Mark, Random Vibration in Mechanical Systems (Academic Press, New York), 1963

M. F. Gardner and J. L. Barnes, Transients in Linear Systems (Wiley, New York), 1942

S. A. Ledbetter and V. L. Alley, "Predictions and Measurement of Natural Vibrations of Multistage Launch Vehicles," AIAA J., 1(2):377 (1963)

L. A. Pipes, Matrix Methods for Engineers (Prentice Hall, Englewood Cliffs, N.J.), 1963

M. F. Rubinstein, Matrix Computer Analysis of Structures (Prentice Hall, Englewood Cliffs, N.J.), 1966

J. H. Wilkinson, Rounding Errors in Algebraic Processes (Prentice Hall, Englewood Cliffs, N.J.), 1964

* * *